Department of Chemical and Process Engineering

COMPUTATIONAL MODELLING OF SELF-ASSEMBLING TRIBLOCK COPOLYMER SURFACTANTS FOR USE IN THE SYNTHESIS MESOPOROUS SILICA

Olivia Nile Sobek

This dissertation is submitted for the degree of

Doctor of Philosophy

December 2018

DECLARATION

This thesis is the result of the author's original research. It has been composed by the author and has not been previously submitted for examination, which has led to the award of a degree.

Olivia Nile Sobek
Glasgow, December 2018

CONTENTS

ABSTRACT

Block copolymers find applications in many fields, including adhesives, plastics, drug delivery and photonics. Several of these rely on the ability of block copolymers to self-assemble into ordered mesophases in solution. One such application of particular interest to our research group is their use as templates in the synthesis of porous silica materials, such as SBA-15. Because of their highly ordered pores, high surface areas, high functionality and low cost, mesoporous silicas have been of great interest for an increasing variety of applications and research. Understanding the synthesis mechanism for this class of materials, however, models that can predict how block copolymer templates self-assemble in aqueous solution. This study aims to produce an accurate coarse-grained, CG, model of self-assembling block copolymers, including those used in the synthesis of SBA-15 mesoporous silica (i.e., Pluronic surfactants). Such a model will enable us to probe the large time and length scales that are needed to describe the mesostructure formation from solution, thus clarifying the mechanisms by which these materials are formed.

Our approach was based on the established MARTINI CG force field, which has been previously applied to model these systems. We have found that existing models were unable to accurately describe micelle aggregation self-assembly of Pluronic surfactants, although they are designed to match single-chain properties.

To parameterise and validate new self-assembly models for Pluronics, we performed a a series of intermediate CG model parameterisations; alkane models, PEO and PPO models, and finally, Pluronic surfactant models. We have thus systematically tested the existing MARTINI parameters for the alkane solvent basis of these systems against experimental values such as density, Gibbs free energies of solvation, enthalpies of vaporisation, self-diffusion coefficients, and radii of gyration. By noting where the MARTINI model was lacking, we were then able to parameterise 1-bead, 2-bead, 3-bead, and 4-bead 2:1, 3:1, 4:1, and 5:1 mapped alkane models, methodically matching Lennard-Jones and bonded parameters to known density, Gibbs free energies

of solvation, and enthalpies of vaporisation properties, and validating the models against experimental self-diffusion coefficients and shear viscosity, and simulated radii of gyration. These models were then parameterised for non-bonded interaction parameters with MARTINI water, specifically for free energy of solvation, and further validated for use in polyethylene, a polymer with a similar carbon backbone to alkanes, by matching densiity and radii of gyration.

We then validated seven existing coarse-grained PEO and four existing coarse-grained PPO models, for 1-bead and 2-bead model simulations, against known experimental and simulated data such as Gibbs free energies of solvation, enthalpies of vaporisation, densities, and self-diffusion coefficients. The two models that best matched the 2-bead simulation results, one for PEO and one for PPO, were chosen and then calibrated for free energy of solvation in our 4:1 and 2:1 mapped hexadecane and hexane models, and a parameterised 3.5:1 heptane model that was interpolated from our original alkane model results. Longer chains of these two models were then validated against simulated end-to-end distances, relaxation times and radii of gyration data, and were observed in polar and nonpolar solvents to ensure their behaviour adhered to theory for self-assembly (i.e. the models displayed the correct hydrophobicity and hydrophilicity typical of PEO and PPO within these solvents).

When we had established alkane and PEO and PPO models that had the best adherence to experimental and simulated data, we finally moved on to Pluronic surfactant simulations. We chose suitable PEO-PPO interaction parameters from the same study as our chosen PPO model, and we create eight Pluronic models for Pluronic L31, L35, L44, L62, L64, P85, P123, and F38. Melts of seven of these models were compared to experimental and simulated properties including densities, shear viscosities, heat capacities, and radii of gyration, and larger chain simulations of three of the models, Pluroincs L35, L44, and P123 were run in MARTINI water. These larger simulations, as well as another of Pluronic P123 in our 2:1 mapped hexane model, were evaluated for self-assembly and aggregation, and the micellisation free energies and aggregation numbers of the resulting aggregates were calculated against experimental data and theory.

This process has lead to improved mapping schemes and adjusted parameters for alkane solvent models, PEO and PPO models with the most accurate properties in themselves and in those alkane solvents, and ultimately, Pluronic models with self-assembly behaviour. It is unfortunate, however that this process also inevitably ended up being more time-consuming and difficult than expected and we were unable to progress any farther with this thesis. We expect that in the future our models will be combined with existing models of silica precursors to effectively model and analyse SBA-15 synthesis.

ACKNOWLEDGEMENTS

These past few years have been mired by personal and family tragedies, but while challenging at times, this PhD. has constantly pushed me towards self-improvement and has taught me more than I thought possible.

I am extremely grateful for my supervisor, Miguel Jorge, for all of his help, and infinite patience and support, throughout this process. I'd also especially like to thank my parents, Mark Sobek and Sena Sobek, my boyfriend, Matt Sim, and all of my wonderful friends in and out of Strathclyde, for their overwhelming love and support during my PhD., and for keeping me from pulling out my hair in the stressful moments.

LIST OF FIGURES

LIST OF TABLES

NOMENCLATURE

Abbreviations:

AA	atomistic, all-atom
BASF	Badische Anilin- und Soda-Fabrik
CG	coarse-grained
CMC	critical micelle concentration
CRW	conditional reversible work
CTAB	cetyltrimetylammonium bromide
DE	dimethyl ether
DEE	1,2-diethoxyethane
DME	1,2-dimethoxyethane
DMP	1,2-dimethoxypropane
DPD	Dissipative Particle Dynamics
FESEM	Field Emission Scanning Electron Microscope
FFT	fast Fourier transformation
GROMACS	GROningen MAchine for Chemical Simulations
HCl	hydrochloric acid
LJ	Lennard-Jones
MCM-41	Mobil Composition of Matter No. 41
MD	molecular dynamics
MOE	methoxyethane
NMR	nuclear magnetic resonance
NPT	system where number, pressure, and temperature are constant
NVT	system where number, volume, and temperature are constant
PEE	polyethyethylene
PEG	polyethylene glycol
PEO	polyethylene oxide
PME	Particle Mesh Ewald
POPC	palmitoyl-oleoyl- phosphatidyl-choline
PPO	polypropylene oxide

PS	polystyrene
PTB	polybutadiene
RBCG	Residue-Based Coarse Graining
SAPO-n	silicoaluminophosphate
SAXD	small angle x-ray diffractions
SBA-15	Santa Barbara Amorphous-15
SMILES	simplified molecular-input line-entry system TEOS tetraethoxysilane
TEM	transmission electron microscopy
TGA	thermogravimetric analysis
TMB	trimethylbenzene
VMD	molecular dynamics visualization programme
XRD	X-ray diffraction

From Formulas:

β	the isothermal compressibility of the system
μ	the scaling factor for one side of the simulation cell box
μ_1°	the chemical potential of the surfactant monomers
μ_N°	the chemical potential of N surfactant aggregates
$\Delta\mu_N^\circ$	the difference between the chemical potentials of a single surfactant molecule in the solution and a surfactant molecule as a part of an aggregate of size N
$\left(\frac{\Delta\mu_N^\circ}{kT}\right)_{\mathrm{Deformation}}$	the positive free energy contribution of the surfactant tails inside the aggregate micelle core due to the constraints of

	maintaining a uniform density on all parts of the surfactant tail, such as the portion closest to the aqueous solution
$\left(\frac{\Delta\mu_N^\circ}{kT}\right)_{\mathrm{Head}}$	the positive free energy contribution of the head portions of the surfactants at the surface of the aggregate micelle core from the repulsive interactions between them
$\left(\frac{\Delta\mu_N^\circ}{kT}\right)_{\mathrm{Interface}}$	the positive free energy contribution of the interface of the portion of the surfactant tail still in contact with the aqueous solution at the surface of the aggregate micelle core
$\left(\frac{\Delta\mu_N^\circ}{kT}\right)_{\mathrm{Transfer}}$	the negative free energy contribution created from the transfer of the tail portion of the surfactant from its unfavourable contact with the solution into the primarily hydrophobic environment of the aggregate micelle core
τ	time coupling constant
η	shear viscosity
λ	scaling factor
λ	coupling factor
ϕ	dihedral torsion angle
σ_{ij}	the equilibrium distance between the two molecules, i and j
τ_P	the barostat relaxation time constant
τ_T	the rise time of a thermostat at temperature T
θ	bond angle
θ_0	the ideal angle

ϵ_{ij}	the minimum of the potential energy between two atoms, i and j
ρ	density
ρ_{exp}	experimental density
$\rho_{MARTINI}$	MARTINI density
$O(\Delta t^4)$	global truncation error
a	acceleration
a_0	the effective head group area of the surfactant
$a(t)$	the acceleration at time t
b	the simulation box vectors
b_0	the ideal bond length
C^l	the time correlation function
C_P	heat capacity
d	dimensionality of a system
D	self-diffusion coefficient
F	force
$F(t)$	the force at time t
g_r	RDF
$g^{AA}(r)$	RDF of AA model
$g_K^{CG}(r)$	RDF of CG model
ΔG_{mic}	Gibbs free energy of micellisation
ΔG_{solv}	Gibbs free energy of solvation
ΔG_{S-solv}	Gibbs free energy of single surfactant in a micelle core
ΔG_{S-mic}	Gibbs free energy of single surfactant in an aqueous solution

δH	change of enthalpy in a system
h	the length of the hydrophobic portion of the surfactant
ΔH_{vap}	enthalpy of vaporisation
k	Boltzmann constant
k_b	bond force constant
k_θ	bond angle force constant
k_ϕ	bond dihedral torsion angle
l	degree length
L	persistence length
m	mass
M_{exp}	experimental molecular mass
m_i	mass of a bead
MSD	Einstein's mean square displacement
N_{beads}	total number of molecules or beads in a particular molecule
n_p	decrease in the correlation between segments as they move farther apart in a chain
N_r	mean number of atoms in a shell
P	critical packing parameter
P(t)	the instantaneous pressure
P_l	Legendre polynomial
P_{md}	the desired pressure of a simulation
P_{xz}	off-diagonal element of the stress tensor
q	charge
r(t)	the position at time t

R	ideal gas constant
Δr	width of a shell of atoms
r0	bond length
r_{cm}	position of the centre of mas of a group of atoms
R_d	root-mean-square end-to-end distance
R_g	radius of gyration
r_i	position of a bead
r_{ij}	the distance between two atoms, i and j
t	time
T	the temperature of the system
Δt	change in time
T_{md}	the reference temperature of the thermostat
T(t)	the temperature at a given time
u	unit vector
U	potential energy function
$U(R)$	potential energy function of R position of all the atoms in the system
U_{angles}	potential energy of angles
U_{bonds}	potential energy of bonds
U_{bonded}	bonded potential energy
$U^{CG}(R)$	CG potential energy function of R position of all the beads in the system
U^{CG}_{bonded}	CG bonded potential energy
U^{CG}_{i}	initial CG potential energy function
$U^{CG}_{i+1}(r)$	CG potential energy function for i+1
$U^{CG}_{non-bonded}$	CG non-bonded potential energy
$U_{ectrostatic/Coulomb\ potential}$	Electrostatic/Coulomb potential potential energy
U_{gas}	potential energy of a molecule in

	a vacuum without any periodic boundary conditions
U_{LJ}	Lennard-Jones potential energy
U_{liq}	average molecular potential energy of a liquid
$U_{non-bonded}$	non-bonded potential energy
$U_{torsions}$	potential energy of torsion dihedral angles
X_1	the mole fraction of the surfactant monomers
v	the volume of the surfactant molecule
V	volume
V_b	the volume of the simulation box
v^{old}	the velocity prior to rescaling
v^{new}	the rescaled velocity
v(t)	the velocity at time t
W	the magnitude of the coupling
X_{CMC}	the CMC
X_N	the mole fraction of N surfactant aggregates

INTRODUCTION 1

Porous materials, found in nature or created through synthetic construction, have found considerable advantage in all facets of humanity. These materials are categorised by the size of their pores; microporous (i.e. pore diameters under 2nm), mesoporous (i.e. pore diameters between 2nm and 50nm), and microporous (i.e. pore diameters above 50nm).[1-3] An illustration of these pore size differences can be seen in **Figure 1.1**.[4] Typical crystalline microporous materials include silicoaluminophosphate, SAPO-n, molecular sieves[1, 2], and naturally occurring and synthetically created zeolites (e.g. clinoptiolites and chabazite). These microporous materials are often used in adsorption/separation applications, as well as chemical catalysis applications due to their ion-exchange characteristics.[1, 5, 6] However, microporous materials have pores too small for larger organic molecules or functional fragments to diffuse through, as well as selective thermal stability which limits their use in applications.[2, 7-11]

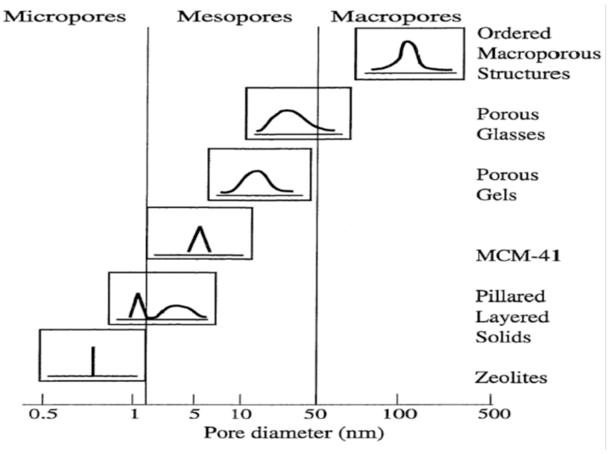

Figure 1.1: Graph of differences in pore size between porous materials [4]

In 1990 Yanagisawa et al.[3] developed a synthetic procedure to allow porous materials to have larger, mesoporous pores, based on the layering structure of kanemite, a layered silicate. Research on this mesoporous synthesis did not grow substantially until 1992[12], when a mesoporous silica was first produced by Mobil labs, in the form of Mobil Composition of Matter No. 41, MCM-41. Silica was of particular interest for use in mesoporous materials, as it has many attractive qualities such as being abundantly available, inexpensive, non-toxic, chemically inert, and thermally stable.[13] MCM-41's pore size could be controlled, and it can be used as a chemical catalyst, support, and adsorbent.[12, 13] Mesoporous silica then garnered more interest when it was synthesised with better hydrothermal stability and larger pore size in 1998 in the form of Santa Barbara Amorphous-15, SBA-15.[14]

SBA-15 is a highly ordered silica mesostructure material with ordered and controllable hexagonal pore arrays, noteworthy for its remarkably large pore spacings and larger specific surface area and thermal stability than its predecessors, MCM-41 and its offsets.[4, 13, 15-19] SBA-15 is synthesised using amphiphilic triblock copolymer surfactants as templates, referred to as Pluronics, and their self-assembly into highly ordered mesophases is responsible for the porous crystalline nature of this mesoporous silica.[12, 15-19]

SBA-15 is synthesised by the sol-gel method from the combination of a template of these Pluronic surfactants with a source of silica.[2, 17-23] This solution is mixed for a given time, and then heated, before the final product is collected by filtration of the solvent or calcination to remove the surfactant template.[2, 20-23]

To gain a more thorough understanding of its formation mechanism, molecular dynamics, MD, simulation, studies, especially those using coarse-grained, CG, models, have been an invaluable method of evaluation, that will be explored later in this chapter.[35-50]

1.1 SBA-15

Of all of the mesoporous silica types that have currently been synthesised, there has been a special attention paid to SBA-15 since it was first reported on in 1998.[14] SBA-15 is a highly ordered silica mesostructure material with tailorable uniform mesopores.[4, 13-19, 24-26] SBA-15 has remarkably innately large pore diameters of 5 to 30 nm, though these diameters can be adjusted with adjustments to the synthesis solution, and larger specific surface area and thermal stability than previously synthesised mesoporous silicas.[4, 13-19, 24-26] SBA-15's thick walls provide hydrothermal stability, and uniform mean pore spacings of approximately 6 nm leave sufficient space for product and reactant diffusion of molecules.[4, 13-19, 24-26] A representation of its pore size and structure is shown in **Figure 1.2**.[27]

SBA-15 is synthesised by the sol-gel method in acidic media from the combination of, most commonly, Pluronic P123, a triblock copolymer surfactant with the composition $PEO_{20} PPO_{70} PEO_{20}$, that will be discussed later.[2, 13-26] A silica precursor, most often tetraethylorthosilicate, TEOS, is then added to the solution of Pluronic P123 self-assembled templates.[2, 13-26, 28] This solution is mixed, and then heated to 80 to 130°C for 1 to 3 days before the final product is collected by filtration or calcinated at a heat of 550°C to remove the template.[2, 14, 20-26, 28]

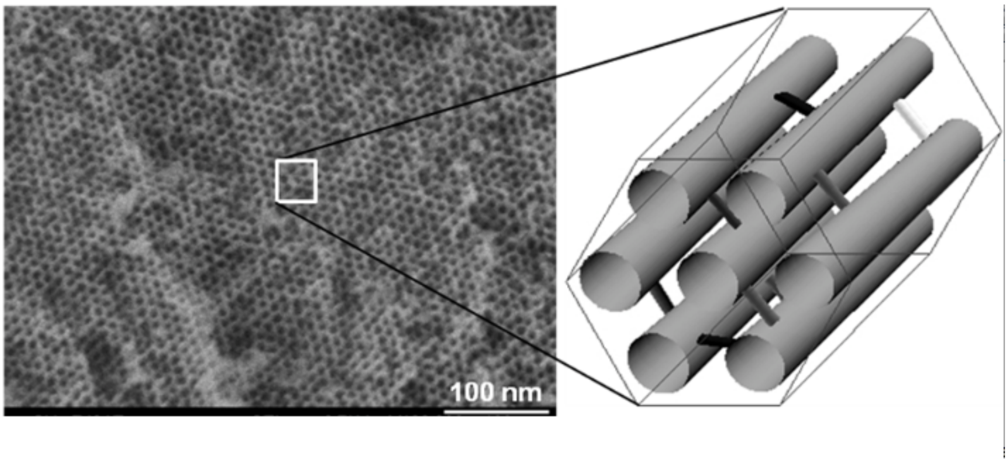

Figure 1.2: Left: High resolution FESEM image of the pore structure of SBA-15; Right: Representation of SBA-15 pore structure SBA-15 is synthesised in acidic media from a polyalkylene oxide triblock copolymer, referred to as Pluronic P123, with a source of silica, most often tetraethylorthosilicate (TEOS).[27]

1.2 Mesoporous silica synthesis mechanism

Mesoporous silica materials are synthesised through a combination of either hard constructed silica particles or most commonly, self-assembling surfactants, which act as a template for the pores, and simultaneous sol-gel condensation around that template.[18, 19, 24, 29] When these surfactants are combined with a solvent into a solution, the surface energy of the solution will decrease rapidly as the surfactants congregate, or self-assemble, and pack together to form micelles.[18, 19, 24, 29] After a specific concentration of surfactants in the solution is exceeded, these micelles begin packing into lamellar, hexagonal, or cubic mesophases.[24, 29, 20] The type of mesostructures and ultimately the type of mesoporous silica they produce depends on the type of self-assembling surfactant that is used.[18, 19, 24, 29, 30] The types of surfactants and a more in-depth explanation of their self-assembly process will be covered in Section 1.4.

As the micelles are forming in the solution, several processes proceed simultaneously. At the same time as the micelle formation, silica precursors, or silicates, are also dissolved into the solution.[24, 29, 30] As the surfactants are segregating and micellar rods continue to form, the silica precursors undergo hydrolysis and then condensation around those micelles.[18, 19, 24, 29] This condensation is the synthesis of the mesoporous silica. After the synthesis of the silica framework, the final step is to remove the template surfactants. Strong or forceful conditions are required to break the typically strong electrostatic bonds between the inorganic species and micelle surfactants.[18, 19, 24, 29] The surfactants can be removed in a variety of ways, including calcination, acid treatment, extraction with supercritical CO2, washing, and reflux extraction.[18, 24, 30] Most often with the synthesis of mesoporous silica though, the surfactant template is removed by washing with pure solvents like acetone, ethanol, or water.[24, 29, 30] Once the surfactants are dissolved, they can be easily removed from the framework and the mesoporous silica, leaving it viable for use. The full templating process and subsequent synthesis of mesoporous silica can be seen below in **Figure 1.3**.[31]

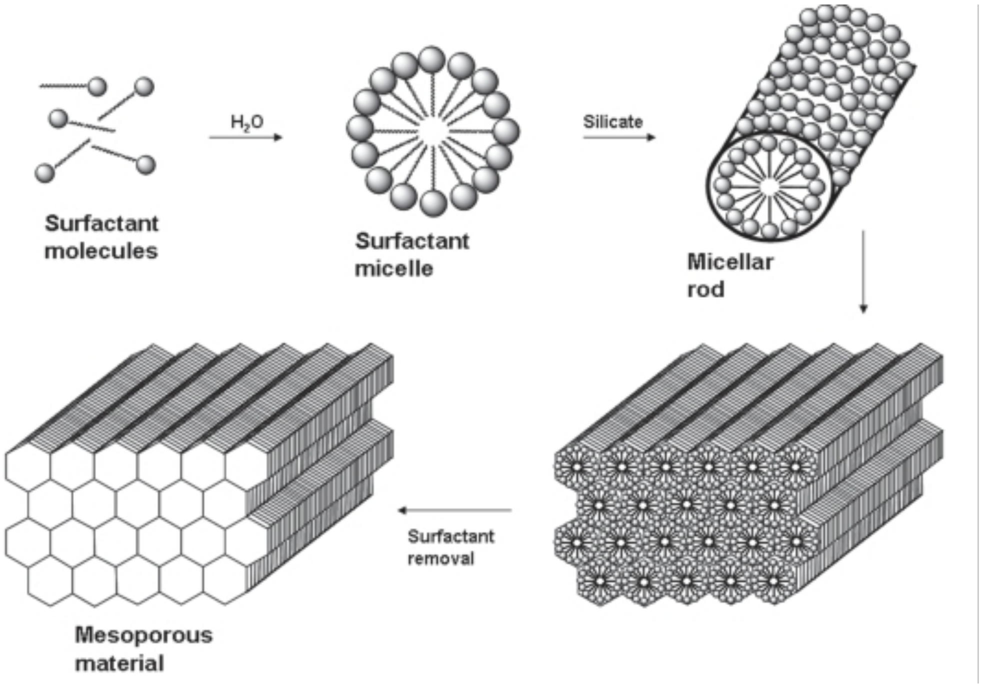

Figure 1.3: Mesoporous material synthesis process[31]

1.2.1 Notable experimental studies of SBA-15

A large number of studies have been dedicated to the synthesis of SBA-15 mesoporous silica after its discovery.[14, 28, 32-34] The earliest and most reproduced and utilised experimental study of SBA-15 mesoporous silica was done by Zhao et al in 1998.[14] The researchers used a variety of Pluronic surfactants to direct the organisation of the polymerising silica structures with uniform two-dimensional hexagonal pores with sizes up to approximately 300 angstroms or 30 nm. The SBA-15 materials were synthesised in acidic media at low temperatures between 35°C and 80°C, resulting in a wide range of pore wall thicknesses, 31 to 64 angstroms, Å, and uniform pore diameters, 46 to 300Å. For one of the first studies done to validate the synthesis of SBA-15, it is incredibly thorough, and its resulting structures and pore sizes have thus been a benchmark for a number of subsequent studies.

A study by Kruk et al. in 2000[32] recreated the SBA-15 ordered mesoporous silicas synthesised using the method reported by Zhao et al.[36] The structures of these mesoporous silica materials were characterised using powder X-ray diffraction, XRD, thermogravimetric analysis, TGA, and nitrogen adsorption. Unlike the previous study however, the synthesis ageing temperature was varied, creating slightly different pore structures in the resulting SBA-15. These observed structural properties validated a dependance on the synthesis temperature, which was attributed to the changes in the degree of penetration of the PEO chains of the triblock copolymer surfactant within the siliceous walls of SBA-15. Despite this emphasis on temperature dependence on structure, this study mainly helped to confirm the use of Pluronic P123 as a suitable Pluronic surfactant for the synthesis of SBA-15.

In 2005, Sun et al. performed a study on the synthesis of SBA-15 in the presence of alkane solvents.[28] The researchers used hexane, heptane, and nonane as alkane solvents in order to provide swelling to the resulting synthesised SBA-15 mesopores, and create consistant mean pores sizes above 12nm. Controlling the initial reaction temperatures, from 10°C to a specific temperature for each alkane used (e.g. heptane at 23°C), the resulting mesopore structures were evaluated using TEM imaging in addition to small angle x-ray diffractions, SAXD. The study found that the decrease of alkane chain length increased the solubility of Pluronic P123 surfactants, and samples synthesised in the alkanes were found to have pores diameters between 12.3nm and 14.2nm, for nonane to hexane respectively. Their results indicated that these alkanes, all with relatively short chain lengths, can be effectively utilised as swelling agents in the synthesis of SBA-15, though the temperature would need to be carefully controlled.

Most studies done past the original 1998 study both validate Zhao et al.'s results and build upon them by studying other synthesis variables. One such study that built upon Zhao et al.'s initial work was a 2014 experiment by Ding et al, focusing on the pH and temperature effects on SBA-15 platelet synthesis.[33]. SBA-15 platelets were directly synthesized using triblock copolymer Pluronic P123, as well as TEOS as a silica source without additives. By tuning the synthesis temperature and the HCl acid concentration, platelet-like SBA-15 particles that ran parallel to the thickness of the platelets, with pore widths between 150 and 350nm, were obtained with relative ease. The researchers found that the acidity and temperature had strong effects on the mesostructural properties of the SBA-15, supporting previous pH variable information, and their conclusions as to silica platelet growth could potentially be applied to further SBA-15 synthesis were it to be further researched.

A more recent example, would be a 2016 study by Melendez-Ortiz et al.[34] In this, the structural order and stability of synthesised SBA-15 was evaluated under highly acidic conditions. As with previous research SBA-15 was synthesised with Pluronic P123 and TEOS, but was given a both high and low HCl acidic concentration, from 34 to 9. At the higher concentration the SBA-15 synthesised with high-ordered pore distribution, and at the higher pH of 9 SBA-15 silica was not formed at all. The samples were characterised by using SAXS, nitrogen adsorption desorption analyses, scanning electron microscopy, SEM, and transmission electron microscopy, TEM, justifying previous experimental results. The researchers however did not repeat their experiment with more than one molar ratio of the P123 and TEOS though, meaning their results could be open to more research.

While the experimental studies mentioned above each provided some insight into particular aspects of the synthesis of SBA-15, they still took considerable time and the control they exerted over the synthesis process was limited. In order to allow for directed design of mesoporous silica with particular properties for specific applications, and facilitate the self-assembly formation mechanisms of the template surfactants, several modelling simulation techniques have been developed and employed.

1.2.2 Modelling of mesoporous silica

To combat our lack of theoretical comprehension, the development of computational models and simulations have allowed for broader understanding of the synthesis of mesoporous silicas.

Modelling of mesoporous silica began with the use of phase diagram lattice models for MCM-41 and its derivatives. Some of the first of this modelling undertaken was done by Siperstein and Gubbins[35, 36] using lattice Monte Carlo, MC, simulations to model part of the self-assembly of MCM-41. Their work was later expanded upon by researchers like Jin et al.[37], who used two methods (e.g. self-assembly and then silica polymerisation, or both self-assembly and silica polymerisation simultaneously) to model the phase equilibrium of mesoporous silica percursors and predict synthesis behaviour.

MCM-41 has also been modelled using atomistic molecular dynamic simulations. Jorge et al. performed the first MD, evaluation of MCM-41 synthesis using atomistic models in 2007.[38] This type of modelling provided insight into the interaction between silicates and small surfactant micelles, and the effect the adsorption of those silicates had on the surface of those micelles. Their atomistic modelling did, however, suffer from high computational costs. To surmount this limitation, coarse-grained modelling for the synthesis of MCM-41 and other MCM type silicas was completed by subsequent researchers, such as Pérez-Sánchez et al.[39, 40] This work managed to describe, for the first time, the formation of silica/surfactant mesostructures in realistic synthesis solutions.

Although experimentally the synthesis mechanism of SBA-15 has received perhaps as much attention as that of MCM-41[41], simulation modelling studies have been much fewer. This is not least because of the much larger size of the surfactant molecules (Pluronic P123 has about 17 times more atoms than CTAB) and micelles, and concomitantly slower dynamics. This puts it firmly outside the scope of detailed atomistic models, except for analysing local phenomena such as single-chain dynamics.[42] As a consequence, the few existing studies on modelling the synthesis of SBA-type materials have been carried out using highly coarse-grained models and have almost exclusively focused on SBA-15.[43-48]

In 2005, Bhattacharya and Gubbins[43] modified the lattice model of Siperstein and Gubbins[35, 36] to describe the self-assembly of triblock copolymers in the presence of an inorganic component meant to describe silica. They considered surfactants made up of five central hydrophobic, T, beads with three hydrophilic, H, beads on each end, i.e. H3T5H3, instead of the original H4T4 arrangement. The size and shape of the surfactant were selected to produce a water/surfactant phase diagram that qualitatively agreed with experimental data for Pluronic P123. By adding silica to the system, they once again observed phase separation between a dilute and a surfactant-rich phase. Depending on the concentrations, the latter formed bicontinuous, hexagonal or lamellar mesostructures. Interestingly, the hexagonal mesophases that are relevant for the synthesis of SBA-15 were only formed at quite low silica concentrations, which was contrary to the observations of Siperstein and Gubbins in their simulations of MCM-41 phase equilibrium.[36] Subsequently, Bhattacharya et al. used the results of the lattice model simulations that formed hexagonal phases to produce realistic models of SBA-15 materials, taking into account the molecular scale roughness of the large cylindrical pores and the presence of interconnecting micropores templated by the hydrophilic corona of P123.[44] The predicted adsorption isotherms were in qualitative, if not necessarily quantitative, agreement with experimental data, leading the authors to suggest that their model was perhaps too rough at the molecular scale.

Bhattacharya and Gubbins also extended their lattice model to include a fourth component, denoted as ‘oil’ and meant to represent the addition of a co-solvent like trimethylbenzene, TMB, to the synthesis mixture.[43] By exploring the quaternary phase diagram, they were able to show a gradual transition between hexagonal (i.e. SBA-15) mesophases and large-scale structures of disordered aggregates reminiscent of the mesocellular foams observed experimentally by gradually adding TMB to the solution.[49] As in the case of MCM-41, the lattice simulations of Gubbins and co-workers were able to qualitatively explore the physics of the phase equilibrium pertaining to block copolymer-templated materials, but it was not possible to carry out quantitative comparisons with the experimental synthesis mechanism due to the inherent simplifications of the model.

An alternative avenue that has been pursued to study the synthesis of SBA-15 is based on the Mesoscopic Dynamics, MesoDyn, simulation method, which has been widely employed to model self-assembly of polymer systems.[50] The MesoDyn method is based on dynamic mean-field density functional theory and the time evolution of the system is propagated through the integration of a set of functional Langevin equations.[43-47, 50] It uses a coarse-grained implicit solvent description of polymers that are represented by a Gaussian chain of beads, which interact with each other through pairwise interactions based on the Flory-Huggins model. Chen et al.[48] applied this approach in the context of SBA-15 synthesis to analyse the effect of temperature on the material pore size. They made use of a previously determined mapping scheme for Pluronic surfactants[50] to describe the P123 triblock copolymer, and used values of the interaction parameters that depended on temperature. Their simulations were able to show the formation of a distribution of spherical polymer micelles at relatively low concentration, and posited that the micelle self-assembly process could be divided into three stages.[45] They also observed that the size of the micelle core, formed of hydrophobic PPO beads, increased with temperature, and they linked this to the observed experimental increase in the pore size of SBA-15 with temperature. However, the comparison was merely qualitative, since Chen et al. simulated a simple aqueous solution of P123 (i.e. without the presence of silica) and were not able to observe the formation of a hexagonal phase or even cylindrical micelles.[45]

In the same year, Yuan et al.[46] used a very similar model to study in more detail the self-assembly of P123 at close to room temperature over a wide concentration range, and examined the effect of PEO charge and shear on the resulting mesostructures. They observed the formation of several distinct mesophases, including spherical micelles, similar to those described by Chen et al.[45], bicontinuous and lamellar phases. When a small positive charge was added to the PEO beads (aiming to describe adsorption of H+ ions by the micellar corona under highly acidic pH) and a constant shear rate was imposed (meant to describe agitation of the solution in experimental SBA-15 synthesis), the authors observed a progressive elongation of the micelles leading to formation of a hexagonal mesophase. Interestingly, hexagonal phases seemed to require the presence of both those factors, and were not formed when either shear or PEO charge were separately added to the model.[49] Once again, comparisons with experimental SBA-15 materials were only qualitative, as the authors did not consider the presence of silica in the system.

In 2012, Chen et al. extended their earlier study to include the effect of silica on P123 self-assembly.[47] They reported having obtained the interaction parameters between silica and the other components of the system from 'estimating the cohesive energy density of different molecules and the miscibility behavior of binary mixtures'[47], but no additional details were provided. They considered neutral and positively charged (at a fixed value of +1, meant to reflect protonation under highly acidic conditions[51]) silica beads, as well as varying the charge of the PEO beads. Confirming the observations of Yuan et al. [46], the authors only observed formation of cylindrical micelles when shear was applied to the system. Furthermore, the ordered hexagonal arrangement of the cylindrical micelles was seen to be highly sensitive to the charge values on silica and on the PEO beads – ordered hexagonal mesophases required a charge of +1 on silica (lower or higher values led to disordered micelle packing) and a charge either around -0.3 or around +0.5 on the PEO beads.[50] The authors also observed that neutral silica tended to form aggregates, while a relatively uniform distribution of silica around P123 micelles was observed when silica was charged. They attributed this effect to the need for charge matching interactions between silica and surfactant in SBA-15 synthesis.[47]

Finally, it is worth mentioning the work of Magee and Siperstein[48], who carried out Dissipative Particle Dynamics, DPD, of ternary systems composed of a diblock copolymer, water, and an inorganic component meant to represent aggregating nanoparticles. DPD is also a mesoscale modelling approach, in which particles interact with each other through soft interactions and with an implicit solvent by way of random (representing Brownian motion) and dissipative (representing friction) forces. Once again, emphasis was placed on mapping the phase diagram of the system. Although the authors were able to observe some interesting physical phenomena, such as the onset of demixing driven by increasing interaction between nanoparticles, it is difficult to draw a direct parallel with realistic experimental systems.

These SBA-15 modelling techniques lead to new insight into its synthesis mechanisms, though they was a lack of multi-scale modelling, leading to various limits on the products of these simulations. It is this lack of a multi-scale model of the synthesis process of SBA-15 that this work will attempt to rectify.

1.3 Surfactant self-assembly

As mentioned above, the synthesis of mesoporous silica is based on the templating processes of self-assembling surfactants, making it an essential component of modelling.[1, 2, 3, 12]

Surfactants, sometimes referred to as surface active agents, are molecules composed of two distinct portions of differing polarity, therefore being referred to as amphiphilic.[20, 29, 52, 53] The first portion of surfactants is usually a non-polar hydrocarbon chain (hydrophobic due to its non-polarity), and the second is a polar group or chain, (hydrophilic due to its polarity); often referred to as the hydrophobic tails and hydrophilic heads, respectively.[13, 20, 29, 52, 53] Surfactants are often used in a variety of applications, including emulsifiers and detergents, in industries ranging from agriculture to pharmaceuticals.[6, 13, 20, 21, 29, 52-54] It is because of their amphiphilic composition that surfactants exhibit two notable characteristics when they are combined with a solvent into a solution.[20, 21, 29, 52-54] At lower concentrations, surfactants will display surface activity, adsorbing on the surfaces, or at the interfaces, of solutions, while at higher concentrations they will cause the surface energy of the solution to decrease rapidly and the surfactants will self-assemble, congregating to form micelles.[20, 21, 29, 52-54] This micelle formation occurs above the critical micelle concentration, CMC, which can often depend on both the pH and temperature of the solution.[29, 52, 53, 55]

Below the CMC, the surface activity of lower surfactant concentrations reduces the tension of the surface of a gas/liquid system, or the interface of two immiscible systems (e.g. two immiscible liquids, or a liquid and an immiscible solid).[20, 21, 29, 52-54] The unequal intermolecular forces at the boundary of the system create this surface and interfacial tension, causing the surface energy to decrease as surfactant molecules begin congregating at the surface of the solution until the CMC is finally met.[20, 21, 29, 52-54]

After the CMC is met, the hydrophilic head portions of the surfactants will turn towards the aqueous solution, as the hydrophobic tail sections of the surfactants turn away from the solution, reducing their contact with the solution, destroying the cohesive forces at the boundaries of the system, and lowering the surface or interface energy.[21, 52-54] Once the CMC has been surpassed with the further addition of surfactants, the surface area further decreases, and the surfaces begin to accumulate in the bulk of the solution.[20, 21, 29, 52-54] The hydrophobic tail sections will then aggregate so that they have minimal contact with the solution, leading to phase segregation and formation of micelles.[17, 52-54] This resulting segregation and micelle formation, called self-assembly, is a process solely determined by these hydrophilic and hydrophobic interactions, as well as other weak interactions such as electrostatics and hydrogen bonds, and is both thermodynamically favourable and spontaneous.[18, 20, 21, 29, 52-54]

Once the CMC has been surpassed further, with the further addition of even more surfactants, the now isotropic micellar solution develops into a liquid crystalline phase, where the micelles begin packing into hexagonal, bicontinous, or lamellar phases.[17, 24, 29, 30, 52-54] The solution now exhibits orientational order, similar to a crystal solid, while still maintaining liquid-like flow.[17, 20, 21, 29, 52-54]

As the self-assembly process of surfactants described above occurs in a matter of nanoseconds at the nanoscale level, it is exceedingly challenging to evaluate self-assembly through traditional experimental studies.[20, 21, 29, 52-54, 56]

1.3.1 Thermodynamics of micellar aggregation

In order to provide a method of evaluation for surfactant self-assembly, a phenomenological thermodynamics model was proposed by Tanford, and then expounded on by Israelachvili et al. and Nagarajan et al.[57, 58, 59] If a solution with both surfactant monomers and aggregated micelles at equilibrium is assumed to be infinitely dilute, then the mutual interactions between them can be considered negligible, and aggregates of different sizes can be considered as distinct chemical species with their own chemical potentials. This model can be seen in **Equation 1.1**:

$$\frac{1}{N}(\mathring{\mu}_N + kT \ln X_N) = \mathring{\mu}_1 + kT \ln X_1 \qquad \textbf{(1.1)}$$

where $\mathring{\mu}_N$ is the chemical potential of surfactant aggregates of size N, X_N is the mole fraction of the surfactant aggregates, $\mathring{\mu}_1$ the chemical potential of the surfactant monomers, k is the Boltzmann constant, T is the temperature of the system, and X_1 is the mole fraction of the surfactant monomers.[57, 58, 59] This equation can be rewritten as an equation for aggregate size distribution, which can be seen in **Equation 1.2**:

$$X_N = X_1^N \exp\left(-\frac{\mathring{\mu}_N - N\mathring{\mu}_1}{kT}\right) = \left(-\frac{N\Delta\mathring{\mu}_N}{kT}\right) \qquad \textbf{(1.2)}$$

where $\Delta\mathring{\mu}_N$ is the difference between the chemical potentials of a single surfactant molecule in the solution and a surfactant molecule as a part of an aggregate of size N.[57, 58, 59]

Because of the typically high value of N, as well as the fact that X_N and X_1 are of the same order of magnitude, the chemical potentials of the system can be simplified by combining and simplifying **Equations 1.1** and **1.2.** This simplification can be seen in **Equation 1.3.**

$$\frac{\mathbf{\overset{\circ}{\mu}_N}}{\mathbf{N}} = \mathbf{\overset{\circ}{\mu}_1 + kT \ln X_1} \qquad \textbf{(1.3)}$$

In the phenomenological models, the standard free energy change associated with the transfer of a surfactant monomer from its dilute state into an aggregate of size N has four major contributions, as shown in **Equation 1.4**:

$$\left(\frac{\Delta\overset{\circ}{\mu}_N}{kT}\right) = \left(\frac{\Delta\overset{\circ}{\mu}_N}{kT}\right)_{\mathbf{Transfer}} + \left(\frac{\Delta\overset{\circ}{\mu}_N}{kT}\right)_{\mathbf{Deformation}} + \left(\frac{\Delta\overset{\circ}{\mu}_N}{kT}\right)_{\mathbf{Interface}} + \left(\frac{\Delta\overset{\circ}{\mu}_N}{kT}\right)_{\mathbf{Head}} \qquad \textbf{(1.4)}$$

where $\left(\frac{\Delta\overset{\circ}{\mu}_N}{kT}\right)_{\text{Transfer}}$ is the negative free energy contribution created from the transfer of the tail portion of the surfactant from its unfavourable contact with the solution into the primarily hydrophobic environment of the aggregate micelle core, $\left(\frac{\Delta\mu_N^{\circ}}{kT}\right)_{\mathrm{Deformation}}$ is the positive free energy contribution of the surfactant tails inside the aggregate micelle core due to the constraints of maintaining a uniform density on all parts of the surfactant tail, such as the portion closest to the aqueous solution, $\left(\frac{\Delta\mu_N^{\circ}}{kT}\right)_{\mathrm{Interface}}$ is the positive free energy contribution of the interface of the portion of the surfactant tail still in contact with the aqueous solution at the surface of the aggregate micelle core, and $\left(\frac{\Delta\mu_N^{\circ}}{kT}\right)_{\mathrm{Head}}$ is the positive free energy contribution of the head portions of the surfactants at the surface of the aggregate micelle core from the repulsive interactions between them.[57, 58, 59]

Based on the above equations, in addition to the fact that the CMC, written here as X_{CMC}, is the value of X_1 where the concentration of the surfactant monomers is equal to the concentration of the surfactants in aggregated micelles in the solution, the CMC can be calculated as a pseudophase approximation that can be seen in **Equation 1.5**.[57, 58, 59]:

$$\ln \mathbf{X}_{\mathbf{CMC}} = \left(\frac{\Delta\mu_N^{\circ}}{kT}\right) = \left(\frac{\Delta\mu_N^{\circ}}{kT}\right)_{\mathbf{Transfer}} + \left(\frac{\Delta\mu_N^{\circ}}{kT}\right)_{\mathbf{Deformation}} + \left(\frac{\Delta\mu_N^{\circ}}{kT}\right)_{\mathbf{Interface}} + \left(\frac{\Delta\mu_N^{\circ}}{kT}\right)_{\mathbf{Head}} \quad \mathbf{(1.5)}$$

From these models we can recognise the important role of free energy in aggregate micelle formation. The free energy of transfer controls the aggregation process itself, the free energy of deformation and the free energy of interface control the growth of the aggregated micelles, and the free energy of the head groups controls the ultimate size of the aggregates with its repulsive forces.[57, 58, 59]

1.3.2 Predicting self-assembly with the critical packing parameter

Israelachvili et al.'s model also first found that the resulting structure of the aggregated micellar phase could be predicted by examining the critical packing parameter, P, of the surfactants.[58] The researchers found that the self-assembly of the surfactants is due to two major factors: the hydrophobic tails of the surfactants and their attractive interactions with each other, and the hydrophilic heads of the surfactants and their repulsive interactions with each other. These factors combined dictate what type of aggregate micelles are formed, as well as how large they are, and can thus be predicted from the geometrical features of the surfactant through the critical packing parameter, as shown in **Equation 1.6**:

$$\mathbf{P} = \frac{\mathbf{v}}{(\mathbf{h})\mathbf{a_0}} \qquad \textbf{(1.6)}$$

where v is the volume of the surfactant molecule, h is the length of the hydrophobic portion of the surfactant, and a_0 is the effective head group area of the surfactant.[63] Representation of this critical packing parameter and its geometrical components, can be seen in **Figure 1.4** for example surfactants.[56]

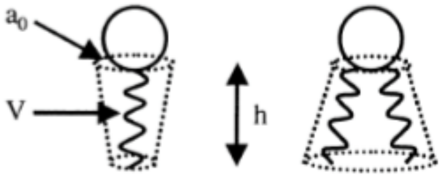

Figure 1.4: Representation of critical packing parameter, P, for example surfactants.[56]

When P is less than 1/3, surfactants have large head groups and thus form spherical micelles, while when P is more than 1/3 and less than 1/2 it implies that the surfactant has a small head group and will typically form a cylindrical micelle or 2d-hexagonal mesophase. When P is a value between 1/2 and 1, the surfactant is assumed to be bulkier with a larger head group, and thus will usually form lamellar vesicles or bicontinuous cubic mesophases due to their inability to pack closely.

When P equals 1 exactly, however, the surfactants tend to be bulkier with smaller head groups, tending to form mesophases of lamellar bilayers. In the less common occasion when P is greater than 1, surfactants have small head groups or large hydrophobic tails and will commonly form reverse micelle mesophases. These critical packing parameters and their common mesophases are shown in **Table 1.1**.[56, 58]

Critical Packing Parameter	**Example Mesophases**
P<1/3	Spherical Micelle
1/3<P<1/2	Cylindrical Micelle, 2d-Hexagonal
1/2<P<1	Lamellar Vesicle, Bicontinuous Cubic
P=1	Lamellar Bilayer
P>1	Reverse Micelle

Table 1.1: Typical mesophases resulting from different *P* values of surfactant.[56, 58]

1.3.3 Surfactant types

As mentioned in previous sections, surfactants are essential to the mesoporous silica synthesis process, as the choice of surfactant plays an important role in the resulting form of the mesostructured material.[21, 52, 53, 86] The most extensively used surfactants to template mesoporous silica can be generally classified into three categories, known as cationic, anionic, and nonionic.[21, 52, 53, 86] Cationic surfactants have a net positive charge and are typically comprised of an alkyl hydrophobic tail and a methyl- ammonium ionic compound head.[21, 52, 53] Examples of these cationic surfactants are quaternary ammonium surfactants, which have typically been used to template the synthesis of MCM-type materials.[3, 21, 52, 53] Anionic surfactants, meanwhile, have a net negative charge and are typically comprised of a sulfonated compound with the formula $R\text{-}SO_3Na$, with R representing an alkyl chain of roughly 11 to 21 carbons.[21, 52, 53] These surfactants include surfactants derived from amino acids, such as *N*-lauroyl-L-glutamic acid, C_{12}GluA, and *N*- myristoyl-L-glutamic acid, C_{14}GluA.[21, 52, 53, 86]

Lastly are nonionic surfactants, which have an uncharged polar group for their hydrophilic heads, such as ether, R-O-R, or alcohol, R-OH, and are often polymeric surfactants.[21, 52, 53] Nonionic polymeric surfactants in the form of triblock copolymers are the most common surfactant in the synthesis of SBA-15 mesoporous silica.[14, 20, 21, 52, 53, 60-63, 86] The charges of anionic and cationic surfactants allow them to separate into charged ions when they are dissolved, which while helping the surfactant molecules interact, limits the size-distribution of the pores they can produce.[14, 21, 52, 53, 60-63, 86] Nonionic surfactants, instead, can template the formation of larger pore-size distributions, such as with SBA-15. A more thorough examination of these surfactants and their components can be seen in the following sections.

1.3.4 Block copolymer surfactants

Block copolymer surfactants are comprised of two or more homopolymer subunits, or blocks, linked together through covalent bonds.[20, 53, 60-63] They are some of the most common surfactants for the synthesis of mesoporous silica, especially SBA-15.[4, 13-16, 62, 63] The most typical homopolymer blocks of these surfactants are the hydrophilic polyethylene oxide, PEO, and the hydrophobic polypropylene oxide, PPO.[20, 53, 60-65] When the number of PEO units in a block exceeds the number of PPO units, the surfactant becomes predominantly hydrophilic, whereas when the reverse happens the surfactant becomes predominantly hydrophobic, which can lead to the formation of disparate mesophases.[20, 53, 60-65] PEO, PPO, and block copolymer surfactants with three distinct blocks, triblock copolymer surfactants, are discussed further below.

1.3.4.1 PEO

Polyethylene oxide is a nonionic homopolymer created through the polymerisation of ethylene oxide, with the chemical formula $(CH_2CH_2O)_n$, where n is the number of monomers.[64] PEO is very soluble in water, and as the ether portions of the molecule give it a hydrophilic nature, it a good choice for the hydrophilic portion of amphiphilic surfactants.[64]

PEO and polyethylene glycol, PEG, have an equatable chemical structure, as well as near identical chemical and physical properties, only differing in their manner of production (i.e. polymerisation of ethylene oxide for PEO, and polycondensation of ethylene glycol for PEG). For this reason experimental properties of PEG are often used as comparison for PEO when PEO values are not available.[64, 66]

The dimer of PEO (i.e. n=2) has a direct chemical structure correspondence to 1,2-dimethoxyethane, DME.[67] Numerous experimental studies have examined DME in its liquid phase as well as in aqueous solutions through various experimental techniques, and these properties are therefore often used as comparison for those of PEO dimers where experimental values are not available.[64, 67]

1.3.4.2 PPO

Polypropylene oxide is a nonionic homopolymer produced through the polymerisation of propylene oxide, with the chemical formula $(CH_3CHCH_2O)_n$, where n is the number of monomers.[65] While PPO is also linear, like PEO, the presence of an extra methyl group, CH_3 , in each unit makes PPO more hydrophobic in nature than PEO.[64, 65]

A small oligomer of PPO corresponds most directly in chemical structure to 1,2-dimethoxypropane, DMP, while the PPO dimer (i.e. n=2) corresponds to 1,2-diethoxyethane, DEE.[68, 69] Because of the close nature of DMP to the dimer (having only one fewer carbon group), as well as the lack of experimental properties of DEE, DMP is often treated as the dimer in comparison work. Available experimental data of these two compounds is therefore often used as comparison for these short PPO chains where their own experimental properties are unavailable.[65, 68, 69]

1.3.4.3 Pluronic triblock copolymer surfactants

One of the most widely used types of nonionic surfactants currently used for the synthesis of mesoporous silica materials are triblock copolymers.[20] They were commercialised by Badische Anilin- und Soda-Fabrik, BASF, with the name Pluronics, with which they are often referred to, and as polymers they are inexpensive and simple to produce.[20, 62, 63]

These surfactants consist of portions of PEO and PPO arranged most commonly in an ABA structure, as PEO_n PPO_m PEO_n, though they can also be arranged in a “reverse Pluronic” BAB structure, as PPO_n PEO_m PPO_n.[20, 53, 60-63] The ABA chemical structure can be seen in **Figure 1.5**.[70]

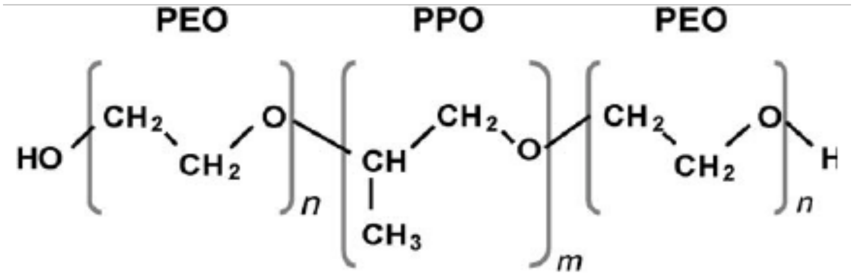

Figure 1.5: Generic chemical structure of Pluronic surfactant [70]

Pluronics are readily soluble in a variety of solvents, including water as well as other polar and non-polar solvents, due to the hydrocarbon chains of their block components.[22, 52, 53, 60, 62, 63] Pluronics are also able to form liquid crystal structures in the solution, with self-assembly due to the presence of a hydrophobic PPO block, creating a variety of micelle mesophases depending on the amounts of PEO and PPO.[22, 53, 60-63] Their aggregated micelles form with an inner core comprised of the PPO blocks and an outer shell of the PEO blocks.[22, 52, 53, 60-63] The self-assembly of these surfactants is most often used in the synthesis of mesoporous silica with much larger pore-size distributions than charged surfactants, because nonionic surfactants do not dissociate into ions when dissolved into the solution, like anionic and cationic surfactants do.[60-63]

Because the lengths of the block components can be customised, Pluronic surfactants are available in different compositions, some examples of which can be seen in **Table 1.2**.[62, 63]

Pluronic Block Copolymers	**Number of PEO blocks (n)**	**Number of PPO blocks (m)**
L64	13	30
P85	26	40
P123	20	70
F38	43	15
L44	10	23

Table 1.2: PEO and PPO block compositions for 5 common Pluronic triblock copolymers.[62, 63]

The names of Pluronics are coded in a particular way.[71] The letter that they start with describes the physical state of the Pluronic at room temperature (i.e. F means flake, or solid, P means paste, and L means liquid).[71] When the first digit after the letter, or the first two digits after the letter in a three-digit number, is multiplied by 300, it gives the approximate molecular weight of the hydrophobic PPO portion of the Pluronic.[71] When the last digit in the name is multiplied by 10, it gives the percentage of the hydrophilic PEO portion of the Pluronic.[71] This means that at room temperature Pluronic P123 is a paste, that its PPO portion has a molecular mass of 3.6 kg/mol, and that it is comprised of 30% PEO.[71]

Pluronic P123, or $PEO_{20}\,PPO_{70}\,PEO_{20}$, is also of special importance as it leads to the synthesis of SBA-15.[14, 22, 60, 62, 63]

1.4 Molecular simulations of PEO, PPO, and Pluronics self-assembly

The previously mentioned experimental studies are all useful for different reasons, though they are all unable to observe the self-assembly formation mechanisms of the template surfactants explained above. To better understand these templating processes, many simulation studies of Pluronic surfactants and/or their block components have been undertaken over the years; either all-atom, AA, simulation models, as well as coarse-grained, CG, simulation models (both of these modelling approaches will be discussed in detail in Chapter 3).

1.4.1 Notable all-atom simulations

An early molecular dynamics study of PEO and PEG was performed by Lee et al. in 2008.[72] Their force field was a revision of the all-atom CHARMM force field, matching dihedral potentials to experimental conformational populations for dimethoxyethane, DME, PEO's dimer at different potential energy values. The researchers ran simulations of PEO at lengths of 9, 18, 27, and 36 monomers, and of PEG homopolymers at lengths of 27, in water. The properties of the homopolymers, including persistence length, radii of gyration based on molecular weight, and hydrated shape anisotropy, were in good agreement with experimental values, while the PEO and PEG homopolymers were found to be statistically equivalent. This simulation study was encouraging, presenting conclusions applicable to both PEO and PEG, indicating their interchangeability in future work. Their results were based on structural properties, however, neglecting thermodynamic properties, indicating a need for further testing of the models.

In 2011, Hezaveh et al. evaluated DME and DMP in aqueous and non-aqueous solutions using a force field based on united-atom models in agreement with GROMOS/OPLS force fields.[73] As mentioned above, DME is a dimer of polyethylene oxide, while DMP is a short oligomer of polypropylene oxide, often comparative to its dimer, and thus a good basis of study for PEO and PPO. The researchers calculated structural and thermodynamic properties, such as densities, diffusion coefficients, and free energies of solvation, of pure DME and DMP solutions at standard temperature and 318K, which were found to be in agreement with experimental data. They also performed simulations of DME and DMP in water, carbon tetrachloride, methanol, and heptane at infinite dilution, and calculated the free energies of solvation in all of the liquids. All of the resulting free energies were found to be in line with experimental data, and consistent with the dielectric constant of the solvents. This study did a good job of modeling the mentioned major properties of DME and DMP, but the lack of exploration in longer chains of PEO or PPO means more work would need to be done to know if these models are suitable for future use in simulation work with other block components.

The following year, Hezaveh et al. completed another simulation study, furthering their earlier work, on the dynamics and conformation properties of PEO and PPO, polymer chains at 298K.[42] The PEO and PPO chains were studied again using a modified united-atom model in agreement with GROMOS/OPLS, simulating melt conditions as well as infinite dilution conditions in water, carbon tetrachloride, methanol, heptane, and chloroform. The calculated density of PEO melt simulations with chains of 2, 3, 4, and 5 monomers and, for PPO melt simulations of chains of 7 monomers, were found to be in good agreement with available experimental data. The conformational preferences of their PEO simulations were in agreement with results of experimental NMR studies, while the radii of gyration for their PEO chains longer than 9 monomers agreed well with light scattering data in water and methanol. End-to-end distances and persistence lengths of these chains at 298K in water and methanol provided further validation with experimental results. The PEO and PPO chains were then joined to create Pluronic P85, $PEO_{26}PPO_{40}PEO_{26}$, and its radius of gyration at 293K in water was found to be comparable to known data. These results were promising, though their absence of longer chain properties, especially for PPO, and only radius of gyration simulation of a single Pluronic implies that more research is needed for the use of this model with Pluronic surfactants.

While these AA models were able to produce some major properties of PEO, PPO, and Pluronic surfactants, they are limited in their ability to simulate Pluronic self-assembly.

1.4.2 Notable coarse-grained simulations

A significant CG model for PEO- polyethyethylene, PEE, diblock copolymers was developed by Srinivas et al. in 2004.[74] This study examined the self-assembly of these copolymers with varying hydrophilic PEO ratios in a CG force field, fitting distribution of bonds, angles, and dihedrals to properties taken from all-atom simulations and experimental data. This lead to PEO and PEE chains with structural chain properties in good agreement with experimental observations, and copolymers with larger PEO components that self-assembled into membranes in CG water. While this study did not delve deeper into important thermodynamic properties of PEO, PEE, or diblock copolymers, thus limiting its transferability to other solvent models, it did provide useful insight into the importantance of longer PEO chains in future CG simulation models.

Another study of generic Pluronic triblock copolymer solutions in thin films was done by Hatakeyama et al. in 2007.[75] This study focused on the self-assembly of one particular triblock copolymer CG model, $PEO_{10}PPO_{20}PEO_{10}$, under confinement conditions. Their simulations were all confined between two walls (hydrophilic and hydrophilic, hydrophobic and hydrophobic, or hydrophilic and hydrophobic), and their influence on the morphology of any subsequent self-assembled structures was noted. While the parameters of their model, including density, radial distribution functions, radius of gyration, mean square displacement, and diffusion constants, were not an accurate representation of any one Pluronic copolymer, it agreed with a number of general behaviours found in earlier studies, specifically the layers and morphologies. However, it was apparent that some of this study's results were strongly dependant on simulation parameters, especially the solubility of the Pluronic chains, which would obviously affect the structure of surface layers. While more work would be needed for solid conclusions, their study did provide a base for CG MD effects on chain solubility dynamics that can be relevant to understanding the lubrication of triblock copolymers on adsorbing surfaces.

A simulation study on PEO and polyethylene glycol, PEG, surfactant components was performed by Lee et al in 2009.[76] A coarse-grained model for PEO and PEG, which as mentioned above can be considered equal in terms of chemical structure, was developed within the framework of the MARTINI force field utilising beads with 3 heavy atoms to 1, or 3:1 mapping. The distributions of bonds, angles, and dihedrals for the force field were taken from the all-atom model CHARMM, and properties such as radius of gyration and chain length, were examined for PEO and PEG in various concentrations. These properties were observed in the simulation and then compared to known data, partially validating the model. The simulation failed, however, to observe other thermodynamic parameterisation properties such as free energies and enthalpies of vaporisation. Due to the lack of matching to thermodynamic properties, the hydrophilicity of the PEO is most likely largely under or overestimated, which will give it poor transferability to other solvents. It did provide, however, a solid base for PEO models, which later simulations would add upon.

In 2011, Velinova et al. simulated the self-organization of alkyl poly(ethylene glycol) surfactants, $C_{12}E_5$, in aqueous solution using the MARTINI force field.[77] The main difference in this study compared to those preceding it was the change in bead type in regards to PEG/PEO components. The previous study by Lee et al.[76] found that PEO-PEO interaction levels were too weak with a larger MARTINI N_a bead, so this study treated these self-interactions as the smaller MARTINI SN_{da} bead type. The resulting aggregation numbers and size of the spherical micelles formed by the $C_{12}E_5$ surfactants in this model were in good agreement with experimental data, and their high aggregation numbers indicated possibilities in modeling drug-delivery systems. While this model provided interesting questions about PEO bead interactions, the fact that the PEO in this model was solely parameterised for $C_{12}E_5$ surfactant aggregation, and not for PEO properties and parameters, means further study would be needed for this model's use with Pluronics.

Another study by Lee et al. was undertaken on the self-assembly of PEG-grafted lipids in 2011.[78] The MARTINI force field was used to parameterise interactions between CG PEG and CG dipalmitoylglycerophosphocholine, DPPC, lipids through density matching monomers of PEG and PEO grafted to the bilayer. The resulting simulations in this model showed mixtures of lipids and PEGylated lipids self-assembled to bicelles, micelles, or liposomes, with higher concentrations of PEGylated lipids producing smaller aggregates, in good agreement with experimental data. The average end-to-end distances of the PEG on the PEGylated lipids were comparable to those in experimental bicelles, micelles, and liposomes, only slightly larger than for PEG in a solution. While this study focused primarily on PEGylated lipids, and it lacked a more thorough parameterisation of PEG with multiple properties, it did provide some insight into the potential for PEG aggregation behaviour for future use in simulation work with other block components.

Another simulation study on a coarse-grained model for polyethylene glycol, PEG, and polyoxyethylene alkyl ether surfactants was performed in 2012 by Rossi et al.[79] The researchers developed a new coarse-grained model of PEG also based on the MARTINI force field. While properties of the PEG and surfactants were simulated and compared to experimental results, the main focus was on the phase behaviour of solutions of water and surfactant as a function of water concentration. Micelle aggregation was successfully obtained with surfactants of different hydrophilic length using this force field in water, but the micelle formation after 7 microseconds failed to reach equilibrium. Coupled with the wide distribution of micelle sizes observed, and the trouble the researchers had finding a working charge for the PEG beads, implies this model's beads may not be parameterised correctly. Further, a later study by Taddese et al.[80], which will be discussed further below, found that this model's surfactants collapsed in hydrophobic solvents.

Another notable study from the same year undertaking a new model of PEO and PPO for Pluronics across a 1,2-dimyristoyl-sn-glycero-3-phosphocholine, DMPC, bilayer was done by Hezaveh et al.[81] The CG model was again based on the MARTINI force field, and the researchers parameterised their models of PEO and PPO using simulation data of previously reported AA models RDFs, with comparison being made to experimental properties of PEO and PPO in water, such as the radii of gyration. These models were then used to simulate Pluronics P85, L64, and F38 in the DMPC bilayer to evaluate their interaction mechanism. Their findings were compared against experimental data, and their results showed favourable property adherence for PEO and PPO chains in water, specifically the radii of gyration they were parameterised against, as well as density profiles of PEO and PPO dimers, with previous AA study results, as well as in comparison to experimental data. Their model also showed that Pluronics consisting of PPO chains of comparable lengths to the DMPC bilayer (i.e. P85) tend to percolate across the lipid bilayer, which was consistent with experimental results. While these results were promising for Pluronics and their components, their focus on bilayer interaction mechanism and their lack of thermodynamic properties indicates a need for further testing.

A new CG force field was developed by Choi et al. for PEG in water in 2013.[82] The force field was based on the MARTINI model, re-parameterising PEG through MARTINI protocol, but replacing the MARTINI water model with a big multipole water, BMW, model for its solvent. This new BMW/MARTINI force field produced more accurate predictions for the density of PEG, as well as removed ring-like conformation and bundling seen with MARTINI water simulations, but also produced slow PEG dynamics and solvent-separated-pairs between chain ends. This highlighted the importance of properly parameterised CG solvents on the effect on polymer-solvent systems, and further research would need to be done to explore the optimisation of MARTINI based solvents.

A 2014 study by Nawaz et al. performed a parametrisation-extensive process using a MARTINI coarse-grained model that has been proven to be a reference for Pluronics of differing sizes at various temperatures, concentrations, and in different solvents.[83] Their PEO model was based on the CG model of Rossi et al.[79] bead model previously discussed, though it was further parameterised to optimise other properties, including end-to-end distance, persistence length, and radius of gyration. Their PPO model was based on traditional MARTINI bead models, parameterised to the free energy of transfer for PPO between octanol and water, while the PEO-PPO interaction was mapped from AA models. These block component models were then used to validate PEO and PPO chains, single chains of CG Pluronics L31, L61, L62, L64, P85, F38, F68, and L44, with strong focus on Pluronic L44, including a self-assembled L44 monolayer in water. Various important aspects of the Pluronics and their components were validated in a vacuum, CG hexane, and in CG water, including chain length, membrane thickness, radius of gyration, self- assembly of longer PEO and PPO chains, and bond, angle, and dihedral distributions, and the surface tension of the self-assembled L44 monolayer, and compared both to previous AA model results, as well as available experimental data. While these models were optimised to produce correct interfacial properties as well as structural data, there is a question as to the transferability into solvents at different temperatures; they only match a small subset of the single Pluronic chains tested, and while they do show self-assembly of the PEO and

PPO chains, the Pluronic models were not simulated for micelle aggregation/self-assembly. This indicates that further testing and potentially parameterisation would be needed to use this model for Pluronic surfactant self-assembly work.

Wood et al carried out another CG study of the self-assembly of Pluronic F127 in 2016, incorporating minor simulation work on Pluronics P85, F38, and L64.[84] Their aim was to understand its interactions with lipid bilayers and its ability to self-assemble in aqueous environments through an adapted MARTINI model and using a polarizable water model. Single chain monomers of Pluronic F127 and Pluronics P85, F38, and L64 were simulated in a palmitoyl-oleoyl-phosphatidyl-choline, POPC, model membrane bilayer and multiple Pluronic F127 chains were simulated with water, and their PEO/PPO compositions and initial conditions were parameterised. While they were able to promisingly recreate the interaction behaviours of these Pluronics with the bilayer, as well as aggregation of one hundred Pluronic F127 unimers in water, their model suggested that coil conformation requires that a Pluronic needed to initially be placed outside of the bilayer core to produce interaction behaviour within the bilayer, and as the model did not take into account many properties of the Pluronics on their own, it may not have much transferability.

In 2017 Grillo et al presented a new model for diblock copolymers developed using a polyethylene oxide-polybutadiene, PEO-PTB, bilayer.[85] The model was also based on the MARTINI force field, refining parameters for PTB using both MD simulations and quantum mechanical calculations, while PEO parameters were taken from the CG model developed by Lee et al. in 2009.[76] This model's simulations showed self-assembly into bilayers and its calculations produced good agreement with structural and mechanical properties, such as mass density profiles, for bilayers and different copolymer length chains. This study helped to further establish the potential viability of the PEO model proposed by Lee et al.[76] for further work, potentially with Pluronic triblock copolymers.

In the same year, Taddese et al. proposed a new MARTINI model of PEO and the effect of its chain length on its partition properties in water.[54] Like the model produced by Velinova et al.[77] before them, this study proposed a new set of parameters for PEO, specifically creating a new MARTINI bead, SN_{a1}, for PEO-PEO interactions. The researchers specifically targeted the actual values of PEO's solvation free energy rather than their difference to attempt to produce a model that more accurately reproduces chain structural properties, such as radius of gyration. Although this model did optimally reproduce these properties, it also failed to reproduce partition properties for homopolymers longer than 10 beads with water. This brings up a transferability problem for the model, and more work for PEO-water interactions would need to be done for properties such as solubility.

Lastly, it is important to discuss the 2018 study by Grunewald et al., which presented a new, extensively optimised, model for PEO.[87] Using the MARTINI force field, the study parameterised DME in various solvents, over a large range of molecular weights, and evaluated their various structural and thermodynamic properties in three different solvents; water, benzene, and diglyme. The researchers created a new MARTINI bead model for PEO for use in DME in order to improve their transferability between solvents. Their DME model did improve upon the free energies of transfer and radii of gyration in all solvents, especially when they compared their results with those from the models used by Rossi et al.[79] and Lee et al.[76, 78], leading to greater agreement with experimental results. In order to validate their model, the researchers also simulated longer PEO chains, PEGylated lipids, alkyl poly(ethylene glycol) surfactants, and combined their model with MARTINI polystyrene, PS, to simulate PS-b-PEO block copolymers. The phase behaviour, structural properties, and aggregation (in the case of the PS-b-PEO block copolymers) were in good agreement with known data and helped to validate their PEO model to a high degree. This parameterisation created a PEO model with a high degree of transferability in different solvents and an ability to be combined with other CG compounds. Further testing would be needed, however, in regards to the model's use with Pluronic triblock copolymers, or for its use in alkane solvents.

These simulation studies were able to observe the self-assembly formation mechanisms and underlying thermodynamics of Pluronics and their PEO and PPO block components, though as with the experimental studies, the simulation studies above all had various weaknesses. In order to later expand upon these simulations (Chapters 5, 6, and 7), the theory of molecular dynamics and coarse-graining is first explored in the next chapter.

1.5 Objectives and structure

At the onset of this thesis, the objective was ultimately to use coarse-grained molecular dynamics simulations to parameterise a new model of the synthesis of SBA-15, in order to further simulation work for this mesoporous silica. To accomplish this we began by attempting to parameterise and validate new self-assembly models for Pluronics through a series of intermediate CG model parameterisations. These included parameterising and validating shorter common CG alkane models (as alkanes are a common solvent for Pluronic self-assembly[6, 15, 16], and they provide a basis for polymers such as polyethylene because of their carbon backbone chain structures[88, 89, 90]), validating existing CG PEO and PPO models at different monomer chain lengths for various properties, and combining those validated PEO and PPO models to create and validate Pluronic models for self-assembly and related properties. This inevitably ended up being far more challenging and time-consuming than expected, and is where the work in this thesis was concluded. In the future, our results can be combined with existing models of silica precursors[42-48] to effectively model SBA-15 synthesis.

Aside from this introductory chapter and the following chapters on molecular dynamics theory and the methodology used in this work (Chapters 2 and 3), this thesis is structured into three main chapters. These are the parameterisation and validation of CG alkane models (Chapter 4), validating PEO and PPO models (Chapter 5), and the modelling of Pluronic triblock copolymers (Chapter 6). Portions of this thesis have been or will be published in:

Chapter 1: M. Jorge, A. W. Milne, O. N. Sobek, A. Centi, G. Pérez-Sánchez, & J. R. Gomes. Modelling the self-assembly of silica-based mesoporous materials. *Molecular Simulation*, *44*(6), 435-452, 2018.

Chapter 4: O. N Sobek & M. Jorge. “Coarse-grained model for alkanes and polyethylene”, In preparation.

Chapters 5/6: O. N Sobek & M. Jorge. “Coarse-grained modeling of PEO PPO, and Pluronics self-assembly”, In preparation.

1.6 References

. [1] C. Bagneris, C. Naylor, A. Cole, N. D'Avanzo, C. Nichols, & B. Wallace. Structure of a bacterial voltage-gated sodium channel pore reveals mechanisms of opening and closing. Nat Commun, 3:1102, 2012.

. [2] J. Fedeyko, G. Vlachos, & R. Lobo. Understanding the differences between microporous and mesoporous synthesis through the phase behavior of silica. Microporous and Mesoporous Materials, 90:102–111, 2006.

. [3] T. Yanagisawa, T. Shimizu, K. Kuroda, & C. Kato. The preparation of alkyltriinethylaininonium–kaneinite complexes and their conversion to microporous materials. *Bulletin of the Chemical Society of Japan*, *63*(4), 988-992, 1990.

. [4] D. Zhao, Y. Wan, & W. Zhou. Ordered Mesoporous Materials. 98-105, 2013.

. [5] A. Pasqua, S. Wallner, D. Kerwood, & J. Dabrowiak. Adsorption of the ptii anticancer drug carboplatin by mesoporous silica. Chemistry and Biodiversity, 6(9):1343–1349, 2009.

. [6] M. Moritz & Gaske-Moritz. Mesoporous materials as multifunctional tools in biosciences: Principles and applications. Materials Science and Engineering, 49:114–151, 2015.

. [7] P. Innocenzi & P. Falcaro. Order-disorder in self-assembled mesostructured silica films: A concepts review. Chemistry of Materials, 21(13):2555–2564.

. [8] L. Giraldo, B. Lopez, L. Perez, S. Urreog, L. Sierra, & M. Mesa. Mesoporous silica applications. Materials, 258(1):129-141, 2007.

. [9] Y. Wang, Q. Zhao, N. Han, & L. Bai. Mesoporous silica nanoparticles in drug delivery and biomedical applications. Nanomedicine: Nanotechnology, Biology and Medicine, 11(2):313-327, 2015.

. [10] S. S. Park, M. Moorthy, & C. Ha. Periodic mesoporous organosilicas for advanced applications. NPG Asia Materials, 6:96, 2014.

. [11] A. de Sousa, C. de Sousa, G. de Sousa, & N. Mohallem. Multifunctional nanocomposites based on mesoporous silica: Potential applications in biomedicine. Nanotechnology and Nanomaterials, 2011.

. [12] J. S. Beck., J. C. Vartuli, W. J. Roth, M. E. Leonowicz, C. T. Kresge, K. D. Schmitt, & J. B. Higgins. A new family of mesoporous molecular sieves prepared with liquid crystal templates. *Journal of the American Chemical Society*, *114*(27), 10834-10843, 1992.

. [13] F. Simon, E. Dragan, & F. Bucatariu. Reactive polyelectrolyte multilayers onto silica particles. Reactive and Functional Polymers, 68(7):1178–1184, 2008.

. [14] D. Zhao, J. Feng, Q. Huo, N. Melosh, G. Fredrickson, B. Chmelka, & G. Stucky. Triblock copolymer syntheses of mesoporous silica with periodic 50 to 300 angstrom pores. Science, 279(5350):548–52, 1998.

. [15] J. Poostforooshan, A. Badiei, G. Farzi, & A. Weber. Mesoporous Silica/Organic Nanocomposites. Unicorn Publications Pvt. Ltd., 104-106, 2016.

. [16] S. Higgins, W. DeSisto, & D. Ruthven. Diffusive transport through mesoporous silica membranes. Microporous and Mesoporous Materials, 117(12):268–277, 2009.

. [17] S. Wu, C. Mou, & H. Lin. Synthesis of mesoporous silica nanoparticles. Chem. Soc. Rev., 42:3862–3875, 2013.

. [18] B. Trewyn, I. Slowing, S. Giri, H. Chen, & V. Lin. Synthesis and functionalization of a mesoporous silica nanoparticle based on the sol-gel process and applications in controlled release. Acc. Chem. Res., 40:846-853, 2006.

. [19] F. Tang, L. Li, & D. Chen. Mesoporous silica nanoparticles: Synthesis, biocompatibility and drug delivery. Adv. Mat., 24:1504-153, 2012.

. [20] Q. Huo, D. Mangolese, & G. Stucky. Surfactant control of phases in the synthesis of mesoporous silica-based materials. Chem. Mater., 8:1147–1160, 1996.

. [21] X. Cui, S. Mao, M. Lui, H. Yuan, & Y. Du. Mechanism of surfactant micelle formation.

Langmuir, 24(19):10771-10775, 2008.

. [22] P. Alexandridis & T. Hatton. Poly(ethylene oxide)-poly(propylene oxide)-poly(ethylene oxide) block copolymer surfactants in aqueous solutions and at interfaces: thermodynamics, structure, dynamics, and modeling. Colloids Surf. A Physicochem. Eng. Asp., 96:1–46, 1995.

. [23] T. Aoyagi. Computer Simulation of Polymeric Materials. Springer Singapore, 139-141, 2016.

. [24] J. Thielemann, F. Girgsdies, R. Schlgl, & C. Hess. Pore structure and surface area of silica sba-15: influence of washing and scale-up. Beilstein Journal of Nanotechnol, 11:110–118, 2011.

. [25] L. Sierra & J. Guth. Synthesis of mesoporous silica with tunable pore size from sodium silicate solutions and a polyethylene oxide surfactant. Microporous and Mesoporous Materials., 27(2-3):243-253, 1999.

. [26] M.C. Hernández-Soriano, A. Pena, & M. Mingorance. Release of metals from metal-amended soil treated with a sulfosuccinamate surfactant: effects of surfactant concentration, soil/solution ratio, and ph. Journal of Environmental Quality. 39(4):1298-1305, 2010.

. [27] F. Kleitz. Ordered nanoporous materials: Synthesis, characterization and functionalization methods. Chemistry Department Laval University, 2012.

. [28] J. Sun, H. Zhang, D. Ma, Y. Chen, X. Bao, A. Klein-Hoffman, N. Pfander, & D. S. Su. Alkanes-assosted low temperature formation of highly ordered SBA-15 with large cylindrical mesopores. Chem. Comm., 5343, 2005.

. [29] A. Dominguez, A. Fernandez, N. Gonzalez, E. Iglesias, & L. Montenegro. Determination of critical micelle concen- tration of some surfactants by three techniques. J. Chem. Educ., 74(10):1227, 1997.

. [30] Z. Qiao, L. Zhang, & M. Guo. Synthesis of mesoporous silica nanoparticles via controlled hydrolysis and condensation of silicon alkoxide. Chem. Mater, 21(16):3823-3829, 2009.

. [31] M. Colili & M. Manzano. Recent advances in ceramic implants as drug delivery systems for biomedical applications. International Journal of Nanomedicine, 2008.

. [32] M. Kruk, M. Jaroniec, C. Ko, & R. Ryoo. Characterization of the porous structure of sba-15. Chem. Mater., 12(7):1961–1968, 2000.

. [33] Y. Ding, H. Dana, X. Lua, Y. Wub, S. Yuana, & X. Maoa. Facile route to synthesize mesoporous silica sba-15 platelets. Materials Chemistry and Physics, 148(1-2):17-20, 2014.

. [34] I. Melez-Ortiza, B. Puente-Urbinab, G. Castruita-de Leona, J. Mata-Padillab, & L. GarcUriosteguic. Synthesis of spherical sba-15 mesoporous silica, influence of reaction conditions on the structural order and stability. Ceramics International, 42(6):7564-7570, 2016.

. [35] F. R. Siperstein, & K. E. Gubbins. Synthesis and characterization of templated mesoporous materials using molecular simulation. *Molecular Simulation*, *27*(5-6), 339-352, 2001.

. [36] F. R. Siperstein, & K. E. Gubbins. Phase separation and liquid crystal self-assembly in surfactant– inorganic– solvent systems. *Langmuir*, *19*(6), 2049-2057, 2003.

. [37] L. Jin, S. M. Auerbach, & P. A. Monson. Simulating the formation of surfactant-templated mesoporous silica materials: a model with both surfactant self-assembly and silica polymerization. *Langmuir*, *29*(2), 766-780, 2012.

. [38] M. Jorge, J. R. B. Gomes, M. N. D. S. Cordeiro, & N. A. Seaton. Molecular simulation of silica/surfactant self-assembly in the synthesis of periodic mesoporous silicas. *Journal of the American Chemical Society*, *129*(50), 15414-15415, 2007.

. [39] G. Pérez-Sánchez, J. R. B. Gomes, & M. Jorge. Modeling self-assembly of silica/surfactant mesostructures in the templated synthesis of nanoporous solids. *Langmuir*, *29*(7), 2387-2396, 2013.

. [40] G. Pérez-Sánchez, S.-C. Chien, J. R. B. Gomes, M. N. D. S. Cordeiro, S. M. Auerbach, P. A. Monson, & M. Jorge. Multiscale model for the templated synthesis of mesoporous silica: the essential role of silica oligomers. *Chemistry of Materials*, *28*(8), 2715-2727, 2016.

. [41] V. L. Zholobenko, A. Y. Khodakov, M. Impéror-Clerc, D. Durand, & I. Grillo. Initial stages of SBA-15 synthesis: an overview. Adv Coll Interface Sci., 142(1-2), 67–74, 2008.

. [42] S. Hezaveh, S. Samanta, G. Milano, & D. Roccatano. Molecular dynamics simulation study of solvent effects on conformation and dynamics of polyethylene oxide and polypropylene oxide chains in water and in common organic solvents. *The Journal of chemical physics*, *136*(12), 124901, 2012.

. [43] S. Bhattacharya, & K. E. Gubbins. Modeling triblock surfactant-templated mesostructured cellular foams. J Chem Phys.,123(13), 2005.

. [44] S. Bhattacharya, B. Coasne, F. R. Hung, & K. E. Gubbins. Modeling micelle-templated mesoporous material SBA-15: atomistic model and gas adsorption studies. *Langmuir*, *25*(10), 5802-5813, 2008.

. [45] H. Chen, Y. Wu, Y. Tan, X. Li, Y. Qian, & H. Xi. MesoDyn and experimental approach to the structural fabrication and pore-size adjustment of SBA-15 molecular sieves. Adsorpt Sci Technol., 27(6), 579–592, 2009.

. [46] S. Yuan, X. Zhang, and K. Chan. Effects of shear and charge on the microphase formation of p123 polymer in the sba-15 synthesis investigated by mesoscale simulations. Langmuir, 25(4):2034-2045, 2009.

. [47] H. Chen, Y. Wu, Y. Tan, X. Li, Y. Qian, & H. Xi. Mesoscopic simulation of surfactant/silicate self-assembly in the mesophase formation of SBA-15 under charge matching interactions. *European Polymer Journal*, *48*(11), 1892-1900, 2012.

. [48] J. E. Magee, & F. R. Siperstein. Formation of ordered mesoporous materials under slow aggregation conditions. *The Journal of Physical Chemistry C*, *113*(5), 1680-1685, 2009.

. [49] J. S. Lettow, Y. J. Han, P. Schmidt-Winkel, P. Yang, D. Zhao, G. D. Stucky, & J. Y. Ying. Hexagonal to mesocellular foam phase transition in polymer-templated mesoporous silicas. *Langmuir*, *16*(22), 8291-8295, 2000.

. [50] P. Altevogt, O. A. Evers, J. G. Fraaije, N. M. Maurits, & B. A. van Vlimmeren. The MesoDyn project: software for mesoscale chemical engineering. *Journal of Molecular Structure: THEOCHEM*, *463*(1-2), 139-143, 1999.

. [51] R. K. Iler. Chemistry of Silica--Solubility, Polymerization, Colloid and Surface Properties, and Biochemistry. New York (NY), Wiley-Interscience, 1979.

. [52] K. Kossig. Surfactants. Ullmann's Encyclopedia of Industrial Chemistry, Wiley-VCH, 2005.

. [53] M. Rosen & J Kunjappu. Surfactants and Interfacial Phenomena. John Wiley Sons. 145-146, 2012.

. [54] J. N. Phillips. The energetics of micelle formation. Trans. Faraday Soc, 51:561–569, 1955.

. [55] T. Chakrabortya, I. Chakrabortyb, & S. Ghosha. The methods of determination of critical micellar concentrations of the amphiphilic systems in aqueous medium. Arabian Journal of Chemistry, 4(3):265-270, 2011.

. [56] G. J. D. A. Soler-Illia, C. Sanchez, B. Lebeau, & J. Patarin. Chemical strategies to design textured materials: from microporous and mesoporous oxides to nanonetworks and hierarchical structures. *Chemical reviews*, *102*(11), 4093-4138, 2002.

. [57] C. Tanford. *The hydrophobic effect: formation of micelles and biological membranes*. Wiley Interscience publication. Wiley,1973.

. [58] J. N. Israelachvili, D. J. Mitchell, & B. W. Ninham. 'Theory of self-assembly of hydrocarbon amphiphiles into micelles and bilayers'. *Journal of Chemical Socirty, Faraday Transaction 2 (*72),1525–1568, 1976.

. [59] R. Nagarajan, & E. Ruckenstein. 'Aggregation of amphiphiles as micelles or vesicles in aqueous media'. *Journal of Colloid and Interface Science* 71(3), pp. 580–604, 1979.

. [60] E. Batrakova & A. Kabanov. Pluronic block copolymers: Evolution of drug delivery concept from inert nanocarriers to biological response modifiers. J Control Release. 130(2):98–106, 2008.

. [61] A. Denkova, E. Mendes, & C. Coppens. Non-equilibrium dynamics of block copolymer micelles in solution: recent insights and open questions. Soft Matter, 6:2351-2357, 2010.

. [62] E. A. Yapar, & Ö Ýnal. Poly (ethylene oxide)–poly (propylene oxide)-based copolymers for transdermal drug delivery: An overview. *Tropical Journal of Pharmaceutical Research*, *11*(5), 855-866, 2012.

. [63] A. V. Kabanov, E. V. Batrakova, & V. Y. Alakhov. Pluronic® block copolymers as novel polymer therapeutics for drug and gene delivery. *Journal of controlled release*, *82*(2-3), 189-212, 2002.

. [64] H. Tadokoro, Y. Chatani, T. Yoshihara, S. Tahara, & S. Murahashi. Structural studies on polyethers,[-(CH2) m-O-] n. II. Molecular structure of polyethylene oxide. *Die Makromolekulare Chemie: Macromolecular Chemistry and Physics*, *73*(1), 109-127, 1964.

. [65] G. Allen, C. Booth, & M. N. Jones. Polypropylene oxide I: An intrinsic viscosity/molecular weight relationship. *Polymer*, *5*, 195-199,1964. [

. [66] H. Yue, Y. Zhao, X. Ma, & J. Gong. Ethylene glycol: properties, synthesis, and applications. *Chemical Society Reviews*, *41*(11), 4218-4244, 2012.

. [67] B. Das, M. N. Roy, & D. K. Hazra. Densities and viscosities of the binary aqueous mixtures of tetrahydrofuran and 1, 2-dimethoxyethane at 298, 308 and 318 K, 1994.

. [68] Y. Sasanuma. Conformational analysis of poly (propylene oxide) and its model compound 1, 2-dimethoxypropane. *Macromolecules*, *28*(25), 8629-8638, 1995.

. [69] J. H. Lii, K. H. Chen, T. B. Grindley, & N. L. Allinger. Alcohols, ethers, carbohydrates, and related compounds. III. The 1, 2-dimethoxyethane system. *Journal of computational chemistry*, *24*(12), 1490-1503, 2003.

. [70] J. Ortega-Vinuesa, M. Santander-Ortega, A. Reyes, & N. Cxaba. Colloidal stability of

Pluronic f68-coated plga nanoparticles: A variety of stabilisation mechanisms. Journal of Colloid and Interface Science, 2006.

. [71] "BASF - Product information the chemicals catalog - Pluronics". *BASF Corporation Website*. Available at: https://worldaccount.basf.com/wa/NAFTA/Catalog/ChemicalsNAFTA/pi/BASF/Brand/pluronic, 2016. [Accessed 28 10 2018].

. [72] H. Lee, R. M. Venable, A. D. MacKerell Jr, & R. W. Pastor. Molecular dynamics studies of polyethylene oxide and polyethylene glycol: hydrodynamic radius and shape anisotropy. *Biophysical journal*, *95*(4), 1590-1599, 2008.

. [73] S. Hezaveh, S. Samanta, G. Milano, & D. Roccatano. Structure and dynamics of 1, 2-dimethoxyethane and 1, 2-dimethoxypropane in aqueous and non-aqueous solutions: A molecular dynamics study. *The Journal of chemical physics*, *135*(16), 164501, 2011.

. [74] G. Srinivas, J. C. Shelley, S. O. Nielsen, D. E. Discher, & M. L. Klein. Simulation of diblock copolymer self-assembly, using a coarse-grain model. *The Journal of Physical Chemistry B*, *108*(24), 8153-8160, 2004.

. [75] M. Hatakeyama, & R. Faller. Coarse-grained simulations of ABA amphiphilic triblock copolymer solutions in thin films. *Physical Chemistry Chemical Physics*, *9*(33), 4662-4672, 2007.

. [76] H. Lee, A. H. de Vries, S. J. Marrink, and R. W. Pastor. A coarse- grained model for polyethylene oxide and polyethylene glycol: Conformation and hydrodynamics. J. Phys. Chem., 113(40):13186-13194, 2009.

. [77] M. Velinova, D. Sengupta, A. V. Tadjer, & S. J. & Marrink. Sphere-to-rod transitions of nonionic surfactant micelles in aqueous solution modeled by molecular dynamics simulations. *Langmuir*, *27*(23), 14071-14077, 2011.

. [78] H. Lee, & R. W. Pastor. Coarse-grained model for PEGylated lipids: effect of PEGylation on the size and shape of self-assembled structures. *The Journal of Physical Chemistry B*, *115*(24), 7830-7837, 2011.

. [79] G. Rossi, P. F. J. Fuchs, J. Barnoud, and L. Monticelli. A coarse- grained martini model of polyethylene glycol and of polyoxyethylene alkyl ether surfactants. J. Phys. Chem. B, 116(49):14353–14362, 2012.

. [80] T. Taddese, & P. Carbone. Effect of Chain Length on the Partition Properties of Poly (ethylene oxide): Comparison between MARTINI Coarse-Grained and Atomistic Models. *The Journal of Physical Chemistry B*, *121*(7), 1601-1609, 2017.

. [81] S. Hezaveh, S. Samanta, A. De Nicola, G. Milano, & D. Roccatano. Understanding the interaction of block copolymers with DMPC lipid bilayer using coarse-grained molecular dynamics simulations. *The Journal of Physical Chemistry B*, *116*(49), 14333-14345, 2012.

. [82] E. Choi, J. Mondal, & A. Yethiraj. Coarse-grained models for aqueous polyethylene glycol solutions. *The Journal of Physical Chemistry B*, *118*(1), 323-329, 2013.

. [83] S. Nawaz & P. Carbone. Coarse-graining poly(ethylene oxide)-poly(propylene oxide)-poly(ethylene oxide) (peo-ppo-peo) block copolymers using the martini force field. J. Phys. Chem. B, 118(6):1648-1659, 2014.

. [84] I. Wood, M. F. Martini, J. M. R. Albano, M. L. Cuestas, V, L, Mathet, & M. Pickholz, M. Coarse grained study of pluronic F127: Comparison with shorter co-polymers in its interaction with lipid bilayers and self-aggregation in water. *Journal of Molecular Structure*, *1109*, 106-113, 2016.

. [85] D. A. Grillo, J. M. Albano, E. E. Mocskos, J. C. Facelli, M. Pickholz, & M. Ferraro. Diblock copolymer bilayers as model for polymersomes: A coarse grain approach. *The Journal of chemical physics*, *146*(24), 244904, 2017.

. [86] S. Kumar, A. Bhattarai, & S. Chatterjee. Applications of Surfactants in modern Science and Technology. Modern Trends in Science and Technology. 147- 158, 2013.

. [87] F. Grunewald, G. Rossi, A. H. De Vries, S. J. Marrink, & L. Monticelli. Transferable MARTINI Model of Poly (ethylene Oxide). *The Journal of Physical Chemistry B*, *122*(29), 7436-7449, 2018.

. [88] A. Peacock. *Handbook of polyethylene: structures: properties, and applications*. CRC Press, 2000.

. [89] D. W. Van Krevelen, & P. J. Hoftyzer. Properties of polymers. Elsevier Scientific Publishing, 1976.

. [90] J. Bicerano. Prediction of polymer properties. New York: Marcel Dekker, (2), 1996.

MOLECULAR DYNAMICS SIMULATIONS

2

First developed by Fermi et al in the mid 1950s[1], molecular dynamics, MD, simulations have become an invaluable tool for researchers seeking to understand physical, chemical, and biological systems. MD simulations are inexpensive and vastly faster alternatives to traditional experimental work, allowing the user to recreate hard to evaluate systems and quantities, like the velocities of atoms and molecules.[2-5] These simulations are now routinely used to evaluate the structure, dynamics and thermodynamics of molecules and their complexes, such as the fluctuations and conformational changes of polymers and the formation of micelles.[2-5]

In this chapter, the fundamentals of MD simulations are discussed, concentrating on the use of force fields and their components. This culminates specifically with the MARTINI coarse-grained force field, which is the basis for the studies in later chapters of this thesis.

2.1 Molecular dynamics

Molecular dynamics is a method for studying the physical movements of atoms and molecules, and is thus a type of N-body simulation.[2-5] The atoms and molecules are allowed to interact for a fixed period of time, giving a view of the dynamical evolution of the system. In the most common version, the trajectories of atoms and molecules are determined by numerically solving Newton's equations of motion for a system of interacting particles, where forces between the particles and their potential energies are calculated using interatomic potentials or molecular mechanics force fields.[2, 3, 6] The main Newtonian principle at work here is force equals mass times acceleration, shown in **Equation 2.1** below.[2]

$$\mathrm{F} = \mathrm{m} * \mathrm{a} \tag{2.1}$$

There are two main families of MD methods, which can be distinguished according to the model chosen to represent a physical system: classical, or quantum first-principles. In the classical mechanics approach to MD simulations molecules are treated as classical objects, sometimes referred to as a 'ball and stick’ model.[2, 7, 8] Atoms correspond to soft 'balls', or beads, and elastic 'sticks', or springs, correspond to bonds. The laws of classical mechanics define the dynamics of the system. The quantum or first-principles MD simulations take explicitly into account the quantum nature of the chemical bond.[3, 7] The electron density function for the valence electrons that determine bonding in the system is computed using quantum equations, whereas the dynamics of ions (nuclei with their inner electrons) is followed classically.[6, 3, 7, 8] Quantum MD, however, is far more probabilistic and less deterministic than classical MD can be for predicting the nature of interactions, and has a much higher computational cost due to the higher level of theory.[2, 6]

The basic requirements of classical MD simulations are simple. For a system of interest, a set of initial positions and initial velocities for all of particles in the system needs to be set.[2, 6] This allows for an interaction potential to derive the forces between the particles. Secondly, classical MD simulations require the system to evolve by solving the above mentioned classical equations of motion.[6, 8] To work efficiently, MD also requires a few very specific conditions.[3, 7] These include specific variables for the system and area being evaluated; defined potential energies for the molecules being modeled, integration algorithms to evaluate their equations of motion, and the temperature and pressure of the system.[4, 5] These conditions allow for classical MD force fields, or sets of rules that defines interactions between atoms or groups of atoms, to run optimally when they are simulated.

2.2 Creating MD simulations

To properly run an MD simulation, there are certain requirements that need to be met. These include a force field that explains both the bonded and non-bonded interactions between the atoms of the system, a time integration algorithm, barostats, and thermostats, and the representation of the atoms in the system as beads.[2, 9, 4, 5] These requirements are clarified in detail below.

2.2.1 Force fields

Force fields are a vital part of classical MD. As simulations are computations based on Newton's second law, force fields are used to study the atomic potential energy of a system to learn specific things about different properties.[2, 4, 5, 8, 9] These computations can be carried out mathematically by hand, but are more often carried out in computer programs where they can look at larger portions of material.[2, 4, 5, 8, 9] In force fields, molecules are defined as a set of atoms held together by harmonic, or elastic forces, and the force field replaces the complex energy landscape with a simplified model to represent it.[2, 4, 5, 8, 9] These elastic forces are built up from two distinct components which describe the interaction between particles (typically atoms): the set of equations called potential energy functions, or the forces, based on harmonic functional interactions for bonds and angles, and the parameters which are used in those functions.[7, 8] This is shown in the overall **Equations 2.2 – 2.4**;

$$\mathbf{U(R) = U_{bonded} + U_{non-bonded}} \tag{2.2}$$

$$\mathbf{U_{bonded} = U_{bonds} + U_{angles} + U_{torsions}} \tag{2.3}$$

$$\mathbf{U_{non-bonded} = U_{LJ} + U_{van\ der\ Waals\ \ potential}} \tag{2.4}$$

where U is a potential energy function of the atomic positions, and R is a function of the position of all the atoms in the system.[2, 4, 5, 7] These functions are expressed in terms of Cartesian coordinates of the atoms.[4, 9]

2.2.1.1 Bonded potential energies

The first portion of the calculated potential energies is the bonded potential energies. The three main functions involve the covalent forces between bonds (1-2 ‘nearest neighbouring atom’ interactions), angles (1-3 'next nearest neighbouring atom' interactions), and dihedrals (1-4 'across molecule' interactions).[2, 4, 5, 7] A graphical representation of these potential energies can be seen in **Figure 2.1**.

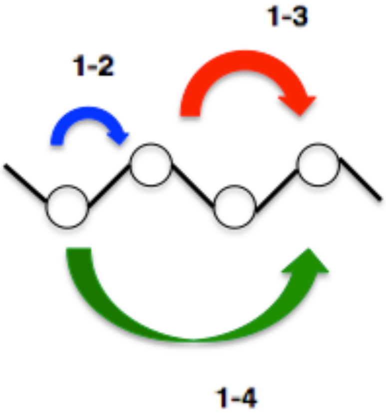

Figure 2.1: Graphical representation of the 1-2, 1-3, and 1-4 'nearest neighbouring atom' interactions for the covalent forces between bonds, angles, and dihedrals respectively.

These functions are represented by **Equations 2.5 – 2.7**;

$$\mathbf{U_{bonds}} = \sum\nolimits_{\mathbf{1,2\ pairs}} \mathbf{k_b}(\mathbf{b} - \mathbf{b_0})^2 \tag{2.5}$$

$$\mathbf{U_{angles}} = \sum\nolimits_{\mathbf{1,3\ pairs}} \mathbf{k_\theta}(\boldsymbol{\theta} - \boldsymbol{\theta_0})^2 \tag{2.6}$$

$$\mathbf{U_{dihedrals}} = \sum\nolimits_{\mathbf{1,4\ pairs}} \mathbf{k_\phi}(\mathbf{1} - \mathbf{cos}(\mathbf{n}\boldsymbol{\phi})) \tag{2.7}$$

where the k constants are equivalent to harmonic constants for each bond, angle, or dihedral pair, b_0 is the ideal bond length, θ_0 is the ideal angle, and ϕ is the ideal rotational torsion dihedral.[4, 5, 7]

Dihedral interactions can also include what are called 'improper' dihedral interactions, where the four atoms defining the angle are not all connected by consecutive covalent bonds.[4, 5, 7]

2.2.1.2 Non-bonded potential energies

The second portion of the calculated potential energies is the non-bonded portion. This is a sum of the van der Waals and the electrostatic interactions between a pair of atoms.[2, 4, 5, 9, 10] Van der Waals interactions between atoms arise from a balance between repulsive and attractive forces, where the repulsive force occurs at short distances where electron on electron interaction is very high, and the attractive force occurs over longer distances from changes in distribution in the various clouds of electrons, typically caused by interactions between instantaneous or induced dipole interactions.[4, 5, 8, 10] Each of these effects only becomes significant when the atomic separation, r, decreases, as they will tend to zero as r tends to infinity [4, 10] These interactions are most commonly represented by the Lennard-Jones 12-6 potential, LJ. [4, 5, 8] The electrostatic interaction between a pair of atoms, can either be attractive or repulsive depending on their charge signs.[2, 9, 4, 5] This is typically represented by using the Coulomb potential.[2, 4, 5]. The non-bonded potential energy functions are shown in **Equations 2.8** and **2.9**. Electrostatic potentials can be described more obviously using classic

Coulomb law, as shown in **Equation 2.8** where $r_{ij}$is the distance between a pair of atoms i and j, q_i and q_j are the charges of those atoms, ϵ_0 is 8.85418782·10^{-12} C^2/m^2N or the cohesive energy or permittivity of free space in the simulation system, and ϵ_r is 1, or the relative cohesive energy or permittivity of the material being simulated.[2, 4, 5, 9]

$$U_{\text{electrostatic/Coloumb potential}} = \frac{1}{4\pi\varepsilon_0}\frac{q_i q_j}{\varepsilon_r r_{ij}}$$

(2.8)

If the two atoms i and j have opposing charges, q_i and q_j, then the potential energy is attractive, while if the charges are the same, the potential energy is repulsive.[2, 4, 5, 9]

A clearer understanding of the LJ potentials is demonstrated in **Equation 2.9**, where i and j are two atoms in the system, ϵ_{ij} is the minimum of the potential energy, r_{ij} gives the distance between two atoms, and σ_{ij} is the equilibrium distance between the two molecules at which the potential energy is 0.[2, 4, 5, 9]

$$U_{LJ} = 4\epsilon_{ij}\left[(\frac{\sigma_{ij}}{r_{ij}})^{12} - (\frac{\sigma_{ij}}{r_{ij}})^{6}\right] \qquad \textbf{(2.9)}$$

The portion of **Equation 2.9** to the 12th power represents repulsive, or short-range, forces between atoms, while the portion to the 6th power represents attractive, or long-range, forces between them.[2, 4, 5, 9] As r_{ij} increases, LJ potential energy approaches 0, so within classical MD simulations it is cut-off at a particular selected radius, reducing the potential to 0.[2, 9] A visual example of this truncation can be seen in **Figure 2.2**.[68, 69] Because of this truncation, MD simulations often employ long-range corrections to ensure the pressure and energy of the system is maintained.[2, 4, 5, 9]

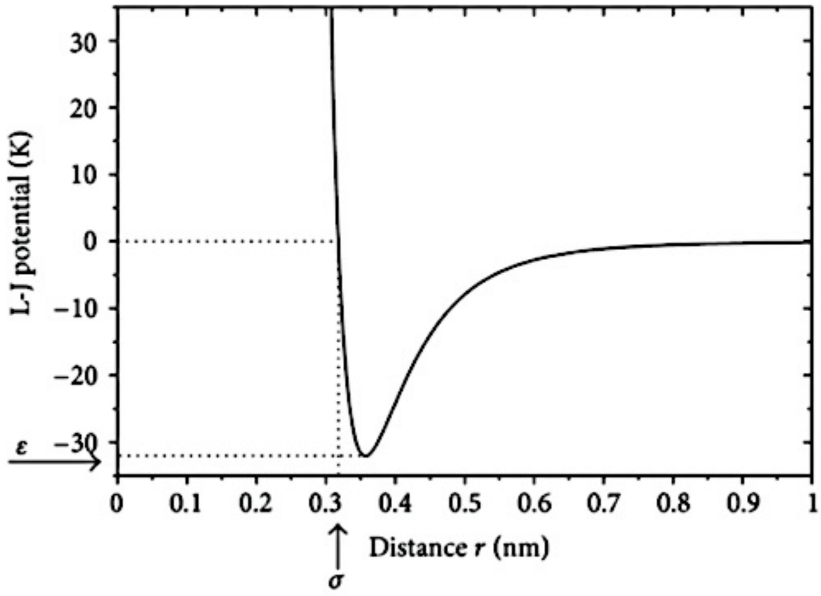

Figure 2.2: Example Lennard-Jones potential of a carbon-hydrogen interaction, ϵ = 0.83 kJ/mol and σ = 0.31 nm taken from [68, 69]

When the two atoms, i and j, happen to be non-identical, **Equation 2.10** and **Equation 2.11** are normally used to determine ϵ_{ij} and r_{ij}.[2, 4, 5, 9] These are called the Lorentz-Berthelot combing rules.[2, 5, 9]

$$\boldsymbol{\sigma}_{\mathbf{ij}} = \frac{1}{2}(\boldsymbol{\sigma}_{\mathbf{ii}} + \boldsymbol{\sigma}_{\mathbf{jj}}) \qquad \textbf{(2.10)}$$

$$\boldsymbol{\epsilon}_{\mathbf{ij}} = (\boldsymbol{\epsilon}_{\mathbf{ii}} * \boldsymbol{\epsilon}_{\mathbf{jj}})^{\frac{1}{2}} \qquad \textbf{(2.11)}$$

Long-range electrostatic or Coulomb interactions are often dealt with using the Ewald summation method.[4, 5, 11] An Ewald sum is based on splitting **Equation 2.8** into two series; a faster variation for an r with a small value, which decays quickly and is therefore negligible past a particular cutoff distance, and a second smoother variation for an r with a large value that allows its Fourier transform to be represented by only a few terms.[4, 5, 11] Ewald sums have some drawbacks however, as cut-offs for reciprocal and real space calculations must be specific, and there is not a uncomplicated way to obtain a favourable set of values, leading to errors.[4, 5, 11] Ewald sums also scale with N^2, or at best $N^{1.5}$, meaning that as the size of a simulated system increases, the efficiency decreases.[4, 5, 11] In order to combat these issues, popular Ewald variants such as Particle Mesh Ewald, PME, have been produced.[11, 12]

PME is a faster algorithm that scales as NlogN, and instead of using implicit fourier transform evaluation it utilises a fast Fourier transformation, FFT, substantially reducing the time needed to solve.[12] FFT is an algorithm that uses Fourier analysis to convert a signal from the time or spatial representation to one of frequency, or vice versa.[12] Their speed and accuracy, however, depend upon the interpolation scheme, mesh size, and other variables that need to be set in the MD input files, making PME more difficult to optimise.[12]

2.2.2 Integration algorithms

Because the potential energy of a system is a complicated function of the specific positions of all the atoms in the system, there is no singular analytical solution to the equations of motion.[5, 13, 14, 15] Time integration algorithms, therefore, are used to numerically solve them.[5, 13, 14, 15] These algorithms discretise time into timesteps, Δt, and use atomistic positions and other derivative quantities from the system at a particular timestep to compute those same quantities at other timesteps, $t + \Delta t$.[5, 13, 14, 15] The algorithms used in MD simulations should consequently conserve the energy and momentum of a system, permit a long time step for integration, and be computationally efficient.[5, 13, 14, 15] There are numerous possible algorithms that have been developed for use in MD, including the leap-frog algorithm, Verlet algorithm, velocity Verlet algorithm, and beemans algorithm.[13, 14, 15] The studies in this thesis primarily utilise the leap-frog and Verlet algorithms, as will be discussed in future chapters, so we will go into more detail on those algorithms explicitly here.

The leap-frog algorithm is a second-order method that is equivalent to updating the velocities and positions of a system at interleaved timesteps, staggered so they "leapfrog" over each other.[5, 13, 15] This can be seen in **Equation 2.12** and **Equation 2.13**;

$$\mathbf{r}(\mathbf{t}+\boldsymbol{\Delta}\mathbf{t}) = \mathbf{r}(\mathbf{t}) + \mathbf{v}(\mathbf{t}+\tfrac{\boldsymbol{\Delta}\mathbf{t}}{\mathbf{2}})\boldsymbol{\Delta}\mathbf{t} \qquad \textbf{(2.12)}$$

$$\mathbf{v}\left(\mathbf{t}+\tfrac{\boldsymbol{\Delta}\mathbf{t}}{\mathbf{2}}\right) = \mathbf{v}\left(\mathbf{t}-\tfrac{\boldsymbol{\Delta}\mathbf{t}}{\mathbf{2}}\right) + \mathbf{a}(\mathbf{t})\boldsymbol{\Delta}\mathbf{t} \qquad \textbf{(2.13)}$$

where r(t) is the position at time t, v(t) is the velocity at time t, and a(t) is the acceleration at time t.[13, 15] The formula to solve the acceleration, a(t), at a particular time can be seen in **Equation 2.14**, where m is the mass of a particle, and F(t) is the force acting on that particle at time t and is calculated from the distance derivative of the potential energy.[5, 13, 15]

$$\mathbf{a}(\mathbf{t}) = \frac{\mathbf{F}(\mathbf{t})}{\mathbf{m}} = -\frac{\mathbf{1}}{\mathbf{m}}\nabla\mathbf{u}\big(\mathbf{r}(\mathbf{t})\big) \qquad \textbf{(2.14)}$$

The second most commonly used integration algorithm in the studies in this thesis is the Verlet algorithm. The Verlet algorithm is similar to the leap-frog algorithm in that it calculates the same velocities using **Equation 2.13**, though with differing positions.[14, 15] These updated positions can be seen in **Equation 2.15**, where $O(\Delta t^4)$ is the global truncation error.[14, 15]

$$\mathbf{r}(\mathbf{t}+\Delta\mathbf{t}) = \mathbf{2r}(\mathbf{t}) - \mathbf{r}(\mathbf{t}-\Delta\mathbf{t}) + \mathbf{a}(\mathbf{t})\Delta\mathbf{t}^2 + \mathbf{O}(\Delta\mathbf{t}^4) \qquad \textbf{(2.15)}$$

2.2.3 Barostats

Barostats and thermostats are necessary portions of executing MD simulations, as it is important to maintain constant pressure and/or temperature in simulated boxes or cells.[2, 4, 5, 8, 9, 10, 16, 17] This is due to it preserving the correct thermodynamics of the systems.[2, 4, 5, 8, 9, 10, 16, 17] To allow for a simulated box to preserve this constant pressure and temperature, an NPT ensemble where volume is allowed to fluctuate is required.[2, 4, 5, 8, 9, 10, 16, 17] This NPT ensemble can allow for a change in volume throughout the simulation cell, i.e. isotropic pressure coupling, or a volume change solely in one direction in the cell, i.e. semi-isotropic pressure coupling.[2, 4, 5, 8, 9, 10, 16, 17] There are several types of barostats that can be used to control the pressure of an MD simulation, including the Berendsen barostat, the Nosé-Hoover barostat, and the Parrinello-Rahman barostat.[2, 4, 5, 8, 9, 10, 16, 17] The studies in this thesis use the Berendsen barostat and the Parrinello-Rahman barostat, so those are covered in more detail below.

One of the simplest barostats to control the pressure of these systems is the Berendsen barostat.[4, 5, 8, 16] Here it was used to relax our simulation systems before production runs.[4, 5, 8, 16] In the Berendsen barostat, the volume of the simulation cell is corrected at a precise specified time.[4, 5, 8, 16] The Berendsen barostat does not generate any known statistical ensemble, especially for small systems, but it is stable for most simulations and therefore a very popular choice to equilibrate MD simulations.[4, 5, 8, 16] This is shown in **Equation 2.16**, where $\mathrm{P_{md}}$ is the desired pressure, P(t) is the instantaneous pressure, and τ_P is the barostat relaxation time constant.[16]

$$\frac{\mathbf{dP(t)}}{\mathbf{dt}} = \frac{\mathbf{P_{md} - P(t)}}{\boldsymbol{\tau_P}} \qquad \textbf{(2.16)}$$

The scaling of this barostat can be seen in **Equation 2.17**, where η is the scaling factor for one side of the simulation cell box, τ is a time coupling constant, and β is the isothermal compressibility of the system.[16]

$$\boldsymbol{\eta = 1 - \frac{\Delta t}{\tau_P}\beta(P - P_0)} \quad \textbf{(2.17)}$$

The other barostat used in this thesis's simulations, specifically for production runs, is the Parrinello-Rahman barostat.[4, 5, 17] This barostat allows the volume and shape of the simulation cell to fluctuate, but with an extra degree of freedom added through an extended Hamiltonian equation.[4, 5, 17] The expression of this barostat can be seen in **Equation 2.18**, where W is the magnitude of the coupling, b represents the simulation box vectors, and V_b is the volume of the simulation box.[17]

$$\boldsymbol{\frac{db^2}{dt^2} = V_b W^{-1} b'^{-1}(P(t) - P_0)} \quad \textbf{(2.18)}$$

2.2.4 Thermostats

To maintain the constant temperature of the simulation box necessitated to run NVT and NPT simulations, MD also uses various thermostats. These include; the Berendsen thermostat, the Nosé-Hoover thermostat, and the v-rescale thermostat.[8, 10, 2, 9, 16, 17, 4, 5] The two thermostats used in this thesis, the Berendsen thermostat and the v-rescale thermostat, are explained in more detail below.

One of the easiest to control thermostats is the Berendsen thermostat, which is taken from the same study that created the Berendsen barostat.[16]. As with the Berendsen barostat, the Berendsen thermostat corrects the volume of the simulation cell at a particular specified time.[8, 16, 4, 5] Also similar to the barostat, this thermostat does not generate any known statistical ensemble, though it is incredibly robust.[8, 16, 4, 5] This thermostat is shown in **Equation 2.19**, where τ is the rise time of the thermostat, describing the strength of the coupling of the system, v is the velocity, $\mathrm{T_{md}}$ is the reference temperature of the thermostat, and T(t) is the temperature at a given time.[16] The scaling factor for this thermostat can be seen in **Equation 2.20**, where λ represents the scaling factor and τ_T is the rise time of the thermostat at temperature T.[16]

$$\frac{\mathbf{dv}}{\mathbf{dt}} = \frac{\mathbf{f}}{\mathbf{m}} + \frac{\mathbf{1}}{\mathbf{2\tau}}\left(\frac{\mathbf{T_{md}}}{\mathbf{T(t)}} - \mathbf{1}\right)\mathbf{v} \qquad \textbf{(2.19)}$$

$$\boldsymbol{\lambda} = \left[\mathbf{1} + \frac{\Delta t}{\tau_T}\left\{\frac{T_0}{T(t-\frac{\Delta t}{2})} - \mathbf{1}\right\}\right]^{\frac{1}{2}} \quad \textbf{(2.20)}$$

The other thermostat used in this thesis is the v-rescale thermostat, which multiplies each atomic velocity by a factor that creates the desired temperature for the system.[4, 5, 18] The scaling done by the v-rescale thermostat can be done at every step or only periodically.[4, 5, 18] It is easy to use, though like the Berendsen methods, its results do not correspond to any ensemble, although the amount they deviate from canonical is quite small.[4, 5, 16, 18] The scaling for this thermostat can be seen in **Equation 2.21;**

$$\mathbf{v}^{\mathbf{new}} = \sqrt{\frac{T_{md}}{T(t)}}\,\mathbf{v}^{\mathbf{old}} \quad \textbf{(2.21)}$$

where v^{old} is the velocity prior to rescaling, v^{new} is the rescaled velocity, T_{md} is the reference temperature of the thermostat, and T(t) is the temperature at a given time.[4, 5, 18]

2.2.5 Bead representations

As described earlier, the atoms and molecules used in MD simulations correspond to soft ‘balls’ or beads connected by elastic ‘sticks’, or springs, and therefore need topologies to describe the beads that a force field uses with its functions.[6, 8, 10] Topologies express the needed Cartesian coordinates of all the beads in the system as well as the connectivity between every type of those beads.[2, 8, 9, 10] These coordinates can be found through online databases of known molecules, such as the US National Institute of Cancer or RCSB Protein Data Bank, or extrapolated based on known properties of the desired molecules.[2, 8, 9, 10, 19] These initial coordinates are then coupled in the topology with any specific equilibrium bond lengths, bond length force constants, bond angles, angle force constants, dihedral angles, dihedral force constants, and possibly improper dihedrals needed to adequately describe the interconnectivity of the beads.[2, 4, 5, 8, 9, 10, 19] Periodic boundary conditions (pbc) are also established so that molecules that leave the simulation cell box will reappear across from where they exited.[2, 4, 5, 8, 9, 10] This allows a simulation to replicate an infinite periodic system using a small simulation box.[2, 4, 5, 8, 9, 10]

The sum of all of these functions and their parameters and coordinates that go into them is what constitutes a force field which can be used in simulations, where a computer program will run the simulation starting from selected atomic coordinates at different time-steps.[2, 9] These force fields do come with some limitations to the types of systems that can be simulated, however, which will be discussed in the next section.

2.3 Limitations of classical atomistic MD

While molecular dynamics simulations are immensely practical tools for researchers, there are a few limitations inherent to their use. The first limitation is, as mentioned above, that classical MD simulations are based on classical descriptions of interatomic interactions.[6, 8, 9] In these simulations electrons are not present explicitly, they are introduced to the system by the potential energy surface that is a function of solely the atomic positions, approximated by an analytic function that gives the potential energy U as a function of coordinates.[6, 7, 8] This potential energy function is often based on fitting to available experimental data, including solvation free energy, enthalpy of vaporisation, density, and radial distribution functions. Though this method is fine for a large system, it becomes a problem as the lack of explicit electrons means decreased detail in the simulation, and the simulations are dependent on the availability of good potential functions.[3, 6]

Another limitation in classical MD simulations is the use of classical Newtonian equations to describe the motion of atoms.[6, 8, 9, 10] This approximation leads to a typical interatomic spacing of 0.1 -0.3 nm, and therefore is useful for most heavier atoms at a sufficiently high temperature where classical mechanics can be applied. Lighter elements, such as hydrogen and helium, or simulations at lower temperature however, often need superimposed quantum corrections to describe their motion.[6, 8, 9, 10]

The arguably most pressing limitations are those of the time of the MD simulation and the size of the MD computational cell (i.e. the number of atoms in a simulation box). In classical MD simulations, the maximum timestep of integration is defined by the fastest motion within the system.[6, 8, 9] In a molecular system, vibrational frequencies go up to 3000 cm^{-1} which corresponds to a period of approximately 10 fs, while optical phonon frequencies range to 10 THz which corresponds to a period of roughly100 fs.[6, 7, 20] Therefore, timesteps in MD simulations are on the order of a femtosecond. Modern computers, however, can only calculate $10^6 – 10^8$ timestep processes, meaning they can only simulate processes between 100 – 1000 ns.[6, 7, 20] This seriously limits MD simulations from being able to render many problems that require larger timescales, such as thermally-activated processes, annealing of irradiation, vapour film deposition, and most relevantly to this study, the self-assembly of surfactants.[2, 6, 7, 8, 20]

Modern computers also limit the number of atoms that can be included in a simulation and thus the size of the computational cell, typically to $10^4 – 10^8$, or a cell in the order of tens of nm.[2, 6, 7, 20] This means that any spatial correlation lengths or any particular features of interest need to be smaller than the computational cell size, leading to a potential lack of detail and limiting the type of simulations that can be rendered.[6, 7, 8, 9] . Larger systems and simulations of processes on timescales beyond 1 microsecond require larger computer resources and extensive time-steps to complete.[21, 22, 23, 24, 26] This makes them prohibitively financially and time expensive, so a more succinct model with reduced representations is needed.

To overcome the time and size limitations of classical atomistic MD simulations, coarse-grained models are often to model and represent systems.[23, 24, 26] These allow for both longer and larger simulations by reducing the degrees of freedom of the model, and are discussed in the following section in more detail.

2.4 Coarse-grained simulations

In order to overcome the previously mentioned prohibitive costs and time associated with atomistic simulations, but still retain their ability to correctly reproduce physical behaviour of simulated systems, coarse-grained models are often used. Coarse-grained, CG, force field simulation models are nearly identical to force fields applied to all atoms in a system, or all-atom, AA, models, except that a number of atoms are grouped together.[23, 24, 26]

Instead of explicitly representing every atom of the system, one uses ”pseudo-atoms” or ”beads” to represent groups of atoms on which the classical MD computations will take place.[23, 24, 25, 26] Each of the atom groups are mapped into beads with a set number of atoms and parameters given by the force field model.[23, 24, 26] An example of this mapping can be seen in **Figure 2.3**.[27] With this model, the entire system, including any solvents, is broken down into these beads for simulation runs.[23, 24, 25] This model reduces the complexity of the system, enhancing the sampling of phase space and allowing for a relatively accurate depiction and feasible running time through computational simulation.[23, 24, 25, 26]

Figure 2.3: Example of coarse-grain beaded block copolymer, $\mathrm{PEO_3PPO_3PEO_3}$ [27]

2.4.1 Coarse-graining theory

As in AA force fields, in the majority of CG force fields, the set of CG interactions is separated in two parts. This can be seen in **Equation 2.22**:

$$\mathbf{U^{CG}(R)} = \mathbf{U^{CG}_{bonded}} + \mathbf{U^{CG}_{non-bonded}} \qquad \textbf{(2.22)}$$

where $\mathrm{U^{CG}(R)}$ is the total potential energy, $\mathrm{U^{CG}_{bonded}}$ is the bonded potential portion, and is $\mathrm{U^{CG}_{non-bonded}}$ the non-bonded potential portion.[25, 26, 34] The intramolecular bonded CG interactions act on groups of neighboring beads in a chain, while the intra- and intermolecular non-bonded CG interactions act between specific pairs of beads within a certain cutoff distance.[25, 26, 34] If beads within the same chain are taken into account by the bonded interactions, however, they are unaffected by non-bonded interactions.[25, 26, 34]

When coarse-graining, there are four major questions to ask. The first is what degrees of freedom need to be included, or what is the basic architecture of the molecules for driving the relevant physics of the simulation?[23, 24, 25, 26, 34] Practically this means choosing the best possible mapping for the beads in the system for what needs to be simulated. For example, if the simulation wants to capture the motion of a Pluronic surfactant chain, it needs to be decided whether the side-chain groups will need beads, or if a few larger beads representing only the backbone chain will suffice.

The next is how many different types of beads are needed?[23, 24, 25, 26, 34] To allow for a basic understanding of the underlying physics, and also whatever else needs to be answered by the simulation, a minimal number of bead types need to be selected. For example, in the case of Pluronic surfactant chains again, a minimum of two bead types would be needed to cover the hydrophilic and hydrophobic portions. This question becomes even more complicated when discussing the solvent of a system.[23, 24, 25, 26]

The final questions to consider are what are the dominant length and dominant energy scales of the system?[23, 24, 25, 26, 34, 35] This translates to how will things like the excluded volume interactions be modelled (i.e. repulsive terms) and will a Lennard-Jones functionality (i.e. repulsive terms and attractive terms) be enough to model the functionalities of the system. To answer these questions, there are two main approaches that can be taken to coarse-graining; the bottom-up approach and the top-down approach. These will be discussed below.

2.4.2 Bottom-up approaches

A bottom-up approach to coarse-graining is used on the basis of a more detailed model, usually an all-atom classical model or one based on quantum mechanics.[34, 35, 36, 40]

These approaches are often valued because of their detail (i.e. at least the atomic level), though in order for this method to produce a reliable CG force field, the accuracy of the atomistic model is imperative.[34, 35, 36, 40] One of the most commonly used types of a bottom-up approach is the structure-based method.[35, 36]

Structure-based coarse-graining seeks to reproduce the pair-correlation functions or the bond, angle, and dihedral distributions of an AA model. These approaches obtain CG models by using the iterative Boltzmann inversion procedure or the inverse Monte Carlo procedure, based on the Henderson uniqueness theorem (i.e. that only one pair potential can exactly reproduce a given, radial distribution function, RDF).[35, 36] The most common is Boltzmann inversion, which starts with an initial guessed potential, which is then corrected using a proportional term from the difference between the RDF of the CG model and that of the AA model it is based on.[35, 36] This is shown in **Equation 2.23**:

$$\mathbf{U_{i+1}^{CG}(r) = U_i^{CG} + kT\ln\left(\frac{g_K^{CG}(r)}{g^{AA}(r)}\right)} \qquad \textbf{(2.23)}$$

where $\mathrm{U_i^{CG}}$ is the initial guessed potential, $\mathrm{U_{i+1}^{CG}(r)}$ is the potential in the iteration i+1, $\mathrm{g^{AA}(r)}$ is the RDF of the AA model, and $\mathrm{g_K^{CG}(r)}$ is the RDF of the CG model.[35, 36] The inverse Monte Carlo procedure uses the same types of interactions to match RDFs, but this procedure also applies the change in the potential function at certain distances away from the correction term.[35, 40] The inverse Monte Carlo is free from the limitations of solving Newton's equations of motions, which leads to faster sampling of equilibrium properties.[35, 40] This also means, however, that dynamical information cannot be gathered from this procedure.[35, 40]

Two other prominent bottom-up approaches of note are the relative entropy and force-matching methods. The relative entropy approach, proposed by Shell et al.[37, 38], is similar to structure-based coarse-graining, though here the relative entropy, instead of the general RDF, is found through minimising the proportional term between the probability distributions in the AA and CG models. In the force-matching approach, on the other hand, originally developed by Ercolessi et al.[30] and then furthered years later by Izvekov et al.[31], the goal is to match the average forces acting on the AA system to the forces acting on CG sites.[30, 31]

Bottom-up approaches allow for easy to create test conditions, allow for corrections if major flaws occur towards the bottom of the program as critical modules are generally built and tested first, and they allow for easier observation of test results.[34, 35, 36, 40] These approaches have their drawbacks however, as they are parametrised for a very specific system, limiting their transferability, and requiring new AA simulations to be run and matched to for any changes wanted in the CG model.[34, 35, 36, 40] Because of this, many researchers opt to use top-down approaches, described in the next section.

2.4.3 Top-down approaches

Unlike bottom-up approaches, top-down coarse-graining approaches derive their CG parameters from macroscopic experimental data.[34, 41, 42, 43, 44] Top-down approaches allow for early detection of design defects as they create an early working module, because of their incremental nature interface errors become easier to correct, and allow for corrections if major flaws occur towards the top of the program.[34, 41, 42, 43, 44] The parameterisation of the CG potentials in this approach is most commonly based on thermodynamic properties, such as the free energy of a particular portion of the system (e.g. free energy of solvation, free energy of vaporisation, etc).[34, 41, 42, 43, 44] These approaches do mean that observation of test output can be more difficult, however.[34, 41, 42, 43, 44]

One of the most widely used hybrid top-down approaches is the MARTINI force field, which is of particular interest to the work done in this thesis and is described in the next section below.

2.4.4 MARTINI force field

Developed by the groups of Tieleman and Marrink for use with

GROMACS simulation software, the MARTINI force field parameter are partly derived from classical atomistic models, especially in relation to bonded interactions, while charges and LJ parameters are empirically fixed.[27, 28, 29] This bond-matching to AA models makes MARTINI a hybrid top-down approach to coarse-graining.[27, 28, 29, 34] The existing MARTINI coarse-grained force field model is based on a four-to-one mapping, or representing an average of four heavy atoms in a system and any of their linked hydrogens as a single bead or interaction centre, with effective bead sizes of approximately 0.47 nm, for both chain molecules and solvents.[27, 28, 29] For ring-type beads a three-to-one mapping is used, with beads denoted by a prefix S- and an effective bead size of 0.43 nm, with scaled down ε values.[27, 28, 29]

In the MARTINI force field, there are four main types of bead based on the molecules the bead is mapping.[27, 28, 29] These types are: polar, P, nonpolar, N, apolar, C, and charged, Q (excluding the S- prefix for ring-type beads).[27, 28, 29] Within each of these bead types, there are then further subtypes denoting the bead's hydrogen-bonding capabilities, where donor is d, acceptor is a, both is da, and none is 0, or degree of polarity ranging from 1 to 5, where 1 indicates low polarity and 5 indicates high polarity.[27, 28, 29] This gives MARTINI eighteen potential bead types.[27, 28] The interactions between these can be classified as: supra attractive, O, attractive, I, almost attractive, II, semi attractive, III, intermediate, IV, almost intermediate, V, semi repulsive, VI, almost repulsive, VII, repulsive, VIII, and supra repulsive, XI.[27, 28] The interaction matrix showing all of the interaction potentials between bead types can be seen in **Tables 2.1** and **Table 2.2**.[27]

		Q				**P**					**N**				**C**				
	sub	da	d	a	0	5	4	3	2	1	da	d	a	0	5	4	3	2	1
Q	da	O	O	O	II	O	O	O	I	I	I	I	I	IV	V	VI	VII	IX	IX
	d	O	I	O	II	O	O	O	I	I	I	III	I	IV	V	VI	VII	IX	IX
	a	O	O	I	II	O	O	O	I	I	I	I	III	IV	V	VI	VII	IX	IX
	0	II	II	II	IV	I	O	I	II	III	III	III	III	IV	V	VI	VII	IX	IX
P	5	O	O	O	I	O	O	O	O	O	I	I	I	IV	V	VI	VI	VII	VIII
	4	O	O	O	O	O	I	I	II	II	III	III	III	IV	V	VI	VI	VII	VIII
	3	O	O	O	I	O	I	I	II	II	II	II	II	IV	IV	V	V	VI	VII
	2	I	I	I	II	O	II	II	II	II	II	II	II	III	IV	IV	V	VI	VII
	1	I	I	I	III	O	II	II	II	II	II	II	II	III	IV	IV	IV	V	VI
N	da	I	I	I	III	I	III	II	II	II	II	II	II	IV	IV	V	VI	VI	VI
	d	I	III	I	III	I	III	II	II	II	II	III	II	IV	IV	V	VI	VI	VI
	a	I	I	III	III	I	III	II	II	II	II	II	III	IV	IV	V	VI	VI	VI
	0	IV	IV	IV	IV	IV	IV	IV	III	III	IV	IV	IV	IV	IV	IV	IV	V	VI
C	5	V	V	V	V	V	V	IV	IV	IV	IV	IV	IV	IV	IV	IV	IV	V	V
	4	VI	VI	VI	VI	VI	VI	V	IV	IV	V	V	V	IV	IV	IV	IV	V	V
	3	VII	VII	VII	VII	VI	VI	V	V	IV	VI	VI	VI	IV	IV	IV	IV	IV	IV
	2	IX	IX	IX	IX	VII	VII	VI	VI	VI	V	VI	VI	V	V	V	IV	IV	IV
	1	IX	IX	IX	IX	VIII	VIII	VII	VII	VI	VI	VI	VI	VI	V	V	IV	IV	IV

Table 2.1: MARTINI bead interaction matrix.

Level	ε (kJ/mol)	σ (nm)
O – supra attractive	5.6	0.47
I – attractive	5.0	0.47
II – almost attractive	4.5	0.47
III – semi attractive	4.0	0.47
IV – intermediate	3.5	0.47
V – almost intermediate	3.1	0.47
VI – semi repulsive	2.7	0.47
VII – almost repulsive	2.3	0.47
VIII – repulsive	2.0	0.47
IX – supra repulsive	2.0	0.62

Table 2.2: LJ levels of MARTINI bead interactions.

The properties used in the parameterisation of this force field include the free energy of hydration, free energy of vaporisation, and partitioning free energies of transfer between water and organic phases of different polarities (e.g. octanol).[27, 28, 29] The hydration and vaporisation energies are reproduced only qualitatively in the MARTINI model, as they are largely overestimated.[27, 28, 29] The MARTINI force field does, however, accurately reproduce the partitioning free energy of transfer between its parameterised standard (i.e. non ring-like) CG beads in both organic oils and aqueous liquid phases, matched from equilibrium densities. This can be seen in **Equation 2.24**:

$$\boldsymbol{\Delta G_{oil/aq} = kT \ln\left(\frac{\rho_{oil}}{\rho_{aq}}\right)} \qquad \textbf{(2.24)}$$

where $\Delta G_{oil/aq}$ is the free energy of transfer between beads in oil and aqueous solutions, ρ_{oil} is the density of the CG bead in oil, and ρ_{aq} is the density of the CG bead in aqueous solutions.[27, 28, 29]

The bonded potential for standard beads in the MARTINI force field can be seen again in **Equations 2.5** and **2.6**. In the MARTINI force field however, the equilibrium bond length in **Equation 2.5**, r_0, is 0.47 nm, and the bond force constant in **Equation 2.5**, k_b, is 1250 kJ/mol*nm^2.[27, 28, 29] In **Equation 2.6**, the equilibrium bond angle, θ, is 180°, and the angle force constant, k_θ, is 25 kJ/mol.[27]

Non-bonded interactions in this force field are modeled through a standard Lennard-Jones potential, using the epsilon, ε, and sigma, σ, values in **Table 2.2** depending on the particular bead.[27, 28] This is shown again in **Equation 2.9**, where σ represents the closest distance between two beads, and ε represents the interaction strength between those beads.[27, 28]

The Coulomb potential is also used to calculate interactions between charge bonds, denoted with a Q- prefix, if present in the system.[27, 28]

2.4.5 Limitations of the MARTINI force field

While the MARTINI coarse-grained force field reduces the complexity of the system, enhancing the sampling of phase space and allowing for a relatively accurate depiction and feasible running time through computational simulation, this reduction has its disadvantages. Even with 8 interaction potential levels, it can be seen in the interaction matrix that multiple bead pairs can produce the same potentials.[27] This means finer details of a modeled system are lost with this force field, and so are the remaining descriptions from those details, meaning the system is not necessarily always realistic.[5, 4, 23, 24]

In the case of solvents, for example, MARTINI uses the same LJ parameters for single bead representations of both propane and butane, resulting in the same thermodynamic properties for both, including the same free energy of self-solvation (ΔG_{solv}).[27] This becomes a problem in accurately simulating bulk systems of a liquid, such as an alkane solvent, which are the most common solvents and used in numerous real chemical applications.[4, 5, 23, 24, 25 ,26]

Another important limitation lies in interpreting the time scale of MARTINI CG simulations compared to their atomistic MD counterparts. CG systems are significantly faster than classical atomic MD simulations, however estimating a factor for this increased speed that can be used to calculate the realistic time is extremely difficult and often dependent on the type of MARTINI beads used.[2, 27, 28, 29]

The MARTINI force field has been parameterised in this thesis to counteract its limitations for CG alkane solvents (Chapter 5) and for CG PEO, PPO, and Pluronic surfactants (Chapters 6 and 7).

2.5 References

. [1] E. Fermi, J. Pasta, S. Ulam, Los Alamos report LA-1940, 1955.

. [2] R. D. Levine. Molecular reaction dynamics. Cambridge University Press, 2005.

. [3] A. Leach *Molecular Modelling: Principles and Applications*. 2nd ed. Prentice Hall, 2001.

. [4] A. Leach. Molecular Modelling: Principles and Applications (2 ed.). Harlow: Prentice Hall, 2001.

. [5] J.W. Ponder and D.A. Case. Interatomic potentials and their relative parameters for protein simulations. Adv. Prot. Chem. 66 27-85, 2003.

. [6] J. P. Holman. *Heat Transfer*. McGraw-Hill, 372-375, 2002.

. [7] T. J. Vlugt, J. P. van der Eerden, M. Dijkstra, B. Smit, and D., Frenkel. *Introduction to Molecular Simulation and Statistical Thermodynamics*. Delft, 95-105, 2009.

. [8] D. Frenkel and B. Smit. *Understanding Molecular Simulation : from algorithms to applications*. 2nd. Vol. 1. Computational Science Series. San Diego: Academic Press, 600-602, 2001.

. [9] M. Meunier. Industrial applications of molecular simulations. CRC Press, 2012.

. [10] M. Lisal. Molecular dynamics simulations of fluorinated ethanes. Molecular Physics, 22(5):4357–4366, 1996.

. [11] D. van der Spoel, E. Lindahl, and B. Hess. *GROMACS User Manual version 4.6.3*. 2013. Available at: ftp.gromacs.org/ pub/manual/manual-4.6.3.pdf [Accessed 4 5 2017].

. [12] M. Di Pierro, R. Elber, B. Leimkuhler. A Stochastic Algorithm for the Isobaric-Isothermal Ensemble with Ewald Summations for all Long Range Forces. Journal of Chemical Theory and Computation, 2015.

. [13] C. K. Birdsall and A. B. Langdon, *Plasma Physics via Computer Simulations*, McGraw-Hill Book Company, 1985.

. [14] L. Verlet. "Computer "Experiments" on Classical Fluids. I. Thermodynamical Properties of Lennard−Jones Molecules". Physical Review. 159: 98–103, 1967.

. [15] W. H. Press, S. A. Teukolsky, W. T. Vetterling, and B. P. Flannery. "Section 17.4. Second-Order Conservative Equations". Numerical Recipes: The Art of Scientific Computing (3rd ed.). New York: Cambridge University Press, 2007.

. [16] H. J. C. Berendsen, J. P. M. Postma, W. F. van Gunsteren, and J. Hermans. Molecular dynamics with coupling to an external bath.J. Chem. Phys. 81, 3684, 1984.

. [17] M. Parrinello and A. Rahman. A. Polymorphic transitions in single crystals: A new molecular dynamics method. *J. Appl. Phys.* **52**:7182-7190, 1981.

. [18] G. Bussi, D. Donadio, and M. Parrinello. Canonical sampling through velocity rescaling. The Journal of Chemical Physics 126, 014101, 2007.

. [19] D. van der Spoel. Gromacs: the road ahead. Wiley Interdisciplinary Reviews: Computational Molecular Science, 1:710–5, 2011.

. [20] T. Schlick. *Molecular Modeling and Simulation: An Interdisciplinary Guide*. Vol. 21. Interdisciplinary Applied Mathematics. New York, NY: Springer New York, 2010.

. [21] B. J. Alder and T. E. Wainwright. Studies in Molecular Dynamics. I. General Method. *J. Chem. Phys*. 31 (2): 459, 1959.

. [22] V.S. Bystrov. Molecular modeling and molecular dynamics simulation of the polarization switching phenomena in the ferroelectric polymers pvdf at the nanoscale. Physics B: Condensed Matter, 432:21–25, 2014.

. [23] T. Aoyagi. Computer Simulation of Polymeric Materials. Springer Singapore, 139-141, 2016.

. [24] J. Barnound and L. Monticelli. Coarse-grained force fields for molecular simulations. Methods Mol Biol., (1215):125– 149, 2015.

. [25] M. van Gunsteren and M. van Gunsteren, C. van Gunsteren. Multigraining: an algorithm for simultaneous fine-grained and coarse-grained simulation of molecular systems. The Journal of chemical physics, 124(15), 2006.

. [26] K. Kremer, P. Kremer, and C. Kremer. Multiscale simulation of soft matter systems: from the atomistic to the coarse-grained level and back. Soft Matter, 124(15), 2009.

. [27] S. Marrink and P. Tieleman. Perspective on the MARTINI model. Chem. Soc. Rev., 42:6801–6822, 2013.

. [28] J. Klepeis, K. Lindor-Larsen, R.O. Dror, and D.E. Shaw. Long-timescale molecular dynamics simulations of protein structure and function. Current opinion in structural biology, 19:120–127, 2009.

. [29] K. Eom. Simulations in Nanobiotechnolgy. CRC Press, 3311-316, 2012.

. [30] F. Ercolessi & J. B. Adams. Interatomic Potentials from First-Principles Calculations: The Force-Matching Method. *EPL (Europhysics Letters)* 26(8), 583, 1994.

. [31] S. Izvekov & G. A. Voth. A multiscale coarse-graining method for bio- molecular systems. *The Journal of Physical Chemistry B* 109(7), 2469– 2473, 2005.

. [32] D. Reith, M. Pütz, & F. Müller-Plathe. Deriving effective mesoscale potentials from atomistic simulations. *Journal of computational chemistry*, *24*(13), 1624-1636, 2003.

. [33] V. Rühle, C. Junghans, A. Lukyanov, K. Kremer, & D. Andrienko. Versatile object-oriented toolkit for coarse-graining applications. *Journal of Chemical Theory and Computation*, *5*(12), 3211-3223, 2009.

. [34] S. O. Nielsen, C. F. Lopez, G. Srinivas, & M. L. Klein. Coarse grain models and the computer simulation of soft materials. *Journal of Physics: Condensed Matter*, *16*(15), R481, 2004.

. [35] R. L. Henderson. Uniqueness theorem for fluid pair correlation-functions. *Physics Letters A*, A 49(3):197–198, 1974.

. [36] F. Muller-Plathe. Coarse-graining in polymer simulation: From the atomistic to the mesoscopic scale and back. *Chemphyschem*, 3(9):754–769, 2002.

. [37] M. S. Shell. The relative entropy is fundamental to multiscale and inverse thermodynamic problems. *Journal of Chemical Physics*, 129(14), 2008.

. [38] A. Chaimovich & M. S. Shell. Coarse-graining errors and numerical optimization using a relative entropy framework. *Journal of Chemical Physics*, 134(9), 2011.

. [40] A. P. Lyubartsev & A. Laaksonen. Calculation of effective interaction potentials from radial-distribution functions - A reverse Monte-Carlo approach. *Physical Re- view E*, 52(4):3730–3737, 1995.

. [41] J. S. Rowlinson. Intermolecular potentials that are functions of thermodynamic variables. *Molecular Physics*, 52(3):567–572, 1984.

. [42] W. G. Noid. Perspective: Coarse-grained models for biomolecular systems. *J. Phys. Chem.*, 139:090901, 2013.

. [43] V. N. Maiorov & G. M. Crippen. Contact potential that recognizes the correct folding of globular proteins. *Journal of Molecular Biology*, 227(3):876–888, 1992.

. [44] B. Smit, K. Esselink, P. A. J. Hilbers, N. M. Vanos, L. A. M. Rupert, & I. Szleifer. Computer-simulations of surfactant self-assembly. *Langmuir*, 9(1):9–11, 1993.

. [45] X. Periole & S. J. Marrink. The Martini coarse-grained force field. *Methods in Molecular Biology*, 924, 2012.

SIMULATION METHODOLOGY 3

In this chapter, the specific simulation methodology and parameters are discussed, including the particular approaches used to construct and analyse the data in the subsequent chapters.

3.1 GROMACS simulation software

The simulations run in the studies in this thesis used GROningen MAchine for Chemical Simulations, GROMACS, software. GROMACS is a molecular dynamics software package originally designed by the Biophysical Chemistry department of University of Groningen for simulating biological systems, consisting of lipids, proteins, and nucleic acids, but is now widely distributed for free and able to process systems with inorganic compounds.[2]

GROMACS works by reading in either .gro files or .pdb files and converting them to .gro files for use.[1] Files with the gro file extension contain the structure of a molecule in Gromos87, a GROMACS force field format, while files with the .pdb extension are similar structure files found in the protein databank.[1, 2] Both of these files can contain the molecule/residue number, molecue/residue name, atom name, atom number, and position coordinates in nm, x y z.[1, 2] Files with .gro however, may also include velocity coordinates in nm/ps (or km/s), x y z. [1, 2] When these positions are known, GROMACS can read them and then apply the given parameters of the simulation.

Along with these files, GROMACS also needs .mdp and topology files to run a simulation.[1, 2] Files with the .mdp extension include pertinent information of the molecular dynamics parameters of the system given in the .gro file.[1, 2]. This includes preprocessing inclusions and definitions, run control, time steps of the simulation, energy minimisation before final runs, output control, searching for molecular neighbours, electrostatics for the molecules, temperature and pressure coupling of the atoms, velocity generation for initial velocity coordinates, bond constraints, and energy group exclusions.[1, 2] These variables could be altered by the user to fit to a variety of simulation conditions as needed. [1, 2] Topology files define the characteristics of the force field and the molecules of the system being simulated.[12, 48] They describe atom types, non-bonded molecular parameters, bonded molecular parameters, and the intermolecular pair interactions of those molecules.[12, 48] When these two files for a system are applied to a given .gro file, they will produce a new .gro file for the new coordinates of the system after the force field is applied, as well as a binary .tpr extension file which is converted from the input files via the GROMACS pre-processor GROMPP, which lists all of the combined systemic data for GROMACS to perform the MD run.[1, 2]

To run the complete simulation, GROMACS first runs an energy minimisation of the system and the resulting .gro file was run through the above steps again.[1, 2] GROMACS then reads the run input file it creates from this, and performs the MD calculations, outputting several files.[1, 2] These files include; a log file detailing the steps of the simulation, a trajectory file containing the coordinates and velocities, a structure file containing the coordinates and velocities of the last step of the simulation, and an energy file containing the energies, pressure, and temperature, and other energy-related parameters of the system.[1, 2] These files can then be analysed through GROMACS visualisation or using other formulas to analyse the simulation.[1]

3.2 All-atom coordinate generation

In order to utilise GROMACS to simulate a system with some degree of realism in this thesis, the atomistic coordinates of the molecules were required, in either a .pdb or .gro file. In order to have reasonably accurate coordinates to place in those files to parameterise them with a force field, this study converted SMILES files and graphical representations of the desired molecules into atomistic coordinates through an online generator created by the US National Institute of Cancer.[4]

SMILES files, or simplified molecular-input line-entry system files, are short ASCII strings representing the structure of chemical species.[3, 4] The atoms of a particular molecule's chemical structure are depicted using letters, such as C for Carbon, though hydrogen is implied by the bonds.[3, 4] Bonds between atoms in SMILES files are assumed to be single unless specified by the symbols '=' and '#', for double, and triple bonds, respectively.[3, 4] This format can be easily read into the aforementioned online simulator to generate .pdb files with atomistic coordinates which can then be used in GROMACS. Examples of this process can be seen in **Figure 3.1** and **Figure 3.2**.[4]

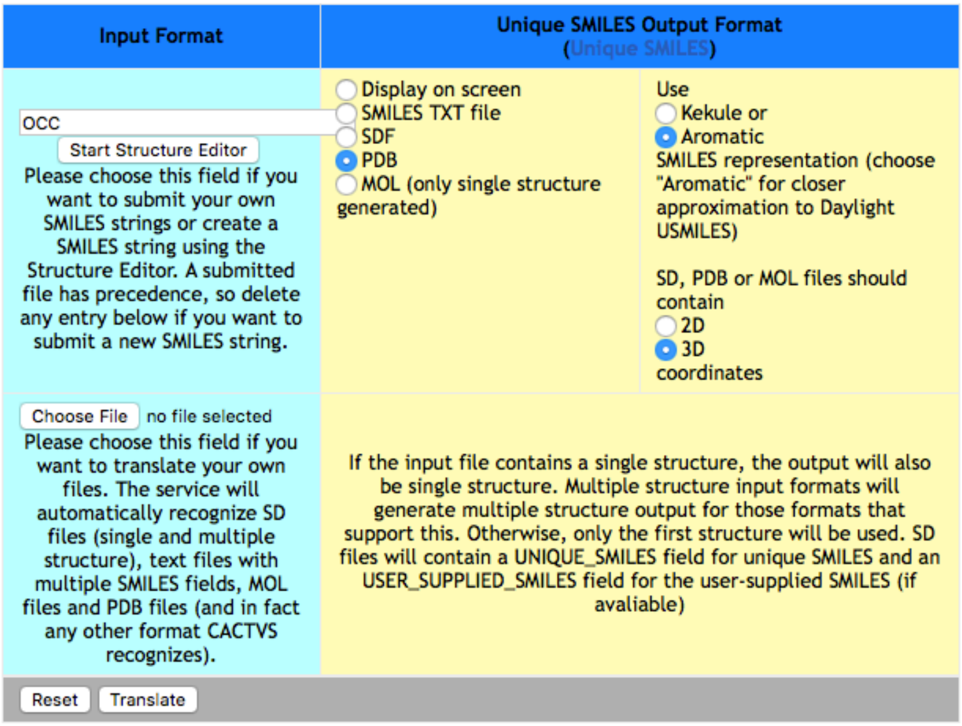

Input Format

Unique SMILES Output Format
(Unique SMILES)

OCC

Please choose this field if you want to submit your own SMILES strings or create a SMILES string using the Structure Editor. A submitted file has precedence, so delete any entry below if you want to submit a new SMILES string.

○ Display on screen
○ SMILES TXT file
○ SDF
● PDB
○ MOL (only single structure generated)

Use
○ Kekule or
● Aromatic
SMILES representation (choose "Aromatic" for closer approximation to Daylight USMILES)

SD, PDB or MOL files should contain
○ 2D
● 3D
coordinates

no file selected

Please choose this field if you want to translate your own files. The service will automatically recognize SD files (single and multiple structure), text files with multiple SMILES fields, MOL files and PDB files (and in fact any other format CACTVS recognizes).

If the input file contains a single structure, the output will also be single structure. Multiple structure input formats will generate multiple structure output for those formats that support this. Otherwise, only the first structure will be used. SD files will contain a UNIQUE_SMILES field for unique SMILES and an USER_SUPPLIED_SMILES field for the user-supplied SMILES (if avaliable)

Figure 3.1: Input of SMILES for ethanol into the online generator [4]

```
ATOM      1  O           0       1.130  -0.322  -0.000  0.00  0.00           O+0
ATOM      2  C           0       0.011   0.566  -0.000  0.00  0.00           C+0
ATOM      3  C           0      -1.285  -0.246   0.000  0.00  0.00           C+0
ATOM      4  H           0       1.925   0.229   0.000  0.00  0.00           H+0
ATOM      5  H           0       0.046   1.195   0.890  0.00  0.00           H+0
ATOM      6  H           0       0.046   1.195  -0.890  0.00  0.00           H+0
ATOM      7  H           0      -2.139   0.432  -0.000  0.00  0.00           H+0
ATOM      8  H           0      -1.320  -0.875  -0.890  0.00  0.00           H+0
ATOM      9  H           0      -1.320  -0.875   0.890  0.00  0.00           H+0
CONECT    1    2    4    0    0                                         NONE  14
CONECT    2    1    3    5    6                                         NONE  15
CONECT    3    2    7    8    9                                         NONE  16
END                                                                     NONE  17
```

Figure 3.2: The .pdb file of ethanol generated from the SMILES string inputted into the online generator

3.3 Mapping coarse-grained .gro files

After establishing the appropriate atomistic coordinate .gro files for the simulations in this thesis, coarse-grained versions were then required to advance. There were two methods and software used to achieve these files, though only the second was ultimately used for this study's simulations, with the first serving as a validation of the index file for beads used in the second method.

The first method used GROMACS to output centres of mass of arbitrary selections in trajectory format as a function of time.[2] This method required the creation of an index file containing one group of atoms per bead, with each group listing the atomistic types of the atoms contained in those beads, and the bonds between those beads.[2, 5] By inputting the number of groups or beads needed for the coarse-grained file and indicating that it should only take the last frame, GROMACS would then take an input of the all-atom trajectory and topology file to be coarse-grained, as well as the created index file of the beads, and output a coarse-grained .gro file.[2, 5] That resulting .gro file could then be visualised with this study's coarse-grained force-field for simulation purposes.[2, 5] Examples of how a polymer might be mapped using this method are shown in **Figure 3.3**.[6]

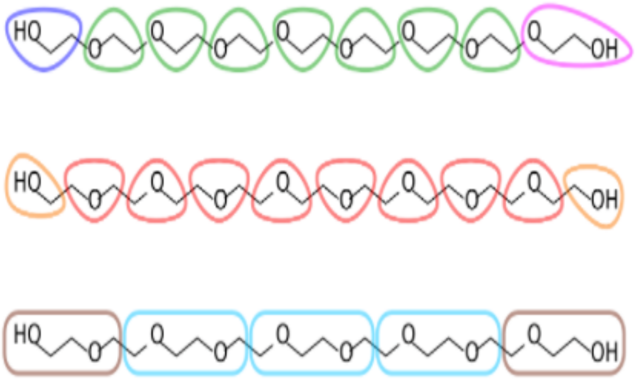

Figure 3.3: Different mapping strategies for PEG9 for use with GROMACS [6]

The second method of creating coarse-grained .gro files, and the one primarily used in this thesis, was achieved by using the Residue-Based Coarse Graining (RBCG) Builder in VMD.[5] VMD is a molecular visualisation program in which .pdb or .gro files of large molecular systems can be displayed and analysed.[5] An atomistic .pdb file needed to be uploaded into VMD, before selecting RBCG option from VMD's CG Builder.[5] This CG Builder is shown in **Figure 3.4**.[5]

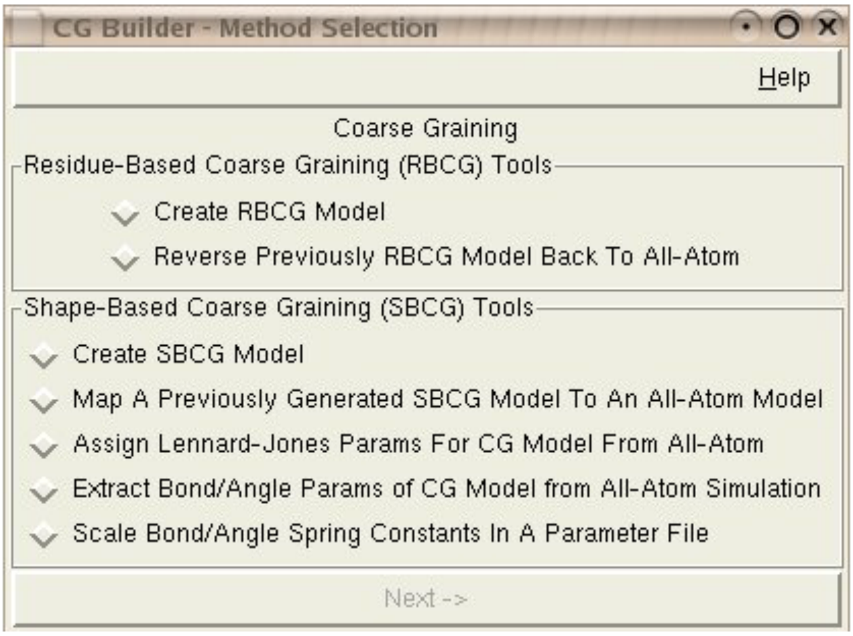

Figure 3.4: CG Builder in VMD [5]

This allowed for an index .cgc file, with the same information as the index file from the first GROMACS method, to be uploaded to define the relationship between the atoms in the all atom .pdb and the desired CG beads.[5] An example .cgc file can be seen in **Figure 3.5**.

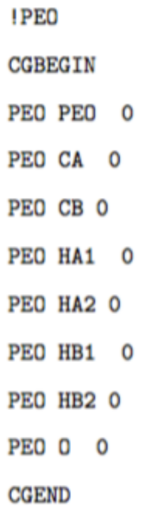

```
!PEO
CGBEGIN
PEO PEO  0
PEO CA  0
PEO CB 0
PEO HA1  0
PEO HA2 0
PEO HB1  0
PEO HB2 0
PEO O  0
CGEND
```

Figure 3.5: Example .cgc bead file for PEO for VMD CG Builder

VMD’s CG Builder then ran an algorithm to position the beads on the atomistic coordinates and connect them by bonds specified in the .cgc file.[5] The program then produced output .pdb files that can then be converted to .gro files using GROMACS.[2, 5] This method allowed for an instant visualisation of the coarse-grained beads over the original atoms within VMD, and provided a confirmation of the bead information used for the coarse-graining method in GROMACS.[5]

3.4 Simulation protocol

The following simulation parameters apply only to the original simulations created for this thesis; any chapters in which there is validation of previous studies or work will include the specific parameters for those simulations.

The individual CG simulations were performed using an isothermal-isobaric NPT ensemble.[8, 9, 11, 12, 15] To yield the most accurate thermodynamic results, a Parrinello-Rahman barostat and a v-rescale thermostat were used to maintain normal standard conditions of 298 K and 1 bar respectively.[2, 8-12, 15] Each simulation used a time-step of 20 fs, with a leap-frog stochastic dynamics integrator for the equations of motion.[1, 2, 9, 11, 12, 15] Long-range dispersion corrections were applied to energy and pressure of the system, with normal dispersion controlled by a switched group cutoff scheme with cutoff between 1.0 – 1.3 nm.[1, 2, 8, 9, 11, 12, 15] Cubic box lengths ranged from a minimum of 2.2 nm to as large as 50 nm, depending on the size of the beads and simulation, in order to account for finite-size effects.[7, 8, 9, 11, 12, 14, 15]

3.5 Analysis methods

There were many properties that were used to validate the simulations in this study that are discussed in further detail below.

3.5.1 Free energy of solvation

Gibbs solvation free energies, ΔG_{solv}, were calculated through thermodynamic integration using GROMACS.[13] Thermodynamic integration, TI, is a method of calculating a free energy difference which implements a coupling parameter, λ, applied to the Hamiltonian or potential of solute-solvent interactions, which is progressively increased from λ = 0 to λ=1 through a series of intermediate simulations of 0>λ>1.[17, 19] These intermediate simulations represent a gradual change from full interactions of the solute molecule with the system (λ = 0) to no interactions of the solute molecule with the system (λ = 1).[17, 18, 19] To then calculate the solvation free energy, the gradient of the resulting Hamiltonians of these simulations in the form of a dV/dl plot, is taken and integrated over λ using a python code, and then analysed.[17, 18, 19] This can be seen in **Equation 3.1**, where V represents the Hamiltonian potential.[17, 18, 19]

$$\boldsymbol{\Delta G_{\mathrm{solv}} = \int_0^1 \langle \frac{\partial V}{\partial \lambda} \rangle \, d\lambda} \qquad \textbf{(3.1)}$$

For insurance of accuracy, the CG simulations in this study used 15 λ points, integrating 51 separate simulations for each λ point. An example of a dV/dl curve can be seen in **Figure 3.6**.

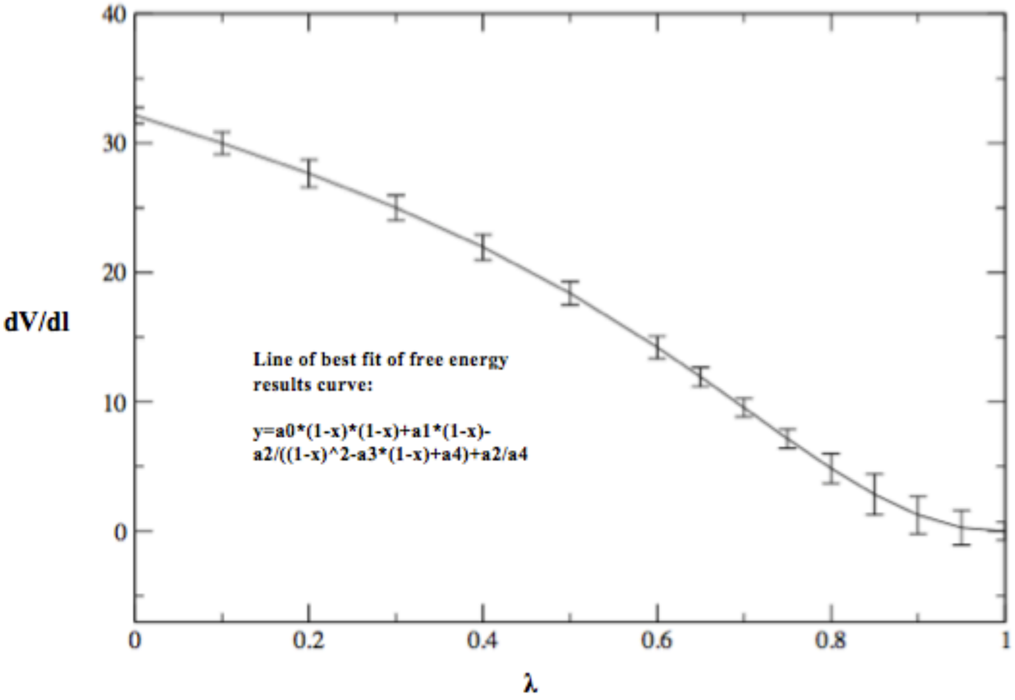

Figure 3.6: Example dV/dl vs λ plot for free energy calculations

3.5.2 Free energy of micellisation

Gibbs free energies of micellisation, ΔG_{mic}, or the free energy necessary to create a micelle, were calculated using the principles explained in Chapter 2.[14] This ΔG_{mic} can normally be calculated using **Equation 3.2**:

$$\Delta \mathbf{G}_{\mathbf{mic}} = \mathbf{RT}\,\mathbf{ln}(\mathbf{CMC}) \qquad \textbf{(3.2)}$$

where ΔG_{mic} is the Gibbs free energy of micellisation, R is the ideal gas constant, T is the absolute temperature of the system, and CMC is the critical micelle concentration.[14] As CMC is nearly incalculable in simulations, however, we used an alternative procedure. The difference between the free energy changes associated with converting a single surfactant in the aqueous solution and the free energy changes of a single surfactant within the micelle core is equal to the different in free energy associated with the micellisation of a single micelle.[18, 19] For simulations that produced micelles, all micelles were removed save one, the simulation of the selected single micelle was rerun, and the free energies of the surfactants comprising the micelle were calculated and combined using the same method detailed in the above section.[18, 42] The thermodynamics of this process can be seen in **Equation 3.3**:

$$\Delta \mathbf{G}_{\mathbf{mic}} = \Delta \mathbf{G}_{\mathbf{S-mic}} - \Delta \mathbf{G}_{\mathbf{S-sol}} \qquad \textbf{(3.3)}$$

where $\Delta G_{\mathrm{S-mic}}$ is the Gibbs free energy of a single surfactant within the micelle core, and $\Delta G_{\mathrm{S-sol}}$ is the Gibbs free energy of a single surfactant in the aqueous solution.[42]

3.5.3 Enthalpy of vaporisation

Enthalpies of vaporisation, ΔH_{vap}, were calculated using the molar potential energy of simulations of a molecule in a vacuum without any periodic boundary conditions, U_{gas}, the average molar potential energy of the liquid simulations, U_{liq}, the temperature of the simulations T, here 298.15K, and the ideal gas constant, R.[16, 17, 20] The enthalpy change was calculated from **Equation 3.4**.[17]

$$\mathbf{\Delta H_{vap} = U_{gas} - U_{liq} + RT} \tag{3.4}$$

3.5.4 Density

Bulk liquid densities, ρ, were calculated by first finding the GROMACS average simulation density output, calculated using **Equation 3.5**:

$$\boldsymbol{\rho}_{\mathbf{exp}} = \boldsymbol{\rho}_{\mathbf{MARTINI}} * \frac{\mathbf{M_{exp}}}{\mathbf{72 * N_{beads}}} \tag{3.5}$$

where ρ_{exp} is the experimental density, $\rho_{MARTINI}$ is the MARTINI density, $\mathrm{N_{beads}}$ is the total number of molecules or beads in a particular molecule, $\mathrm{M_{exp}}$ is the molecular mass of that molecule (i.e., 58.12g/mol for butane, 86.18g/mol for hexane, etc.), and 72 is the assigned molecular mass of a MARTINI bead (i.e. 72g/mol).[13, 14, 15, 26, 27]

3.5.5 Self-diffusion coefficient

Self-diffusion coefficients, D, for the pure liquid simulations were calculated using Einstein's mean square displacement (MSD) equation, through GROMACS.[20] MSD is proportional to the observation time in the limit that the observation time goes to infinity, and the proportionality constant that relates the MSD to the observation time is the self-diffusivity.[28, 30] This is shown in **Equation 3.6**, where the numerator is the MSD, d is the dimensionality of the system (3 for bulk liquids), and D is the self-diffusion coefficient.[28, 30]

$$\mathbf{D = \frac{1}{2d} lim_{t\to\infty} \frac{\langle [r(t_o+t)-r(t_0)]^2\rangle}{t}} \qquad \textbf{(3.6)}$$

3.5.6 Shear viscosity

The shear viscosities, η, of the fluid systems in this study were calculated using an integrated Green-Kubo equation through GROMACS, shown in **Equation 3.7**, where η is the shear viscosity of the fluid simulation, V is the volume of the system, k is the Boltzmann constant, and $\mathrm{P_{xz}}$ is the off-diagonal element of the stress tensor.[26, 33, 34, 41]

$$\boldsymbol{\eta = \frac{V}{kT}\int_0^\infty dt\{P_{xz}(0)P_{xz}(t)\}} \qquad \textbf{(3.7)}$$

3.5.7 End-to-end distance

The root-mean-square end-to-end distance, $\mathrm{R_d}$, of a molecule represents the average distance between the first and the last segment of the molecule, and ranges between a minimum value and a maximum value.[38] GROMACS calculates distances between pairs of positions as a function of time, and writes the end-to end distance as average distance over all segments of a chain structure.[2, 38] A simplified version of the ultimate method used can be seen in **Equation 3.8:**

$$\sqrt{\langle \mathbf{R_d}^2 \rangle} = \mathbf{Nl^2} \tag{3.8}$$

where R_d is the end-to-end distance, N is the number of segments in the overall chain, and l is the Kuhn length.[38, 39]

3.5.8 Persistence length

Persistence length, L, of a molecule or polymeric chain is a way of measuring the point at which a polymer ceases to be treated elastically and can be treated statically.[36, 37] It is defined as the minimum distance between two segments at which the correlations between them are negligible.[36, 37] It is incredibly difficult to determine persistence length experimentally, but theoretical models are generally accepted, as the persistence length is valuable in determining such terms as Gaussian radius of gyration.[37] The persistence length was calculated with GROMACS using **Equation 3.9**:

$$\mathbf{L} = \mathbf{n_p R_d} = \frac{\mathbf{R_d}}{\mathbf{ln\,cos\,\theta}} \tag{3.9}$$

where R_d is the end-to-end length of a segment, n_p is the decrease in the correlation between segments as they move farther apart in a chain, and cosθ is the angle between the two segments.[36, 37]

3.5.9 Relaxation times

Relaxation times are important timescales associated with the large scale motions of larger molecules, specifically the entirety of a polymer chain.[40] The relaxation times in this study were by using a time correlation function, as seen in **Equation 3.10**, where C^l is the time correlation function, P_l is a Legendre polynomial, l is the degree number, and u is a unit vector auto-correlation function.[40]

$$\mathbf{C^l = \langle P_l(u(t) \cdot u(0)) \rangle} \qquad \textbf{(3.10)}$$

In this study, we used created the unit vectors using the beginning and end coordinates of the polymer chains, to be used as auto-correlation functions, and a degree of 2 was chosen for convergence. The time correlation was then integrated to obtain the relaxation time of the polymers, as shown in **Equation 3.11**:

$$\boldsymbol{\tau} = \int_0^\infty \mathbf{C^1(t)dt} \qquad \textbf{(3.11)}$$

where τ is the relaxation time.[40]

3.5.10 Radius of gyration

The radius of gyration, R_g**,** are the average squared distance of any point in the simulated molecule from it's center of mass, giving a sense of size to the molecules in a solution.[32, 35, 37] GROMACS was used to calculate radii of gyration as the root mean square distance of the simulation beads about the x-, y- and z-axes of the cubic simulation box as a function of time.[32, 35] This is shown in **Equation 3.12**, where M is the total mass of the group of beads, $\mathbf{r_{cm}}$ is the position of the centre of mass of the group of beads, m_i is the mass of a bead, r_i is the position of a bead, and the sum is over all atoms in the group.[32, 35, 37]

$$\mathbf{R_g^2 = \frac{1}{M}\sum_i m_i\,(r_i - r_{cm})^2} \qquad \textbf{(3.12)}$$

3.5.11 Radial distribution functions

A radial distribution function, g_r or RDF, of a system describes how the atoms in a system are radially packed around each other.[8, 36] GROMACS can calculate how this density of a system varies as a function of distance from a selected reference particle.[1, 8, 13, 36] It is an effective way of describing the average structure of disordered molecular systems and is described by **Equation 3.13**:

$$\mathbf{g_r = \frac{N_r}{\rho 4\pi r^2 \Delta r}} \qquad \textbf{(3.13)}$$

where g_r is the radial distribution function, N_r is the mean number of atoms in a shell, ρ is the mean density of the atoms, and Δr is the width of the shell, r is the distance of the shell from the reference site.[1, 8, 13, 36]

3.5.12 Heat capacity

Heat capacity at constant pressure, C_P, of a system is the amount of heat required to change its temperature by one degree.[16, 41] Specifically, this refers to the change in the enthalpy of the system.[16, 41] GROMACS can calculate this using the enthalpy and temperature data of a bulk system, after a simulation md run, using the equation shown in **Equation 3.14**:

$$\mathbf{C_P} = \frac{\langle \mathbf{\delta H^2} \rangle}{\mathbf{kT^2}} \tag{3.14}$$

where C_P is the heat capacity at constant pressure, δH is the change in the enthalpy of the system, k is the Boltzmann constant, and T is the temperature of the system.[13, 16, 41]

3.5.13 Aggregation numbers

Aggregation numbers are the number of surfactants present in a micelle after the CMC has been reached, and can be used to evaluate the aggregation behaviour of self-assembling surfactants.[43, 44] For simulations in this study that produced micelles, aggregation numbers were calculated using the gmx clustsize command in GROMACS.[2, 13] Solvents were removed before using this command, as gmx clustsize computes the size distributions of molecular or atomic clusters in the gas phase.[2, 13]

3.6 References

. [1] S. Pronk, S. P, R. Schulz, P. Larsson, P. Bjelkmar, P. Apostolov, and M. Shirts. Gromacs 4.5: a high-throughput and highly parallel open source molecular simulation toolkit. Bioinformatics, 55, 2013.

. [2] D. van der Spoel. Gromacs: the road ahead. Wiley Interdisciplinary Reviews: Computational Molecular Science, 1:710–5, 2011.

. [3] J. Hur and J. Wild. Chemistry Central Journal, 1–7, 2008.

. [4] F. Oellien and M. C. Nicklaus. Online SMILES translator and structure file generator. 2004.

. [5] NIH Biomedical Research Center for Macromolecular Modeling and Bioinformatic. Vmd users manual version 1.9.2. 1.9.2, 2014.

. [6] S. Marrink and P. Tieleman. Coarse Grain Forcefield for Biomolecules. Available at: http://www.cgmartini.nl/index.php/tutorials-general-introduction/37-tutorial2, 2015, August 24. [Accessed 11 2 2017].

. [7] M. Henkel. Conformal invariance and critical phenomena. Springer Science & Business Media, 102-124, 2013.

. [8]] R. D. Levine. Molecular reaction dynamics. Cambridge University Press, 2005.

. [9] M. Meunier. Industrial applications of molecular simulations. CRC Press, 2012.

. [10] T. Doiron. "20 °C – A Short History of the Standard Reference Temperature for Industrial Dimensional Measurements" (PDF). *National Institute of Standards and Technology*. Journal of Research of the National Institute of Standards and Technology, 2007.

. [11] H. J. C. Berendsen, J. P. M. Postma, W. F. van Gunsteren, and J. Hermans. Molecular dynamics with coupling to an external bath.J. Chem. Phys. 81, 3684,

1984.

. [12] M. Parrinello and A. Rahman. A. Polymorphic transitions in single crystals: A new molecular dynamics method. *J. Appl. Phys*. 52:7182-7190, 1981.

. [13] D. van der Spoel, E. Lindahl, and B. Hess. *GROMACS User Manual version 4.6.3*. 2013. Available at: ftp.gromacs.org/ pub/manual/manual-4.6.3.pdf [Accessed 4 5 2017].

. [14] J. N. Israelachvili, D. J. Mitchell, & B. W. Ninham. 'Theory of self-assembly of hydrocarbon amphiphiles into micelles and bilayers'. *Journal of Chemical Socirty, Faraday Transaction 2 (*72),1525–1568, 1976.

. [15] J.W. Ponder and D.A. Case. Interatomic potentials and their relative parameters for protein simulations. Adv. Prot. Chem. 66: 27-85, 2003.

. [16] W. Greiner, L. Neise, and H. Stöcker. *Thermodynamics and statistical mechanics*. Springer-Verlag. 101, 1995.

. [17] I. Müller. *A History of Thermodynamics – the Doctrine of Energy and Entropy*. Springer. ISBN 978-3-540-46226-2, 2007.

. [18] M. Griebel, S. Knapek, and G. Zumbusch. *Numerical simulation in molecular dynamics*. Berlin: Springer. 193-197, 2007.

. [19] D. Oxtoby, H. Gills, and A. Campion. *Principles of modern chemistry* (7th ed.). Belmont, Calif.: Brooks/Cole Cengage Learning, 2012.

. [20] D. W. Ball, J. W. Hill, and R. J. Scott. *The Basics of General Organic and Biological Chemistry*, Flat World Education, 2011.

. [21] D. van Velzen, R. Cardozo, and H. Langenkamp. Enthalpy of Vaporization Measurements of Liquid Methane, Ethane, and Methane + Ethane by Differential Scanning Calorimetry at Low Temperatures and High Pressures. *J. Chem. Eng. Data*, *62* (8), 2253–2260, 2017.

. [22] J. Jovanovic and D. Grozdanic. Reliable prediction of heat of vaporization of n-alkanes at 298.15 K. J. Serb. Chem. Soc. 75 (7) 997–1003, 2010.

. [23] Engineering ToolBox,. *Hydrocarbons - physical data*. [online] Available at: https://www.engineeringtoolbox.com/hydrocarbon-boiling-melting-flash-autoignition-point-density-gravity-molweight-d_1966.html, 2017 [Accessed 12 2 2018].

. [24] C. Viton, M. Chavret, and J. Jose. Enthalpy of Vaporization of N-Alkanes (from Nonane to Pentadecane). Experimental Results - Correlation. In: Caliste JP., Truyol A., Westbrook J.H. (eds) Thermodynamic Modeling and Materials Data Engineering. Data and Knowledge in a Changing World. Springer, Berlin, Heidelberg, 1998.

. [25] I. A. Hossenlopp and D. W. Scott. Vapor heat capacities and enthalpies of vaporization of five alkane hydrocarbons. *The Journal of Chemical Thermodynamics.* 13(5) 415-421, 1981.

. [26] S. Marrink and P. Tieleman. Perspective on the MARTINI model. Chem. Soc. Rev., 42:6801–6822, 2013.

. [27] J. G. Kirkwood. Statistical mechanics of fluid mixtures, J. Chem. Phys., 3:300-313,1935.

. [28] S.R. De Groot and P. Mazur. *Non-equilibrium Thermodynamics*. North-Holland, Amsterdam, 1962.

. [29] M. S. Green, Markoff Random Processes and the Statistical Mechanics of Time-Dependent Phenomena. II. Irreversible Processes in Fluids, J. Chem. Phys. 22, 398–413, 1954.

. [30] F. Bachl and H.-D. Liidemann. Pressure and Temperature Dependence of Self-Diffusion in Liquid Linear Hydrocarbons. Z. Naturforsch. 41 a, 963-970, 1986.

. [31] P. Padilla and S. Toxvaerd. Self-diffusion in n-alkane fluid models Scilight relation icon.The Journal of Chemical Physics 94, 5650, 1991.

. [32] S. O. Nielsen, C. Lopez, G. Srinivas, and M. Klein. “A coarse grain model for n-alkanes parameterized from surface tension data”. J. Chem. Phys., 114 (14), 2003.

. [33] J. P. Holman. *Heat Transfer*. McGraw-Hill, 372-375, 2002.

. [34] F. Incropera and D. P. DeWitt. *Fundamentals of Heat and Mass Transfer*. Wiley,

2007.

. [35] G. Toth and A. Baranyai. Molecular dynamics analog of the reverse Monte Carlo method. J. Chem. Phys. 114, 2027, 2001.

. [36] H. Su, A. Strachan, and W.A. Goddard. Density functional theory and molecular dynamics studies of the energetics and kinetics of electroactive polymers: Pvdf and p(vdf-trfe). Phys. Rev. B, 70(6), 2004.

. [37] L. Girifalco. Statistical Mechanics of Solids. Oxford University Press, 2000.

. [38] P. J. Flory. *Statistical Mechanics of Chain Molecules*. JohnWiley&Sons, Inc. 1969.

. [39] M. Doi, & S. f. Edwards. *The Theory of Polymer Dynamics*. International series of momographs on physics, Oxford University Press., 1986.

. [40] J. P. Hansen, & I. R. McDonald, *Theory of Simple Liquids* Academic, 10-45, 1986 .

. [41] D. Halliday, & R. Resnick. *Fundamentals of Physics*. Wiley, 524-525, 2013.

. [42] B. C. Stephenson, K. A. Stafford, K. J. Beers, & D. Blankschtein. Application of computer simulation free-energy methods to compute the free energy of micellization as a function of micelle composition. 2. implementation. *The Journal of Physical Chemistry B*, *112*(6), 1641-1656, 2008.

. [43] Y. Moroi. Micelles: theoretical and applied aspects. Springer Science & Business Media, 1992.

. [44] N.E. Olesen. Journal of Colloid and Interface Science. 453, 79-89, 2015.

COARSE-GRAINED MODEL FOR ALKANES AND POLYETHYLENE

4

As mentioned in Chapter 2, there are currently a number of limitations to atomistic MD models, and restrictions to CG models of Pluronics simulations.[1-8] Previous principal CG studies mentioned in Chapter 1 were not complete, some missing thermodynamics parameterisation, some an unproven transferability of models.[9-22] Most, however, utilized some version of the MARTINI force field.[9-22]

Our work with alkanes in this chapter was done for a few reasons; alkanes are a common co-solvent for Pluronic self-assembly in the synthesis of SBA-15[23, 24, 25], work in coarse-graining alkanes has been performed but either not for shorter common alkanes (i.e. hexane, octane, etc.) or not for a number of properties[26-31], and also because parameterising CG alkanes allowed for a basis for coarse-graining polymers such as polyethylene, as polyethylene can be considered an alkane chain in terms of composition.[33, 34, 35]

Previous CG parameterisation studies explicitly for alkanes have had some varied success, but have had assorted shortcomings.[26-31] A brief overview of some prominent studies and their parameterisation methods, and their limitations, is provided below.

A coarse-grained model for alkanes that used the Morse potential for parameterisation, as opposed to Lennard-Jones, was produced by Chiu et al. in 2010.[26] The researchers described both a MARTINI based force field for alkanes adapted for use with the Morse potential (instead of LJ potentials), as well as a simulation method with variously sized beads, both 3 to 1 and 4 to 1 mapped, designed to provide flexibility in modelling longer alkane chains. The alkane models were parameterised using three adjustable parameters in the Morse form for enthalpies of vaporisation, bulk densities, and surface tensions. This method did lead to good agreement between experimental data and free energies of self-solvation and compressibilities, good agreement in trend with experimental values of self-diffusion coefficients, as well as excellent agreement with AA models in terms of radial distribution functions, RDFs, and end-to-end distances. While these were promising results, the use of Morse potentials over Lennard-Jones has some inherent disadvantages; Morse potential allows a bond to stretch to an unrealistic length, and structures with long bonds based on Morse potentials may have convergence problems or provide nonphysical results due to a lack of force-pulling.[32] In regards to this study, not enough testing has been done to determine if these disadvantages will affect large systems, though the researchers did encounter a major drawback in the form of greater time-consumption per time step. This means that this alkane model may be prohibitive for use in regards to coarse-graining the intrinsically more time-consuming self-assembly simulations.

Dallavalle et al. undertook an evaluation of conditional reversible work, CRW, mapping schemes using for coarse-grained alkanes of longer chain lengths in 2017.[27] The researchers introduced a model to examine the influence of different CG resolutions on the thermodynamic and structural properties such as densities, compressibilities, thermal expansion coefficients, surface tensions, RDFs, and enthalpies of vaporisation of higher alkanes (i.e. having nine or more carbon atoms) in a liquid state. These higher alkanes were considered as adequate test-systems for chains of polyethylene. In total, the study considered four different mapping schemes of differing CG resolutions, created using a CRW bottom-up coarse-graining method, which derived non-bonded pair potentials from the underlying molecular interactions that theoretically should provide thermodynamic transferability. The thermodynamic and structural properties of dodecane and tetracosane in the liquid state were both specifically tested with all four CG models and had a high degree of comparison to known data, though as the size of the mapping increased, the ability of the CG models to accurately describe the system greatly deteriorated. To help correct CG models with lower resolution, the researchers posited that correcting the sampling of the system would improve the models behaviour. The CRW based models in this study did include good agreement for structural and limited thermodynamic properties and known experimental and AA data. However, these models were not validated for free energies, and more testing is needed to know whether the alkane models would behave as expected when combined with other molecular model types. Their sole focus on longer chains, without testing short chains, also potentially limits the models' ability to correctly model important alkanes such as hexane, heptane, or octane.

For the purposes of our work, due to its popularity in self-assembly simulations[28], the MARTINI force field was of particular interest. Marrink et al. produced one of the earliest attempts at coarse-graining alkanes in an early version of their MARTINI force field, as of then yet to be named.[29] Accurate reproduction of structural details was not a focus for the researchers, as their approach aimed for a broader range of applications without the need to reparametrise the model each time by calibrating their models against oil/water partitioning coefficient thermodynamic data. They created a CG model for alkanes with 3 to 1 and 4 to 1 bead mapping, and performed simulations of bulk alkanes with 1-5 beads (i.e. butane, octane, dodecane, hexadecane, and eicosane) and obtained comparable densities, compressibilities, and self-diffusion coefficients to experimental values. This was due to the researchers assigning different masses to each CG bead, resulting in different effective densities and diffusion rates. The chain stiffness of the alkane models was also comparable to those of AA models. Their CG model also reproduced the correct trend for free energies of hydration and vaporisation, though due to the energy interactions between the alkane beads, the actual values are systematically too high and there was an over estimation between CG alkane and water models. When updating and formally naming the MARTINI force field in 2007[30], Marrink et al. slightly changed the Lennard-Jones interaction level of ε between the alkane beads from their original model from 3.4 to 3.5 kJ mol^{-1}, and increased ε between the alkane and water models from 1.8 to 2.0 kJ mol^{-1}. This was done in an attempt to correct their earlier values, but it was noted by the researchers that to produce more accurate models and improve the relative stability of the fluid phase of their alkane models, a complete reparameterisation would be needed. In a 2013 perspective on the MARTINI model[28], Marrink et al. admitted that their particular approach of using the Lennard-Jones potentials for their alkane models to describe their non-bonded interactions leads to over-structuring of the simple alkane fluids compared to AA models (e.g. in the RDFs). They also found that while they had tested a broader range of thermodynamic properties in liquid alkanes by comparing to AA models, the temperature dependence of their alkane models was markedly weaker than in AA models or experimental data. Overall the MARTINI model provides some good comparative values with structural and thermodynamic properties, but they themselves even admit that their models produce over-structuring of alkane fluids, poor temperature dependence, and a complete reparameterisation would be needed to improve the stability of the fluid phases of their alkane models.

An early study of 3 to 1 mapped coarse-grained, smaller-chained alkanes was performed by Nielsen et al. in 2003.[31] The researchers parameterised beads representing 3 carbon atoms by optimising Lennard-Jones non-bonded and harmonic bond and angle parameters, matching them to CHARMM AA simulation and experimental data for alkanes. To cover the remaining alkanes not produced from multiples of 3 carbon atoms, the researchers proposed a scaling procedure to produce beads that mimicked 2 carbons by scaling the mass, bond length, bond force constant, and the two Lennard-Jones parameters of the 3 carbon bead models. This CG model accurately reproduced experimental surface tension and bulk density data for their linear alkanes, while radii of gyration, end-to-end distances, and radial distribution functions, were in good agreement with AA models. While this parameterisation did lead to an alkane model with good agreement with experimental density and surface tension data, this study failed to test other thermodynamic properties such as free energies and enthalpies of vaporisation, which indicates a need for further testing for transferability. It is of note, however, that this particular model used polyethylene experimental data in lieu of longer alkane chains; a process further discussed below.

Polyethylene, PE, is a polymer built as a chain of ethylene monomers, with chemical formula of (C2H4)n.[33] Due to its similarity to linear alkanes (which are essentially carbon chains fully saturated with hydrogens), research has been done into estimating their properties through those of linear alkanes.[34, 35] Two prominent books by Van

Krevelen[34] and Bicerano[35] outline a suggested method to use n-alkanes as polyethylene oligomers to estimate their properties, as unlike polyethylene, n-alkanes can be prepared so that accurate properties can be determined. While using n-alkanes however, some properties (e.g. boiling points and tensile strength) are either irrelevant or lacking for PE.

This method has been utilised in simulation work, however, with some success over the years since its conception.[31, 36, 37, 38] These successful simulations include an AA model simulation analysing polyethylene crystallisation with n-alkanes in 1993 by Kavassalis et al.[36], an AA model simulation from the same year that focused on the enthalpy of vaporisation, density, and packing of polyethylene melts by Pant et al.[37], an AA model simulation centered around the clustering of water in polyethylene by Fukuda[38] in 1998, and the previously mentioned CG work done by Nielsen et al.[31] in 2003.

As our alkane models are coarse-grained (i.e. the heavy atoms, here the carbons, are the most important elements to map), and polyethylene is essentially a long alkane chain, longer chains of our models should theoretically also provide experimental properties for polyethylene, and an added layer of validation.[1, 34, 35]

In this chapter we choose to adopt the MARTINI approach for simplicity and added transferability, as well as consistently with our group's previous work on modeling mesoporous silica.[85, 86] However the MARTINI model for alkanes needs to be reparameterised to produce more realistic alkane properties.[28, 29, 30] The previously discussed self-assembly simulations did not explicitly parameterise their CG alkane solvents for structural and thermodynamic properties[9-22], and parameterising MARTINI alkane solvents to match experimental values, and then testing this parameterisation through a polyethylene model, will lead to better PEO, PPO, and Pluronic behaviour.

4.1 Methodology

4.1.1 Current MARTINI force field

As previously explained in Chapter 2, the existing MARTINI coarse-grained force field model is based on a four-to-one mapping, or representing an average of four heavy atoms in a system and any of their linked hydrogens as a single bead or interaction centre, with effective standard (i.e. non ring-like) bead sizes of 0.47 nm.[28, 29] The interaction potentials between these beads are categorized as: supra attractive, O, attractive, I, almost attractive, II, semi attractive, III, intermediate, IV, almost intermediate, V, semi repulsive, VI, almost repulsive, VII, repulsive, VIII, and supra repulsive, XI.[28] A refresher of the full MARTINI interaction matrix and of the Lennard-Jones interaction levels of this force field, originally shown in Chapter 2, can be seen in **Figures 4.1a-b**.[28]

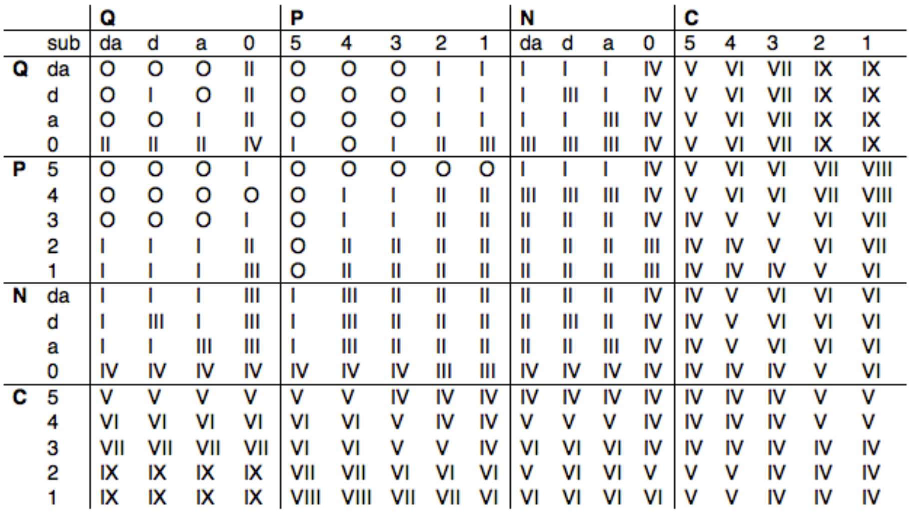

		Q				**P**					**N**				**C**				
	sub	da	d	a	0	5	4	3	2	1	da	d	a	0	5	4	3	2	1
Q	da	O	O	O	II	O	O	O	I	I	I	I	I	IV	V	VI	VII	IX	IX
	d	O	I	O	II	O	O	O	I	I	I	III	I	IV	V	VI	VII	IX	IX
	a	O	O	I	II	O	O	O	I	I	I	I	III	IV	V	VI	VII	IX	IX
	0	II	II	II	IV	I	O	I	II	III	III	III	III	IV	V	VI	VII	IX	IX
P	5	O	O	O	I	O	O	O	O	O	I	I	I	IV	V	VI	VI	VII	VIII
	4	O	O	O	O	O	I	I	II	II	III	III	III	IV	V	VI	VI	VII	VIII
	3	O	O	O	I	O	I	I	II	II	II	II	II	IV	IV	V	V	VI	VII
	2	I	I	I	II	O	II	II	II	II	II	II	II	III	IV	IV	V	VI	VII
	1	I	I	I	III	O	II	II	II	II	II	II	II	III	IV	IV	IV	V	VI
N	da	I	I	I	III	I	III	II	II	II	II	II	II	IV	IV	V	VI	VI	VI
	d	I	III	I	III	I	III	II	II	II	II	III	II	IV	IV	V	VI	VI	VI
	a	I	I	III	III	I	III	II	II	II	II	II	III	IV	IV	V	VI	VI	VI
	0	IV	IV	IV	IV	IV	IV	IV	III	III	IV	IV	IV	IV	IV	IV	IV	V	VI
C	5	V	V	V	V	V	V	IV	IV	IV	IV	IV	IV	IV	IV	IV	IV	V	V
	4	VI	VI	VI	VI	VI	VI	V	IV	IV	V	V	V	IV	IV	IV	IV	V	V
	3	VII	VII	VII	VII	VI	VI	V	V	IV	VI	VI	VI	IV	IV	IV	IV	IV	IV
	2	IX	IX	IX	IX	VII	VII	VI	VI	VI	V	VI	VI	V	V	V	IV	IV	IV
	1	IX	IX	IX	IX	VIII	VIII	VII	VII	VI	VI	VI	VI	VI	V	V	IV	IV	IV

a)

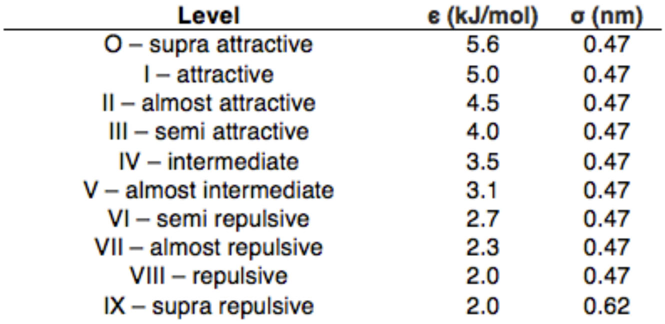

Level	**ε (kJ/mol)**	**σ (nm)**
O – supra attractive	5.6	0.47
I – attractive	5.0	0.47
II – almost attractive	4.5	0.47
III – semi attractive	4.0	0.47
IV – intermediate	3.5	0.47
V – almost intermediate	3.1	0.47
VI – semi repulsive	2.7	0.47
VII – almost repulsive	2.3	0.47
VIII – repulsive	2.0	0.47
IX – supra repulsive	2.0	0.62

b)

Figures 4.1a-b: **a)** MARTINI bead interaction matrix, **b)** MARTINI interaction levels and LJ parameters [28]

The beads used in this study are the larger standard MARTINI beads, as opposed to the smaller ring-like types, to most accurately represent the linear alkanes.[28]

4.1.2 Simulation protocol

The individual CG simulations run in this study used GROningen MAchine for Chemical Simulations, or GROMACS, software.[39] The original AA models used as a basis for our coarse-graining were converted from their chemical structures using the online SMILES generator, and then mapped to the CG models using Residue-Based Coarse Graining (RBCG) Builder in VMD.[41, 42] The simulations were performed using an isothermal-isobaric NPT ensemble[43], and to yield the most accurate thermodynamic results, a V-rescale thermostat and a Parrinello-Rahman barostat to maintain normal standard conditions of 298 K and 1 bar respectively, save for the polyethylene melt simulations that were run at 723.15K and 773.15K.[39, 44, 69, 70] Each simulation used a time-step of 20 fs, with a leap-frog stochastic dynamics integrator for the equations of motion.[45] Long-range dispersion corrections were applied to energy and pressure of the system, with normal dispersion controlled by a switched group cutoff scheme with cutoff between 1.0 - 1.3 nm.[39, 45] Cubic box lengths ranged from a minimum of 3.2 nm to as large as 4.8 nm, depending on the size of the beads, in order to account for finite-size effects.[40]

4.1.3 Current MARTINI bead simulations and models

Our work with the current MARTINI model was done in 2 stages; running self-solvation (i.e. the same solute and solvent) simulations of single bead systems at different interaction levels to gain a better understanding of the original model, and then simulating MARTINI alkane models in themselves and in the MARTINI hexadecane model and calculating their thermodynamic and physical properties (i.e. self-solvation free energy, enthalpy of vaporisation, density, and self-diffusion coefficients) for comparison with experimental values. All of the properties were calculated using the equations previously discussed in Chapter 4.

In order to understand the full range of MARTINI interactions for non-charged beads, 74 simulations were run for single P0 to P5, N0 to Nda, and C1 to C5 bead solvation in single P0 to P5, N0 to Nda, C1 to C5, MARTINI beads.[28] This covered all possible combinations of interactions in the MARTINI matrix. The solvation free energies, $\Delta\mathrm{G}_{\mathrm{solv}}$, were then taken and evaluated for trend with the various interaction levels' epsilons, ε. A complete overview of these simulated systems can be seen in **Table 4.1.**

MARTINI Solvents-Solvents Interaction Levels	**MARTINI Solutes-Solvents Interaction Levels**								
	0	I	II	III	IV	V	VI	VII	VIII
0	✓	✓			✓	✓	✓	✓	✓
I	✓	✓	✓	✓	✓	✓	✓	✓	✓
II	✓		✓	✓	✓	✓	✓	✓	
III		✓	✓	✓	✓	✓	✓	✓	✓
IV				✓	✓	✓	✓	✓	

Table 4.1: Simulation details for standard, non-charged MARTINI single-bead solvation at various interaction levels.

After observing the nature of standard, non-charged MARTINI bead interaction levels, we tested MARTINI alkane models directly. Solvation simulations of the five models for MARTINI alkanes were then run in themselves and MARTINI hexadecane.[28] To better understand how MARTINI alkanes fit with experimental data, self-solvation free energies, $\Delta\mathrm{G}_{\mathrm{solv}}$, and subsequently the enthalpies of vaporization, $\Delta\mathrm{H}_{\mathrm{vap}}$, of these simulations were then calculated through thermodynamic integration, and matched to experimental and interpolated data for linear alkanes at room temperature.[46-51] The self-solvation simulations were then further compared against available experimental physical properties, specifically density, ρ[52, 53], and self-diffusion coefficients, D.[54] The parameter data for all of the MARTINI alkane models, along with their MARTINI mapping schemes, can be seen in **Table 4.2**.[28]

Mapping Scheme	**MARTINI CG Alkane Models**	**Bead types**	**Number of beads**	**Non-bonded Interactions**		**Bonded Interactions**			
				σ (nm)	**ε (kJ/mol)**	**r_0 (nm)**	**k_b (kJ/mol*nm^2)**	**θ (deg.)**	**k_θ (kJ/mol)**
3:1	**Propane (C3H8)**	**C2**	**1**	0.47	3.5	n/a	n/a	n/a	n/a
4:1	**Butane (C4H10)**	**C1**	**1**	0.47	3.5	n/a	n/a	n/a	n/a
4:1	**Octane (C8H18)**	**C1**	**2**	0.47	3.5	0.47	1250	n/a	n/a
4:1	**Dodecane (C12H26)**	**C1**	**3**	0.47	3.5	0.47	1250	180	25
4:1	**Hexadecane (C16H34)**	**C1**	**4**	0.47	3.5	0.47	1250	180	25

Table 4.2: MARTINI alkane model parameters for several alkanes studied here.[28]

4.1.4 Alkane and polyethylene parameterisation simulations and models

Our alkane parameterisation work was done in 4 phases; 1-bead model simulations with varying Lennard-Jones parameters, 2-bead model simulations with varying bond length and bond force constant parameters, 3-bead model simulations with varying bond angle and bond angle force constant parameters, and 4-bead model simulations varying dihedral and dihedral force constant parameters. Every subsequent set of data utilised the parameters of the systems that were optimised before it, (i.e. the Lennard-Jones parameters that were parameterised for 1-bead models were used in the 2-bead models, and those Lennard-Jones parameters and the bond length and bond force constant parameters optimised in the 2-bead models were used in the 3-bead solvent system, etc.) and all properties were calculated using the equations in Chapter 4. As we were optimising the MARTINI force field, it was the base structure for all of this study's simulations, with parameters being adjusted systematically for agreement to experimental data.

A graphical representation of the overall parameterisation process described above is seen in **Figure 4.2**.

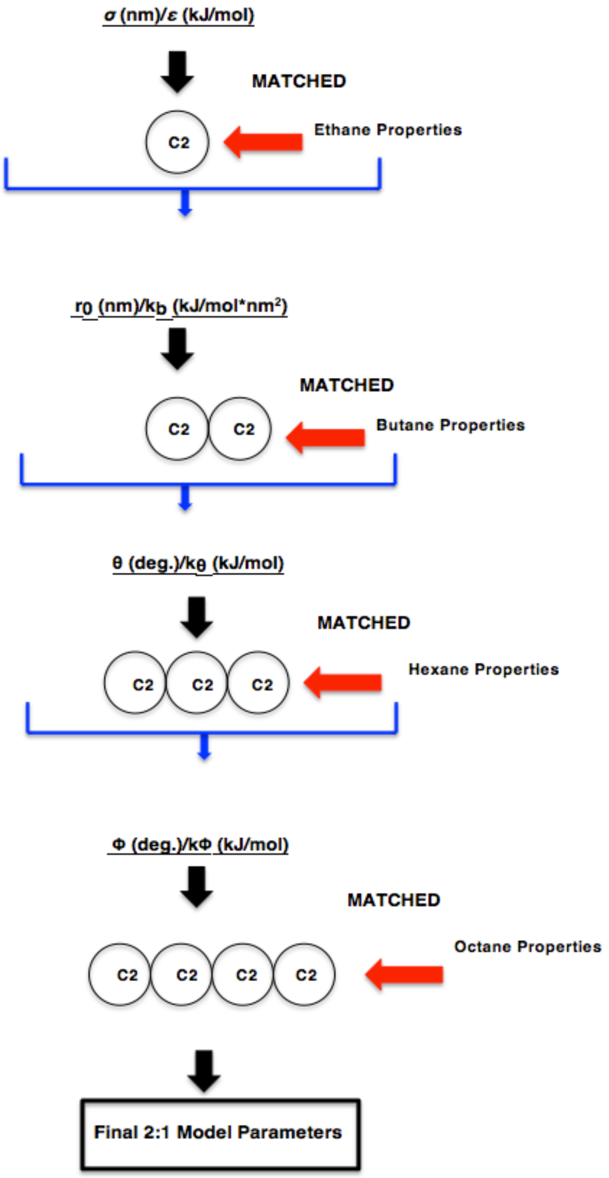

Figure 4.2: Example graphical representation of alkane this parameterisation protocol for beads representing 2 carbon atoms, simulating the desired parameter pairs (i.e. σ/ε, r_0/k_b , θ/k_θ, and Φ/k_Φ) and matching each n-bead simulation results to those of the desired alkane for the bead model, before taking the matched parameter pairs and using them in the subsequent simulations (i.e. the matched σ/ε pair for the 1-bead, 2 carbon ethane model is then used in the 2-bead r_0/k_b simulations, and so on for the 3-bead and 4-bead parameterisations). The same strategy was repeated for the 3:1, 4:1, and 5:1 mapped models.

In order to cover a large range of potential Lennard-Jones parameters, 1-bead model self-solvation simulations (i.e. the same solute and solvent, as shown in the first part of **Figure 4.2**), were run for twenty-one sigmas, *σ,* ranging between 0.37nm - 0.47nm at six different epsilons, *ε*, from 1kJ/mol - 6kJ/mol.[28, 56, 57] The well established OPLS-AA force field model's Lennard-Jones variables for methane were a *σ* of approximately 0.371 nm and an *ε* of approximately 1.2 kJ/mol[57], while MARTINI uses a constant *σ* of 0.47 nm and a constant *ε* of 3.5 kJ/mol for most all of its alkane representations.[28] These *σ/ε* ranges were chosen to cover both previous successful MD model data for the smallest linear alkane potentially possible with MARTINI, methane, and the existing MARTINI bead parameters, and were thus a good starting range for trying to find 1:1, 2:1, 3:1, 4:1, and 5:1 mapped equivalent linear alkanes for 1-bead simulations. These parameters can be seen in **Table 4.3.**[28, 56, 57]

1-Bead Simulation Parameters											
***σ* (nm)**	0.37	0.38	0.39	0.4	0.41	0.42	0.43	0.44	0.45	0.46	0.47
	0.375	0.385	0.395	0.405	0.415	0.425	0.435	0.445	0.455	0.465	
***ε* (kJ/mol)**	1		2		3		4		5		6

Table 4.3: Simulation parameters for our 1-bead alkane parameterisation work.[28, 57]

The self-solvation free energies, ΔG_{solv}, of the 1-bead model simulations were calculated through thermodynamic integration, and then subsequently from them the enthalpies of vaporization, ΔH_{vap}, were also found, and both were matched to experimental and interpolated data for linear alkanes at room temperature, which are discussed in a following section.[46-51] The pairings that most closely matched to alkane self-solvation free energy and enthalpy of vaporisation data were then further matched to available experimental density, ρ[52, 53], narrowing down the beads to four σ/ε pairings for single beads, representing 2:1, 3:1, 4:1, and 5:1 mapped models respectively. After determining these models, they were further validated against experimental self-diffusion coefficients, D[29], shear viscosity, η[58, 59], and AA simulation results for radii of gyration, R_g[31, 60].

The Lennard-Jones parameters, σ/ε, for the 1-bead models were then used in 2-bead model self-solvation simulations (as shown in the second portion of **Figure 4.2**), which were focused on optimising the bond lengths, r_0, and bond force constants, k_b, of the models. They covered eight equilibrium bond lengths, r0, between 0.21nm - 0.54nm and eight bond force constants, k_b, from 1250 kJ/mol*nm^2 - 17500 kJ/mol*nm^2. These values encompassed experimental values for ethane to pentane bond lengths of 0.24 nm, 0.335 nm, 0.44 nm, and 0.54 nm and force constants of 17500 kJ/mol*nm^2[40, 43, 46, 56, 61, 62, 63], and the constant MARTINI value of 0.47 nm for bond length and 1250 kJ/mol*nm^2 for the bond force constant.[28] These parameters are shown in **Table 4.4**.[28, 40, 43, 46, 56, 61, 62, 63]

2-Bead Simulation Parameters								
r_0 (nm)	0.21	0.257	0.304	0.351	0.398	0.445	0.492	0.54
k_b (kJ/mol*nm^2)	1250	3570	5890	8210	10530	12850	15170	17500

Table 4.4: Simulation parameters for our 2-bead alkane parameterisation work.[28, 40, 43, 46, 56, 61, 62, 63]

Just as with the 1-bead models, the analysis and property matching (i.e. self-solvation free energy, enthalpy of vaporisation, and density for parameter calibration, and then self-diffusion coefficients, shear viscosity, and radii of gyration for further validation) was repeated for the 2-bead systems until four 2-bead models, representing 2:1, 3:1, 4:1, and 5:1 mapped alkanes, were chosen.[31, 46-54, 58, 59, 60] The $\sigma/\varepsilon/r_0/k_b$ parameters of the four chosen 2-bead models where then used in the 3-bead model simulation (as seen in the third part of **Figure 4.2**), which were focused on optimising the bond angles and bond angle force constants of the models. The 3-bead model simulations were run again to include available known data for alkanes[40, 43, 46, 56, 61, 63] and the original MARTINI model structure[28], for angle potentials including eight bond angles, θ, ranging between 109.47°-180° at eight bond angle force constants, k_θ, ranging from 25.0 kJ/mol

- 65.0 kJ/mol, shown in **Table 4.5**.[28, 40, 43, 46, 56, 61, 63]

3-Bead Simulation Parameters								
θ (deg.)	109.47	120	130	140	150	160	170	180
k_θ (kJ/mol*nm^2)	25	31	36	42	48	54	60	65

Table 4.5: Simulation parameters for our 3-bead alkane parameterisation work.[40, 43, 46, 56, 61, 63]

The previous property-matching verification steps were repeated, and four 3-bead models, representing 2:1, 3:1, 4:1, and 5:1 mapped alkanes, were further matched to the data of more realistic linear alkanes[31, 46-51, 54, 58, 59, 60], the $\sigma/\varepsilon/r_0/k_b/\theta/k_\theta$ parameters of which where then used in singular 4-bead system parameterisation.

The 4-bead model simulation parameterisation (as shown in the fourth part of **Figure 4.2**) focused on optimising the dihedral angles and dihedral angle force constants of the models. They were run for torsion potentials for four dihedral angles, Φ, between 109.47°- 180° at four bond dihedral force constants, kΦ, ranging from 8.135 kJ/mol - 25.0 kJ/mol, as well as without any torsion potentials. These values included experimental values for ethane to pentane bond torsion angles of

109.47° and force constants of 8.135 kJ/mol[18, 32, 33, 34], the constant MARTINI value of 180° for bond angles and 25.0 kJ/mol for the bond angle force constant[28], and the lack of bond torsion angles or force constants also from MARTINI.[28] The inclusion of the bond angle parameters from MARTINI along with its lack of torsion angles was done to provide a large range for optimisation. These 4-bead model simulation parameters can be seen in **Table 4.6**.[28, 56, 61, 63, 64] As with the previous simulations, these results were compared to experimental and simulated property data[31, 46-51, 54, 58, 59, 60], and four final 4-bead models representing 2:1, 3:1, 4:1, and 5:1 mapped alkanes, with optimised $\sigma/\varepsilon/r_0/k_b/\theta/k_\theta/\Phi/k\Phi$ parameters, were matched to true alkanes, as seen in the final portion of **Figure 4.2**.

4-Bead Simulation Parameters					
Φ (deg.)	109.47	133	156.5	180	n/a
kΦ (kJ/mol)	25	38	52	65	n/a

Table 4.6: Simulation parameters for our 4-bead alkane parameterisation work.[8, 18, 32, 33, 34]

After all sixteen alkane models (i.e. the four 1-bead models with 2:1, 3:1, 4:1, and 5:1 mapping, the four 2-bead models with 2:1, 3:1, 4:1, and 5:1 mapping, etc.) were parameterised, the models were then tested for their thermodynamic properties (i.e. ΔG_{solv}) in MARTINI water. The standard MARTINI interaction parameters between MARTINI water, P4 beads, and propane, C2 beads, are a σ of 0.47nm and an ε of 2.3kJ/mol[28], while those between MARTINI water and the other MARTINI alkane models, C1 beads, are a σ of 0.47nm and an ε of 2.0kJ/mol.[28] Therefore, to ensure the proper interactions for our beads, and to cover a large range of values, simulations were run for the 1-bead, 2-bead, 3-bead, and 4-bead models over twenty-one σ ranging between 0.37nm - 0.47nm at eleven different ε from 0kJ/mol – 2.5kJ/mol. These parameters are shown in **Table 4.7**.[28]

Our Alkane Models-W Simulation Parameters											
σ (nm)	0.37	0.38	0.39	0.4	0.41	0.42	0.43	0.44	0.45	0.46	0.47
	0.375	0.385	0.395	0.405	0.415	0.425	0.435	0.445	0.455	0.465	
ε (kJ/mol)	0	0.25	0.5	0.75	1	1.25	1.5	1.75	2	2.25	2.5

Table 4.7: Simulation parameters for our alkane models with MARTINI water.[28]

The same type of analysis and property matching for the solvation free energies in water was then done, comparing our results with experimental data[65, 66, 67, 68] and Lennard-Jones parameters for each alkane model (i.e. 2:1, 3:1, etc.) and MARTINI water were optimised.

After the final alkane models were optimised for water interactions, we turned to validating our 2:1 and 4:1 mapped beads for polyethylene. Due to the previously mentioned 2 carbons in the polyethylene repeating unit and the similar nature of polyethylene and near alkane chains, the 2:1 and 4:1 mapped bead models were the focus of the PE simulations.[34, 35] Long chains of our 2:1 and 4:1 bead models were run at melt temperatures for polyethylene, their density was re-calculated based on the molecular weight of polyethylene, and the resulting ρ values, as well as the calculated $\mathrm{R_g}$, of those models were compared against simulation values for polyethylene.[69, 70, 72]

4.1.5 Data analysis

The alkane self-solvation free energies were primarily compared against the interpolated and standard experimental data from the Minnesota Solvation Database by Marenich et al.[46], experiments done by Hünenberger et al.[47], and the solvation free energy database by Katritzky et al.[51] All interpolation of experimental values was carried out when experimental data for the necessary conditions was not available, and when analysis of the existing data yielded linear trends with a high degree of correlation. We expect the errors inherent in this procedure to be much lower than approximations of the CG model. An example of the interpolation work done on all interpolated experimental sources can be seen in **Figure 4.3**, showing the interpolation of the free energies of self-solvation for linear alkanes from Katritzky et al.[51]

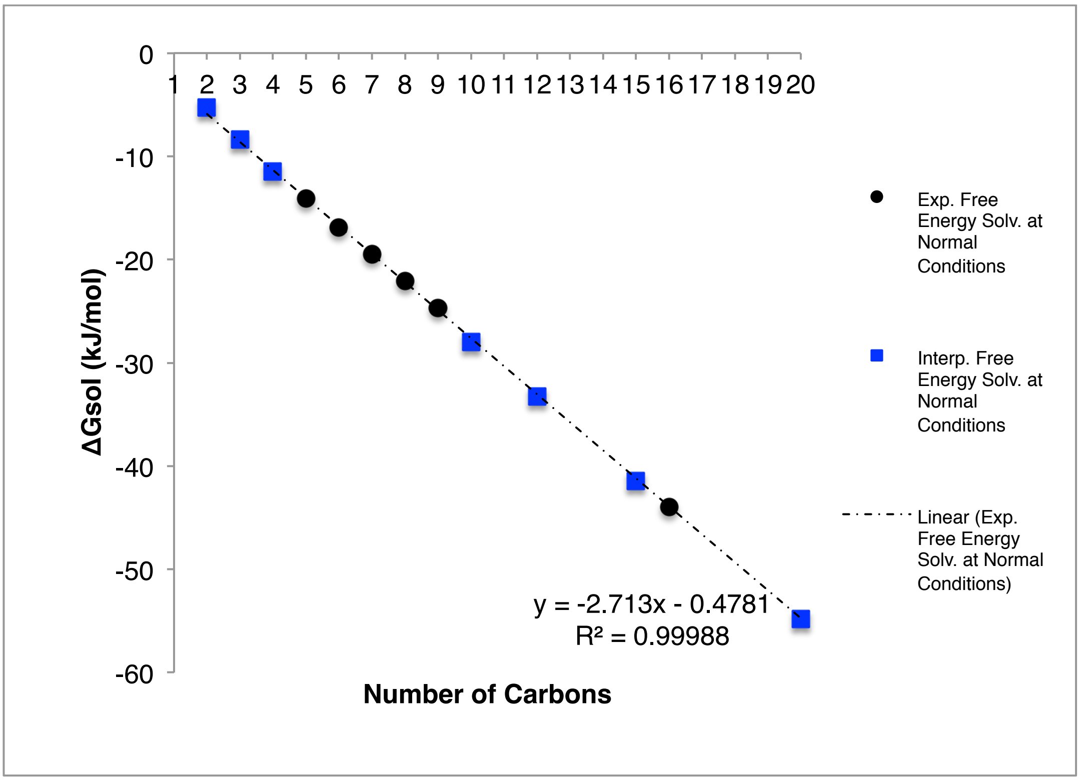

Figure 4.3: Experimental and interpolated self-solvation free energies of linear alkanes from ethane to eicosane. The black circles represent known values, the dashed black line represents the linear interpolation of these values based on data trend, and the blue squares represent the interpolated values for other unknown linear alkanes based on the linear interpolation.[51]

The alkane model densities in this study were compared against experimental data taken from Astle et al.[52], as well as an online experimental database.[53] Enthalpy of vaporisation results were compared to experimental studies by van Velzen et al.[48], Viton et al.[49], and Hossenlopp et al.[50]

Self-diffusion coefficient results for our alkane models were compared against interpolated experimental data from Bachl et al.[54]

Our shear viscosity results were compared to standard and interpolated experimental data by van Velzen et al.[58] and Sivebaek et al.[59]

Radius of gyration is incredibly difficult to examine experimentally, so our radii of gyration were compared to two levels of theoretical results from an AA model by Toth et al.[60] and the CG model by Nielsen et al.[31] While the simulation studies were obviously not at the same degree of comparative value as the experimental results, as they were considered successful models, they were used here in lieu of experimental data, as none could be found.

The alkane solvation free energies in water were compared against interpolated or standard experimental values taken from studies by Hutacharoen et al.[65], Plyasunov et al.[66], Ferguson et al.[67], and

Sutton et al.[68]

The polyethelyene density and radius of gyration results for our 2:1 and 4:1 mapped bead chains at 723.15K were compared to AA simulation data from Harmandaris et al.[69] and to AA simulation data from Daoulas et al.[71]. The density and radius of gyration results for our 2:1 and 4:1 mapped bead chains at 773.15K were compared to the CG and AA data from Peters et al.[69] These results were compared to simulated data, as no known data for density could be obtained for specific chain lengths of polyethylene, while the radii of gyrations were still extremely difficult to measure experimentally, as mentioned above.

All of our results were calculated using the equations described in Chapter 3.

4.2 Results

4.2.1 Current MARTINI model results

In **Figures 4.4** the self-solvation free energy of 1-bead MARTINI systems corresponding to all possible interaction levels for non-charged beads is shown to decrease non-linearly with increasing ε.

This trend is as expected with theory, as an increasing the solvent-solvent ε increases the solvent-solvent interactions, increasing cohesive energy of the fluid (i.e. the solute), making it harder to accommodate the solute, making ΔG_{solv} more unfavourable (i.e. more positive).[47, 72, 73, 79, 80, 81] As the solute-solvent ε increases, however, it strengthens the solute-solvent interactions, increasing the solubility of the solute in the solvent, making ΔG_{solv} more favourable (i.e. more negative).[47, 72, 73, 79, 80, 81] In these cases the σ LJ component is not a factor, as σ is a constant 0.47 nm for all beads simulated.[28]

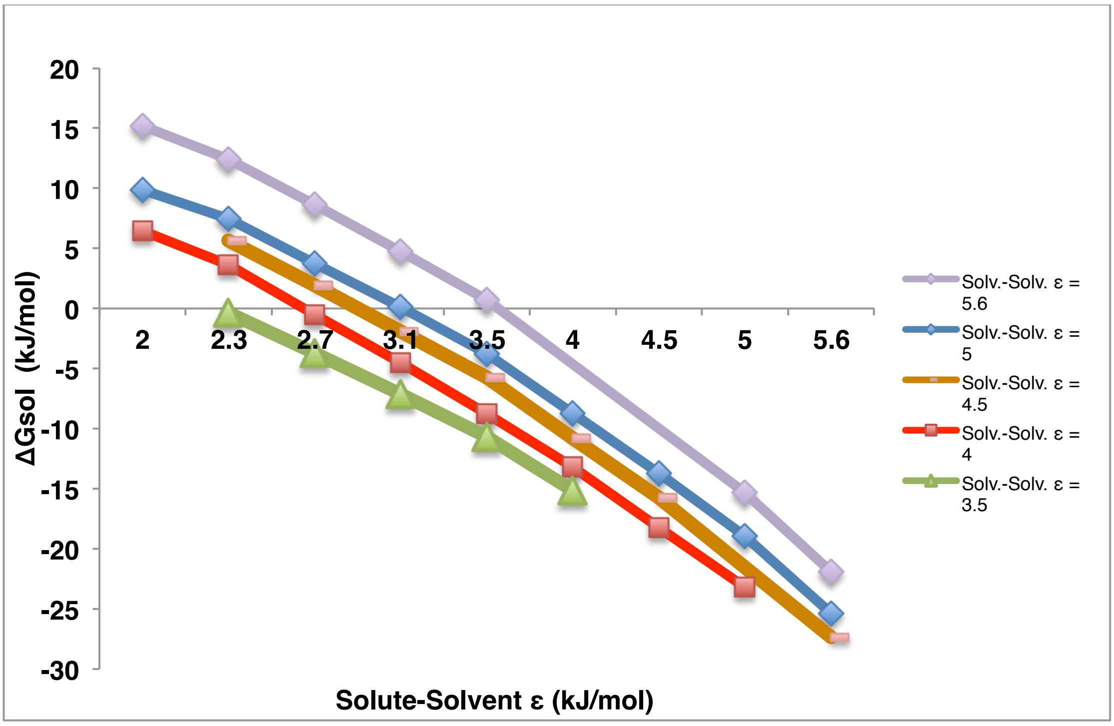

Figure 4.4: MARTINI bead interaction solvation free energy results for possible combinations of solute-solvent and solvent-solvent interaction parameters, as per the values from **Figures 4.1 a** and **b**.[28]

These results are promising, as they clearly establish an adherence to expected theory, and could be helpful in future work looking to match a particular MARTINI bead interaction level ΔG_{solv} results to known data. For the purposes of this work though, the MARTINI alkane results were of more interest.

In **Figure 4.5** we see the adjusted mass density results for the MARTINI alkane models. The results show an increase in ρ with increasing alkane chain length, which is expected from theory as the increase in the molecular energy of the molecules with increasing size, or chain length, causes an increase in the density.[3, 48, 62, 72, 74] The MARTINI ρ results are within the margin of error for interpolated experimental densities at standard conditions (see **Table 4.12** in **Appendix A**)[52, 53], but not for propane or hexadecane, and the trends between the MARTINI models and experimental values are disparate.[52, 53] This could be because the MARTINI models were not specifically matched to ρ, and the results for butane, octane, and dodecane were due to the close matching of ε for enthalpy of vaporisation, shown below.

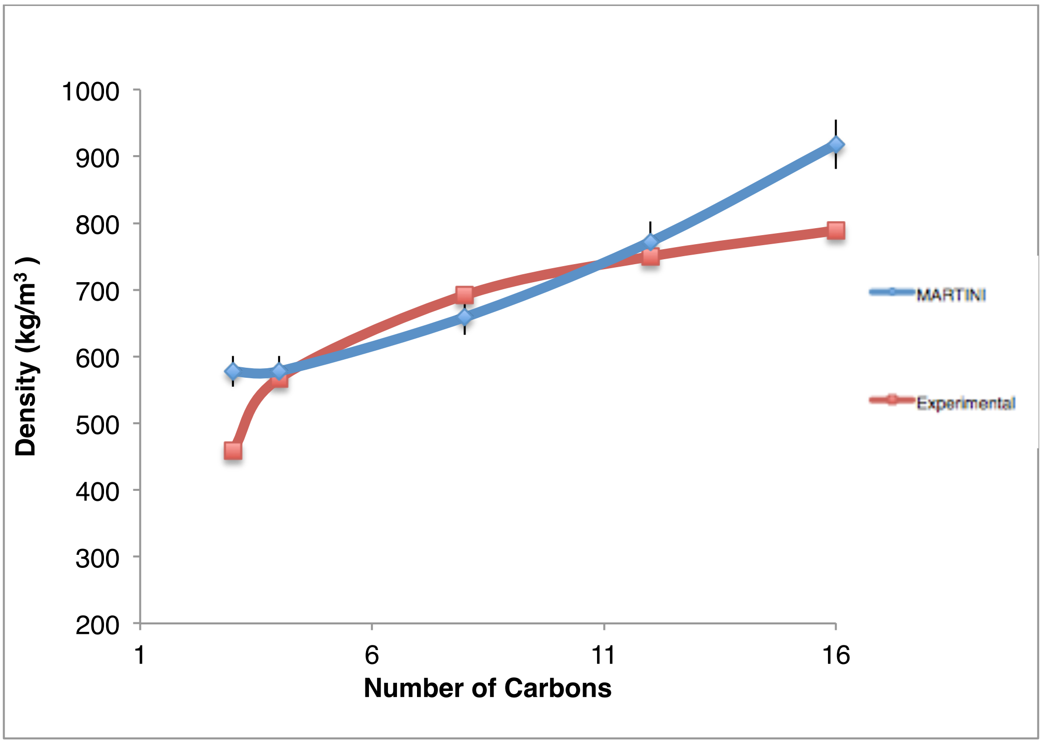

Figure 4.5: MARTINI alkane model density results compared against experimental values for those alkanes at room temperature and standard pressure.[52, 53]

Figure 4.6 shows an increasing non-linear trend in the enthalpy of vaporisation with increasing chain length for the MARTINI alkane models. An increase of chain length leads to an increase in the solution interaction energies, or cohesive energy, leading to an increase in ΔH_{vap}.[48, 62, 70, 74, 81, 84] This increase in ΔH_{vap} is also expected considering theory in regards to these models' results for ΔG_{solv} (shown in the next section), as solvation and vaporisation occur in converse directions between the liquid and gas phases.[48, 62, 70, 74] Here these enthalpies of vaporisation are within the margin of error for experimental values (see **Table 4.13** in **Appendix A**)[48, 49, 50], indicating that the MARTINI force field was correctly optimised for these properties. However, once again the largest discrepancies were obtained for the propane and hexadecane models.

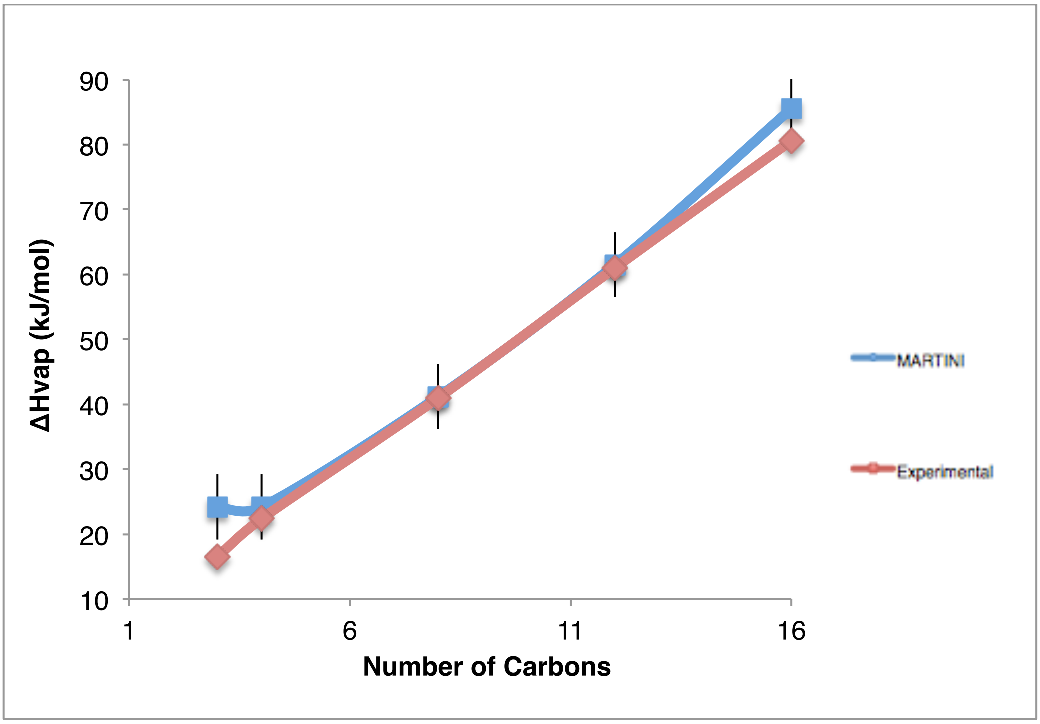

Figure 4.6: MARTINI alkane model enthalpy of vaporisation results compared against experimental values.[48, 49, 50]

In **Figure 4.7** and **Figure 4.8** the ΔG_{solv} of MARTINI alkanes in both themselves and MARTINI hexadecane can be shown to decrease with increasing size, or chain length, of the alkane models. Though the LJ interactions between C1 (and C2 in the case of MARTINI propane) are the same with C1 and C2 beads, the addition of an increasing bead chain length in MARTINI octane, dodecane, and hexadecane decreases the $\Delta G_{solv}$of the system.[28] This is expected from theory, as the increasing chain lengths caused a decrease in the ΔG_{solv} (i.e. made ΔG_{solv} more favourable), similar to ΔH_{vap}.[47, 72, 73, 79, 80, 81, 83] In comparison with experimental values for self-solvation (seen in **Table 4.14** in **Appendix A**)[46, 47, 51] and solvation in hexadecane (found in **Table 4.11** in **Appendix A**)[46, 47, 51], it is clear that while MARTINI alkane models are not a perfect match in either system, they do show similar trends between increasing bead chains, meaning they could easily be adjusted to fit in further work.

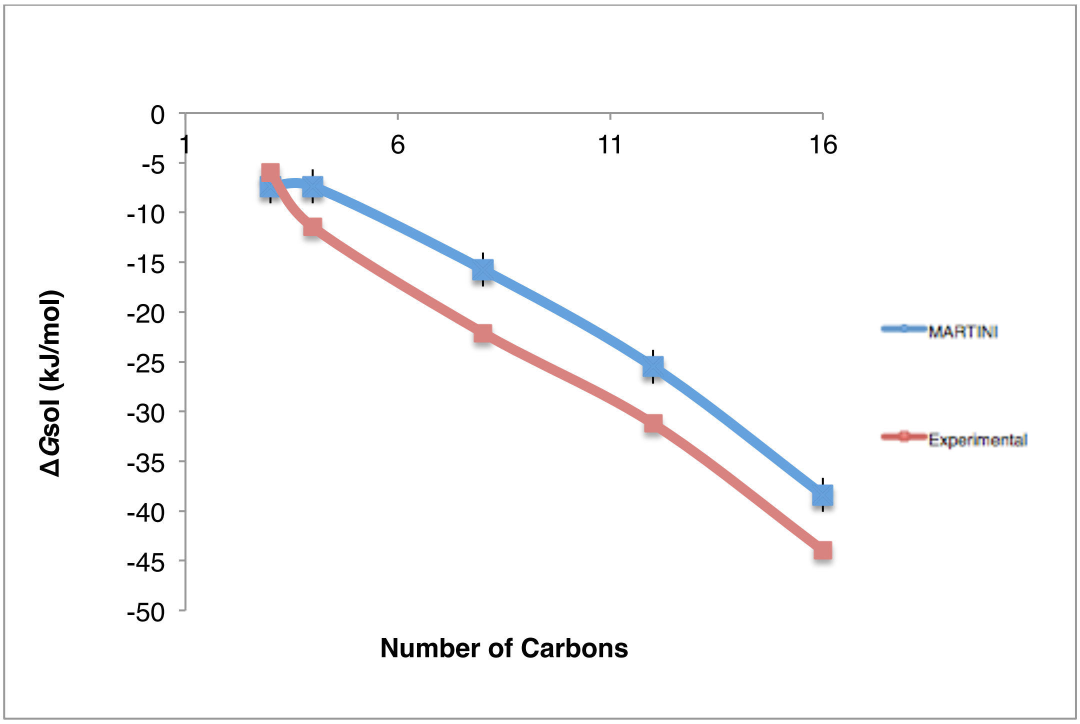

Figure 4.7: MARTINI alkane model self-solvation free energy results compared against experimental values for those alkanes at room temperature.[46, 47, 51]

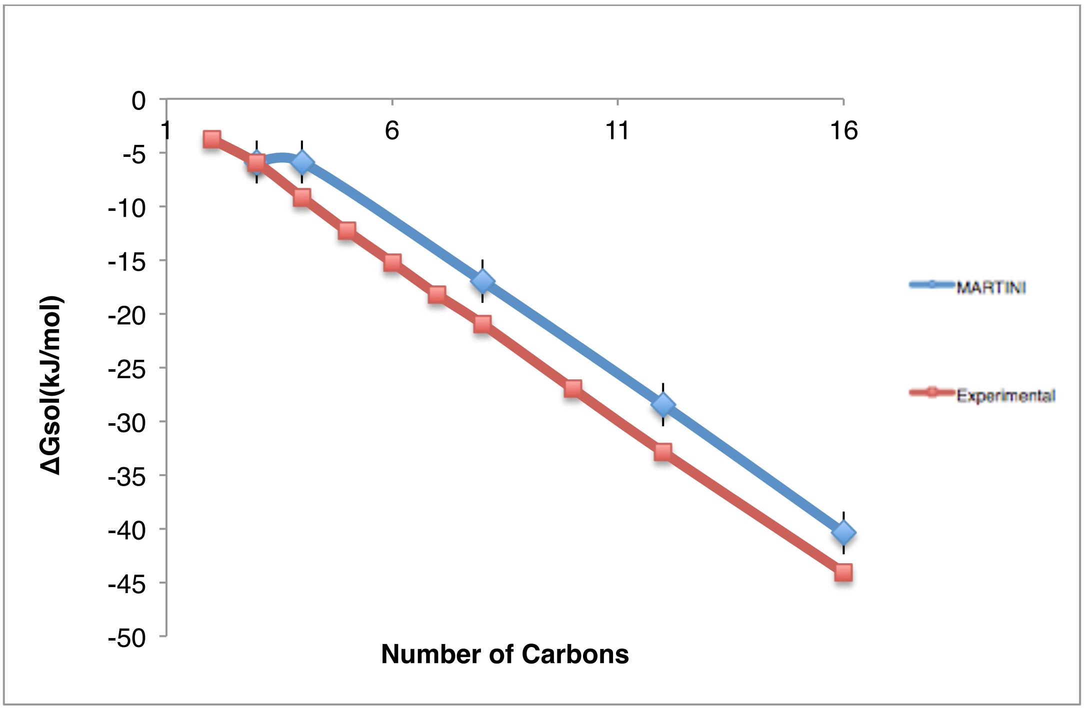

Figure 4.8: MARTINI alkane model solvation free energy in hexadecane results compared against experimental values at room temperature.[46, 47, 51]

Self-diffusion coefficients exhibit a strong dependence on the number of particles in the simulated system.[47, 72, 75, 76] The simulations were fully solvated at the standard size based on MARTINI examples for consistency.[28] As can be seen in **Figure 4.9**, the MARTINI alkane models produce self-diffusion coefficients far outside the margin of error in comparison to experimental values (see **Table 4.15** in **Appendix A**).[31, 54, 77] This could be due to a lack of parameterisation for this property, or could in fact be due to the disparate values for density these models produce with experimental values, as self-diffusion coefficients are dependent on density and temperature (though temperature was kept constant here at standard values).[31, 54, 75, 76, 77]

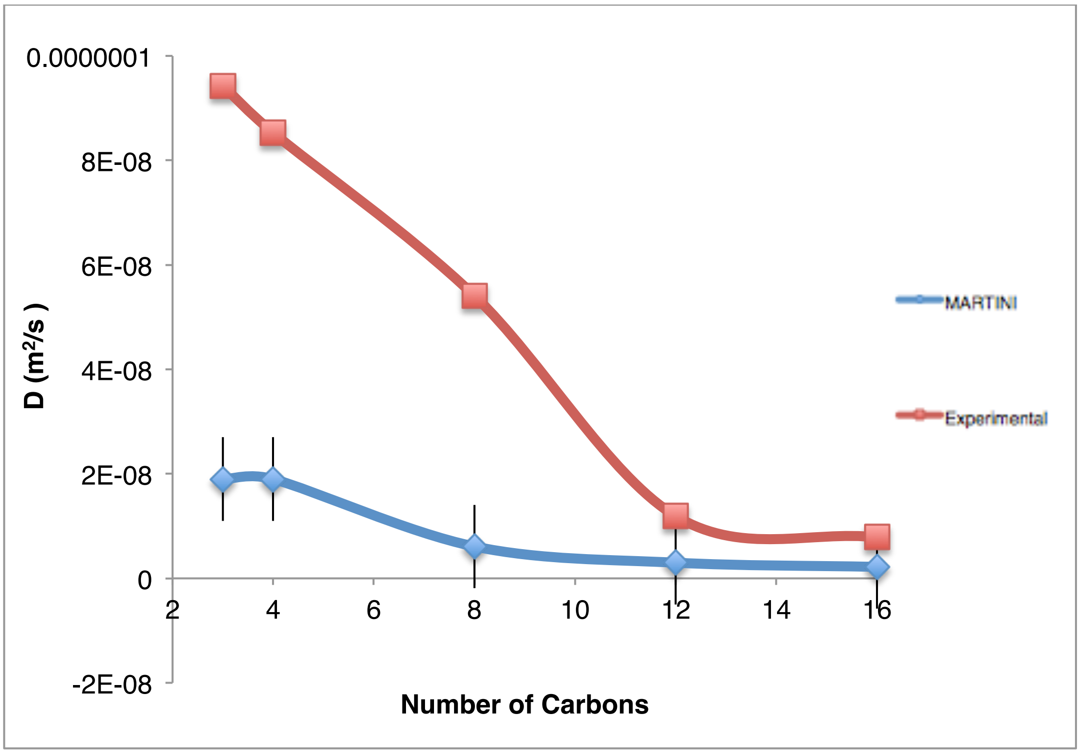

Figure 4.9: MARTINI alkane model self-diffusion coeffiecient results compared against experimental values.[54]

MARTINI matches well with $\Delta \mathrm{H}_{\mathrm{vap}}$, okay with ρ, but there is a systematic overestimation of $\Delta \mathrm{G}_{\mathrm{solv}}$, as well as an underestimation of D. Hence, reparameterisation was needed.

4.2.2 Parameterised alkane results

4.2.2.1 Non-bonded parameters (σ, ε)

As shown in **Figure 4.2**, we first began our alkane parameterisation by matching the ρ, $\Delta\mathrm{H}_{\mathrm{vap}}$, $\Delta\mathrm{G}_{\mathrm{solv}}$ properties to σ and ε pairs. An example for the adjusted ρ for the 1-bead model simulations representing ethane (i.e. 2:1 mapping) can be seen in **Figures 4.10a-b**. Selected results for propane (i.e. 3:1 mapping), butane (i.e. 4:1 mapping), and pentane (i.e. 5:1 mapping) can be seen in **Figures 4.33a-b**, **4.35a-b**, and **4.37a-b** in **Appendix A**. The adjusted density results for the 1-bead model systems are shown here to increase non-linearly with ε and increase linearly with σ. These results were expected with theory, as the increase in the volume of exclusion of the molecules with increasing σ causes a decrease in the ρ, while the increase in the molecular energy of the molecules with increasing ε causes an increase in the density.[3, 48, 62, 72, 74]

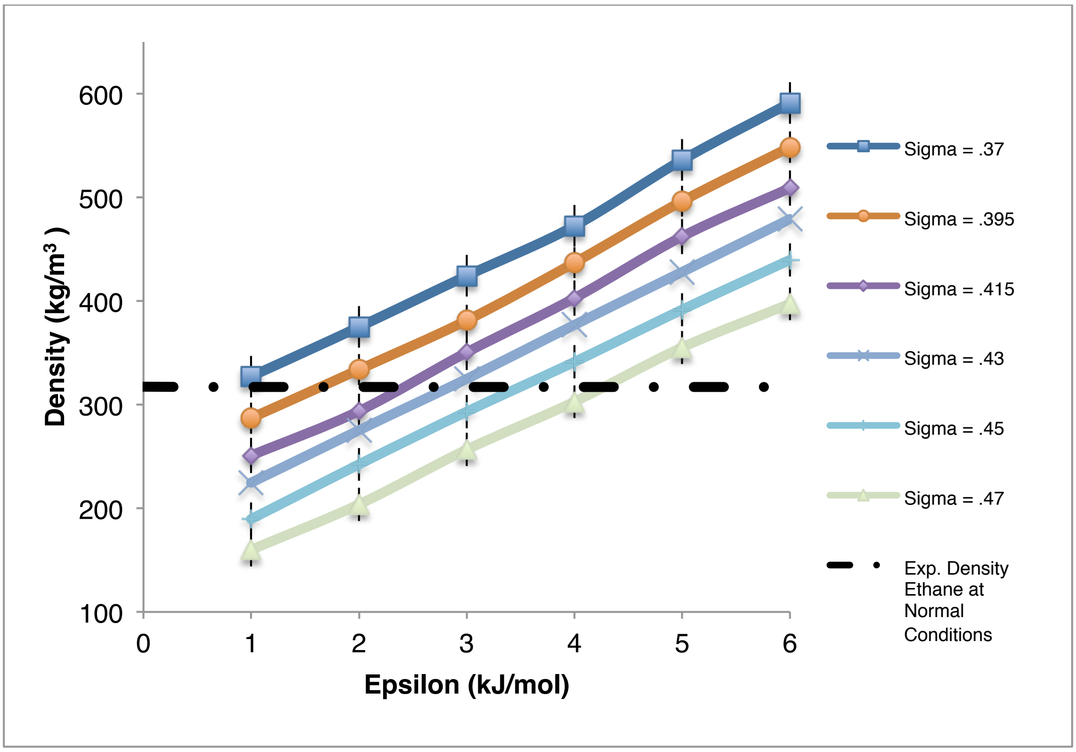
600
500
400
300
200
100
Density (kg/m^3)
0
1
2
3
4
5
6
Epsilon (kJ/mol)
Sigma = .37
Sigma = .395
Sigma = .415
Sigma = .43
Sigma = .45
Sigma = .47
Exp. Density Ethane at Normal Conditions

a)

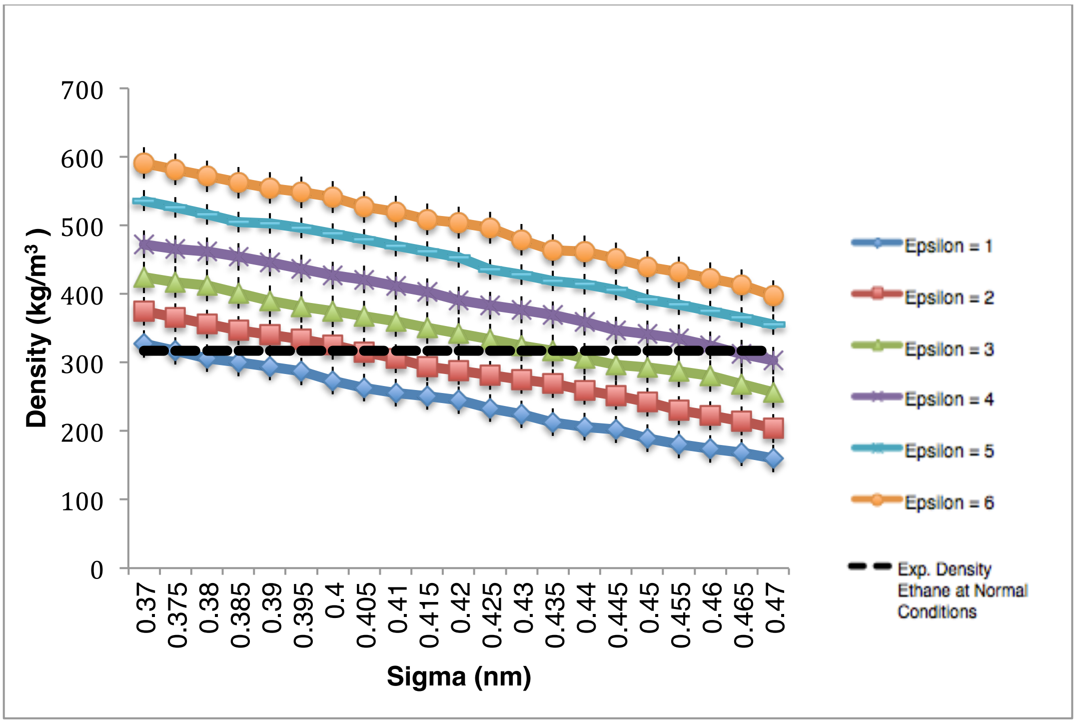

b)

Figures 4.10a-b: Selected densities determined for ethane's molecular weight, of the 1-bead solvent systems for different values of the Lennard-Jones parameters: **a)** selected sigmas at different epsilon values, and **b)** epsilons at different sigma values. The black dashed line represents the experimental reference value for liquid ethane at room temperature.[52, 53]

As we can see, there are multiple, and essentially infinite, pairs of σ and ε that can match experimental ρ of ethane (i.e. the points of intersection of the experimental values with each set of sigma values per epsilon value, or epsilon values per sigma value). We have used linear interpolation to find the set of (σ, ε) pairs that yield optimal agreement with the density of each alkane, as discussed in more detail later.

Figures 4.11a-b show $\Delta \mathrm{H}_{\mathrm{vap}}$ results for the 1-bead model simulations. An increasing non-linear trend in the enthalpy of vaporisation with increasing ε and an increasing linear trend with increasing σ can be seen in the figures. As previously mentioned, an increase of σ and ε also leads to an increase in the solution interaction energies, leading to an increase in $\Delta \mathrm{H}_{\mathrm{vap}}$.[48, 50, 62, 72, 74, 84] The increase in σ leads to an increase in the volume of exclusion of the molecules, though it is of minor importance to the overall $\Delta \mathrm{H}_{\mathrm{vap}}$ here.[47, 48, 62, 72, 74, 80, 84] This increase is also expected considering the results for $\Delta \mathrm{G}_{\mathrm{solv}}$, as solvation and vaporisation occur in converse directions between the liquid and gas phases.[48, 62, 72, 74, 80, 83, 84]

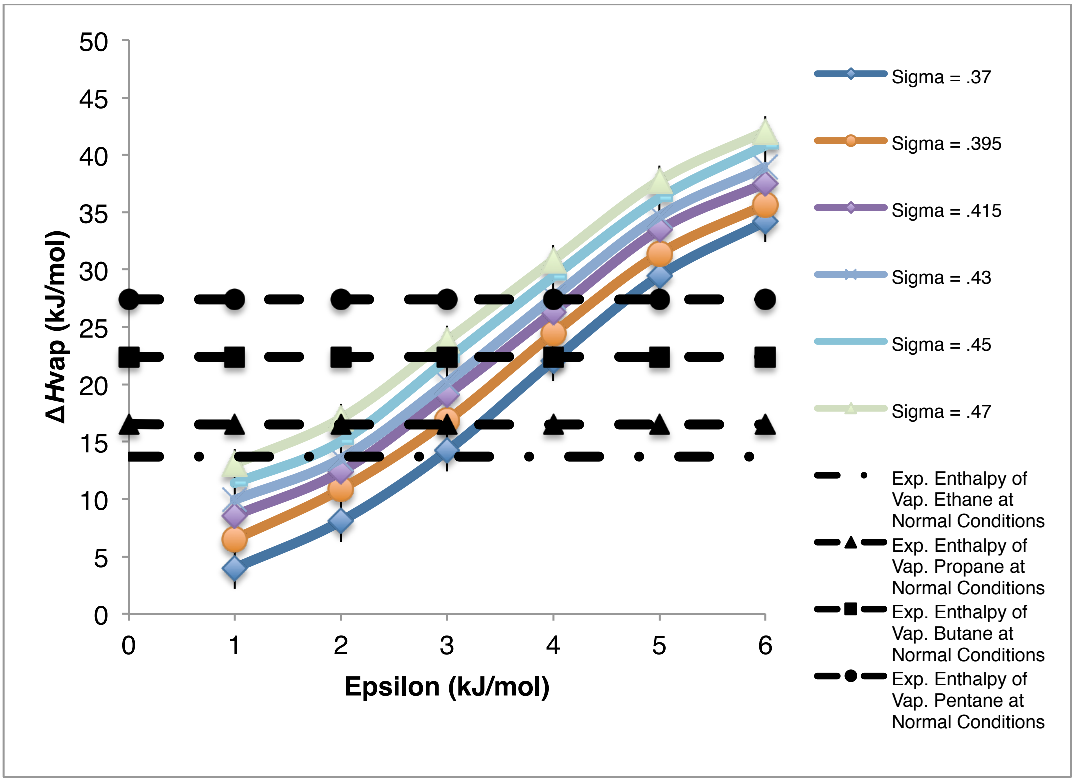
50
45
40
35
30
25
20
15
10
5
0
ΔHvap (kJ/mol)
0
1
2
3
4
5
6
Epsilon (kJ/mol)
Sigma = .37
Sigma = .395
Sigma = .415
Sigma = .43
Sigma = .45
Sigma = .47
Exp. Enthalpy of Vap. Ethane at Normal Conditions
Exp. Enthalpy of Vap. Propane at Normal Conditions
Exp. Enthalpy of Vap. Butane at Normal Conditions
Exp. Enthalpy of Vap. Pentane at Normal Conditions

a)

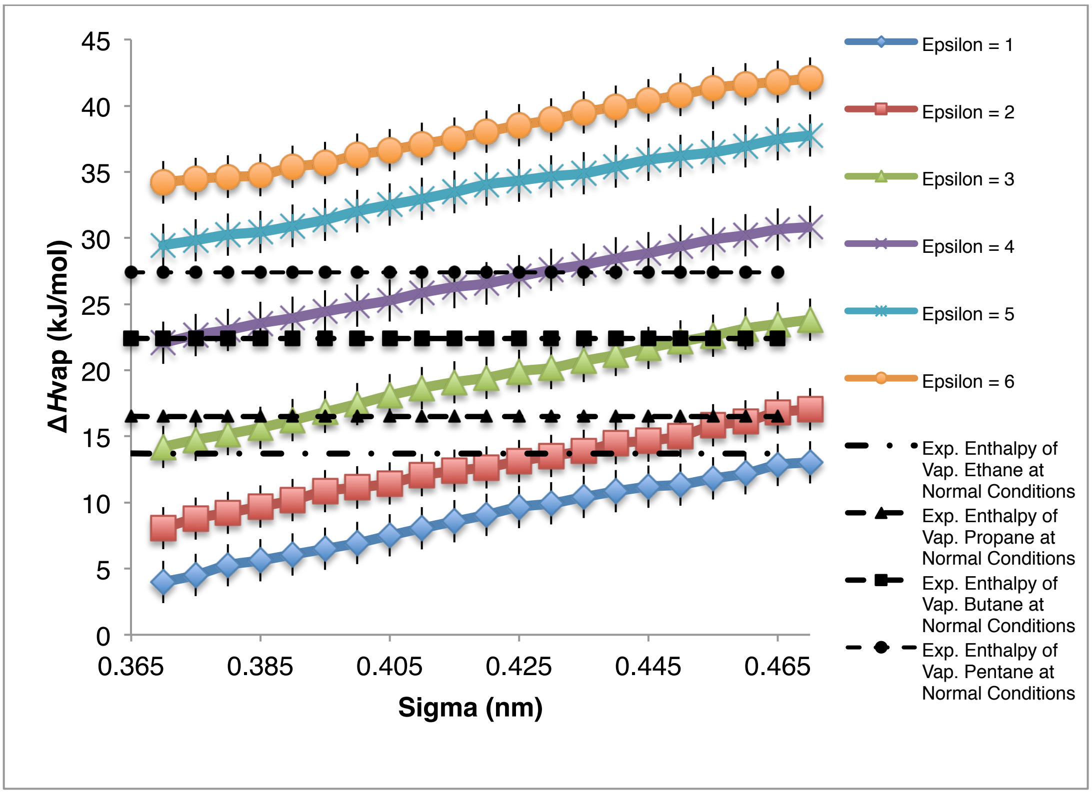

b)

Figures 4.11a-b: Selected enthalpies of vaporization of the 1-bead solvent systems for different values of the Lennard-Jones parameters: **a)** selected sigmas at different epsilon values, and **b)** epsilons at different sigma values. The black horizontal dashed lines represent the experimental reference values for each alkane at room temperature: ethane (no symbols), propane (triangles), butane (squares), and pentane (circles).[48, 49, 50]

As with density, we can also find a set of (σ, ε) pairs that yield optimal agreement with ΔH_{vap} for each alkane.

In **Figures 4.12a-b**, the self-solvation free energy of 1-bead model systems is shown to decrease non-linearly with increasing ε and also decrease linearly with increasing σ. This trend is as expected with theory, as σ and ε increased, the strength of the solvent-solute interactions increased, making $\Delta\mathrm{G}_{\mathrm{solv}}$ more favourable.[47, 72, 73, 79, 83] In the case of σ in particular, the increased solvent-solute interactions meant the enthalpic gain of making a solute bead outweighed the entropic cost (i.e. the $\Delta\mathrm{G}_{\mathrm{solv}}$ becomes more negative or favourable), and the increased volume of exclusion of both the solute and solvent molecules caused a decrease in systemic density (i.e. the $\Delta\mathrm{G}_{\mathrm{solv}}$ becomes more positive or unfavourable).[47, 72, 73, 80, 83, 84] As evidenced by the clearly favourable trend for $\Delta\mathrm{G}_{\mathrm{solv}}$, the unfavourable volume of exclusion component seems to have a negligible effect on the overall $\Delta\mathrm{G}_{\mathrm{solv}}$ here.

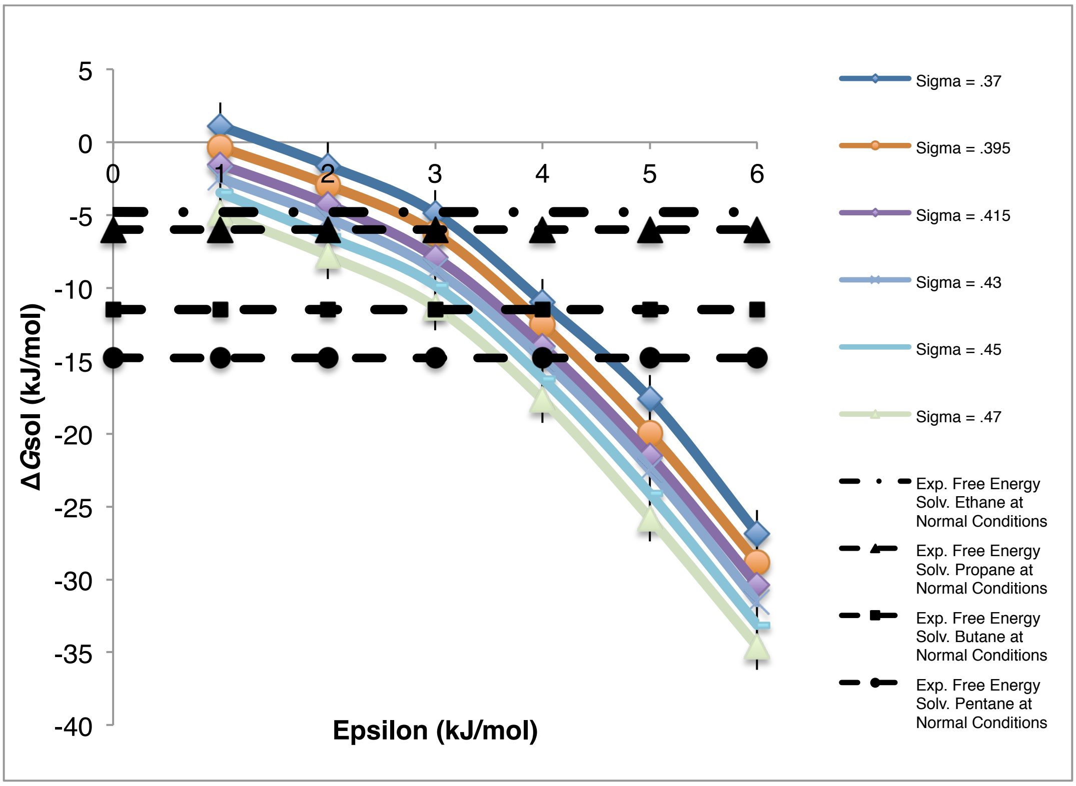
5
0
-5
-10
-15
-20
-25
-30
-35
-40
0
1
2
3
4
5
6
ΔGsol (kJ/mol)
Epsilon (kJ/mol)
Sigma = .37
Sigma = .395
Sigma = .415
Sigma = .43
Sigma = .45
Sigma = .47
Exp. Free Energy Solv. Ethane at Normal Conditions
Exp. Free Energy Solv. Propane at Normal Conditions
Exp. Free Energy Solv. Butane at Normal Conditions
Exp. Free Energy Solv. Pentane at Normal Conditions

a)

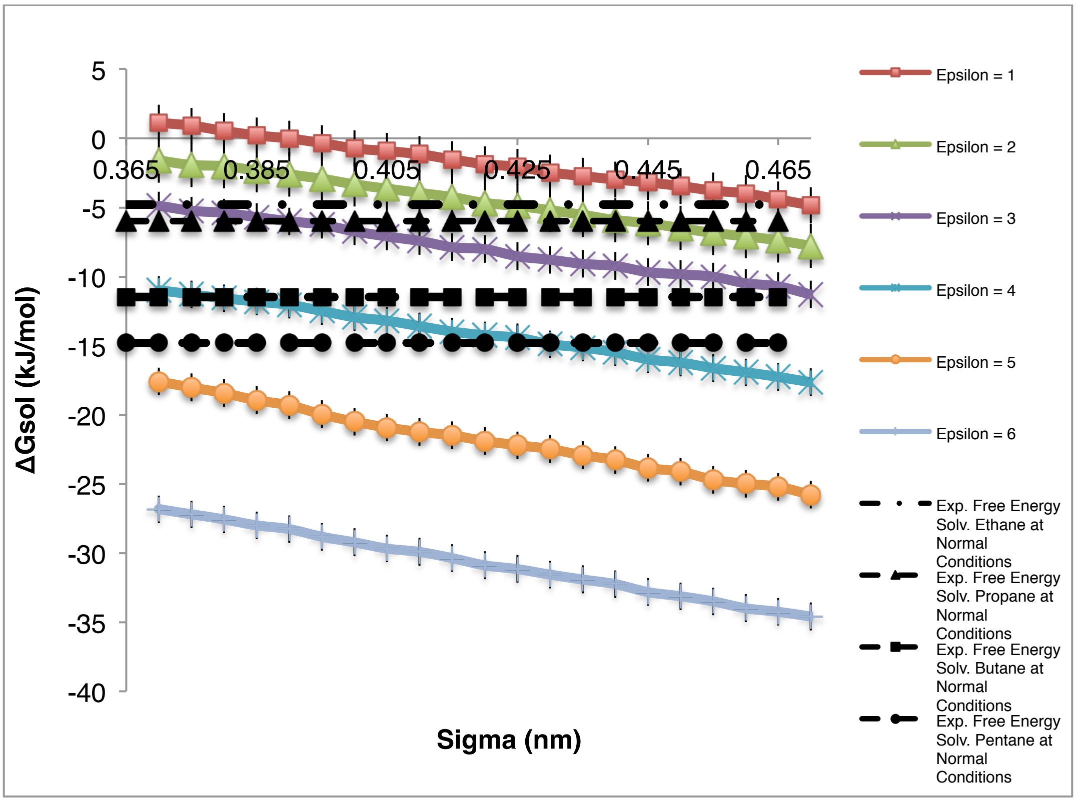

b)

Figures 4.12a-b: Selected self-solvation free energies of the 1-bead solvent systems for different values of the Lennard-Jones parameters of **a)** selected sigmas at different epsilon values, and **b)** epsilons at different sigma values. The black horizontal dashed lines represent the experimental reference values for each alkane at room temperature: ethane (no symbols), propane (triangles), butane (squares), and pentane (circles).[46, 47, 51]

With the above set of results, we can plot three lines in the (σ, ε) parameter space, corresponding to the optimal set of parameters for each property (i.e. ρ, $\Delta\mathrm{H}_{\mathrm{vap}}$, and $\Delta\mathrm{G}_{\mathrm{solv}}$). The overall best set of parameters lie at the intersection of these lines. An example graphical representation of this optimisation for the determination of the most applicable parameters for the 2:1 mapping of 1-bead simulations can be seen in **Figures 4.13**. The other graphical representations for 3:1, 4:1, and 5:1 bead mapping matching 1-bead parameters can be seen in **Figures 4.34**, **4.36**, and **4.38** in **Appendix A**.

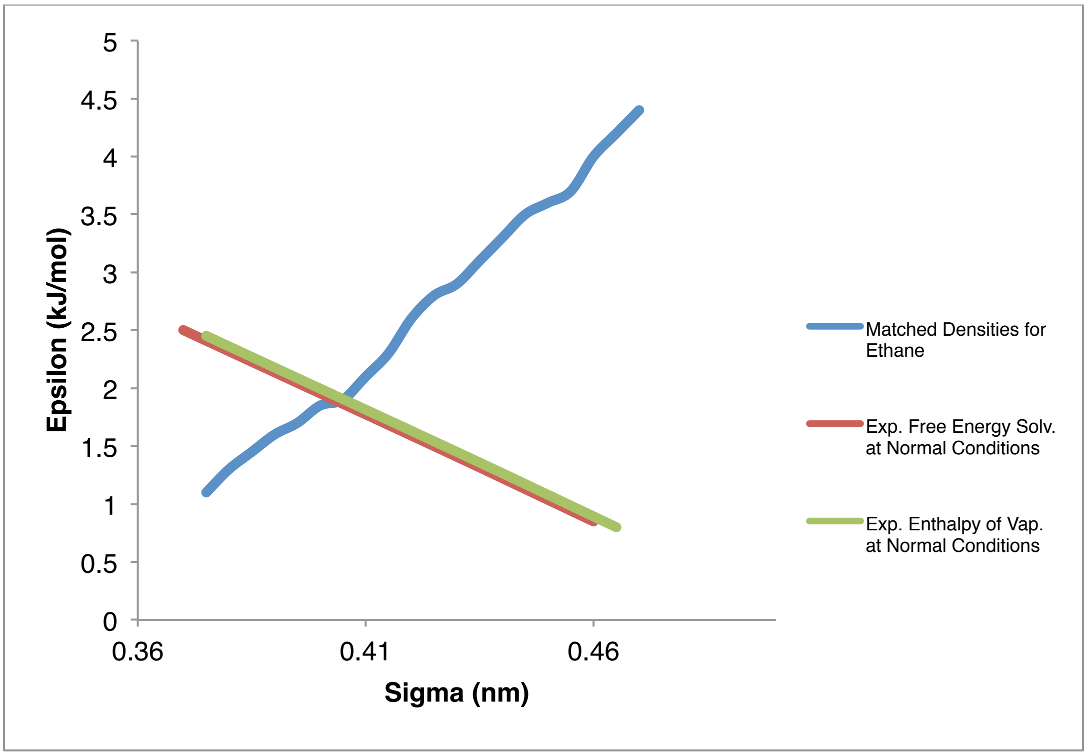

Figure 4.13: Determination of optimal set of parameters for 2:1 mapped 1-bead models. The full lines show each property at standard temperature and pressure: density (blue), free energy of self-solvation (red), and enthalpy of vaporisation (green).[52, 53]

4.2.2.2 Bond stretching parameters (r_0, k_b)

As explained previously in **Figure 4.2**, the optimal σ and ε values determined above were carried forward to the optimisation of bonded parameters. Selected adjusted ρ for the 2-bead model simulations representing butane (i.e. 2:1 mapping) are shown in **Figures 4.14a-b**, while selected results for hexane (i.e. 3:1 mapping), octane (i.e. 4:1 mapping), and decane (i.e. 5:1 mapping) can be seen in **Figures 4.39a-b**, **4.43a-b**, and **4.47a-b** in **Appendix A**. The adjusted density of the 2-bead simulations is shown here to decrease nearly linearly with r_0 and increase linearly with increasing k_b. These results were expected with theory, as larger bond length leads to less efficient packing of molecules and causes a decrease in the density.[3, 48, 62, 72, 74] The increase in the bond force constant causes the bonds to be "stiffer", and leads to an increase in the ρ through facilitated packing of more rigid molecules.[3, 48, 62, 72, 74] We note also that the effect of k_b is much smaller here than that of r_0. Furthermore, the density is much less sensitive to the bond stretching parameters than to σ and ε (compare to **Figure 4.10**).

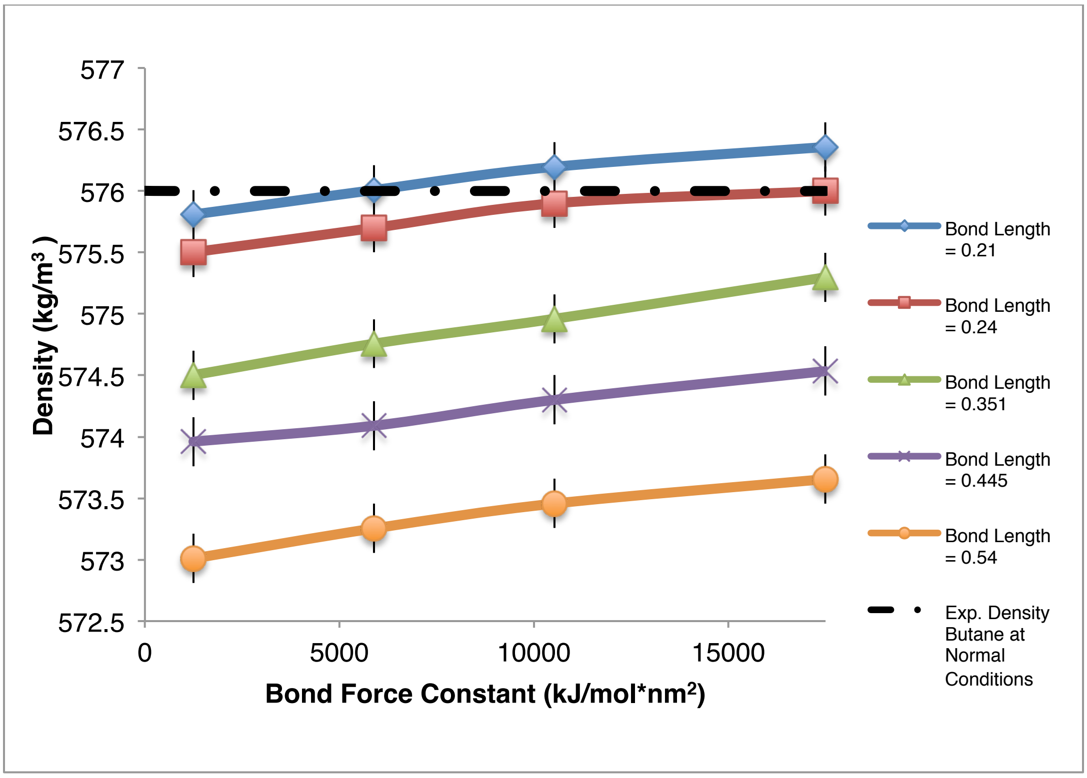
577
576.5
576
575.5
575
574.5
574
573.5
573
572.5
Density (kg/m³)
0
5000
10000
15000
Bond Force Constant (kJ/mol*nm²)
Bond Length = 0.21
Bond Length = 0.24
Bond Length = 0.351
Bond Length = 0.445
Bond Length = 0.54
Exp. Density Butane at Normal Conditions

a)

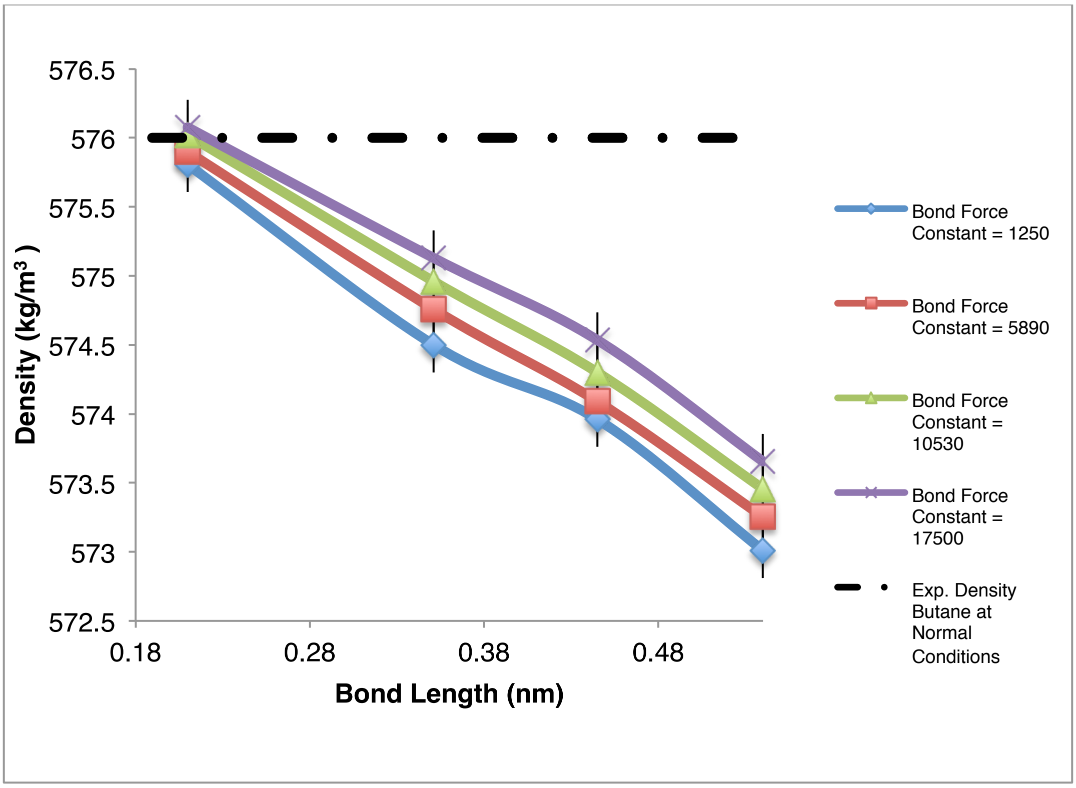

b)

Figures 4.14a-b: Selected densities determined for butane’s molecular weight, of the 2-bead solvent systems for different values of the bond length and bond force constant parameters: **a)** selected bond lengths at different bond force constants, and **b)** bond force constants at different bond length values. The black dashed line represents the experimental reference values for butane at room temperature.[52, 53]

As done previously for σ and ε, we determined the optimal (r_0, k_b)

pairs to match each of the experimental ρ of each target alkane.

Enthalpy of vaporisation results for the 2-bead model simulations representing butane (i.e. 2:1 mapping) are shown in **Figures 4.15a-b**, while those for hexane (i.e. 3:1 mapping), octane (i.e. 4:1 mapping), and decane (i.e. 5:1 mapping) are available in **Figures 4.40a-b**, **4.44a-b**, and **4.48a-b** in **Appendix A**. A decreasing linear trend in the enthalpy of vaporisation with increasing r_0 and an increasing non-linear trend with increasing k_b can be seen in the figures. These results agree with theory, as an increasing bond length decreases molecule packing and hence lowers the interaction energy, while an increase in the bond force constant contributes to a greater molecular energy, and thusly a greater ΔH_{vap}.[48, 62, 72, 74, 84] As mentioned before, this increase was again expected due to the ΔG_{solv} results, as solvation and vaporisation are inversely related.[48, 62, 72, 74, 80, 83, 84]

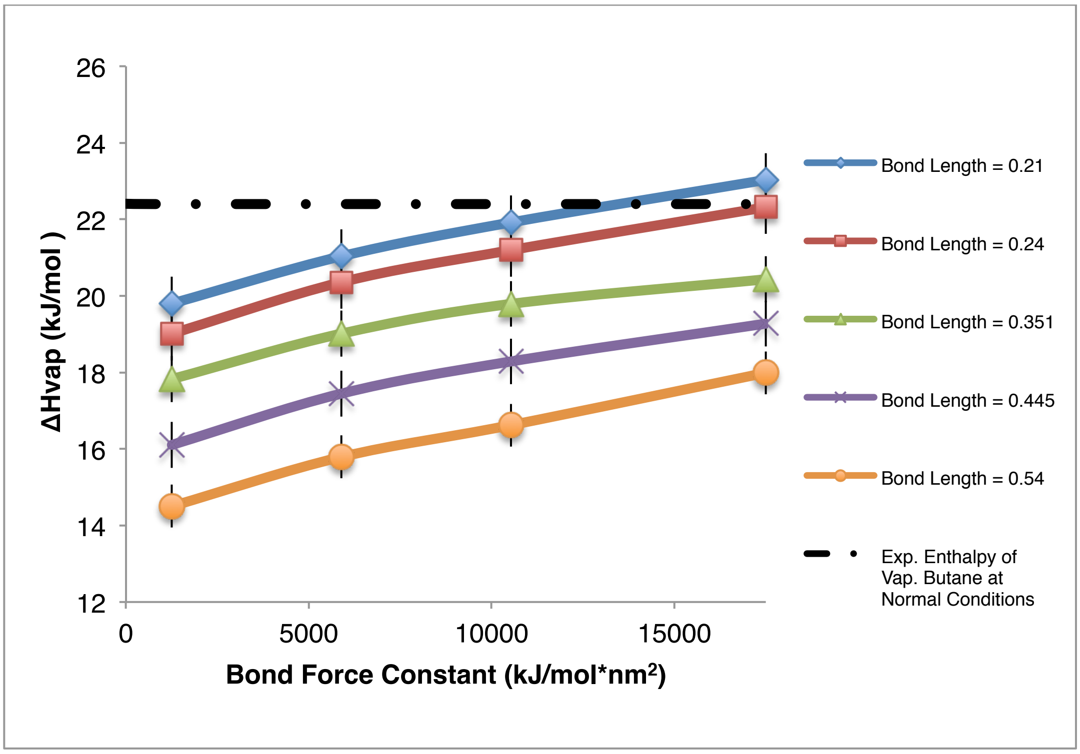
ΔHvap (kJ/mol)
26
24
22
20
18
16
14
12
0
5000
10000
15000
Bond Force Constant (kJ/mol*nm²)
Bond Length = 0.21
Bond Length = 0.24
Bond Length = 0.351
Bond Length = 0.445
Bond Length = 0.54
Exp. Enthalpy of Vap. Butane at Normal Conditions

a)

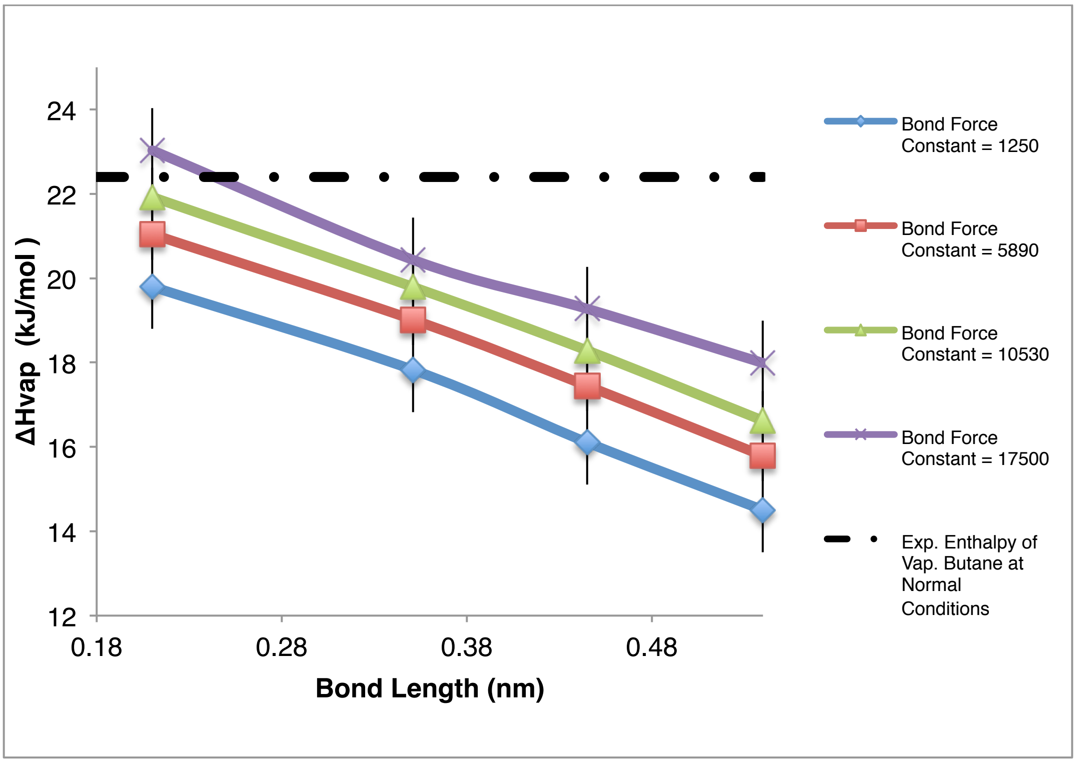

b)

Figures 4.15a-b: Selected enthalpies of vaporization of the 2-bead solvent systems for different values of the bond length and bond force constant parameters: **a)** selected bond lengths at different bond force constants, and **b)** bond force constants at different bond length values. The black dashed line represents the experimental reference values for butane at room temperature.[48, 49, 50]

Self-solvation free energy results for the 2-bead model simulations representing butane (i.e. 2:1 mapping) can be seen in **Figures 4.16a-b**. As before, ΔG_{solv} results for hexane (i.e. 3:1 mapping), octane (i.e. 4:1 mapping), and decane (i.e. 5:1 mapping) are shown in **Figures 4.41a-b**, **4.45a-b**, and **4.49a-b** in **Appendix A**. The self-solvation free energy results are shown here to increase linearly with increasing r_0 and slightly decrease linearly with increasing k_b. This trend adhered to expected theory; as stated above, larger bond length leads to less efficient packing of molecules and causes a decrease in the interaction energy, causing an increase in ΔG_{solv} (i.e. ΔG_{solv} is made more positive or unfavourable), while an increase in the bond force constant contributes to a greater molecular energy and a decrease in the ΔG_{solv} (i.e. ΔG_{solv} is made more negative or favourable).[3, 48, 62, 72, 74, 83, 84] As solvation and vaporisation occur in converse directions between the liquid and gas phases, these ΔG_{solv} results are in agreement with the ΔH_{vap} results discussed above. We note that the effect of k_b on ΔG_{solv} is practically negligible in these systems.

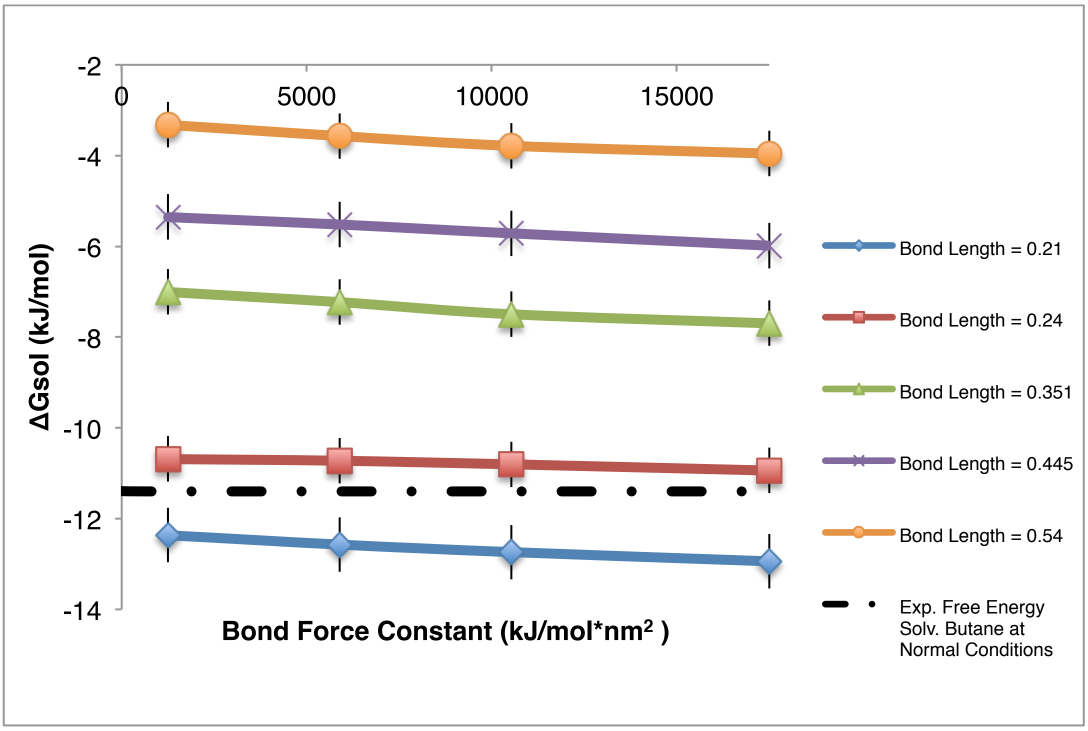
-2
-4
-6
-8
-10
-12
-14
0
5000
10000
15000
ΔGsol (kJ/mol)
Bond Force Constant (kJ/mol*nm^2)
Bond Length = 0.21
Bond Length = 0.24
Bond Length = 0.351
Bond Length = 0.445
Bond Length = 0.54
Exp. Free Energy Solv. Butane at Normal Conditions

a)

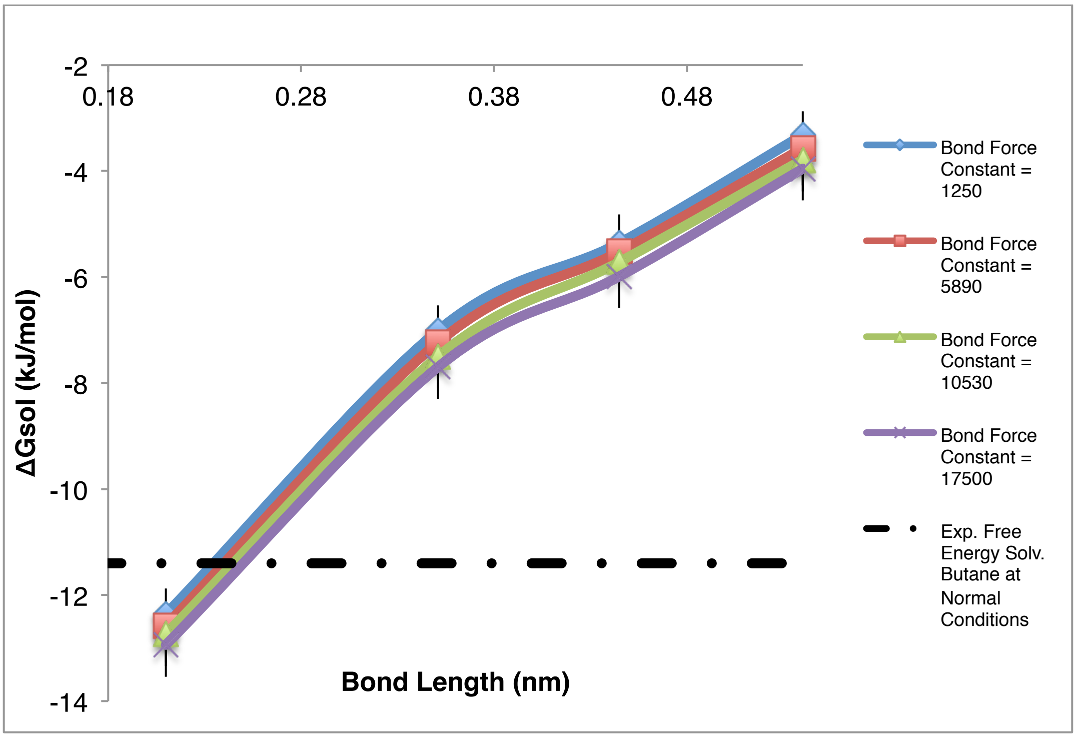

b)

Figures 4.16a-b: Selected self-solvation free energies of the 2-bead solvent systems for different values of the bond length and bond force constant parameters: **a)** selected bond lengths at different bond force constants, and **b)** bond force constants at different bond length values. The black dashed line represents the experimental reference values for butane at room temperature.[46, 47, 51]

Based on the above results, we have determined the optimal (r_0, k_b) parameters by finding the intersection of the lines corresponding to ρ, ΔH_{vap}, and ΔG_{solv}, as shown in the graphical representation of this mapping scheme for the 2:1 mapping in **Figure 4.17**. The other graphical representations for 3:1, 4:1, and 5:1 bead mapping matching

2-bead parameters can again be found in **Figures 4.42**, **4.46**, and **4.50** in **Appendix A**.

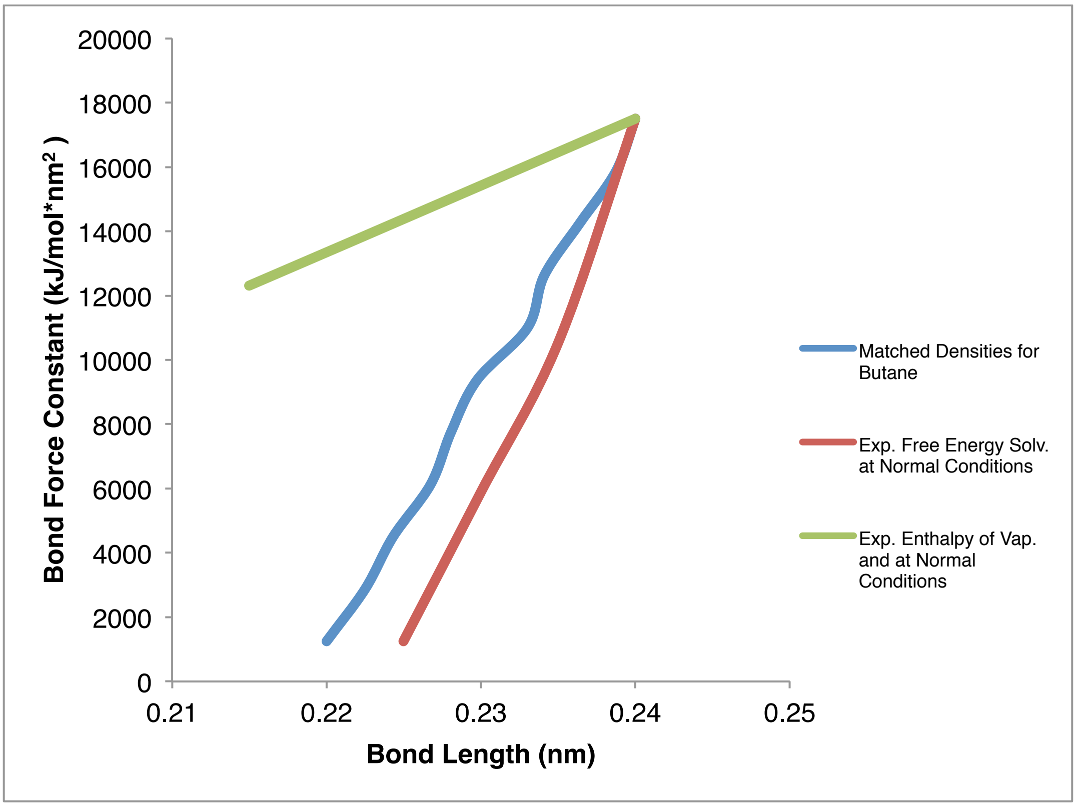

Figure 4.17: Determination of optimal set of parameters for 2:1 mapped 2-bead models. The full lines show each property at standard temperature and pressure: density (blue), free energy of self-solvation (red), and enthalpy of vaporisation (green).[52, 53]

4.2.2.3 Angle bending parameters (θ, k_θ)

Using the optimal values of σ, ε, r_0, and k_b for each mapping scheme, we proceeded to determine θ and k_θ, as shown in the third step of **Figure 4.2**. Selected adjusted ρ for the 3-bead model simulations representing hexane (i.e. 2:1 mapping) can be seen in **Figures 4.18a-b**. As before, selected ρ results representing nonane (i.e. 3:1 mapping), dodecane (i.e. 4:1 mapping), and pentadecane (i.e. 5:1 mapping) can be found in **Figures 4.51a-b**, **4.55a-b**, and **4.59a-b** in **Appendix A**. The chosen adjusted density of the 3-bead model simulations is shown here to decrease non-linearly with increased θ and increase non-linearly with k_θ*.* The results adhered to expected theory, as increasing bond angles create a decrease in bond strength, which leads to less efficient packing of molecules and causes a decrease in the density, and the increase in the bond angle strength causes an increase in the molecular energy and, through facilitated packing of more rigid molecules, an overall increase in ρ.[3, 48, 62, 72, 74]

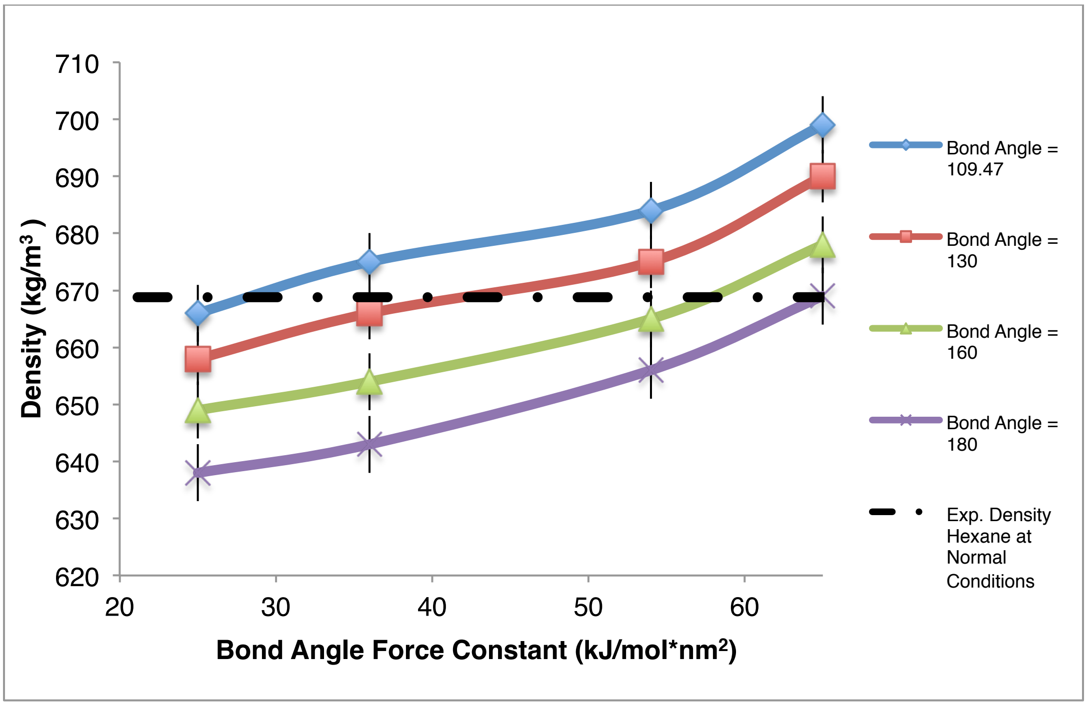
Density (kg/m³)
710
700
690
680
670
660
650
640
630
620
20
30
40
50
60
Bond Angle Force Constant (kJ/mol*nm²)
Bond Angle = 109.47
Bond Angle = 130
Bond Angle = 160
Bond Angle = 180
Exp. Density Hexane at Normal Conditions

a)

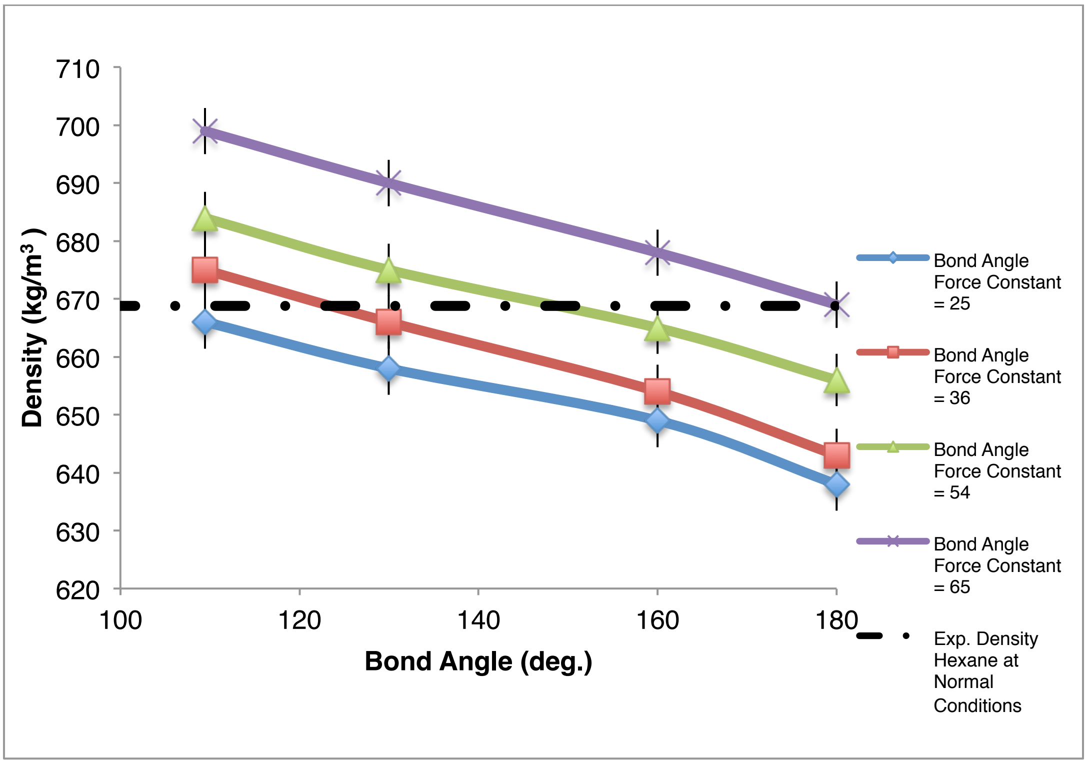

b)

Figures 4.18a-b: Selected densities determined for hexane's molecular weight, of the 3-bead solvent systems for different values of the bond angle and bond angle force constant parameters: **a)** selected bond angles at different bond force constants, and **b)** bond angle force constants at different bond length values. The black dashed line represents the experimental reference values for hexane at room temperature.[52, 53]

Figures 4.19a-b show ΔH_{vap} results for the 3-bead model simulations representing hexane (i.e. 2:1 mapping), with those representing nonane (i.e. 3:1 mapping), dodecane (i.e. 4:1 mapping), and pentadecane (i.e. 5:1 mapping) available in **Figures 4.52a-b**, **4.56a-b**, and **4.60a-b** in **Appendix A**. The enthalpy of vaporisation results of these chosen 2-bead simulations is shown here to decrease non-linearly with θ and increase non-linearly with increasing kθ. This was expected with theory, due to the previously mentioned decrease in bond strength with increasing bond angles leading to a less efficient packing of molecules and decrease in ΔH_{vap}, and the increase in molecular energy caused by the bond angle strength leading to an increase in ΔH_{vap}.[48, 62, 72, 74, 83, 84]

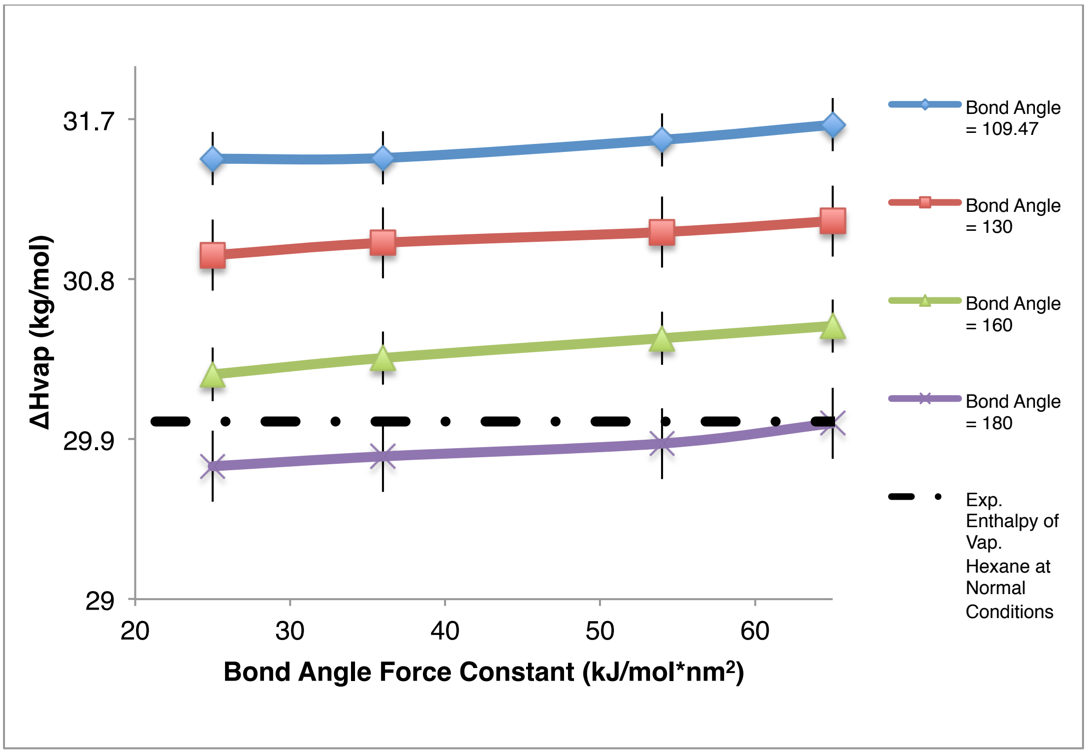

a)

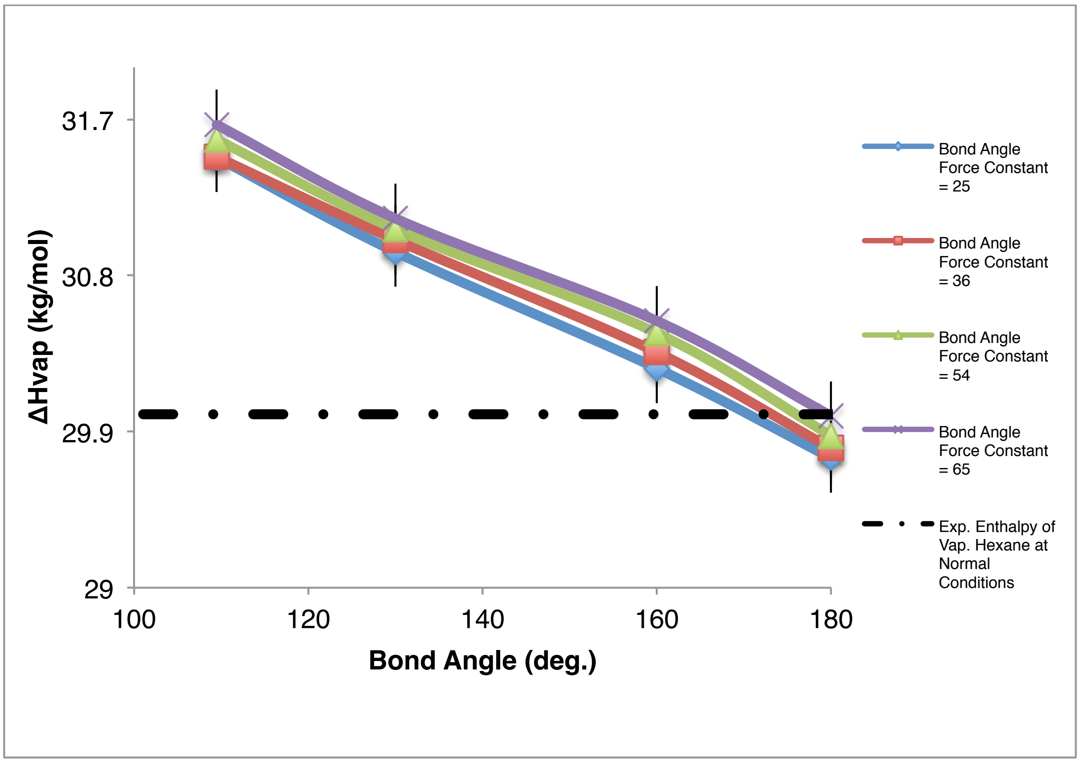

b)

Figures 4.19a-b: Selected enthalpies of vaporization of the 3-bead solvent systems for different values of the bond angle and bond angle force constant parameters: **a)** selected bond angles at different bond angle force constants, and **b)** bond angle force constants at different bond angle values. The black dashed line represents the experimental reference values for hexane at room temperature.[48, 49, 50]

In **Figures 4.20a-b**, selected self-solvation free energy of 3-bead model simulations representing hexane (i.e. 2:1 mapping), are shown to increase non-linearly with increasing θ, while slightly decreasing linearly with increasing kθ. Selected ΔG_{solv} results from 3-bead model simulations representing nonane (i.e. 3:1 mapping), dodecane (i.e. 4:1 mapping), and pentadecane (i.e. 5:1 mapping) can be found in **Figures 4.53a-b**, **4.57a-b**, and **4.61a-b** in **Appendix A**. These ΔG_{solv} results are again in-line with theory, as the aforementioned decrease in bond strength with increasing bond angles produces an increase in ΔG_{solv} (i.e. the ΔG_{solv} becomes more positive or unfavourable), and the increased molecular energy created from the increased bond angle force constant producing a decrease in free energy (i.e. the ΔG_{solv} becomes more negative or favourable).[48, 62, 72, 74, 79] The free energies are also again in agreement with what can be predicted from the ΔH_{vap} results. We note again that both ΔH_{vap} and ΔG_{solv} are mainly independent of kθ.

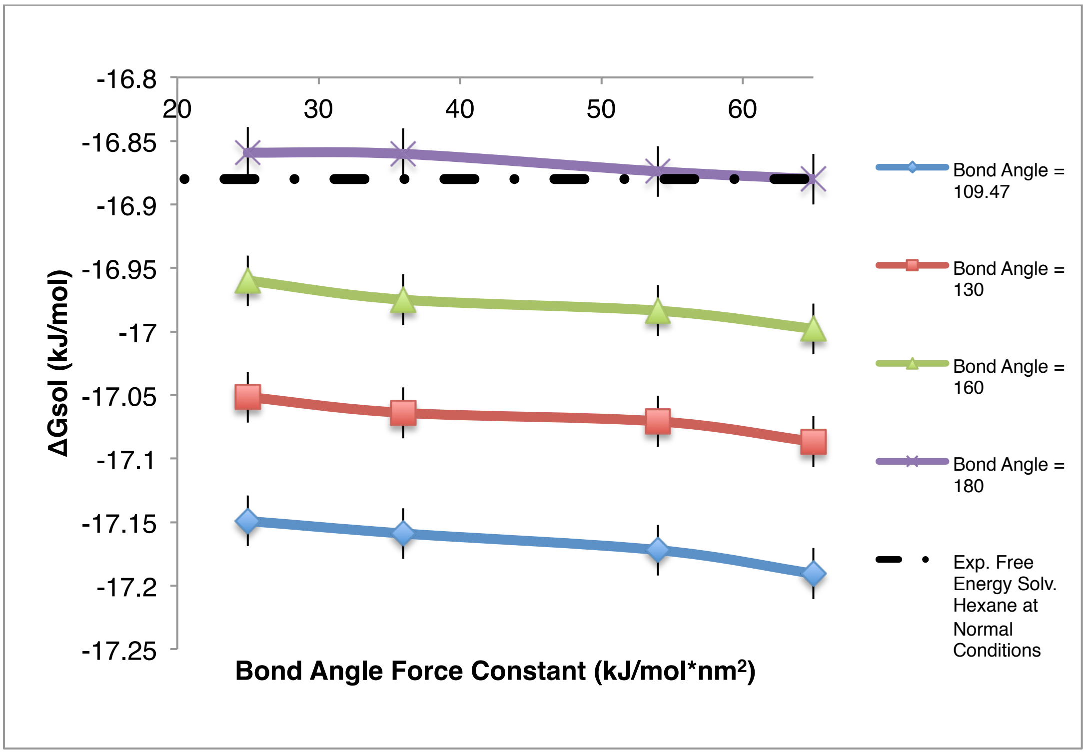
-16.8
-16.85
-16.9
-16.95
-17
-17.05
-17.1
-17.15
-17.2
-17.25
20
30
40
50
60
ΔGsol (kJ/mol)
Bond Angle Force Constant (kJ/mol*nm2)
Bond Angle = 109.47
Bond Angle = 130
Bond Angle = 160
Bond Angle = 180
Exp. Free Energy Solv. Hexane at Normal Conditions

a)

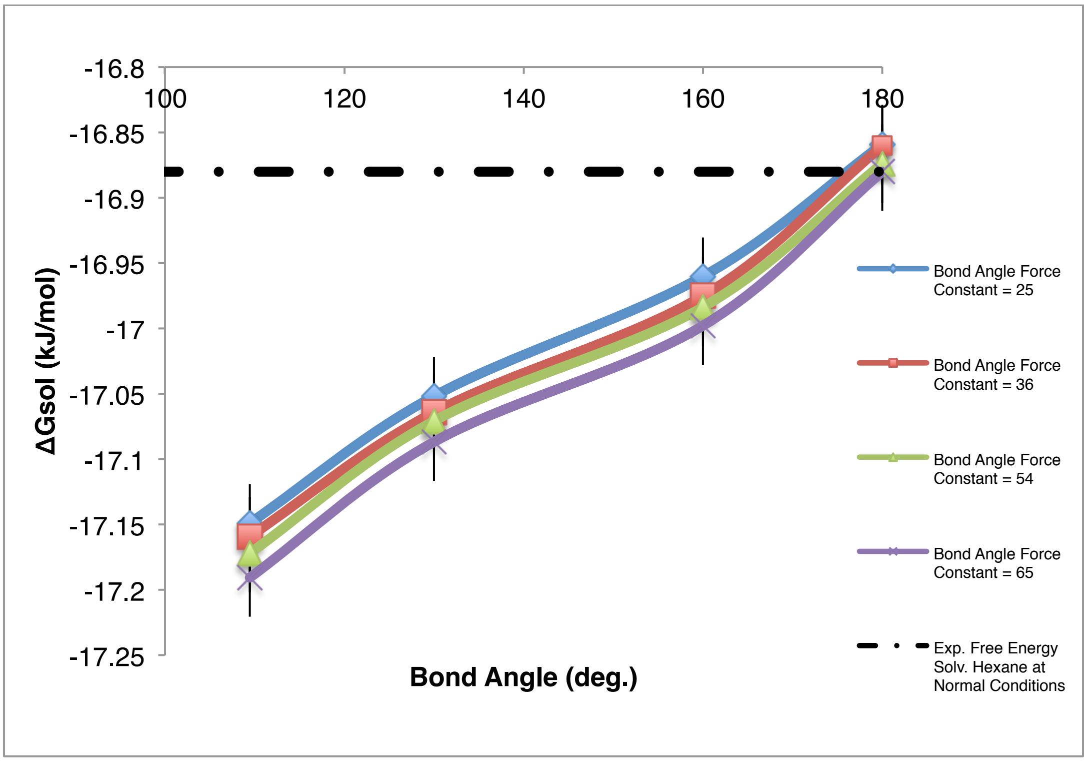

b)

Figures 4.20a-b: Selected self-solvation free energies of the 3-bead solvent systems for different values of the bond length and bond force constant parameters: **a)** selected bond lengths at different bond force constants, and **b)** bond force constants at different bond length values. The black dashed line represents the experimental reference values for hexane at room temperature.[46, 47, 51]

Using the same graphical procedure as used previously, we found the optimal (θ, kθ) pairs of parameters for each mapping scheme. The graphical representation of the parameterisation of the most applicable parameters for the 2:1 mapping of 3-bead simulations can be seen in **Figure 4.21**, the graphical representations for 3:1, 4:1, and 5:1 bead mapping matching 3-bead parameters can again be found in **Figures 4.54**, **4.58**, and **4.62** in **Appendix A**

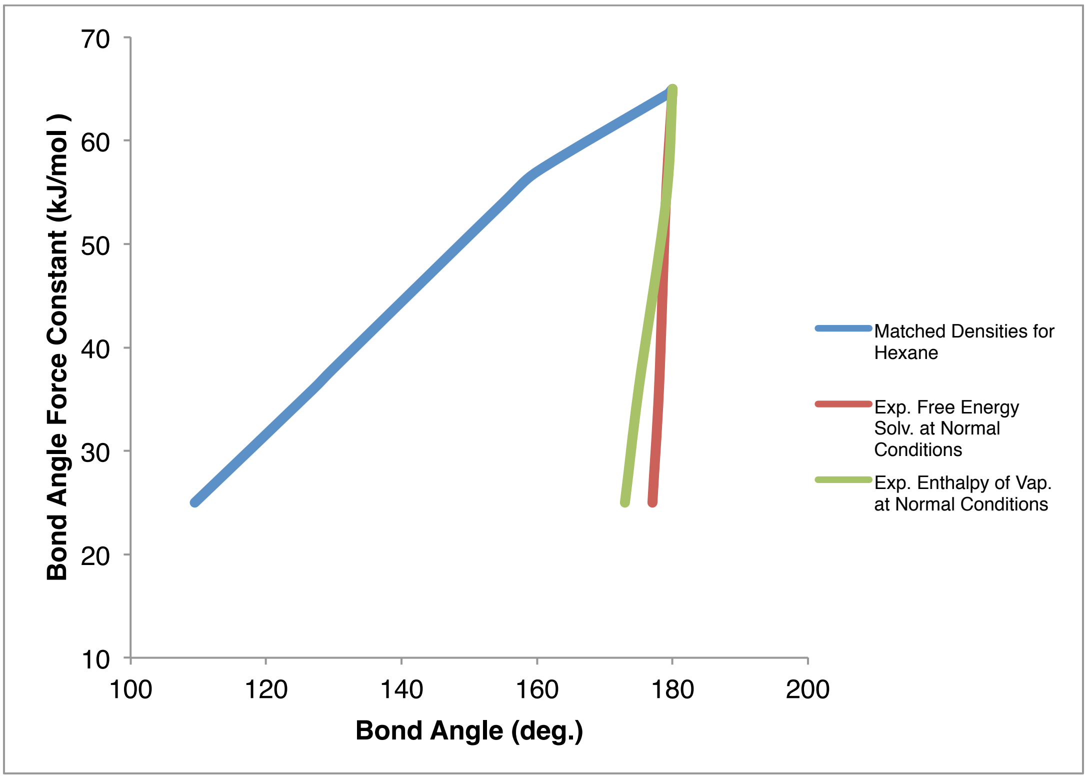

c)

Figure 4.21: Determination of optimal set of parameters for 2:1 mapped 3-bead models. The full lines show each property at standard temperature and pressure: density (blue), free energy of self-solvation (red), and enthalpy of vaporisation (green).[52, 53]

4.2.2.4 Dihedral torsion parameters (Φ, kΦ)

The adjusted density, enthalpy of vaporisation, and free energy of self-solvation results for the 4-bead models, without dihedral angles and dihedral angle force constants, in comparison with experimental results can be seen in **Tables 4.8a-c**.[46-51] Dihedral angles and dihedral force constants were found to have a negligible effect on the overall properties, and were thus omitted from the final models. The increase in the density and enthalpy of vaporisation properties between mapping sizes (i.e. 2:1, 3:1, 4:1, and 5:1 mapping) can be attributed to the increased mapping, but also most directly to the increased σ and ε between the 2:1, 3:1, 4:1, and 5:1 mapping in each system.[83, 84] The same factors create a decrease in the solvation free energies (i.e. they are made more favourable).[83, 84]

Mapping Scheme	**4-Bead CG Alkane Models**	**Density (this study, kg/m^3)**	**Density (experimental[52, 53], kg/m^3)**
2:1	Octane (C8H18)	689.58 ± 3.81	692
3:1	Dodecane (C12H26)	747.53 ± 4.79	750
4:1	Hexacane (C16H34)	766.64 ± 4.87	770
5:1	Eicosane (C20H42)	784.52 ± 4.64	789

a)

Mapping Scheme	**4-Bead CG Alkane Models**	**ΔHvap (this study, kJ/mol)**	**ΔHvap (experimental[48, 49, 50], kJ/mol)**
2:1	Octane (C8H18)	39.8 ± 0.65	41
3:1	Dodecane (C12H26)	60.58 ± 0.69	61
4:1	Hexacane (C16H34)	78.85 ± 0.72	80.6
5:1	Eicosane (C20H42)	87.89 ± 0.79	100.1

b)

Mapping Scheme	**4-Bead CG Alkane Models**	**ΔGsol (this study, kJ/mol)**	**ΔGsol (experimental[46, 47, 51], kJ/mol)**
2:1	Octane (C8H18)	-22.34 ± 0.78	-22.1
3:1	Dodecane (C12H26)	-32.12 ± 0.69	-31.23
4:1	Hexacane (C16H34)	-43.91 ± 0.82	-43.96
5:1	Eicosane (C20H42)	-59.88 ± 0.77	-60.21

c)

Tables 4.8a-c: The 4-bead models', without dihedral angles of dihedral angle force constants, properties for **a)** matched densities, **b)** enthalpies of vaporisation, and **c)** free energies of self-solvation, compared to experimental data.[46, 47, 48, 49, 50, 51, 52, 53]

4.2.3 Validation of new alkane model parameters

Tables 4.9a-c show the optimal parameters for each of the 1-bead, 2-

bead, and 3-bead models, matched to ρ, $\Delta\mathrm{H}_{\mathrm{vap}}$, and $\Delta\mathrm{G}_{\mathrm{solv}}$ for selected alkanes. While we have not parameterised a model with 1:1 mapping, our results can be compared to a united-atom model of methane, parameterised to the same set of experimental properties; $\sigma = 0.371$ nm and $\varepsilon = 1.2$ kJ/mol.[55] The parameters for 2:1, 3:1, 4:1, and 5:1 mapping in the 1-bead simulations follow the trend of increasing σ and ε with an increase in the number of carbons each bead represents, as seen in **Table 4.9a**. The resulting 1-bead 5:1 LJ parameters in particular are only slightly lower than the MARTINI standard.[28]

The r_0 and k_b parameter pairs for the 2-bead models that produced the closest equivalents to known alkanes for the 2:1, 3:1, 4:1, and 5:1 mapping models are shown in **Table 4.9b**. The best matches for the r_0 for all mappings (i.e. 2:1, 3:1, 4:1, and 5:1) were found to be only slightly higher than experimental lengths for alkanes[40, 43, 46, 56, 61, 62, 63], while k_b was found to produce the best results when kept at the higher values tested[40, 43, 46, 56, 61, 62, 63], rather than the much lower k_b standard in the current MARTINI force field.[28] This difference between experimental parameters and our matched r_0 lengths is most likely due to the larger size needed for a CG bead to represent both heavy atoms and hydrogens in comparison to the real molecules they are mapping.[83] The values of r_0 follow a much steeper increasing trend with number of carbons per bead than the LJ σ. In fact, for the 5:1 mapping, $\sigma < r_0$, which is somewhat unphysical.

This suggests we may be reaching the limit of accuracy of this modeling approach.

The best equivalent values for the resulting 2:1, 3:1, 4:1, and 5:1 mapped models in the 3-bead simulations can be seen in **Table 4.9c**. The θ results that provided the most accurate matches to experimental data for real alkanes were much higher than MARTINI values[28], as opposed to the fairly low experimental values.[40, 43, 46, 56, 61, 62, 63] This can again be attributed to the inherently larger size of the CG beads, meaning a greater degree of θ may be needed to represent the molecules they are mapping.[83] The k_θ however were found to produce the best results when kept at the higher values of 65 kJ/mol.[40, 43, 46, 56, 61, 62, 63]

The best corresponding values for the 4-bead models at 2:1, 3:1, 4:1, and 5:1 mapping were produced through the exclusion of dihedral angles or dihedral force constants, so the 4-bead models and beyond are specified by the set of parameters in **Tables 4.9a-c**.

It is also important to note that the parameters of our alkane models were optimised to match properties at room temperature, and it is therefore not evident that these parameters are necessarily transferrable to different temperatures.

Mapping Scheme	**1-Bead CG Alkane Models**	**σ (nm)**	**ε (kJ/mol)**
2:1	Ethane (C_2H_6)	0.405	2.05
3:1	Propane (C_3H_8)	0.42	2.5
4:1	Butane (C_4H_{10})	0.445	2.8
5:1	Pentane (C_5H_{12})	0.46	3.3

a)

Mapping Scheme	**2-Bead CG Alkane Models**	**r_0 (nm)**	**k_b (kJ/mol*nm^2)**
2:1	Butane (C_4H_{10})	0.24	17500
3:1	Hexane (C_6H_{14})	0.335	17500
4:1	Octane (C_8H_{18})	0.44	17500
5:1	Decane ($C_{10}H_{22}$)	0.54	17500

b)

Mapping Scheme	**3-Bead CG Alkane Models**	**θ (deg.)**	**k_θ (kJ/mol)**
2:1	Hexane (C_6H_{14})	180	65
3:1	Nonane (C_9H_{20})	180	65
4:1	Dodecane ($C_{12}H_{26}$)	180	65
5:1	Pentadecane ($C_{15}H_{32}$)	180	65

c)

Tables 4.9a-c: a) Lennard-Jones parameters for 1-bead solvent systems and their corresponding alkanes, **b)** bond length parameters for 2-bead solvent systems and their corresponding alkanes, and **c)** bond angle parameters for 3-bead solvent systems and their corresponding alkanes. As the 4-bead solvent systems were optimised without torsion angle parameters, they are thusly excluded here, and only the previous parameters were used.

It is also important to note that we were not able to match experimental

ΔH_{vap} for the 5:1 mapping scheme with any set of tested bonded parameters, as can be seen in **Figures 4.11a-b,** and **Figures 4.48a-b** and **4.60a-b** in **Appendix A**. This, together with the somewhat unphysical bond lengths discussed above, ascribes a low degree of confidence in our 5:1 mapped model.

4.2.3.1 Density

Figures 4.22a-d show an increasing trend in ρ with increasing level of mapping for all of the solvent simulation systems (i.e. 2:1, 3:1, 4:1, and 5:1 mapped 1-bead, 2-bead, 3-bead, and 4-bead systems) in comparison with both experimental and standard MARTINI results for their particular alkane representations.[28, 52, 53] A complete table of all model's ρ results compared to experimental values is available in **Table 4.12** in **Appendix A**. This increase between the 1-bead, 2-bead, 3-bead, and 4-bead models, and between the 2:1, 3:1, 4:1, and 5:1 mapping in each system, is expected, due to the changes in parameters discussed above, and in particular the increasing molecular energy from the increased σ and ε.[3, 48, 62, 72, 74, 83] Increasing r0 with increasing mapping levels in each system to match experimental values allowed the best agreement in the 2-bead models, while increasing the bond angle from the MARTINI standard and maintaining the experimental angle force constant led to the best agreement in the 3-bead models.[28, 40, 43, 61] This was due to the increase in the molecule energy with the increasing bond and angle force constants in the parameters, as the increase in r_0 was negligible between mapping levels and θ was kept constant between mapping levels.[3, 40, 43, 61, 62, 74] Dihedral angles and dihedral force constants were also found to have no significant contribution to the overall ρ of the 4-bead models, possibly because of the smaller chain lengths of our CG models and the minimal effects dihedrals have on them, and were thus omitted from our models.[40, 43, 61]

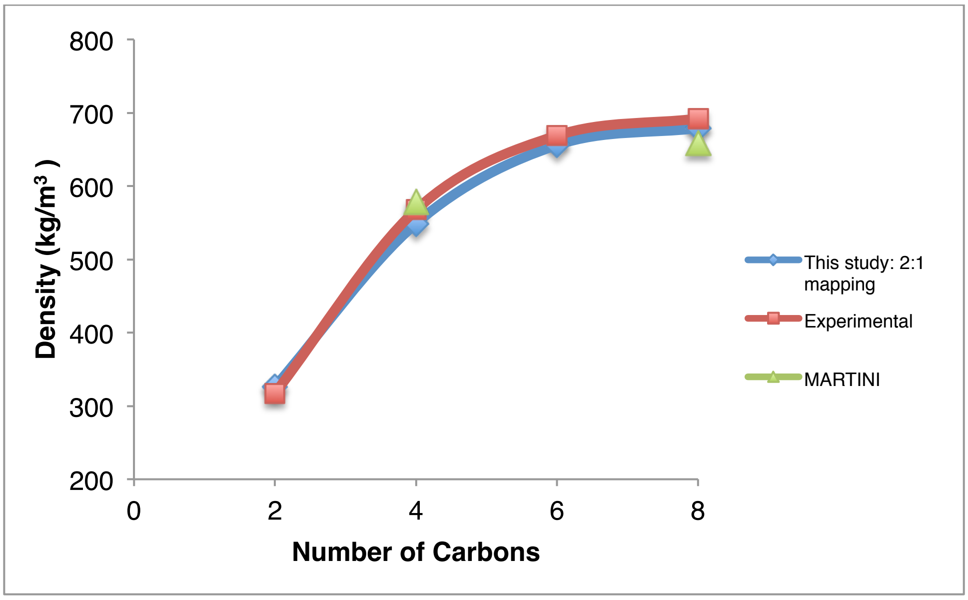

a)

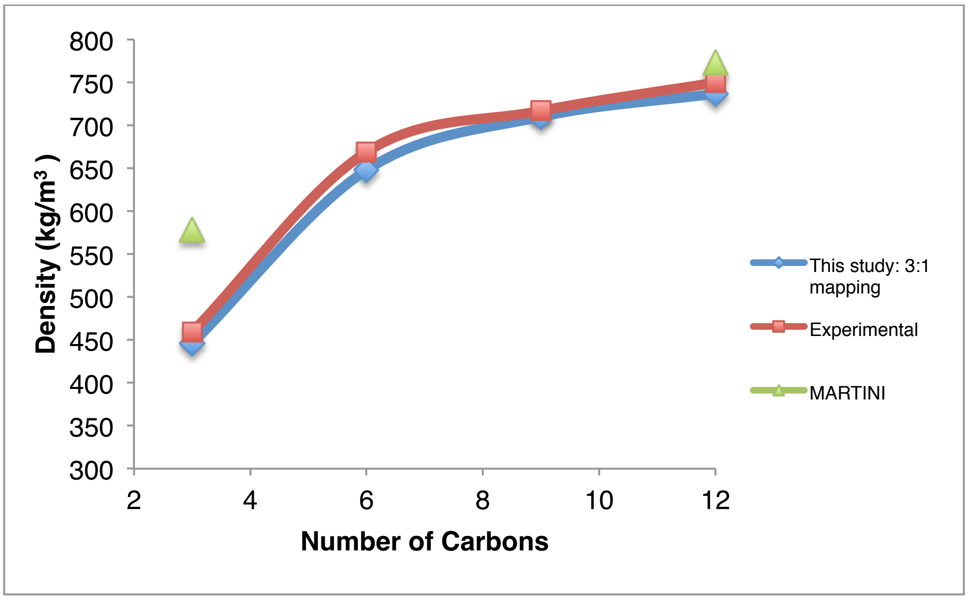
Density (kg/m³)
800
750
700
650
600
550
500
450
400
350
300
2
4
6
8
10
12
Number of Carbons
This study: 3:1 mapping
Experimental
MARTINI

b)

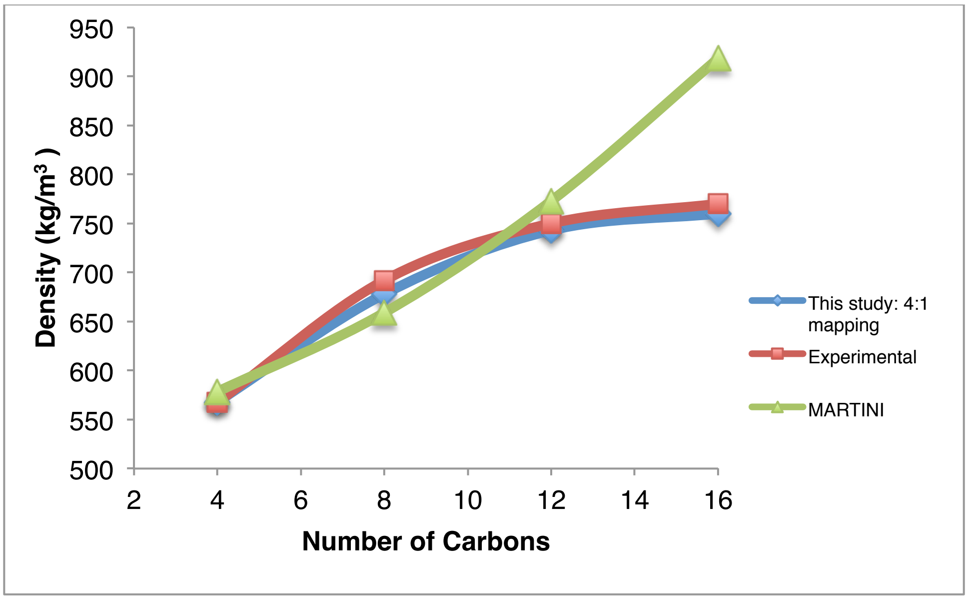
Density (kg/m³)
950
900
850
800
750
700
650
600
550
500
2
4
6
8
10
12
14
16
Number of Carbons
This study: 4:1 mapping
Experimental
MARTINI

c)

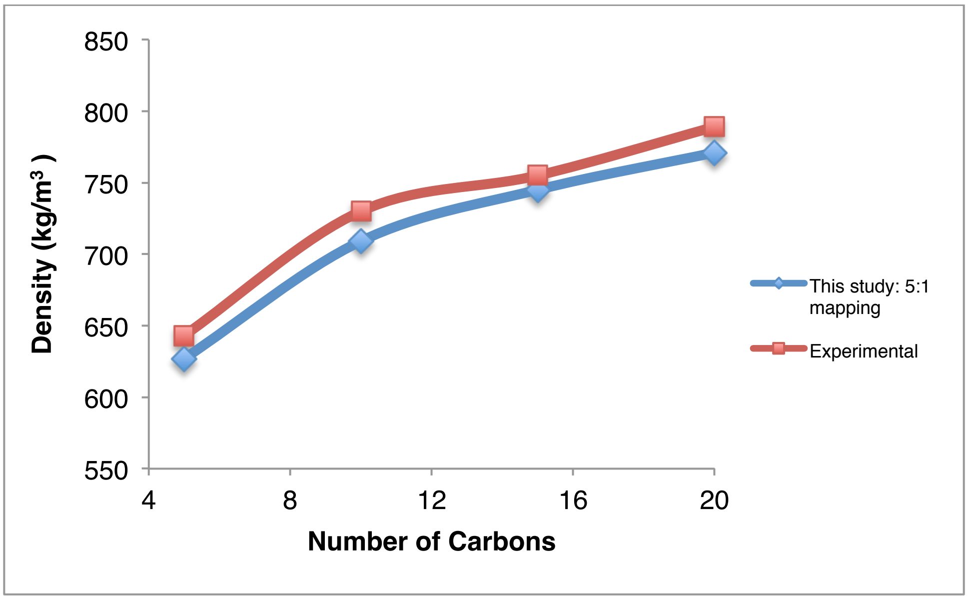

d)

Figures 4.22a-d: Comparison between this study's model for linear alkanes, the alkanes explicitly covered by MARTINI, and experimental data for linear alkane densities (i.e., ethane, propane, butane, and pentane for the 1-bead systems, butane, hexane, octane, and decane for the 2-bead systems, etc.) for our 1-bead, 2-bead, 3-bead, and 4-bead systems for our **a)** 2:1 bead mapping, **b)** 3:1 bead mapping, **c)** 4:1 bead mapping, and **d)** 5:1 bead mapping.[28, 52, 53]

As seen in ρ **Figures 4.22a-d**, our models fit well within margins of error for experimental values of density, which indicates they are fitted satisfactorily in regards to ρ.[52, 53] This is another promising factor in validating our models for alkanes.

4.2.3.2 Enthalpy of vaporisation

Increasing ΔH_{vap} trends can be seen in the final 2:1, 3:1, 4:1, and 5:1 mapped 1-bead, 2-bead, 3-bead, and 4-bead model results in **Figures 4.23a-d**, in comparison with both experimental and standard MARTINI results for their particular alkane representations. Again a complete table of all model's ΔH_{vap} results compared to experimental values is shown in **Table 4.13** in **Appendix A**. As previously discussed, a decrease in enthalpy of vaporisation occurs with increasing inter- and intramolecular energies.[48, 62, 74] The σ and ε provide the greatest contribution to the ΔH_{vap} here, but the bond and angle properties also played a part.[40, 43, 55] While increasing r0 causes ΔH_{vap} to decrease and increasing kb and kθ cause ΔH_{vap} to increase, the increased number of beads between the 1-bead, 2-bead, 3-bead, and 4-bead models, and the increased σ and ε between the 2:1, 3:1, 4:1, and 5:1 mapping in each system, creates an increase in the overall molecular energy of the models.[83, 84] This causes the increasing trend between 2:1, 3:1, 4:1, and 5:1 mapped models in each system. Keeping bond lengths between the beads and bond force constants near theoretical experimental values for alkane lead to the best agreement in the 2-bead models, while increasing the bond angle to the MARTINI standard and maintaining the experimental angle force constant led to the best agreement in the 3-bead models.[28, 40, 43, 55] As the θ and kθ were kept constant between all 2:1, 3:1, 4:1, and 5:1 mapped models, the increase in ΔH_{vap} between them and the 1-

bead, 2-bead, 3-bead, and 4-bead models can most likely be attributed to the increase in molecular energy from the previous parameters, and the increasing number of beads.[83, 84] Dihedral angles and dihedral force constants, however, were found to be negligible to the overall of the 4-bead models, and were thus excluded.[40, 43, 55] This is again potentially due to the smaller chain lengths of our smaller CG models and the minimal effects dihedrals have on their formation and chain length.

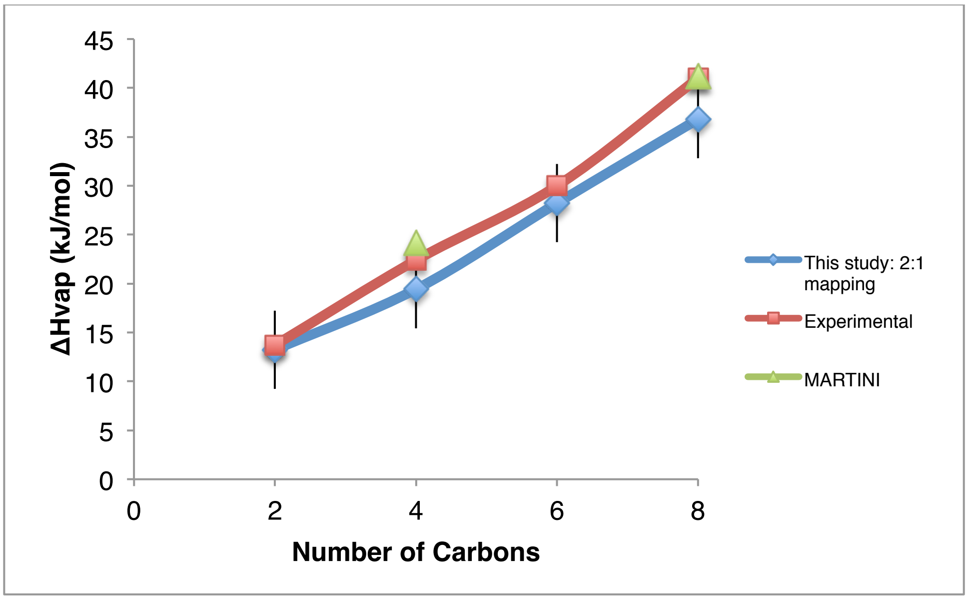

a)

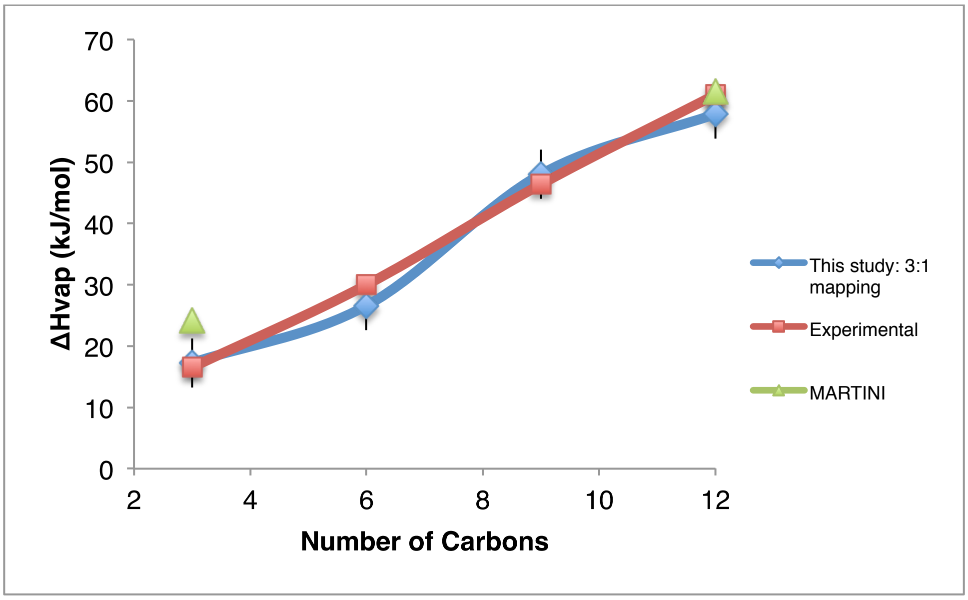
ΔHvap (kJ/mol)
70
60
50
40
30
20
10
0
2
4
6
8
10
12
Number of Carbons
This study: 3:1 mapping
Experimental
MARTINI

b)

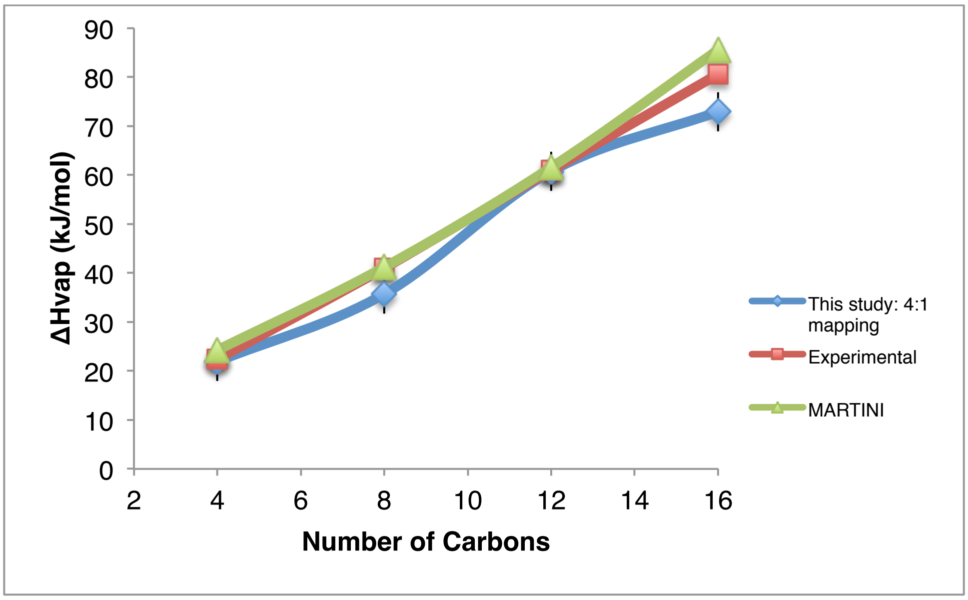
ΔHvap (kJ/mol)
90
80
70
60
50
40
30
20
10
0
2
4
6
8
10
12
14
16
Number of Carbons
This study: 4:1 mapping
Experimental
MARTINI

c)

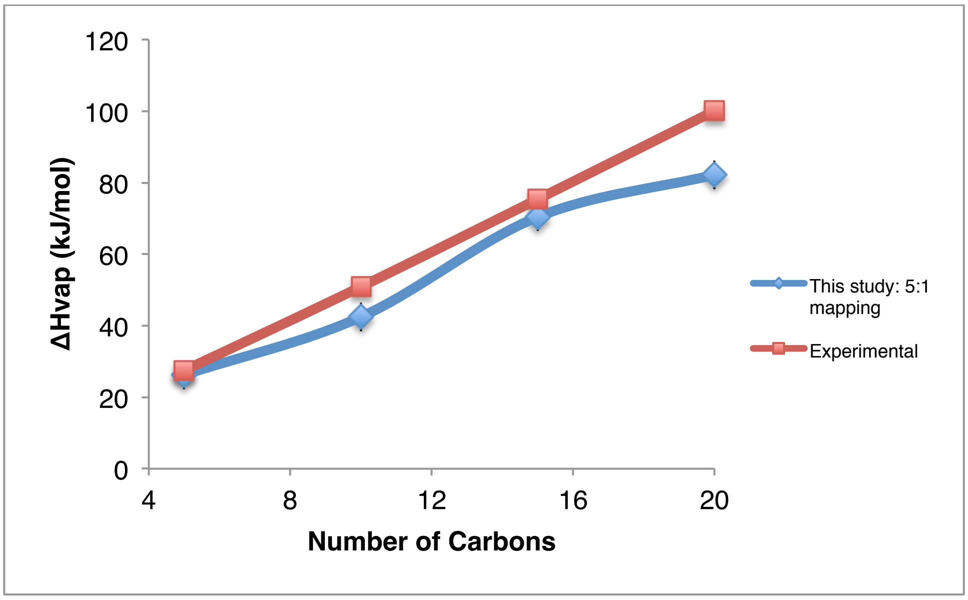

d)

Figures 4.23a-d: Comparison between this study's model for linear alkanes, the alkanes explicitly covered by MARTINI, and experimental data for linear alkane enthalpies of vaporisation (i.e., ethane, propane, butane, and pentane for the 1-bead systems, butane, hexane, octane, and decane for the 2-bead systems, etc) for our 1-bead, 2-bead, 3-bead, and 4-bead systems for our **a)** 2:1 bead mapping, **b)** 3:1 bead mapping, **c)** 4:1 bead mapping, and **d)** 5:1 bead mapping. [28, 48, 49, 50]

While the majority of our models fit with the margin of errors for $\Delta\mathrm{H}_{\mathrm{vap}}$ of known alkane models, there are some notable exceptions. While all of our bead models seem to follow similar increasing trend, our 2-bead 4:1 and 5:1 mapped models (i.e. representing octane and decade), and

4-bead 3:1 dodecane models are significantly lower than their respective experimental values.[48, 49, 50] This could be because ΔH_{vap}, as explained in a previous section, is inversely related in sign to ΔG_{solv}, and that while the given LJ parameters do give very well-matched ΔG_{solv}, the change between them in our models does not match the experimental molecular energy change needed to match enthalpies of vaporisation.[48, 49, 50]

4.2.3.3 Self-solvation free energy

An decreasing trend in free energy of self-solvation can be seen in the 2:1, 3:1, 4:1, and 5:1 mapped models from the 1-bead, 2-bead, 3-bead, and 4-bead system simulations, shown in **Figures 4.24a-d**, in comparison with both experimental and standard MARTINI results for their respective alkane representations. A comprehensive table of all model's ΔG_{solv} results in comparison to experimental values can be found in **Table 4.14** in **Appendix A**. While k_b and k_θ do cause a decrease, or favourable, change in ΔG_{solv} in each 1-bead, 2-bead, and 3-bead system, they are negligible in variance between the 2:1, 3:1, 4:1, and 5:1 mapped models, and the difference in bond lengths and bond angles can contribute in a greater way to an increased, or unfavourable, change in ΔG_{solv}.[40, 43, 47, 62, 72, 73] Changing the bond and bond angle force constants from MARTINI's values to the much higher theoretical parameters therefore helped to match the free energies of our models to within experimental values.[47, 62, 72, 73] While bond and angle force constants had negligible effect on ΔG_{solv}, due to their importance on other properties explained in further detail later, they were optimised at experimental values for their force constants.[47, 62, 72, 73] As with our density and enthalpy of vaporisation matching, the 4-bead models had the best results by excluding dihedrals, possibly because their formation and chain length would only allow for minimal dihedral effects in these smaller CG chains.[40, 43, 55]

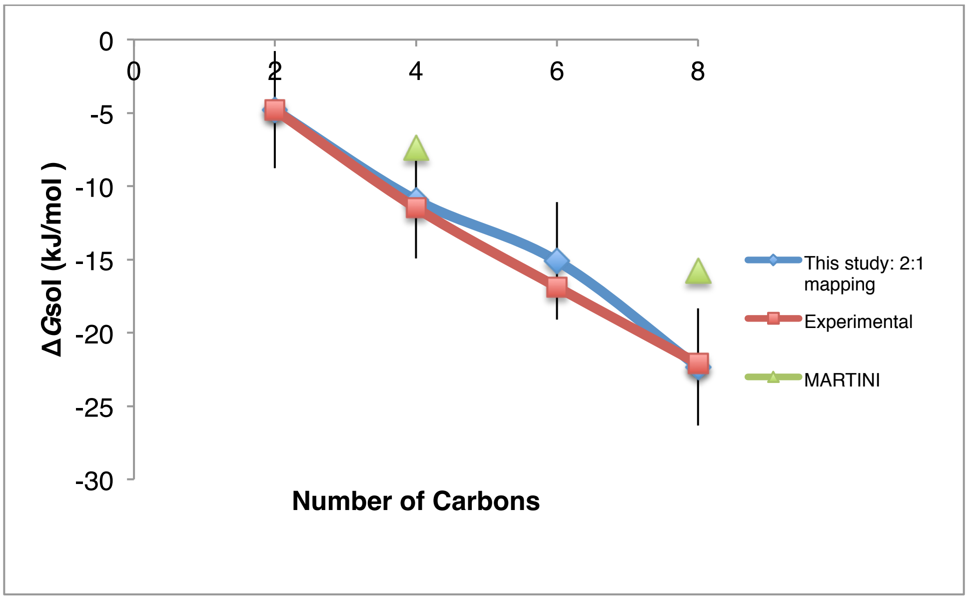

a)

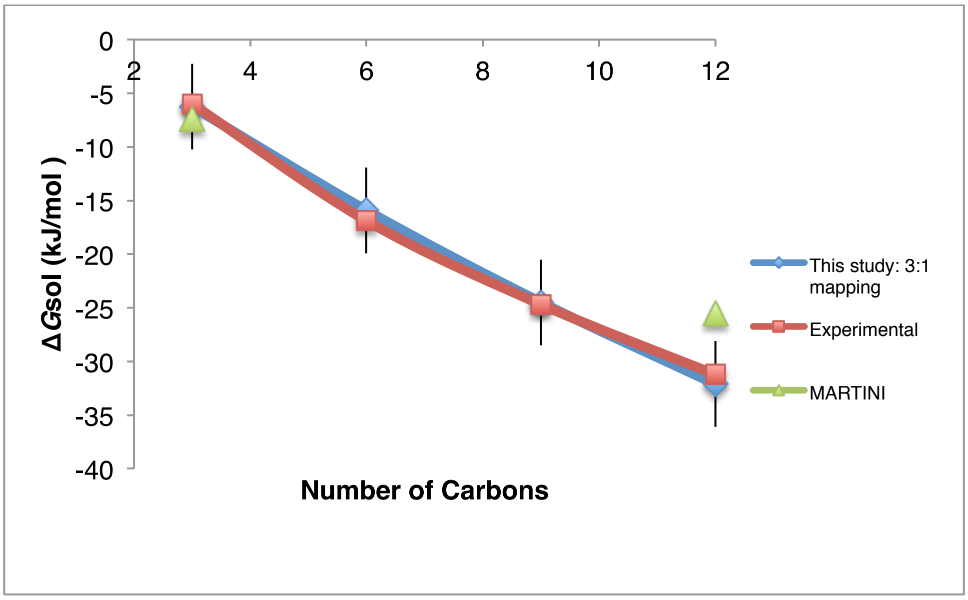
0
-5
-10
-15
-20
-25
-30
-35
-40
2
4
6
8
10
12
ΔGsol (kJ/mol)
Number of Carbons
This study: 3:1 mapping
Experimental
MARTINI

b)

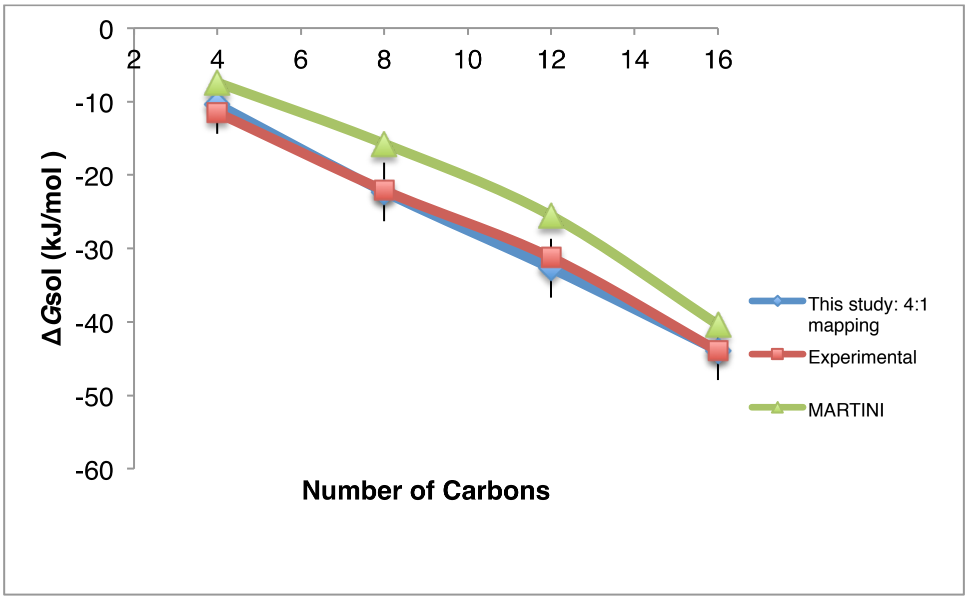
0
-10
-20
-30
-40
-50
-60
2
4
6
8
10
12
14
16
ΔGsol (kJ/mol)
Number of Carbons
This study: 4:1 mapping
Experimental
MARTINI

c)

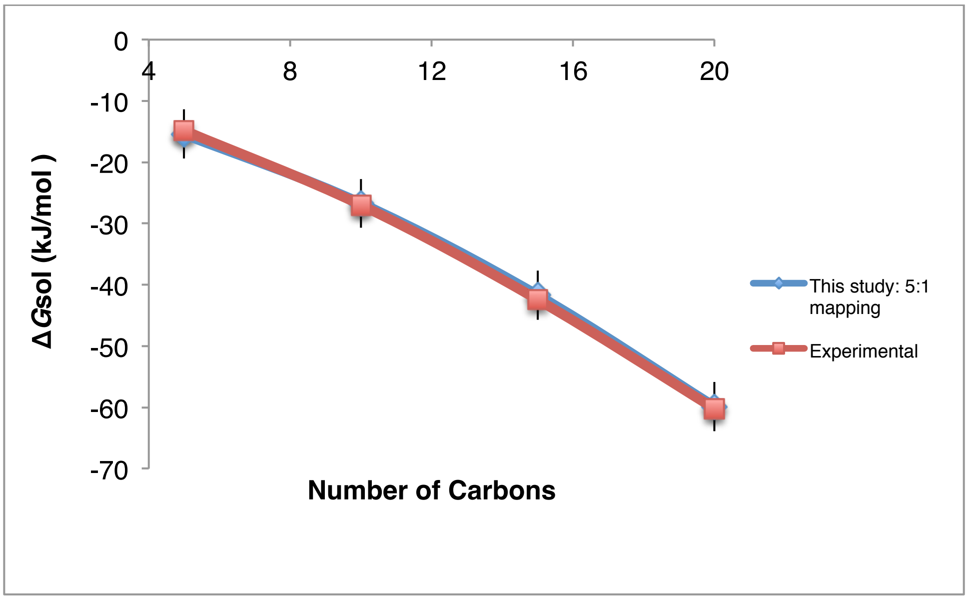

d)

Figures 4.24a-d: Comparison between this study's model for linear alkanes, the alkanes explicitly covered by MARTINI, and experimental data for linear alkane self-solvation free energies (i.e., ethane, propane, butane, and pentane for the 1-bead systems, butane, hexane, octane, and decane for the 2-bead systems, etc) for our 1-bead, 2-bead, 3-bead, and 4-bead systems for our **a)** 2:1 bead mapping, **b)** 3:1 bead mapping, **c)** 4:1 bead mapping, and **d)** 5:1 bead mapping.[28, 46, 47, 51]

In comparison with experimental values, our models fit well within margins of error for experimental values, as shown in **Figures 4.24a-d**, which indicates they are well matched in regards to ΔG_{solv} of self-solvation. This is promising, as ΔG_{solv} is an important property in the context of self-assembly simulations.[46, 47, 51]

4.2.3.4 Self-diffusion coefficient

Figures 4.25a-d show the decreasing trend of self-diffusion coefficients of each subsequent parameterisation of the 2:1, 3:1, 4:1, and 5:1 mapped 1-bead, 2-bead, 3-bead, and 4-bead systems in comparison with available experimental results. A complete table of these results for all bead systems and mapping schemes compared to experimental values is available in **Table 4.15** in **Appendix A**. As mentioned before, self-diffusion coefficients exhibit a strong dependence on the number of particles in the simulated system.[75, 76, 78, 79] The simulations were thus kept at the same number of particles and model for every bead type (i.e. 1-bead simulations were kept at one size, 2-bead another, etc), as these models lead to density near experimental values.[52, 53, 75, 76] Our self-diffusion results lie within the margin of error for the known experimental values of alkanes, as well as following increasing theoretical trend, helping to further validate our optimised parameters.[54] In particular, our model shows a marked improvement over the original MARTINI parameters, which strongly underestimated D.

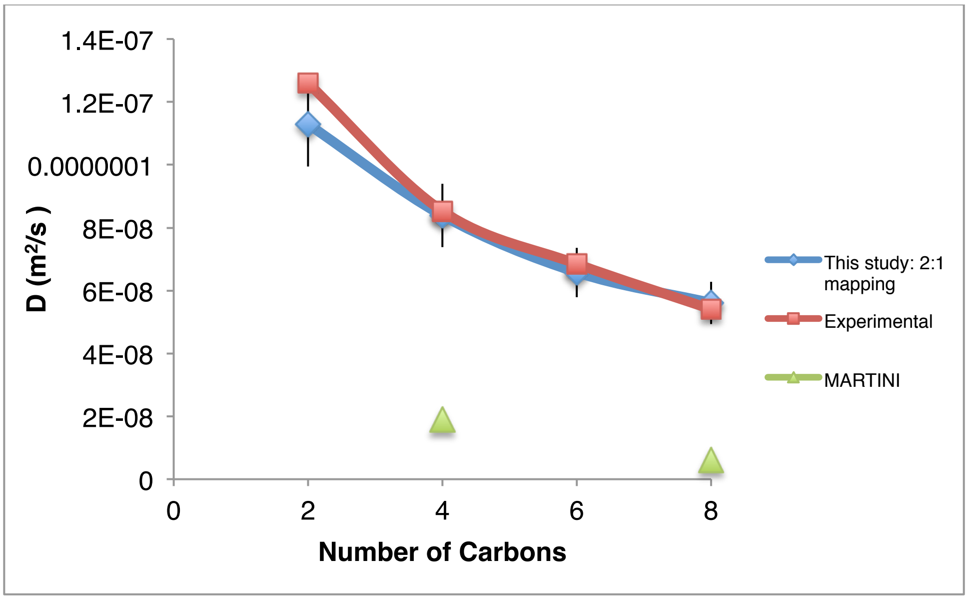
1.4E-07
1.2E-07
0.0000001
8E-08
6E-08
4E-08
2E-08
0
D (m²/s)
0
2
4
6
8
Number of Carbons
This study: 2:1 mapping
Experimental
MARTINI

a)

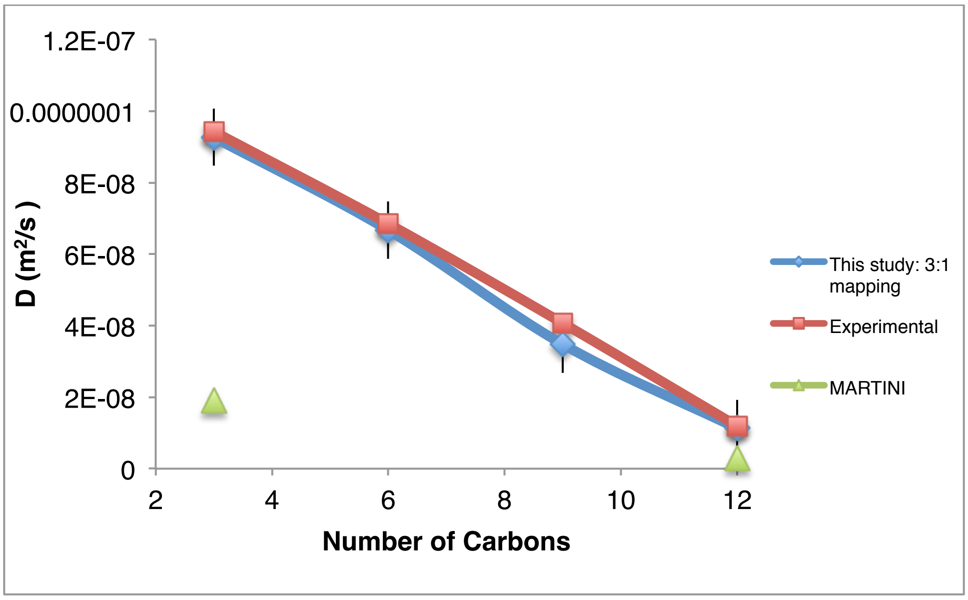
1.2E-07
0.0000001
8E-08
6E-08
4E-08
2E-08
0
D (m²/s)
2
4
6
8
10
12
Number of Carbons
This study: 3:1 mapping
Experimental
MARTINI

b)

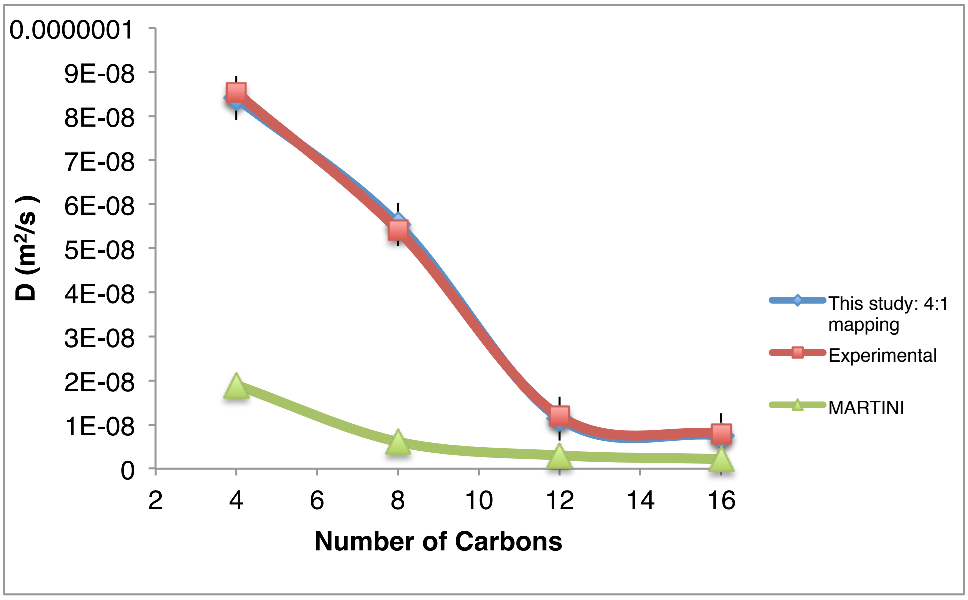
0.0000001
9E-08
8E-08
7E-08
6E-08
5E-08
4E-08
3E-08
2E-08
1E-08
0
D (m²/s)
2
4
6
8
10
12
14
16
Number of Carbons
This study: 4:1 mapping
Experimental
MARTINI

c)

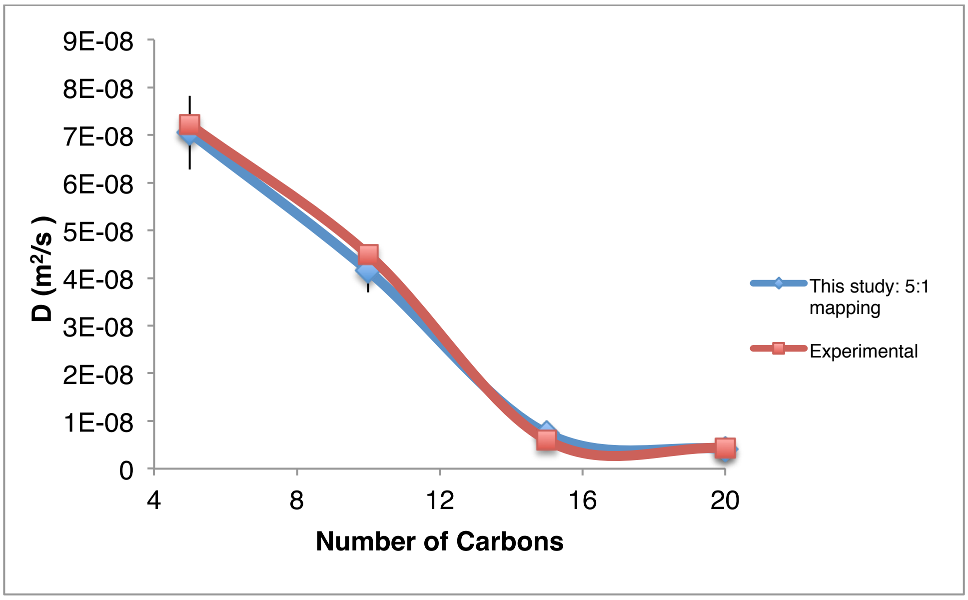

d)

Figures 4.25a-d: Self-diffusion coefficient results for this study's model for linear alkanes, the alkanes explicitly covered by MARTINI, and interpolated experimental and experimental data results for our 1-bead, 2-bead, 3-bead, and 4-bead systems for our **a)** 2:1 bead mapping, **b)** 3:1 bead mapping, **c)** 4:1 bead mapping, and **d)** 5:1 bead mapping.[58]

4.2.3.5 Shear viscosity

Figures 4.26a-d show the increasing trend of the mean shear viscosity of each subsequent parameterisation of the 2:1, 3:1, 4:1, and 5:1 mapped 1-bead, 2-bead, 3-bead, and 4-bead systems in comparison with available experimental results.[75, 76] A complete table of these results for all bead systems and mapping schemes compared to experimental values an again be found in **Table 4.16** in **Appendix A**. When there is a change in the total potential energy between two molecules, it affects the total viscosity of a substance, meaning a liquid with smaller molecules with lower LJ forces has a lower viscosity, or ability for molecules to slide past each other, than a liquid with larger molecules with higher LJ forces.[75, 76, 77, 78, 82] The viscosity of our models therefore adheres to theory as it increases with ε and σ, as well as increasing bond lengths. The stronger intermolecular forces of each of our subsequent alkane representations inhibits molecular flow, resulting in higher viscosity.[75, 76, 77, 78, 82] Our shear viscosity results also appear to lie within the margin of error for the known experimental values of alkanes, further justifying our optimised parameters.[58, 59] Again, our model rectifies the overestimation of shear viscosity observed with the original MARTINI parameters.

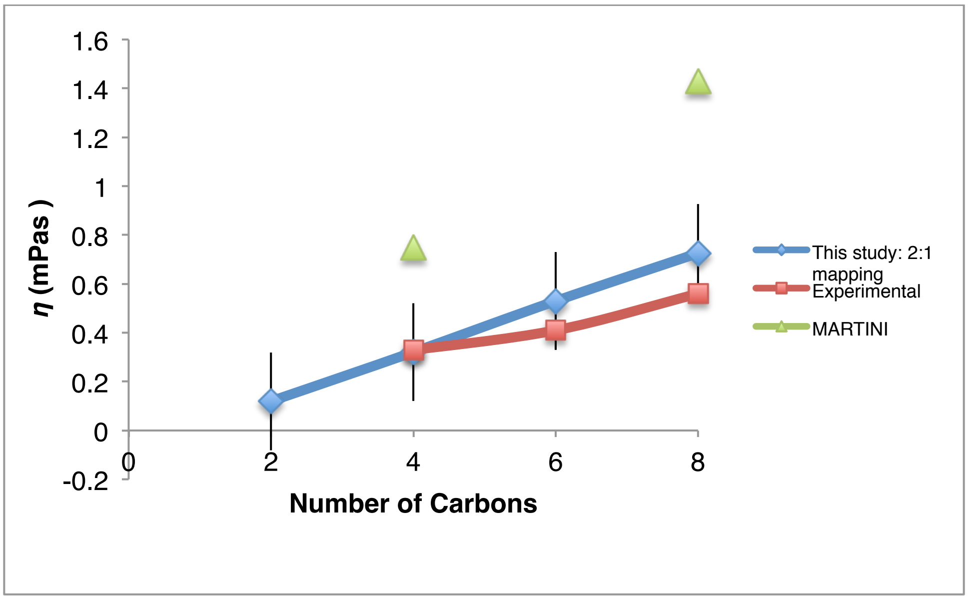
1.6
1.4
1.2
1
0.8
0.6
0.4
0.2
0
-0.2
η (mPas)
0
2
4
6
8
Number of Carbons
This study: 2:1 mapping
Experimental
MARTINI

a)

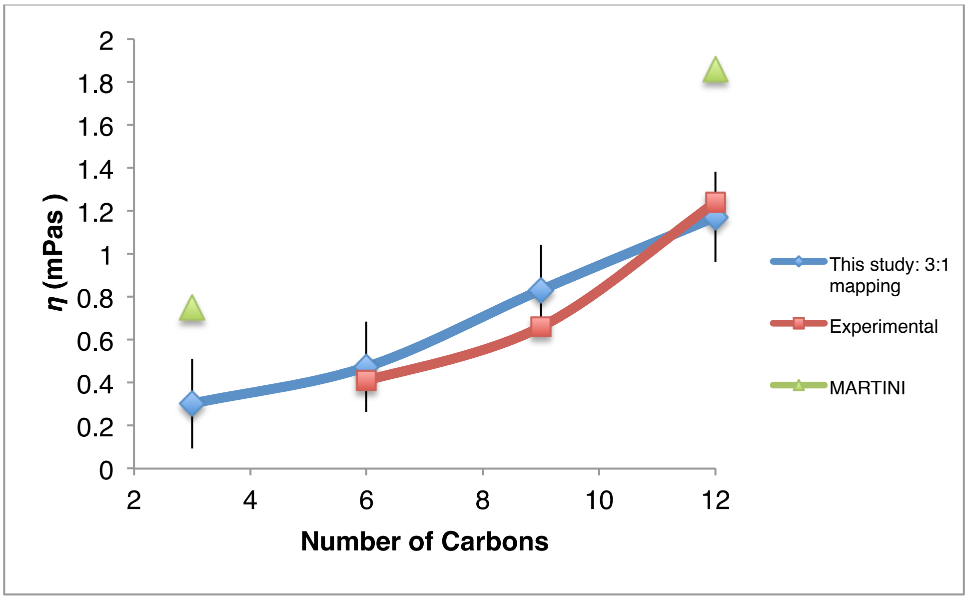
2
1.8
1.6
1.4
1.2
1
0.8
0.6
0.4
0.2
0
η (mPas)
2
4
6
8
10
12
Number of Carbons
This study: 3:1 mapping
Experimental
MARTINI

b)

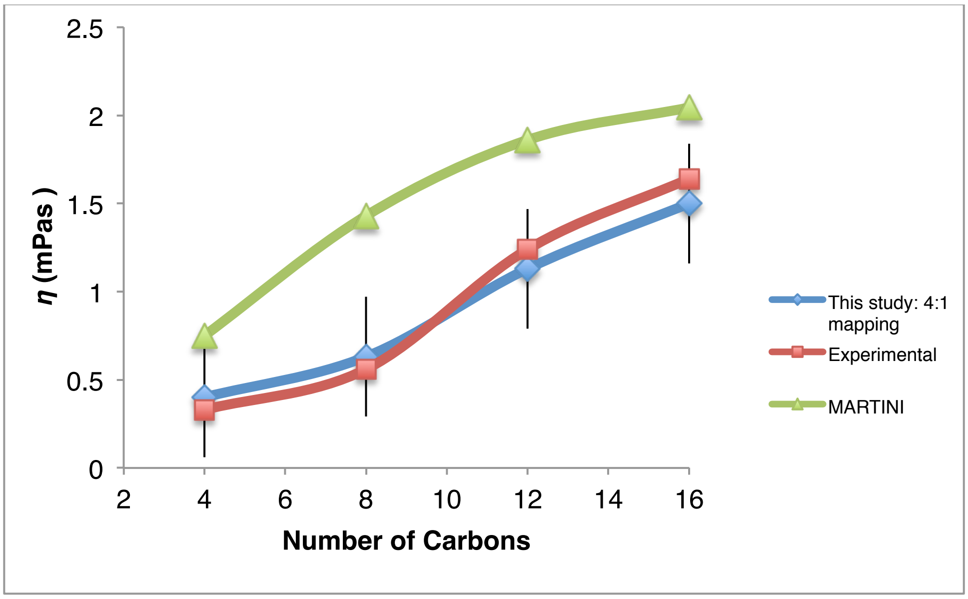
2.5
2
1.5
1
0.5
0
η (mPas)
2
4
6
8
10
12
14
16
Number of Carbons
This study: 4:1 mapping
Experimental
MARTINI

c)

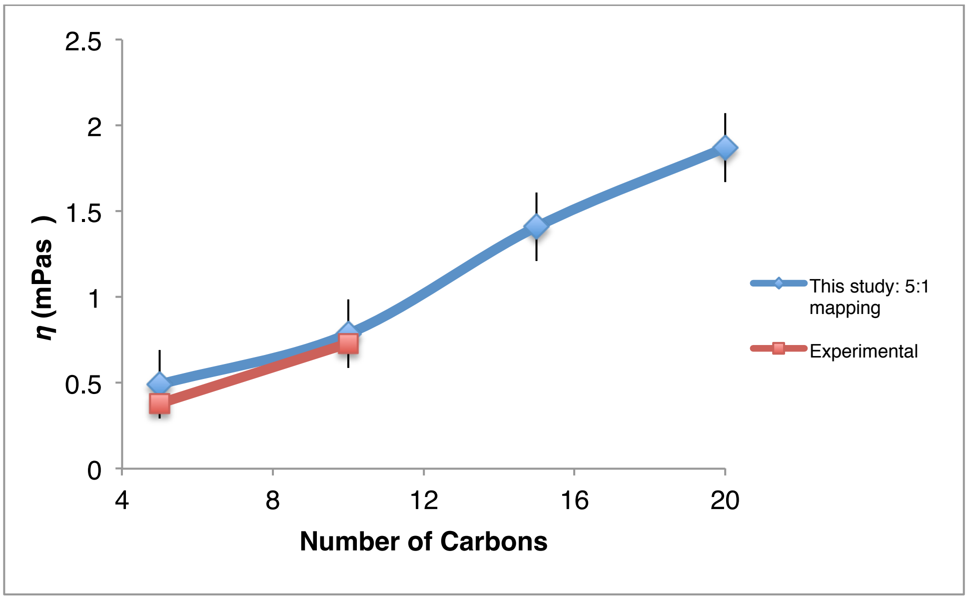

d)

Figures 4.26a-d: Shear viscosity results for this study's model for linear alkanes, the alkanes explicitly covered by MARTINI, and interpolated experimental data for our 1-bead, 2-bead, 3-bead, and 4-bead systems for our **a)** 2:1 bead mapping, **b)** 3:1 bead mapping, **c)** 4:1 bead mapping, and **d)** 5:1 bead mapping.[58, 59]

4.2.3.6 Radius of gyration

Figures 4.27a-c show the increasing trend of mean radii of gyrations of each subsequent parameterisation of the of the 2:1, 3:1, 4:1, and 5:1 mapped 2-bead, 3-bead, and 4-bead systems in comparison with available simulation results; those from an AA model, and those from a CG model, which were in good agreement to each other.[31, 60] A complete table of these results for the 2-bead, 3-bead, and 4-bead systems for all mapping schemes compared to experimental values is available in **Table 4.17** in **Appendix A**. As the radius of gyration is the average squared distance of any point in a molecule chain from it's centre of mass, the results for the 1-bead simulations are negligible to the overall data, but do promisingly show a slight increase in trend with increase in *σ* and LJ radius as per what is expected with theory.[2] The radii of gyration for the 2-bead, 3-bead, and 4-bead simulations show the same increasing trend, though they too are significantly lower than the simulation values, though within margins of error for most values. This is most likely due to size of CG alkane chain in comparison to the other models' alkanes.[31, 60] The property was therefore only important to show trend for our models.

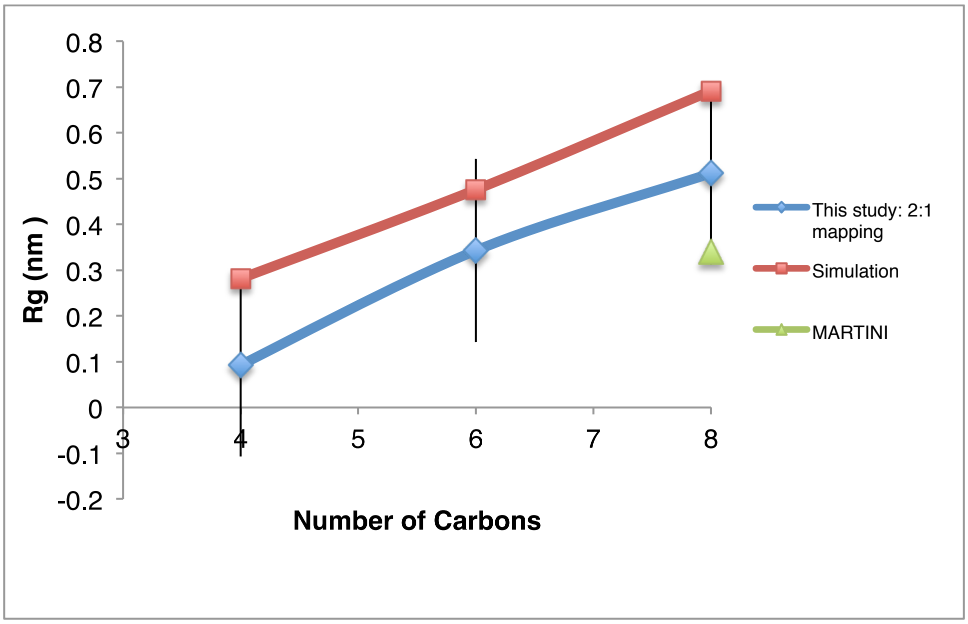

a)

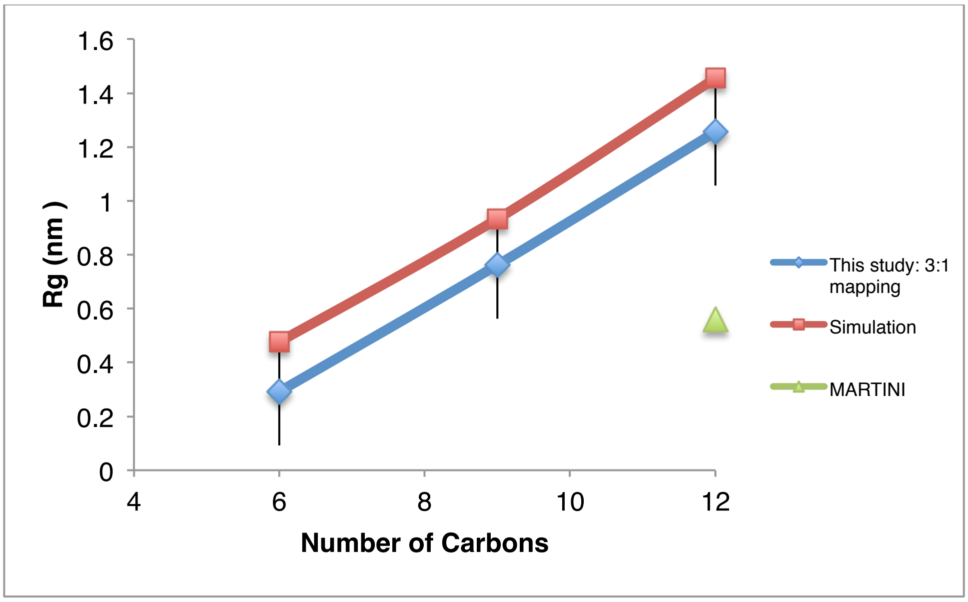
Rg (nm)
1.6
1.4
1.2
1
0.8
0.6
0.4
0.2
0
4
6
8
10
12
Number of Carbons
This study: 3:1 mapping
Simulation
MARTINI

b)

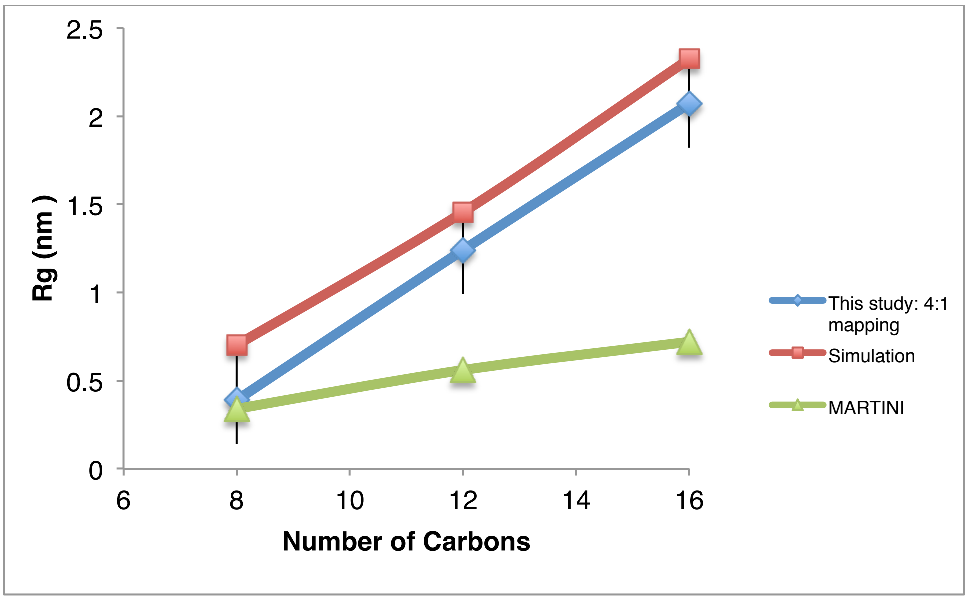
Rg (nm)
2.5
2
1.5
1
0.5
0
6
8
10
12
14
16
Number of Carbons
This study: 4:1 mapping
Simulation
MARTINI

c)

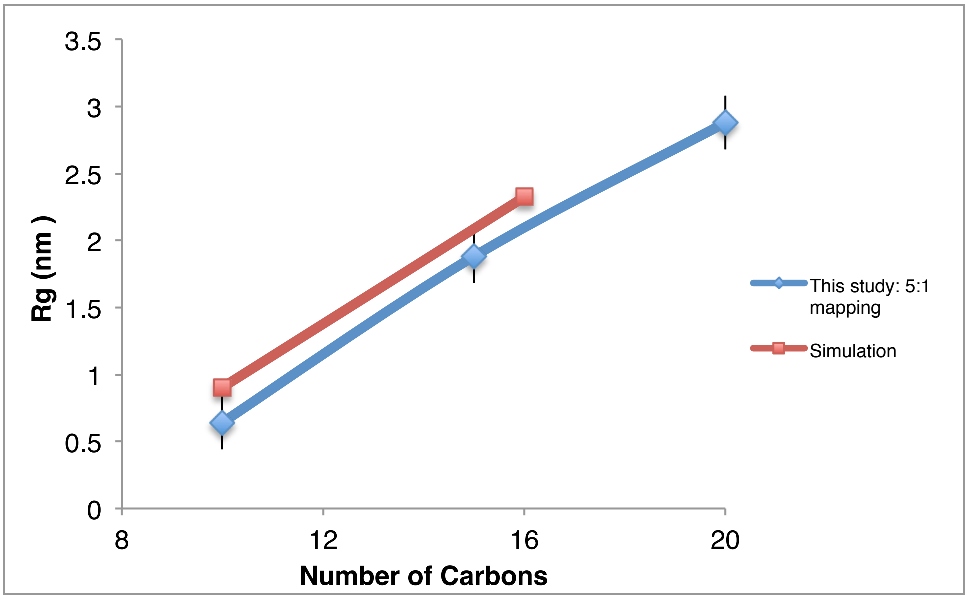

d)

Figures 4.27a-d: Radii of gyration results for this study's model for linear alkanes, the alkanes explicitly covered by MARTINI, and simulated data for our 1-bead, 2-bead, 3-bead, and 4-bead systems for our **a)** 2:1 bead mapping, **b)** 3:1 bead mapping, **c)** 4:1 bead mapping, and **d)** 5:1 bead mapping.[31, 60]

4.2.3.7 Hydration free energy

Table 4.10 shows the closest matches of Lennard-Jones parameters for each of models for alkane-water interactions, with MARTINI water P4 beads. Because the free energy of solvation of these alkanes in water is fairly unfavourable, the decreasing trend of σ and ε with increasing alkane chain is expected with theory (i.e. as stated before, when σ and ε decreases the ΔG_{solv} becomes more positive or unfavourable).[47, 72, 73] This is shown further in **Figures 4.28a-d.**

Mapping Scheme	**Alkanes-W**	
	Non-bonded Interactions	
	σ (nm)	**ε (kJ/mol)**
2:1	0.47	0.605
3:1	0.46	0.61
4:1	0.43	0.525
5:1	0.4	0.475

Table 4.10: Non-bonded Lennard-Jones parameter results for 1-bead, 2-bead, 3-bead, and 4-bead 2:1, 3:1, 4:1, and 5:1 mapped alkane models and CG MARTINI water.

In **Figures 4.28a-d** the solvation free energy of the 2:1, 3:1, 4:1, and 5:1 mapped 1-bead, 2-bead, 3-bead, and 4-bead systems in MARTINI water is shown in comparison with both experimental and standard MARTINI results for their respective alkane representations. A complete table of these results compared to experimental alkane values can also be found in **Table 4.18** in **Appendix A**. It can be seen in these figures that the MARTINI values are typically slightly lower in the case of smaller alkane chain representations (i.e. 1-bead, 2-bead, and 3-bead models), but imply a stronger focus on parameterisation with water in the case of its hexadecane model. The solvation free energies in MARTINI water of our alkanes were matched well to the experimental free energy values (see **Table 4.18**)[65, 66, 67, 68], with all of our alkane models' results within margins of error.[65, 66, 67, 68]

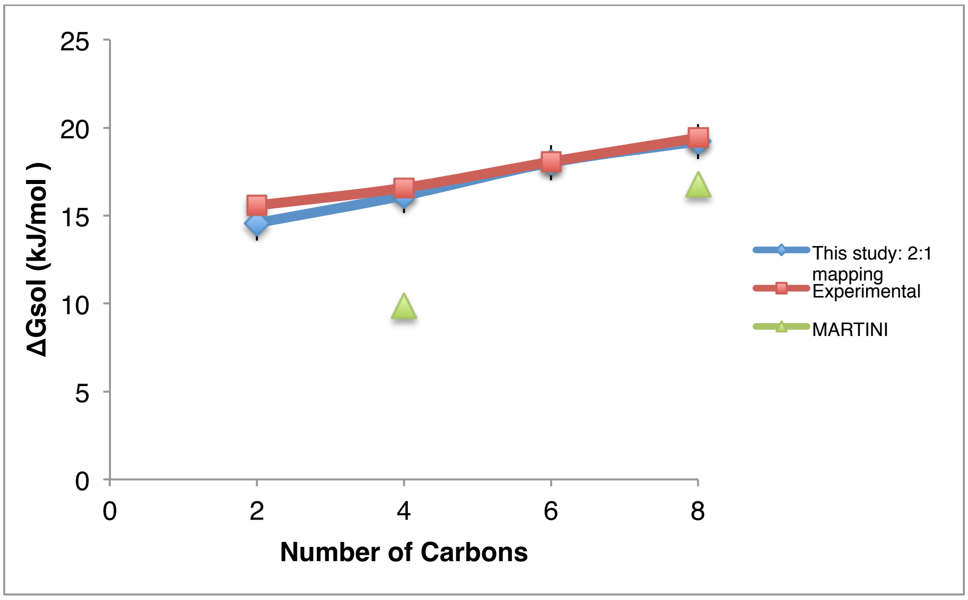

a)

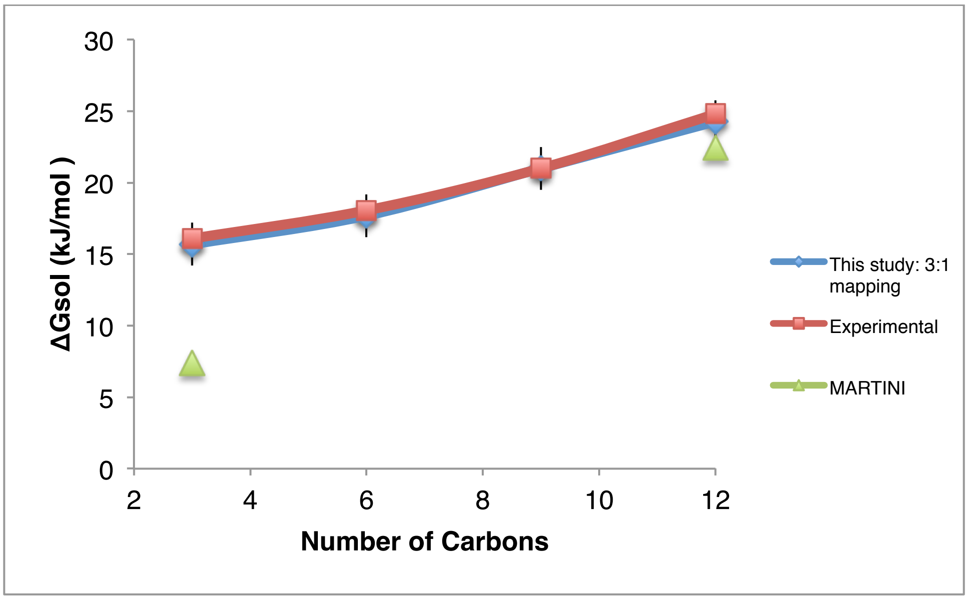
30
25
20
15
10
5
0
ΔGsol (kJ/mol)
2
4
6
8
10
12
Number of Carbons
This study: 3:1 mapping
Experimental
MARTINI

b)

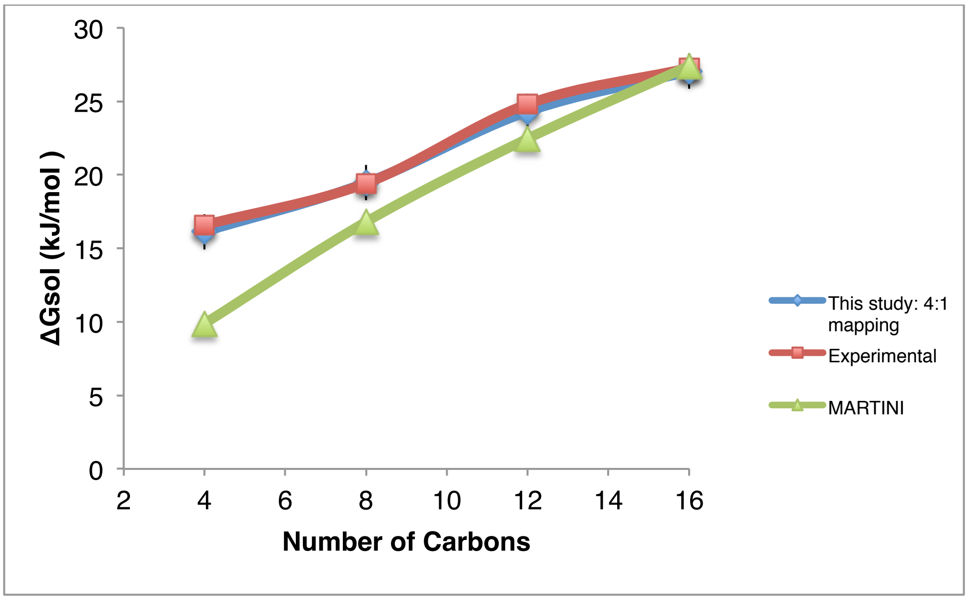
30
25
20
15
10
5
0
ΔGsol (kJ/mol)
2
4
6
8
10
12
14
16
Number of Carbons
This study: 4:1 mapping
Experimental
MARTINI

c)

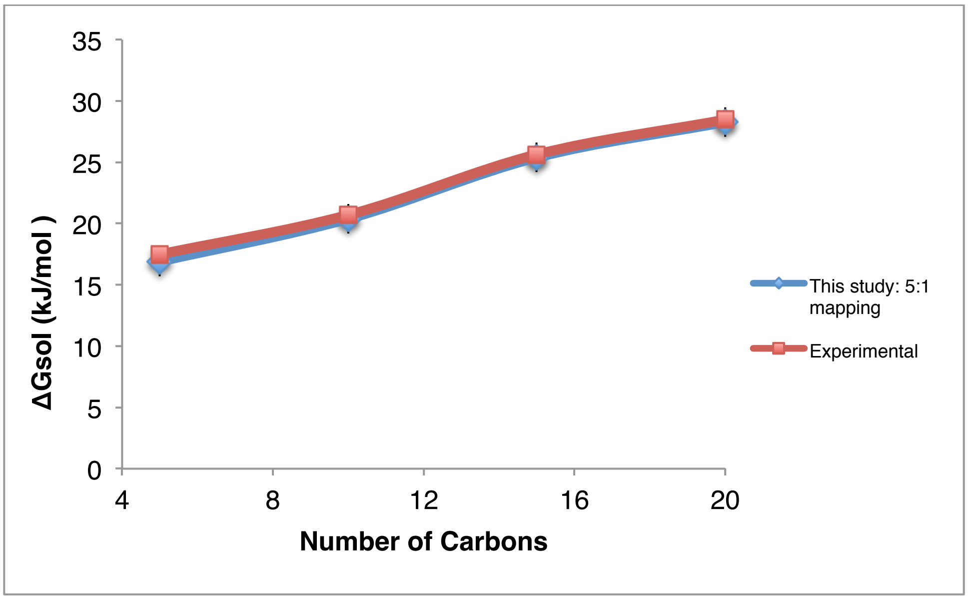

d)

Figures 4.28a-d: Comparison between this study's model for linear alkanes, the alkanes explicitly covered by MARTINI, and experimental data for linear alkane solvation free energies in water (i.e., ethane, propane, butane, and pentane for the 1-bead systems, butane, hexane, octane, and decane for the 2-bead systems, etc) for our 1-bead, 2-bead, 3-bead, and 4-bead systems for our **a)** 2:1 bead mapping, **b)** 3:1 bead mapping, **c)** 4:1 bead mapping, and **d)** 5:1 bead mapping.[28, 65, 66, 67, 68]

4.2.4 Validation for polyethylene

Figure 4.29 shows the adjusted ρ of our 2:1 mapped 78-bead and 90-bead models and our 4:1 mapped 39-bead and 45-bead models for polyethylene melts at 723.15K. These models were compared to simulated data for polyethylene of chain length C156 and C180, respectively.[69, 70] **Figure 4.30** shows the adjusted density for our 2:1 mapped 48-bead model and our 4:1 mapped 24-bead model, compared to polyethylene of chain length C96 melts at 773.15K.[71] All of our melt ρ results, while slightly lower than the simulated density results for the polyethylene melts (i.e. 790 kg/m^3 for polyethylene of chain length C156 and 795 kg/m^3 for polyethylene of chain length C180, at 723.15K[69, 70], and 720 kg/m^3 for polyethylene of chain length C96 at 773.15K[71]), fall within their margins of error, implying both that longer chains of our 2:1 and 4:1 mapped alkanes meet within expected values for melt properties, and can potentially be used for polyethylene simulations.[34, 35, 69, 70, 71]

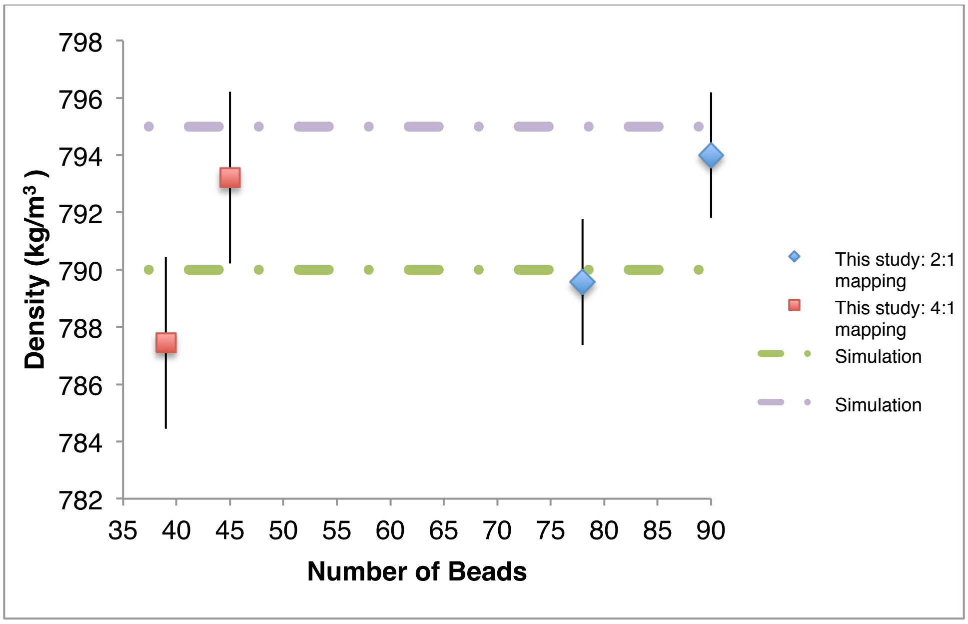

Figure 4.29: Selected densities determined for polyethylene's molecular weight for our 2:1 mapped 78-bead and 90-bead models and our 4:1 mapped 39-bead and 45-bead models for polyethylene melts at 723.15K. The purple dashed line represents the simulated density values for polyethylene at chain length C156, while the green dashed line represents the simulated density for polyethylene at chain length C180.[69, 70]

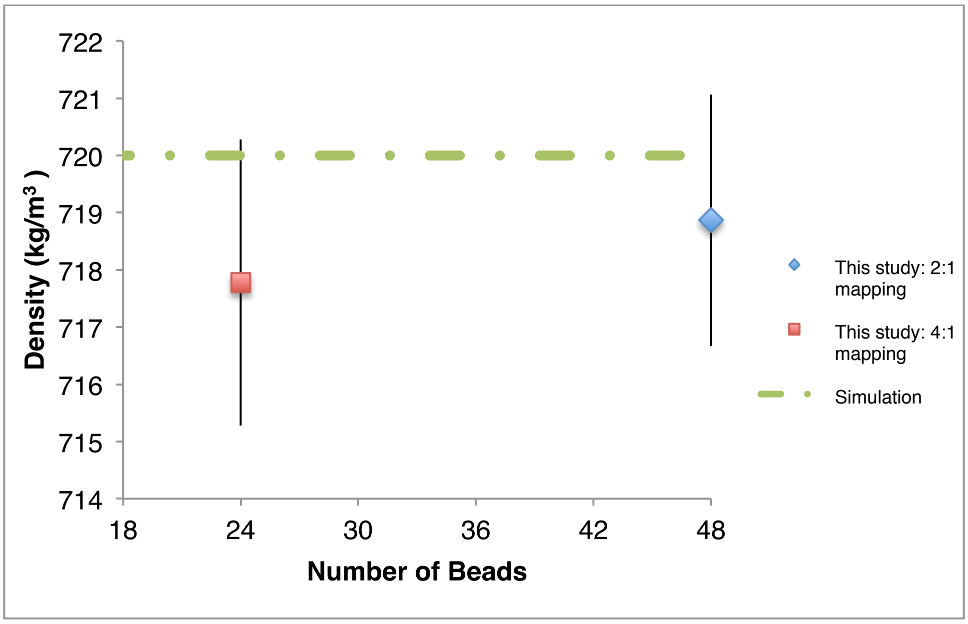

Figure 4.30: Selected densities determined for polyethylene's molecular weight for our 2:1 mapped 48-bead model and our 4:1 mapped 24-bead model for polyethylene melts at 773.15K. The purple dashed line represents the simulated density values for polyethylene at chain length C156, while the green dashed line represents the simulated density for polyethylene at chain length C180.[71]

In **Figure 4.31** shows the radii of gyration of our 2:1 mapped 78-bead and 90-bead models and our 4:1 mapped 39-bead and 45-bead models for polyethylene melts at 723.15K, compared to polyethylene melt data for polyethylene chain lengths of C156 and C180.[69, 70] **Figure 4.32** shows the radius of gyration results for our 2:1 mapped 48-bead model and our 4:1 mapped 24-bead model at 773.15K compared to polyethylene melt data for chain length of C96.[71] As with the density results above, all of the radius of gyration results, while lower than the simulated data (i.e. 2.26 ± 0.25 nm for polyethylene of chain length C156 and 2.43 ± 0.30 nm for polyethylene of chain length C180, at 723.15K[69, 70], and 3.8 ± 0.6 nm for polyethylene of chain length C96 at 773.15K[71]) fall within their margin of error. Overall these results indicate that based on the previously discussed method developed by Krevelen[34] and Bicerano[35] (i.e. using linear alkanes to estimate properties of polyethylene) our alkane models have been properly parameterised.

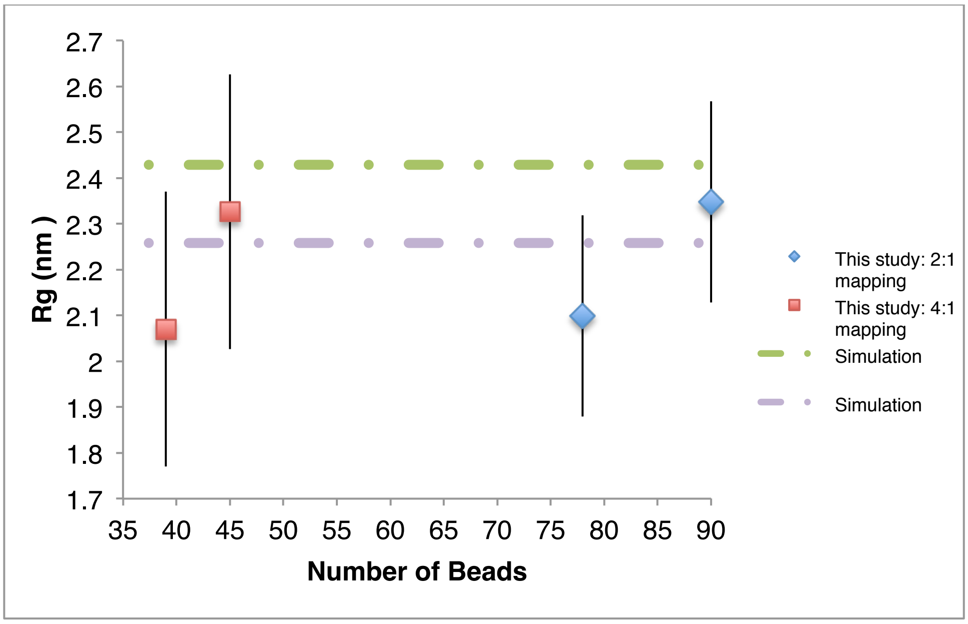

Figure 4.31: Radii of gyrations determined for polyethylene's molecular weight for our 2:1 mapped 78-bead and 90-bead models and our 4:1 mapped 39-bead and 45-bead models for polyethylene melts at 723.15K. The purple dashed line represents the simulated radius of gyration values for polyethylene at chain length C156, while the green dashed line represents the simulated radius of gyration for polyethylene at chain length C180.[69, 70]

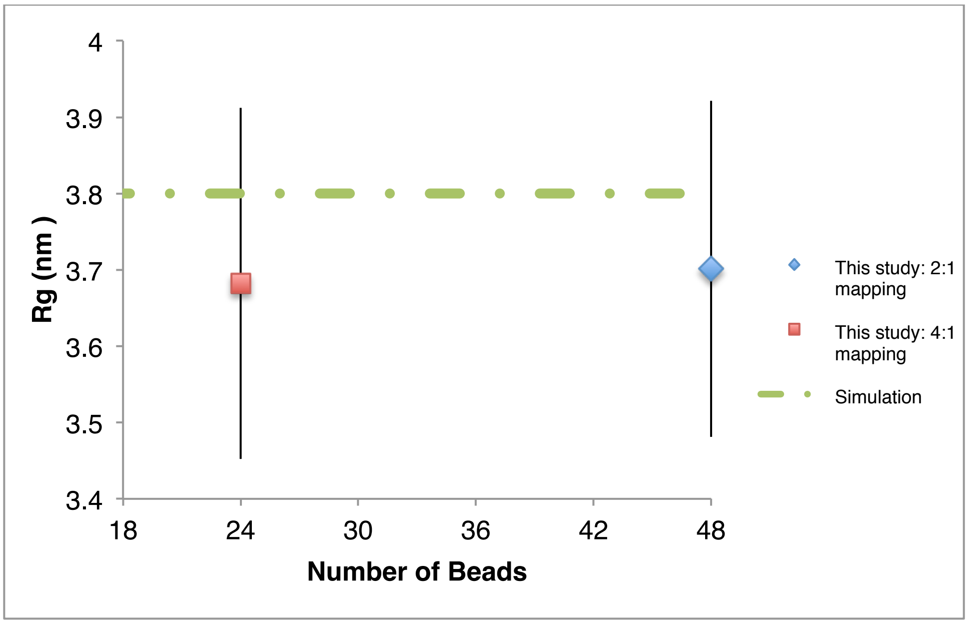

Figure 4.32: Radii of gyrations determined for polyethylene's molecular weight for our 2:1 mapped 48-bead model and our 4:1 mapped 24-bead model for polyethylene melts at 773.15K. The purple dashed line represents the simulated radius of gyration values for polyethylene at chain length C156, while the green dashed line represents the simulated radius of gyration for polyethylene at chain length C180.[71]

4.3 Conclusions

In this chapter, a look at standard MARTINI beads, testing of MARTINI alkane models, and a thorough parameterisation of our own beads and alkane models was presented. Simulations were run for P0-P5, N0-

Nda, and C1-C5 MARTINI beads for all of their noted interaction levels.[28] Because MARTINI solvents are classically standard size and non-charged, Q type beads and smaller, ring-type S-versions of beads were excluded.[28] After determining the inherent nature of the underlying thermodynamic solvation free energies adhered to established thermodynamic theory, explicit MARTINI alkane model properties were tested in comparison to experimental data.[28] Solvation free energies, enthalpies of vaporisation, densities, self-diffusion coefficients, and shear viscosities for the published MARTINI alkane models were compared to experimental data for evaluation.[46-51] The MARTINI alkanes appeared to have been parameterised mostly for $\Delta\mathrm{H}_{\mathrm{vap}}$, as disregarding the duplicate models for propane and butane, the results matched closely to experimental data.[21, 35, 36] The $\Delta\mathrm{G}_{\mathrm{solv}}$, ρ, and D results were less promising in regards to experimental comparisons, however, with $\Delta\mathrm{G}_{\mathrm{solv}}$ only following a similar trend to known data, ρ matching some points, but with an incongruous trend, and D being incredibly off from established experimental work.[46, 47, 51, 52, 53, 54] This gave us a solid basis on which to parameterise them for additional and more realistic properties.

This study's parameterisation of MARTINI for alkanes began with a focus on tailoring non-bonded interactions of singular 1-bead fluid systems, given by a 12-6 Lennard-Jones potential, to known and interpolated self-solvation free energies and enthalpies of vaporisation of alkanes.[46-51, 57] Lennard-Jones combinations that corresponded to these variables for specific alkanes were further compared to densities, and in some cases self-diffusion coefficients, viscosities, and radii of gyration from simulation studies, to validate agreement.[31, 52, 53, 54, 58, 59, 60] The 1-bead parameters that most closely matched data for experimental alkanes were then used in singular 2-bead bonded fluid systems. The bonded potentials, described by typical harmonic potentials, were then optimised in the same way as the Lennard-Jones potentials in the 1-bead systems, and those that matched the experimental data for the alkanes most closely were subsequently used in singular 3-bead bonded fluid systems.[31, 46-54, 58, 59, 60] The process proceeded with 3-bead systems for angle potentials, and then after those were optimised, singular 4-bead fluid systems were parameterised for torsion potentials.[31, 46-54, 58, 59, 60]

This approach's refined model led to better agreement with experimental thermodynamic properties, specifically $\Delta \mathrm{G}_{\mathrm{solv}}$, [46, 47, 51], though the $\Delta \mathrm{H}_{\mathrm{vap}}$ results were not as close of a match compared to MARTINI alkane models.[21, 35, 36] This underestimation of enthalpies of vaporisation at more than 2 CG beads appears to be a problem inherent in our modeling, and further work would need to be done to potentially rectify it.

Our models' physical properties also showed good agreement with experiment, especially ρ [52, 53], D [54], and η [58, 59], which all fell within margins of error, over a large range of linear alkane solvents. The $\mathrm{r_g}$ of our models also fell within margins of error for results from a previous AA simulation study[60] and a previous CG simulation study[31], and while this is also a net positive for our model, as there was no available experimental data, it was therefore only important to show trend for our models.[31, 60]

The parameterization of our alkane models' Lennard-Jones parameters for interactions with MARTINI water lead to good agreement with experimental solvation free energies of alkanes within water.[65, 66, 67, 68] This added another parameterization level for these models' use in future work.

Our 2:1 mapped 78-bead and 90-bead models and our 4:1 mapped 39-bead and 45-bead models for polyethylene melts at 723.15K, and our 2:1 mapped 48-bead model and our 4:1 mapped 24-bead model at 773.15K were found to provide suitable estimates for the simulated melt densities and radius of gyration results of polyethylene at chain lengths of C156 and C180 at 723.15K[69, 70], and chain length C96 at 773.15K.[71] These results indicate that our 2:1 mapped alkane models at least have been properly parameterised, based on the previously discussed method of using linear alkanes to estimate properties of polyethylene.[34, 35]

While there is room for further testing and improvement, our alkane models provide overall better adherence to known data than the standard MARTINI models, and it is the hope that this parameterisation will ultimately help facilitate surfactant self-assembly in future PEO, PPO, and Pluronic optimisation work.

4.4 References

. [1] J. Barnound & L. Monticelli. Coarse-grained force fields for molecular simulations. Methods Mol Biol., (1215):125– 149, 2015.

. [2] J. P. Ryckaert, & A. Bellemans. Molecular dynamics of liquid alkanes. *Faraday Discussions of the Chemical Society*, 66, 95-106, 1978.

. [3] L. J. Fetters, D. J. Lohse, D. Richter, T. A. Witten, & A. Zirkel. Connection between polymer molecular weight, density, chain dimensions, and melt viscoelastic properties. *Macromolecules*, *27*(17), 4639-4647, 1994.

. [4] K. Kremer, P. Kremer, & C. Kremer. Multiscale simulation of soft matter systems: from the atomistic to the coarse-grained level and back. Soft Matter, 124(15), 2009.

. [5] M. van Gunsteren & c. van Gunsteren. Multigraining: an algorithm for simultaneous fine-grained and coarse-grained simulation of molecular systems. The Journal of chemical physics, 124(15), 2006.

. [6] R. D. Levine. Molecular reaction dynamics. Cambridge University Press, 2005.

. [7] B. J. Alder & T. E. Wainwright. Studies in Molecular Dynamics. I. General Method. *J. Chem. Phys*. 31 (2): 459, 1959.

. [8] J. Klepeis, K. Lindor-Larsen, R.O. Dror, & D.E. Shaw. Long-timescale molecular dynamics simulations of protein structure and function. Current opinion in structural biology, 19:120–127, 2009.

. [9] G. Srinivas, J. C. Shelley, S. O. Nielsen, D. E. Discher, & M. L. Klein. Simulation of diblock copolymer self-assembly, using a coarse-grain model. *The Journal of Physical Chemistry B*, *108*(24), 8153-8160, 2004.

. [10] M. Hatakeyama, & R. Faller. Coarse-grained simulations of ABA amphiphilic triblock copolymer solutions in thin films. *Physical Chemistry Chemical Physics*, *9*(33), 4662-4672, 2007.

. [11] H. Lee, A. H. de Vries, S. J. Marrink, & R. W. Pastor. A coarse- grained model for polyethylene oxide and polyethylene glycol: Conformation and hydrodynamics. J. Phys. Chem., 113(40):13186-13194, 2009.

. [12] S. Yuan, X. Zhang, & K. Chan. Effects of shear and charge on the microphase formation of p123 polymer in the sba-15 synthesis investigated by mesoscale simulations. Langmuir, 25(4):2034-2045, 2009.

. [13] M. Velinova, D. Sengupta, A. V. Tadjer, & S. J. & Marrink. Sphere-to-rod transitions of nonionic surfactant micelles in aqueous solution modeled by molecular dynamics simulations. *Langmuir*, *27*(23), 14071-14077, 2011.

. [14] H. Lee, & R. W. Pastor. Coarse-grained model for PEGylated lipids: effect of PEGylation on the size and shape of self-assembled structures. *The Journal of Physical Chemistry B*, *115*(24), 7830-7837, 2011.

. [15] G. Rossi, P. F. J. Fuchs, J. Barnoud, and L. Monticelli. A coarse- grained martini model of polyethylene glycol and of polyoxyethylene alkyl ether surfactants. J. Phys. Chem. B, 116(49):14353–14362, 2012.

. [16] S. Hezaveh, S. Samanta, A. De Nicola, G. Milano, & D. Roccatano. Understanding the interaction of block copolymers with DMPC lipid bilayer using coarse-grained molecular dynamics simulations. *The Journal of Physical Chemistry B*, *116*(49), 14333-14345, 2012.

. [17] E. Choi, J. Mondal, & A. Yethiraj. Coarse-grained models for aqueous polyethylene glycol solutions. *The Journal of Physical Chemistry B*, *118*(1), 323-329, 2013.

. [18] S. Nawaz & P. Carbone. Coarse-graining poly(ethylene oxide)-poly(propylene oxide)-poly(ethylene oxide) (peo-ppo-peo) block copolymers using the martini force field. J. Phys. Chem. B, 118(6):1648-1659, 2014.

. [19] I. Wood, M. F. Martini, J. M. R. Albano, M. L. Cuestas, V, L, Mathet, & M. Pickholz, M. Coarse grained study of pluronic F127: Comparison with shorter co-polymers in its interaction with lipid bilayers and self-aggregation in water. *Journal of Molecular Structure*, *1109*, 106-113, 2016.

. [20] D. A. Grillo, J. M. Albano, E. E. Mocskos, J. C. Facelli, M. Pickholz, & M. Ferraro. Diblock copolymer bilayers as model for polymersomes: A coarse grain approach. *The Journal of chemical physics*, *146*(24), 244904, 2017.

. [21] T. Taddese, & P. Carbone. Effect of Chain Length on the Partition Properties of Poly (ethylene oxide): Comparison between MARTINI Coarse-Grained and Atomistic Models. *The Journal of Physical Chemistry B*, *121*(7), 1601-1609, 2017.

. [22] F. Grunewald, G. Rossi, A. H. De Vries, S. J. Marrink, & L. Monticelli. Transferable MARTINI Model of Poly (ethylene Oxide). *The Journal of Physical Chemistry B*, *122*(29), 7436-7449, 2018.

. [23] J. Poostforooshan, A. Badiei, G. Farzi, & A. Weber. Mesoporous Silica/Organic Nanocomposites. Unicorn Publications Pvt. Ltd., 104-106, 2016.

. [24] S. Higgins, W. DeSisto, & D. Ruthven. Diffusive transport through mesoporous silica membranes. Microporous and Mesoporous Materials, 117(12):268–277, 2009.

. [25] M. Moritz & M. Gaske-Moritz. A review: Fundamental aspects of silicate mesoporous materials. Materials, 5:2874– 2902, 2012.

. [26] S. W. Chiu, H. L. Scott, & E. Jakobsson. A coarse-grained model based on Morse potential for water and n-alkanes. J. Chem. Theory Comput., 6, 851–863, 2010.

. [27] M. Dallavalle, & N. F. van der Vegt. Evaluation of mapping schemes for systematic coarse graining of higher alkanes. *Physical Chemistry Chemical Physics*, *19*(34), 23034-23042, 2017.

. [28] S. Marrink & P. Tieleman. Perspective on the martini model. Chem. Soc. Rev., 42:6801–6822, 2013.

. [29] S. J. Marrink, A. H. De Vries, & A. E. Mark. Coarse grained model for semiquantitative lipid simulations. *The Journal of Physical Chemistry B*, *108*(2), 750-760, 2004.

. [30] S. J. Marrink, H. J. Risselada, S. Yefimov, D. P. Tieleman, & A. H. De Vries. The MARTINI force field: coarse grained model for biomolecular simulations. *The journal* *of physical chemistry B*, *111*(27), 7812-7824, 2007.

. [31] S. O. Nielsen, C. Lopez, G. Srinivas, & M. Klein. “A coarse grain model for n-alkanes parameterized from surface tension data”. J. Chem. Phys., 114 (14), 2003.

. [32] A. Requena, R. Peña, & A. Serna. Energy levels for perturbed Morse oscillators. *International Journal of Quantum Chemistry*, *17*(5), 931-942, 1980.

. [33] A. Peacock. *Handbook of polyethylene: structures: properties, and applications*. CRC Press, 2000.

. [34] D. W. Van Krevelen, & P. J. Hoftyzer. Properties of polymers. Elsevier Scientific Publishing, 1976.

. [35] J. Bicerano. Prediction of polymer properties. New York: Marcel Dekker, (2), 1996.

. [36] T. A. Kavassalis, & P. R. Sundararajan. A molecular-dynamics study of polyethylene crystallization. *Macromolecules*, *26*(16), 4144-4150, 1993.

. [37] P. K. Pant, J. Han, G. D. Smith, & R. h. Boyd. A molecular dynamics simulation of polyethylene. *The Journal of chemical physics*, *99*(1), 597-604, 1993.

. [38] M. Fukuda. Clustering of water in polyethylene: a molecular-dynamics simulation. *The Journal of chemical physics*, *109*(15), 6476-6485, 1998.

. [39] D. van der Spoel. Gromacs: the road ahead. Wiley Interdisciplinary Reviews: Computational Molecular Science, 1:710–5, 2011.

. [40] M. Henkel. Conformal invariance and critical phenomena. Springer Science & Business Media, 102-124, 2013.

. [41] F. Oellien and M. C. Nicklaus. Online SMILES translator and structure file generator. 2004.

. [42] NIH Biomedical Research Center for Macromolecular Modeling and Bioinformatic. Vmd users manual version 1.9.2. 1.9.2, 2014.

. [43] M. Di Pierro, R. Elber, & B. Leimkuhler. “A Stochastic Algorithm for the Isobaric-

Isothermal Ensemble with Ewald Summations for all Long Range Forces.", *Journal of Chemical Theory and Computation*, 2015.

. [44] T. Doiron. "20 °C – A Short History of the Standard Reference Temperature for Industrial Dimensional Measurements" (PDF). *National Institute of Standards and Technology*. Journal of Research of the National Institute of Standards and Technology, 2007.

. [45] S. Pronk, S. P, R. Schulz, P. Larsson, P. Bjelkmar, P. Apostolov, & M. Shirts. Gromacs 4.5: a high-throughput and highly parallel open source molecular simulation toolkit. Bioinformatics, 2013.

. [46] A. V. Marenich, J. D. Thompson, C. P. Kelly, G. D. Hawkins, C. C. Chambers, D. J. Giesen, P. Winget, C. J. Cramer, & D. G. Truhlar, *Minnesota Solvation Database - Version 2012*; University of Minnesota: Minneapolis, 2012.

. [47] P. H. Hünenberger, & M. M. Reif. Single-ion solvation: Experimental and Theoretical Approaches to Elusive Thermodynamic Quantities, Royal Society of Chemistry, London, 1, 2011.

. [48] D. van Velzen, R. Cardozo, & H. Langenkamp. Enthalpy of Vaporization Measurements of Liquid Methane, Ethane, and Methane + Ethane by Differential Scanning Calorimetry at Low Temperatures and High Pressures. *J. Chem. Eng. Data*, *62* (8), pp 2253–2260, 2017.

. [49] C. Viton, M. Chavret, & J. Jose. Enthalpy of Vaporization of N-Alkanes (from Nonane to Pentadecane). Experimental Results - Correlation. In: Caliste JP., Truyol A., Westbrook J.H. (eds) Thermodynamic Modeling and Materials Data Engineering. Data and Knowledge in a Changing World. Springer, Berlin, Heidelberg, 1998.

. [50] I. A. Hossenlopp, & D. W. Scott. Vapor heat capacities and enthalpies of vaporization of five alkane hydrocarbons. *The Journal of Chemical Thermodynamics.* 13(5), p. 415-421, 1981.

. [51] A. R. Katritzky, A. A. Oliferenko, P. V. Oliferenko, R. Petrukhin, D. B. Tatham, U. Maran, A. Lomaka, & W. E. Acree. A General Treatment of Solubility. 1. The QSPR Correlation of Solvation Free Energies of Single Solutes in Series of Solvents. *J.*

Chem. Inf. Comput. Sci. 43, 1794, 2003.

. [52] M. J. Astle, & R. C. Weast. Handbook of Data on Organic Compounds, CRC Press, Boca Raton, FL, USA, 1985.

. [53] Engineering ToolBox,. *Hydrocarbons – physical data*. [online] Available at: https://www.engineeringtoolbox.com/hydrocarbon-boiling-melting-flash-autoignition-point-density-gravity-molweight-d_1966.html, 2017 [Accessed 12 2 2018].

. [54] F. Bachl, & H.-D. Liidemann. Pressure and Temperature Dependence of Self-Diffusion in Liquid Linear Hydrocarbons. Z. Naturforsch. 41(a), 963-970, 1986.

. [55] M. Jorge, N. M. Garrido, C. J. Simões, C. G. Silva, & R. M. Brito. Predicting hydrophobic solvation by molecular simulation: 1. Testing united-atom alkane models. Journal of computational chemistry, 38(6), 346-358, 2017.

. [56] M. Griebel, S. Knapek, & G. Zumbusch. *Numerical simulation in molecular dynamics*. Berlin: Springer, 193-197, 2007.

. [57] B. Chen, M. G. Martin, & J. I. Siepmann. Thermodynamic properties of the williams, opls-aa, and mmff94 all-atom force fields for normal alkanes. *The Journal of Physical Chemistry B*, *102*(14), 2578-2586, 1998.

. [58] D. van Velzen, R.Cardozo, & H. Langenkamp. “A Liquid Viscosity-Temperature Chemical Constitution Relation for Organic Compounds“. Eng.Chem.Fundam., Vol. 11, 1, 1972.

. [59] I. M. Sivebaek, V. N. Samoilov, & B. N. J. Persson. “Squeezing molecular thin alkane lubrication films between curved solid surfaces with long-range elasticity: Layering transitions and wear”.J. Chem. Phys., Vol. 119, 4, 2003.

. [60] G. Toth, & A. Baranyai. Molecular dynamics analog of the reverse Monte Carlo method. J. Chem. Phys. 114, 2027, 2001.

. [61] J. G. Kirkwood. Statistical mechanics of fluid mixtures, J. Chem. Phys., 3:300-313,1935.

. [62] R. Smith. The Relationship of Force Constant and Bond Length. *J. Phys. Chem.*, *60*

(9), pp 1293–1296, 1956.

. [63] D. Oxtoby, H. Gills, & A. Campion. *Principles of modern chemistry* (7th ed.). Belmont, Calif.: Brooks/Cole Cengage Learning, 2012.

. [64] E. Anslyn & D. Dougherty. *Modern Physical Organic Chemistry*. University Science., 95, 2006.

. [65] P. Hutacharoen, S. Dufal, V. Papaioannou, R. M. Shanker, C. S. Adjiman, G. Jackson, & A. Galindo. Predicting the solvation of organic compounds in aqueous environments: from alkanes and alcohols to pharmaceuticals. *Industrial & Engineering Chemistry Research*, *56*(38), 10856-10876, 2017.

. [66] A. V. Plyasunov, & E. L. Shock. Thermodynamic functions of hydration of hydrocarbons at 298.15K and 0.1 MPa *Geochim. Cosmochim. Acta*, 64, 439– 468, 2000.

. [67] A. L. Ferguson, P. G. Debenedetti, & A. Z. Panagiotopoulos. Solubility and molecular conformations of n-alkane chains in water. *The Journal of Physical Chemistry B*, *113*(18), 6405-6414, 2009.

. [68] C. Sutton, & J. A. Calder. Solubility of higher-molecular-weight normal-paraffins in distilled water and sea water. *Environmental Science & Technology*, *8*(7), 654-657, 1974.

. [69] V. A. Harmandaris, V. G. Mavrantzas, D. N. Theodorou, M. Kröger, J. Ramirez, H. C. Öttinger, & D. Vlassopoulos. Crossover from the rouse to the entangled polymer melt regime: signals from long, detailed atomistic molecular dynamics simulations, supported by rheological experiments. *Macromolecules*, *36*(4), 1376-1387, 2003.

. [70] K. C. Daoulas, V. A. Harmandaris, & V. G. Mavrantzas. Detailed atomistic simulation of a polymer melt/solid interface: structure, density, and conformation of a thin film of polyethylene melt adsorbed on graphite. *Macromolecules*, *38*(13), 5780-5795, 2005.

. [71] B. L. Peters, K. M. Salerno, A. Agrawal, D. Perahia, & G. S. Grest. Coarse-grained modeling of polyethylene melts: effect on dynamics. *Journal of chemical theory and computation*, *13*(6), 2890-2896, 2017.

. [72] W. Greiner, L. Neise, & H. Stöcker. *Thermodynamics and statistical mechanics*. Springer-Verlag., 101, 1995.

. [73] D. Evans, *Response theory as a free energy extremum*, Phys. Rev. A 32, 2923, 1985.

. [74] D. W. Ball, J. W. Hill, & R. J. Scott. *The Basics of General Organic and Biological Chemistry*, Flat World Education, 128-133, 2011.

. [75] J. C. Li, & P. Chang. Self-Diffusion Coefficient and Viscosity in Liquids. *The Journal of Chemical Physics*, *23*(3), 518-520, 1955.

. [76] R. Zwanzig. On the relation between self-diffusion and viscosity of liquids. *The Journal of chemical physics*, *79*(9), 4507-4508, 1983.

. [77] P. Padilla, & S. Toxvaerd. Self-diffusion in n-alkane fluid models Scilight relation icon.The Journal of Chemical Physics 94, 5650, 1991.

. [78] F. Incropera, & D. P. DeWitt. *Fundamentals of Heat and Mass Transfer*. Wiley, 2007.

. [79] M. Mouas, J.-G. Gasser, S. Hellal, B. Grosdidier, A. Makradi, & S. Belouettar. “Diffusion and viscosity of liquid tin: Green-Kubo relationship-based calculations from molecular dynamics simulations”. J. Chem. Phys.,136, 094501, 2012.

. [80] S. Boresch, & M. Karplus. The role of bonded terms in free energy simulations: 1. Theoretical analysis. *The Journal of Physical Chemistry A*, *103*(1), 103-118, 1999.

. [81] I. Müller. *A History of Thermodynamics – the Doctrine of Energy and Entropy*. Springer. ISBN 978-3-540-46226-2, 2007.

. [82] H. B. Philllips. “A Formula for the Viscosity of Liquids”. *Proceedings of the National Academy of Sciences of the United States of America*, 7(6), 172-177, 1921.

. [83] C. Mundy, K. Bagchi, J. Siepmann, & M. Klein. Equilibrium and non-equilibrium simulation studies of fluid alkanes in bulk and at interfaces. *Faraday Discussions*, 104 (2), 1996.

. [84] J. Jovanovic, & D. Grozdanic. Reliable prediction of heat of vaporization of n-alkanes at 298.15 K. J. Serb. Chem. Soc. 75 (7) 997–1003, 2010.

. [85] M. Jorge, J. R. B. Gomes, M. N. D. S. Cordeiro, & N. A. Seaton. Molecular simulation of silica/surfactant self-assembly in the synthesis of periodic mesoporous silicas. *Journal of the American Chemical Society*, *129*(50), 15414-15415, 2007.

. [86] G. Pérez-Sánchez, J. R. B. Gomes, & M. Jorge. Modeling self-assembly of silica/surfactant mesostructures in the templated synthesis of nanoporous solids. *Langmuir*, *29*(7), 2387-2396, 2013.

COARSE-GRAINED MODELS FOR PEO AND PPO 5

As mentioned in previous chapters, block copolymers, referred to as Pluronics, are one of the most widely used types of nonionic surfactants, from biological applications to pharmaceutical drug-delivery systems.[1, 2, 5, 6 ,8] Their basic chemical structure of, PEO_n PPO_m PEO_n, can be seen in Chapter 1, though as a reminder it is shown here again in **Figure 5.1**.[2, 3, 4]

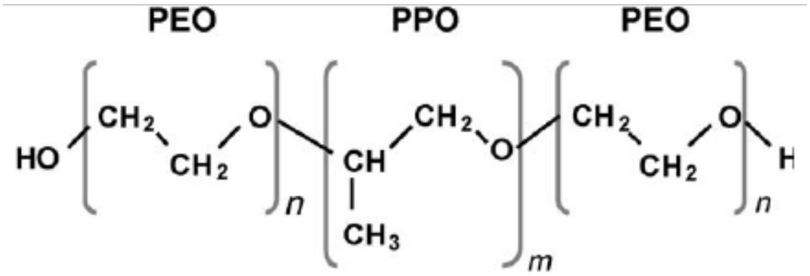

Figure 5.1: Generic chemical structure of Pluronic surfactant

The CG Pluronics simulations done to observe the self-assembly of these surfactants, as covered in Chapters 1 and 2, still contain a number of limitations and restrictions.[1, 2, 4-7, 9]

Many of the CG studies explored in Chapter 1 had strong focus on both PEO and PPO models, though none of these models was completely tested for a host of thermodynamic properties such as free energies of solvation in various solvents and enthalpies of vaporisation, as well as physical properties such as densities, self-diffusion coefficients, sheer viscosities, and radii of gyration.[15, 17-23]

In this chapter, we aimed to complete two main goals; to examine the best PEO and PPO models from selected CG studies described in Chapter 1 through testing of properties, and to further our work with our new MARTINI alkane models by testing the free energies of these models in alkanes. Free energies of solvation were of particular importance, due to their involvement in block copolymer surfactant self-assembly.[1]

5.1 Methodology

5.1.1 Simulation protocol

As with the work done in Chapter 4, the CG simulations run in this chapter used GROMACS software, and were performed using an isothermal-isobaric NPT ensemble.[11] The original AA models used as a basis for our coarse-graining were again converted from their chemical structures using the online SMILES generator, and then mapped to the CG models using Residue-Based Coarse Graining (RBCG) Builder in VMD.[74, 75] Again, to yield the most accurate thermodynamic results, a V-rescale thermostat and a Parrinello-Rahman barostat were used to maintain normal standard conditions of 298K and 1 bar respectively, and the simulations used a time-step of 20fs, with a leap-frog stochastic dynamics integrator for the equations of motion.[11, 12, 13] The normal dispersion was again controlled by a switched group cutoff scheme with cutoff between 1.0 - 1.3 nm, and long-range dispersion corrections were applied to energy and pressure of the system.[11,13] In order to account for finite-size effects, the cubic box lengths were kept between 3.2 nm and 35 nm, depending on the size of the beads or CG polymer chains.[14]

5.1.2 Coarse-grained models

As with our previous work, this study made use of the MARTINI force field, which was explained in full in Chapter 2, or in a smaller capacity in Chapter 4.[13]

This study's investigation began with a focus on previous CG models for the fundamental components of Pluronics; polyethylene oxide, PEO, and polypropylene oxide, PPO. Eight PEO models and four PPO models were taken from studies covered in Chapter 2. The studies included were those by Hatakeyama et al.[21], Lee et al.[17], Rossi et al.[18], Hezaveh et al.[22], Nawaz et al.[20], Wood et al.[23], Taddese et al.[15] and Grunewald et al.[19]

All of these studies provided solid basis for our PEO and PPO simulations, providing varying properties of interest, in numerous environments, at variable levels of success or direct previous contribution with Pluronics.[15, 17-23] Uniquely with regards to Nawaz et al., there was a correction to their published model's PEO-W and PPO-W interactions, so both their original and corrected ones were tested in our solvation free energy in water.[16, 20]

The 7 different models of PEO beads with different bonded and non-bonded parameters can be seen in **Table 5.1**. As will be discussed further below, we were initially interested in 2-bead models (i.e. PEO2 and PPO2) which means only the bond length and bond force constant bonded parameters were initially relevant.

PEO Models		**PEO-PEO**				**PEO-W**	
		Non-bonded Interactions		**Bonded Interactions**		**Non-bonded Interactions**	
		σ **(nm)**	***ε*** **(kJ/mol)**	**r_0 (nm)**	**k_b (kJ/mol*nm^2)**	***σ*** **(nm)**	***ε*** **(kJ/mol)**
1	Taddese et al.[15]	0.43	2.925	0.33	7000	0.47	3.75
2	Lee et al[17], Wood et al.[23]	0.43	3.375	0.33	17000	0.47	4
3	Rossi et al.[18]	0.43	3.75	0.322	7000	0.47	4.25
4	Grunewald et al.[19]	0.43	3.4	0.322	7000	0.47	3.5
5	Nawaz et al.[20]	0.43	3.375	0.265	17000	0.47	3.19
6	Hatakeyama et al.[21]	0.47	4.2	0.47	1250	0.47	3.4
7	Hezaveh et al.[22]	0.48	3.5	0.28	8000	0.47	4.5

Table 5.1: Lennard-Jones non-bonded interaction parameters for PEO models with themselves and with water, and bonded parameters for bond length and force constant.[15, 17-23]

The 4 PPO models taken from the previously discussed studies can be seen in **Table 5.2**.

PPO Models		**PPO-PPO**				**PPO-W**	
		Non-bonded Interactions		**Bonded Interactions**		**Non-bonded Interactions**	
		σ (nm)	**ε (kJ/mol)**	**r_0 (nm)**	**k_b (kJ/mol*nm^2)**	**σ (nm)**	**ε (kJ/mol)**
8	Nawaz et al.[20]	0.43	2.625	0.355	17000	0.47	2.625
9	Wood et al.[23]	0.47	3.4	0.33	17000	0.47	1.8
10	Hatakeyama et al.[21]	0.47	3.4	0.47	1250	0.47	1.8
11	Hezaveh et al.[22]	0.5	2.6	0.28	5000	0.47	3.5

Table 5.2: Lennard-Jones non-bonded interaction parameters for PPO models with themselves and water, and bonded parameters for bond length and force constant.[20-23]

To gain an initial understanding of the models' parameters, and give a preliminary indication of which models might be the best fit for PEO and PPO, we first ran 1-bead monomer simulations of all of the models. This was because PEO and PPO are coarse-grained in MARTINI to single beads, each representing a solitary EO and PO. For the PEO monomer, results were compared to dimethyl ether, DE, which had known experimental values, and for the PPO monomer[76], results were compared to methoxyethane, MOE, which also had available experimental values, though it should be noted that it lacks the methyl group attached to the carbon atom backbone inherent in the true PPO monomer.[77] The self-solvation free energies, ΔG_{solv}, of these monomer models were calculated through thermodynamic integration, a and the results were compared to estimated experimental values.[75, 76] Enthalpies of vaporization, ΔH_{vap}, were then calculated and compared to known values for DE and MOE.[83, 84] Results were also matched to available experimental and simulated density, ρ.[75, 76]

Due to the fact that 1-bead simulations are solely reliant upon non-bonded parameters of interaction (i.e. σ and ε), this study focused predominantly on the dimers of PEO and PPO, PEO2 and PPO2, for a more comprehensive set of model parameters (i.e. σ, ε, r_0, and k_b). In the case of the PEO dimer, 1,2-dimethoxyethane, DME, there was a good amount of simulation and experimental data for comparison.[2, 10, 28, 57] For the true PPO dimer, 1-3ethoxy-2-methoxypropane, there was no equivalent simulation or experimental work available, so the shorter molecule, 1,2-dimethoxypropane, DMP, was chosen for comparison to our dimer model.[2, 10, 28, 57] Previous studies have compared DMP with PPO dimers with some success, as it is only one methyl group away from being a true dimer, but when available, we tried to also compare with any known data for a closer representation of the PPO dimer, 1,2-diethoxyethane, DEE, as well as with DMP.[64, 65]

As PEO2 and PPO2 are only 2-bead models, they do exclude angle and dihedral parameters, so those aspects were later discussed.

In order to find the best parameters for PEO2 and PPO2, the self-solvation free energies, ΔG_{solv}, of these molecules were calculated through thermodynamic integration, and then subsequently the enthalpies of vaporization, ΔH_{vap}, were calculated. Both of these properties were then matched to known experimental data for the dimers/oligomers at standard conditions and in the case of self-solvation, the results of a previous AA study as well.[20, 24, 25, 26, 27, 64, 65, 66] The models were then further matched to available experimental and simulated density, ρ.[26, 64, 65, 66]

The PEO2 and PPO2 models were then further validated against to available experimental and simulated physical properties, specifically self-diffusion coefficients, D, and shear viscosity, η, narrowing down the models to two representations (i.e. one for PEO2 and one for PPO2) that corresponded most accurately to real dimers.[20, 24, 25, 27, 28, 29]

Solvation free energies of the models were then calculated in various solvents; CG MARTINI water, as well as our new models for hexadecane, heptane, and hexane from Chapter 5.[15, 30, 32] These alkanes were chosen to show a clear trend in the solvation energy, provide direct experimental comparison between the PEO and PPO models and DE and MOE (okay approximations of the true PEO and

PPO monomers, respectively), as well as between the PEO2 model and DME in hexadecane, comparison of previous simulation work for our PEO2 and PPO2 in heptane, comparison of previous simulation work with our PEO2, and to validate our previous alkane work for use with PEO and PPO. Our initial hexadecane model was a 4-bead representation with 4:1 mapped parameters, our heptane model was a 2-bead representation 3.5:1 mapped parameters, and our hexane model was a 2-bead representation with 3:1 mapped parameters, shown in **Table 5.3**. Note that for our heptane model, the 3.5:1 mapping parameters were interpolated from the values provided in **Tables 4.12**, **4.13**, and **4.14** from Chapter 4 and available in **Appendix A**.

Mapping Scheme	**CG Alkane Models**	**Number of beads**	**Non-bonded Interactions**		**Bonded Interactions**					
			σ (nm)	**ε (kJ/mol)**	**r_0 (nm)**	**k_b (kJ/mol*nm^2)**	**θ (deg.)**	**k_θ (kJ/mol)**	**Φ (deg.)**	**$k\Phi$ (kJ/mol)**
4:1	Hexadecane (C16H36)	4	0.445	2.8	0.44	17500	180	65	n/a	n/a
3.5:1	Heptane (C7H16)	2	0.432	2.63	0.3875	17500	180	65	n/a	n/a
3:1	Hexane (C6H14)	2	0.42	2.5	0.335	17500	180	65	n/a	n/a

Table 5.3: Lennard-Jones non-bonded and bonded interaction parameters for our CG hexadecane model's, heptane model's, and hexane model's beads.

Because these alkanes had not yet been tested with polymers, the interaction non-bonded parameters between our alkane beads and the chosen PEO and PPO models had to be calibrated. In the case of our hexane model with the PEO models, initial parameters were taken and tested from the simulated work by Taddese et al. (i.e. $\sigma = 0.47$ and $\varepsilon = 2.9$).[15] The parameterisation of our hexadecane with the PEO models, and our heptane with the PEO and PPO models was based off of MARTINI's own interaction levels, specifically IV through IX, as well as our own LJ values.[11] This range is because PEO is naturally more hydrophilic and PPO more hydrophobic, a major reason block copolymers utilising them are popular in micelle formation.[2, 3, 5] The solvation free energies of all interaction levels between the PEO2 and PPO2 models and our alkanes were then matched to the experimental and simulated values of DE, MOE, DME and DMP in hexadecane, heptane, and hexane.[20, 24, 25]

For further validation, the end-to-end distance, $\mathrm{R_d}$, of PEO and PPO homopolymers of lengths 2 and 36 in water and heptane, the persistence length, L, of PEO and PPO monomers, and the relaxation times of PEO and PPO homopolymers of length 30 in both MARTINI water and our hexane, and of length 36 in heptane, were calculated and compared to results in previous simulation studies.[20, 31, 51] These properties were chosen to ensure the models adhered to the statistical measures of chain size and behavior for their respective polymers.

To validate the chosen model's angle and dihedral parameters, long chains of PEO and PPO monomers were simulated with lengths of 30, 60, and 90, and their radii of gyration, $\mathrm{R_g}$, were calculated. The radii of gyration of chains of 36 PEO and PPO monomers were also simulated in our CG heptane, to further confirm our alkane models and to compare to those in water. All of these radii were then compared to results from previous simulations for justification.[20, 22] The resulting files from these simulations were put into VMD to compare how they behaved with how experimental PEO or PPO would (i.e. whether or not the PEO and PPO models showed any signs of hydrophilicity by remaining in a longer chain form without curling in on themselves to avoid the solvents).[50]

A complete overview of the simulated systems of PEO and PPO in this study can be seen in **Table 5.4**.

PEO and PPO Model Solutes	Solvated Systems							
	PEO	PEO2	PPO	PPO2	MARTINI Water	Our Hexadecane	Our Heptane	Our Hexane
PEO	✓					✓		
PEO2		✓			✓	✓	✓	✓
PEO30					✓			✓
PEO36					✓		✓	✓
PEO60					✓			
PEO90					✓			
PPO	✓					✓		
PPO2				✓	✓		✓	
PPO30					✓			✓
PPO36					✓		✓	
PPO60					✓			
PPO90					✓			

Table 5.4: Simulation details for our PEO and PPO work.

5.1.3 Data analysis

The densities for the PEO and PPO monomer models in this study were compared against experimental data; for PEO this data was taken from an online database for DE[76], and for PPO this data was taken from an online database for MOE.[77] Enthalpy of vaporisation results were also compared to experimental work; ; for PEO this data was taken from an online database for DE[83], and for PPO this data was taken from an online database for MOE.[84]

There is no known self-solvation experimental data for DME, DMP, or DEE, however these self-solvation free energy values can be estimated from vapour pressure data (here at room temperature). The method of calculation used can be seen in **Equation 5.1**:

$$\Delta G^{\circ} = -RT \ln \frac{P}{P^{0} * M} \qquad \textbf{(5.1)}$$

where ΔG° is the calculated free energy, R is the ideal gas constant, T is the temperature of the simulation, P is the vapour pressure, P^{0} is the pressure of an ideal gas at 298K and 1 molar concentration, and M is the equilibrium molarity of the pure solution, which is obtained from its density.[73]

The self-solvation free energy results for the PEO monomer models were calculated using experimental vapour pressure data for DE, taken from an online database[76], and those for the PPO monomer were calculated using experimental vapour pressure data for MOE, taken from an online database.[77]

The densities for the PEO2 and PPO2 models in this study were compared against experimental data; for PEO2 these were taken from an experimental study of DME by Roy et al.[52] and an online database for DME[66], for PPO2 these were also taken from the study of DMP by Roy et al.[52] a separate online database for DMP[26], and two online databases for DEE.[64, 65] Enthalpy of vaporisation results were also compared to experimental work; for PEO2, the study of DME by Majer et al.[27] and the online database for DME[66] were used, and for PPO2 the online database for DMP[26] and the online database for DEE[65] were used.

The self-solvation free energy results for the PEO2 models were calculated using experimental vapour pressure data for DME, taken from an online database[66], and from experiments done by Aucejo et al.[57]. For another degree of validation, the results were also compared against an AA study of PEO2 by Hezaveh et al.[25]

The self-solvation free energy results for the PPO2 models were calculated using experimental vapour pressure data, taken from an online database[26] for vapour pressures of both DMP and DEE, the experimental study by Aucejo et al.[57] for vapour pressures of DMP, and two separate online databases for vapour pressures of DEE.[64, 65]

The solvation free energies of the PEO2 models in water were compared to experimental values of DME from two studies; a review of experimental values by Majer et al.[27], and the quasi-elastic neutron scattering portion of a study by Bedrov et al.[28] Due to a lack of available experimental values for either DMP or DEE, the solvation free energies of the PPO2 models in water were compared to the AA study of PPO2 by Hezaveh et al.[25]

The solvation free energies of the PEO, PPO, PEO2 models in our hexadecane solvent model were compared against experimental data for DE, MOE, and DME from the solvation free energy database by Katritzky et al.[24], and due to a lack of either experimental or simulation work for DMP or DEE in hexadecane, no simulations were run for PPO2.

As no available experimental data for solvation free energies of DME, DMP, or DEE in heptane was available, both the PEO2 and the PPO2 models in our heptane solvent model were compared against further simulation work from the AA study by Hezaveh et al.[25]

For a final validation of our solvation free energy results and our alkane models, the solvation free energies of the PEO2 models in our hexane solvent model were compared against three simulation studies; a CG study by Taddese et al[15] which also reported on the results of the model proposed by Lee et al.[30], as well as estimated results form an AA study by Jorgensen et al.[32]

Self-diffusion coefficient results for the PEO2 models were compared against extrapolated experimental data from the study by Bedrov et al.[28], while the results for the PPO2 models were compared to the simulation work done in the AA study by Hezaveh et al.[25]

The shear viscosity results of the PEO2 models were compared to extrapolated experimental data from a study by Barthel et al.[29], while due to the lack of experimental values, the PPO2 models were compared again to the simulation work done for DMP in the AA study by Hezaveh et al.[25]

We were unable to find experimental values of the end-to-end distances, persistence lengths, and relaxation times calculated in this study, and thus had to compare our values against previous simulation work. The end-to-end distances calculated for PEO and PPO homopolymers of lengths 2 and 36 in water and in heptane were compared against an AA study performed by Hezaveh et al.[51]

The persistence lengths of single monomers of both PEO and PPO were compared to a CG study by Nawaz et al.[20], and then to further validate our results and compare to a study with a higher degree of detail, the persistence length of just PEO was compared to an AA study performed by Lee et al.[31]

Relaxation times for PEO and PPO chains of length 30 in both water and hexane were compared to the results of the aforementioned CG study by Nawaz et al.[20], and the relaxation times for PEO and PPO chains of length 36 in heptane were compared again to the study by Hezaveh et al.[51]

As mentioned in Chapter 5, radii of gyration are extremely difficult to examine experimentally, so the radius of gyration results for the longer PEO and PPO chains were compared to obtainable simulation work; a CG study by van Gunsteren et al.[12] for the PEO chains, and an AA study by Hezaveh et. al[51] for the PPO chains.

All of the results in this study were calculated again using the equations described in Chapter 3.

5.2 Results

5.2.1 PEO and PPO monomers

Figures 5.2a-b show the density results of the PEO and PPO monomer models, corrected and compared for DE for the PEO monomer models, and MOE for the PPO monomer models.[76, 77] A complete table of these results can be found in **Tables 5.15a-b** in **Appendix B**. These results were expected from theory, as the densities were shown to decrease with the σ and increase with the ε of the models' LJ interaction parameters (see **Table 5.1** and **Table 5.2**).[11, 33, 39, 47, 54, 58, 59] The increase in the volume of exclusion of the molecules with increasing σ causes a decrease in the ρ, while the increase in the molecular energy of the molecules with increasing ε causes an increase in the ρ.[11, 39, 47, 58, 59]

The results seem to favour 1 and 8 models for the PEO and PPO monomer models, respectively. All of the other models fall outside the margins of error for the experimental values of 735 kg/m^3 for DE[76], and 725 kg/m^3 for MOE[77].

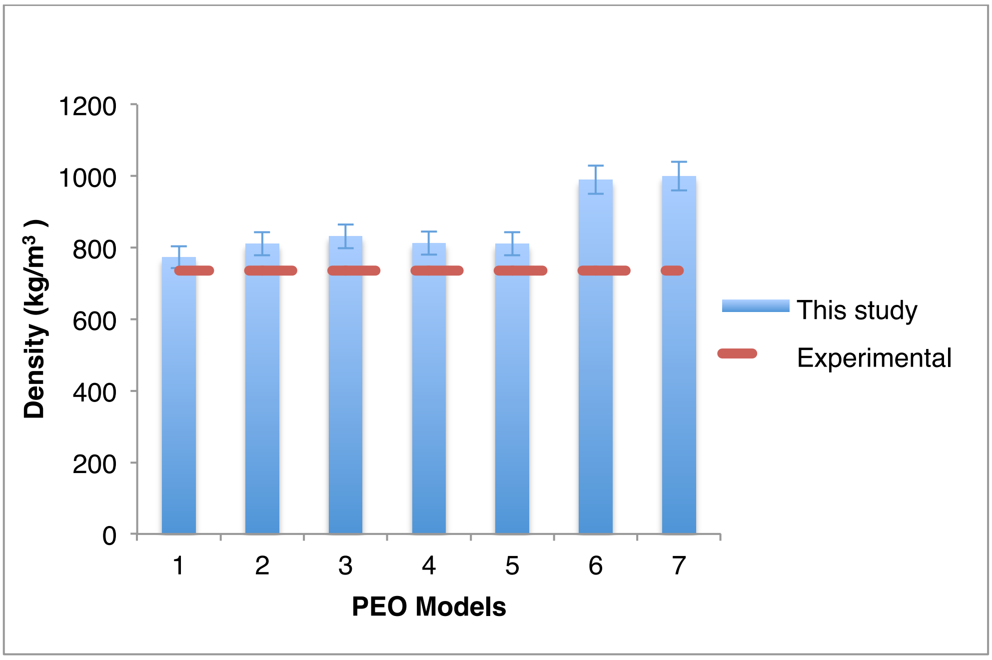

a)

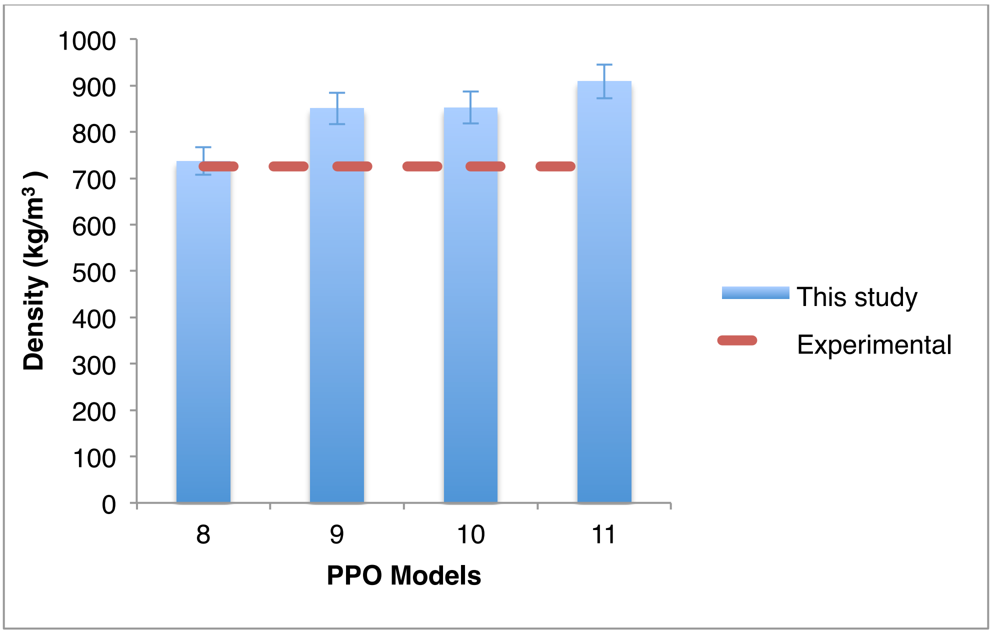

b)

Figures 5.2a-b: Comparison between the mass density of this study's models[15,17-23] and experimental data for **a)** DE[76] **b)** and MOE.[77]

In **Figures 5.3a-b**, the enthalpy of vaporisation results of the PEO and PPO monomer models can be seen. A complete table of these results is again available in **Tables 5.16a-b** in **Appendix B**. The ΔH_{vap} results are expected with theory as they can be seen to increase with both increasing ε and increasing σ.[33, 34, 37, 38, 47, 54, 58, 59] As the strength of the solvent-solute interactions increased, ΔH_{vap} increases, while the increased volume of exclusion of the solute and solvent molecules produced by the increasing σ, appears to have a negligible effect on the overall ΔH_{vap} here.[33, 34, 37, 38, 47, 54, 58, 59] This increase in the enthalpy of vaporisation results was also expected considering the results for ΔG_{solv}, which will be discussed below, as between the liquid and gas phases, solvation and vaporisation occur in converse directions.[47, 58, 59]

The result for model 1 is within the margins of error for the experimental enthalpy of vaporisation DE at 19.8 kJ/mol[83], while models 9 and 10 of the PPO monomer models fall within the margins of error for the experimental enthalpy of vaporisation of MOE at 24.5 kJ/mol[84], though just barely.

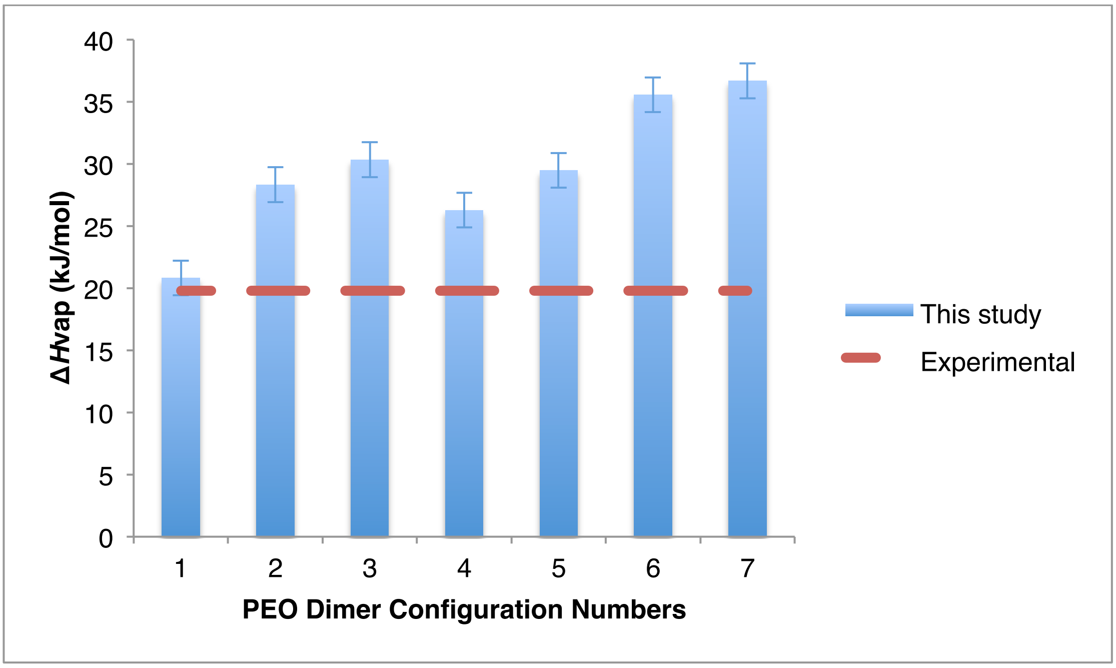
40
35
30
25
20
15
10
5
0
ΔHvap (kJ/mol)
1
2
3
4
5
6
7
PEO Dimer Configuration Numbers
This study
Experimental

a)

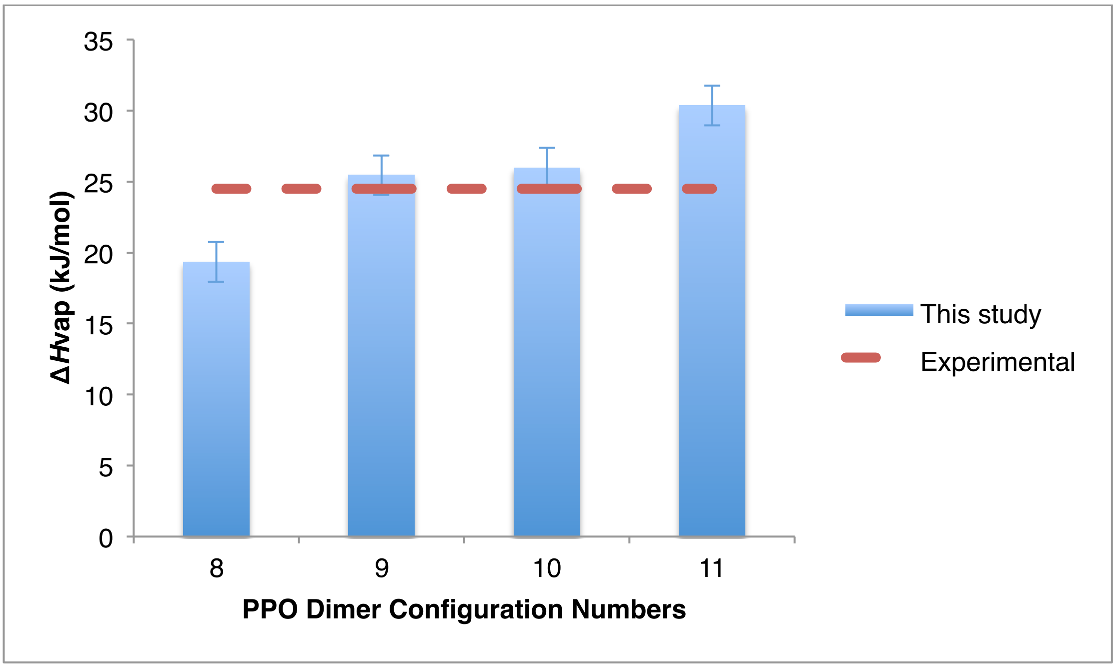

b)

Figures 5.3a-b: Comparison between the enthalpy of vaporisation of this study's models[15,17-23] and experimental data for **a)** DE[83] **b)** and MOE.[84]

The self-solvation free energies of the PEO and PPO monomer models can be seen in **Figures 5.4a-b**. A complete table of these results is again available in **Tables 5.17a-b** in **Appendix B**. The self-solvation free energy of these systems is shown to decrease with increasing ε and also with increasing σ, which is expected with theory.[34, 35, 36, 59] As the strength of the solvent-solute interactions increased, making ΔG_{solv} more favourable.[58, 59]. The increased volume of exclusion of the solute and solvent molecules produced by the increasing σ, caused a decrease in systemic density (i.e. the ΔG_{solv} becomes more positive or unfavourable), as shown above in the monomer density results.[58, 59] The increased solvent-solute interactions meant, however, that the enthalpic gain of making a solute bead outweighed the entropic cost (i.e. the ΔG_{solv} becomes more negative or favourable).[58, 59] Because of the trend of these results, the volume of exclusion component, appears to have a negligible effect on the overall ΔG_{solv} here.

The result for model 1 is within the margins of error for the estimated experimental self-solvation free energy of DE at -11.08 kJ/mol[76], while none of the PPO monomer models fall within the margins of error for the estimated self-solvation free energy of MOE at -13.09 kJ/mol[77], though models 9 and 10 come closest to the experimental target.

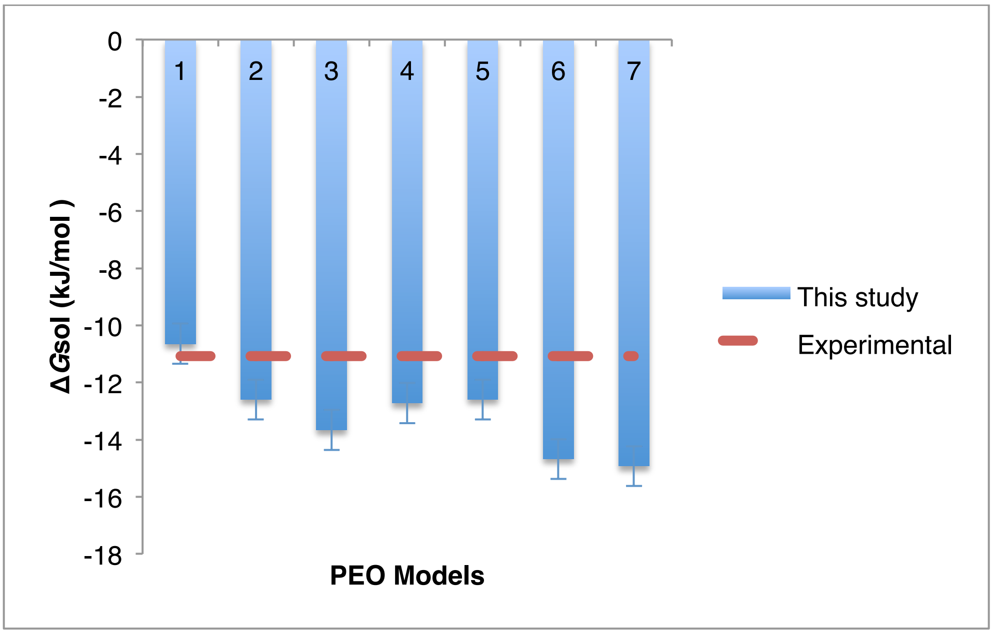

a)

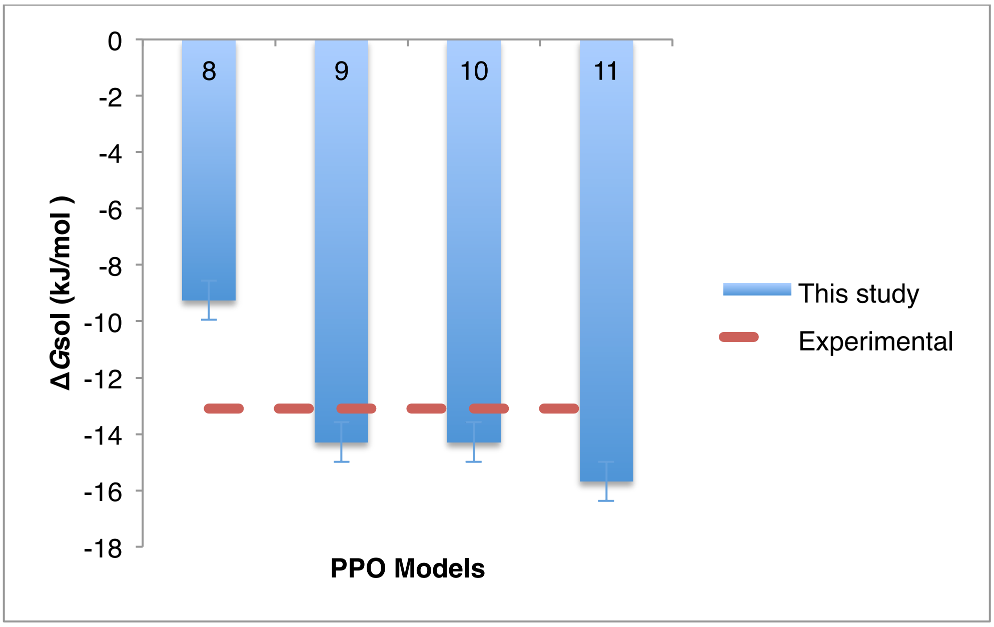

b)

Figures 5.4a-b: Comparison between the self-solvation of this study’s models[15,17-23] and estimated experimental data for **a)** DE[76] and **b)** MOE.[77]

While some conclusions can be made from these results in matching model parameters to PEO and PPO ρ, $\Delta\mathrm{H}_{\mathrm{vap}}$, and $\Delta\mathrm{G}_{\mathrm{solv}}$ data, more model parameters (in 2-bead models) needed to be tested to select the best models.

5.2.2 Pure PEO2 and PPO2

Figures 5.5a-c show the density results of the PEO2 models and the PPO2 models, with **Figure5.5b** showing the PPO2 models densities corrected and compared for DMP, and **Figure5.5c** showing the same with DEE. A complete table of all model results can be found in **Tables 5.18a-c** in **Appendix B**. As with the monomer models, the densities of the dimer models were generally shown to decrease with the σ and increase with the ε of the models, as is expected with theory for ρ.[11, 33, 39, 47, 54, 58, 59]

The ρ results seem to favour 1 and 8 models for PEO2 and PPO2 respectively. While they are not perfect matches for the experimental values of 945 kg/m^3 for DME, 855 kg/m^3 for DMP, and 801 kg/m^3 for DEE, the percent difference between the known data and the simulated ρ were at less than or near 10% for 2 of the values (6.34% for DME and 10.76% for DMP).[25, 26, 29, 52, 64, 65, 66] These percentage errors are comparable to those in former work which is promising, though the percent difference for DEE is 35.58%, which makes it unsuitable as a match for the simulated dimer.[17, 25]

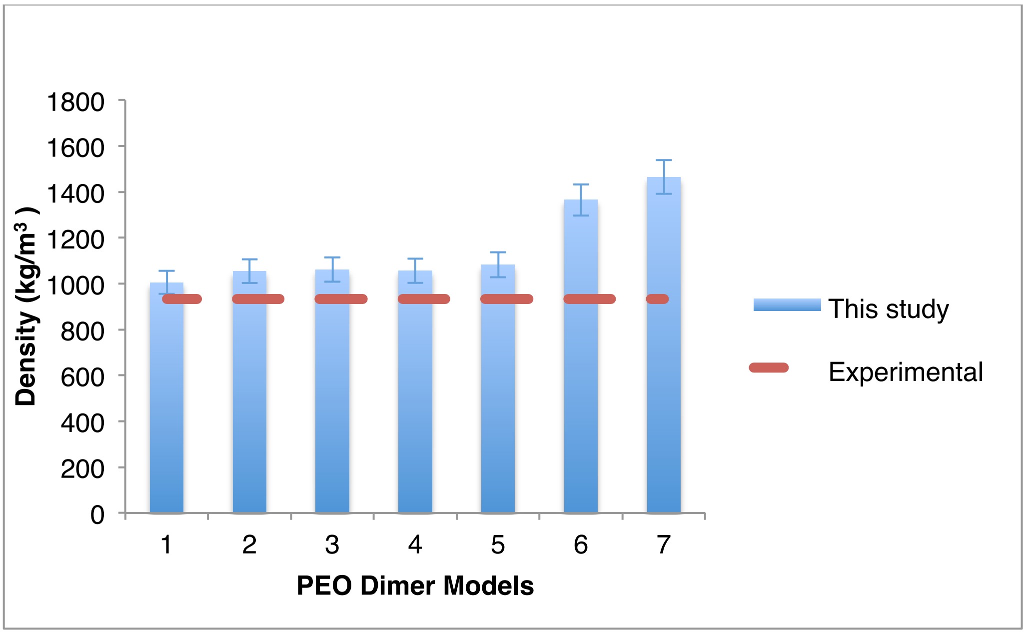

a)

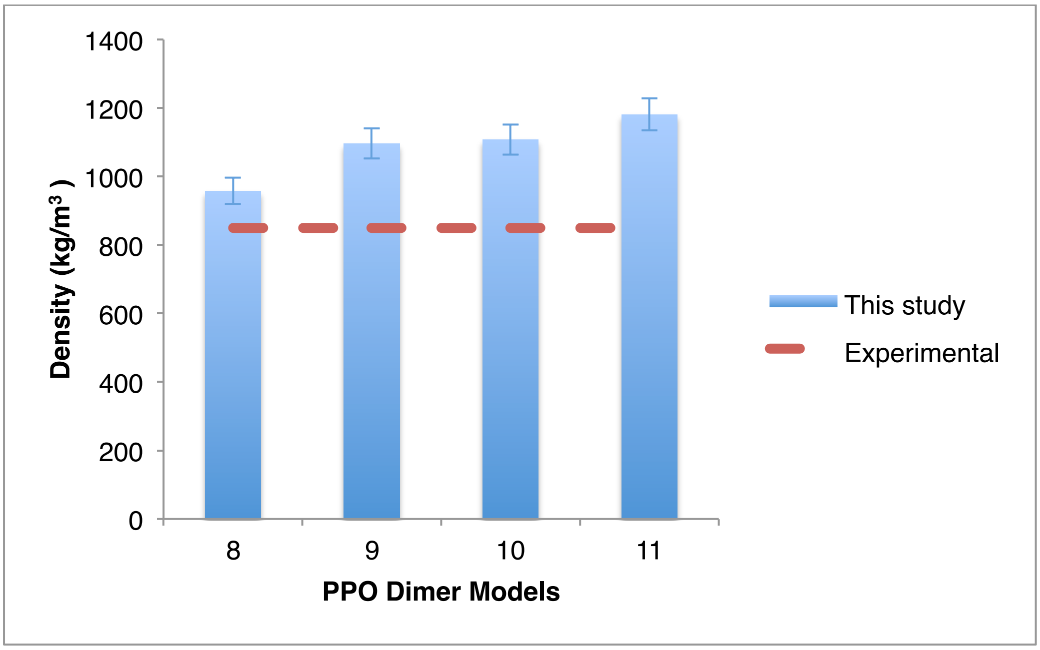

b)

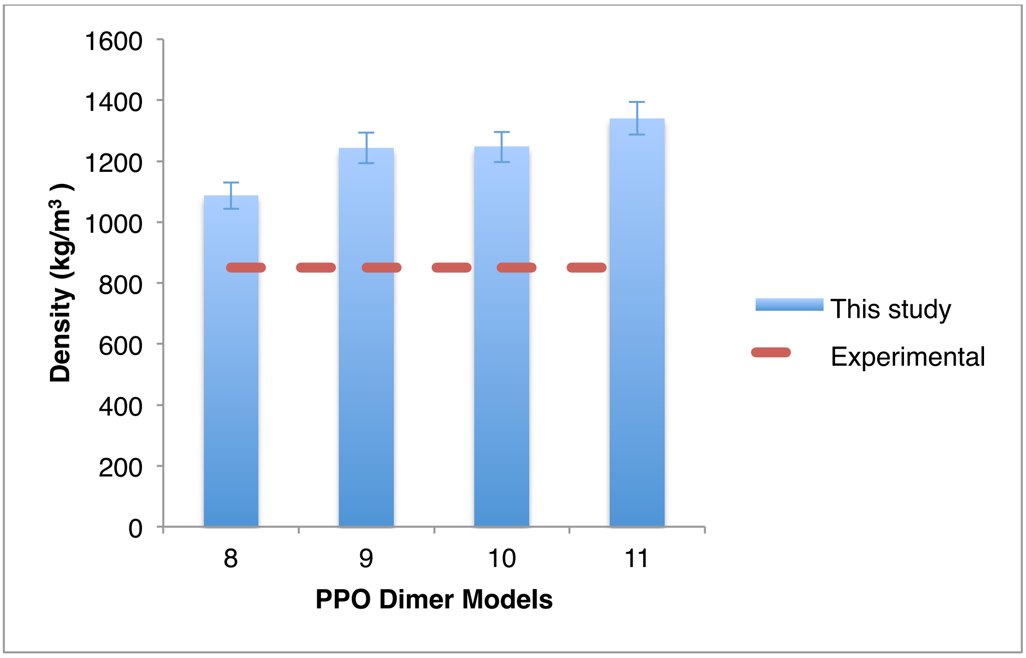

c)

Figures 5.5a-c: Comparison between the mass density of this study's models[15,17-23] and experimental data for **a)** DME[52, 66] **b)** DMP[26, 52], and **c)** DEE.[64, 65]

Figures 5.6a-b show the enthalpy of vaporisation results of both dimer simulation systems. A complete table of all of these results can again be found in **Tables 5.19a-c** in **Appendix B.** These figures show an increasing trend in the ΔH_{vap} with increasing ε as well as an increasing trend with increasing σ in our dimer systems. An increase of σ and ε also leads to an increase in the solution interaction energies, leading to an increase in ΔH_{vap}.[33, 34, 37, 38, 47, 54, 58, 59] The increase in σ leads to an increase in the volume of exclusion of the molecules, though as with ΔG_{solv} which will be shown in the next sections, it is negligible to the overall ΔH_{vap} here. This increase is also expected considering the results for ΔG_{solv}, as solvation and vaporisation occur in converse directions between the liquid and gas phases.[47, 58, 59]

These results show closest similarity of models 2 and 4, as well as model 8 with experimental values of 36.4kJ/mol for DME, and 37.02 kJ/mol and 36.3 kJ/mol for DMP and DEE respectively.[26, 27, 65, 66]. Model 1 is below the experimental values for DME, but was near enough that analysis of free energy results was needed before choosing a PEO2 model.

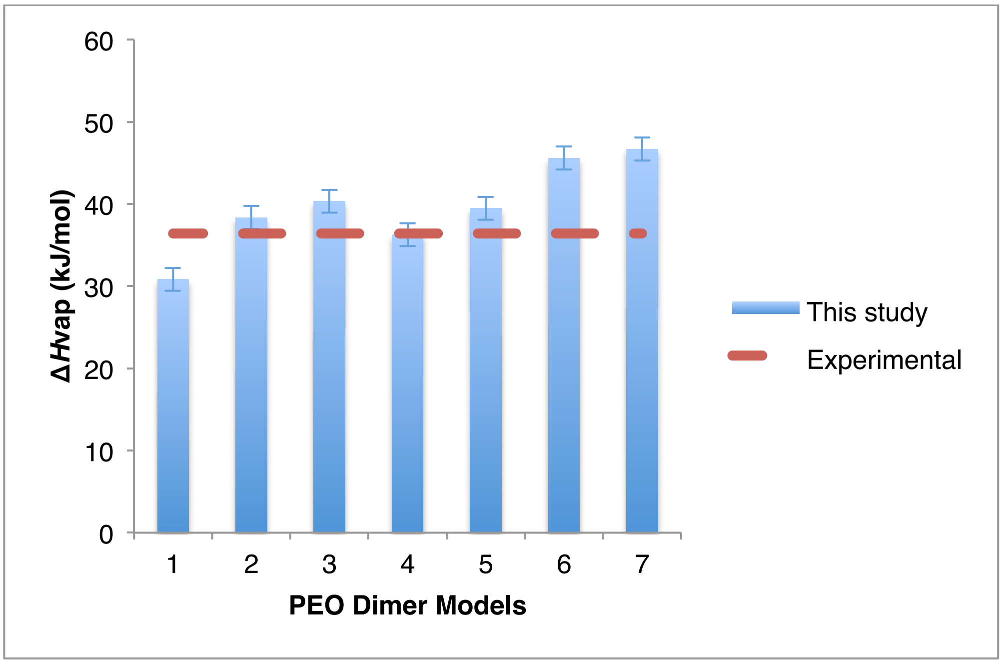

a)

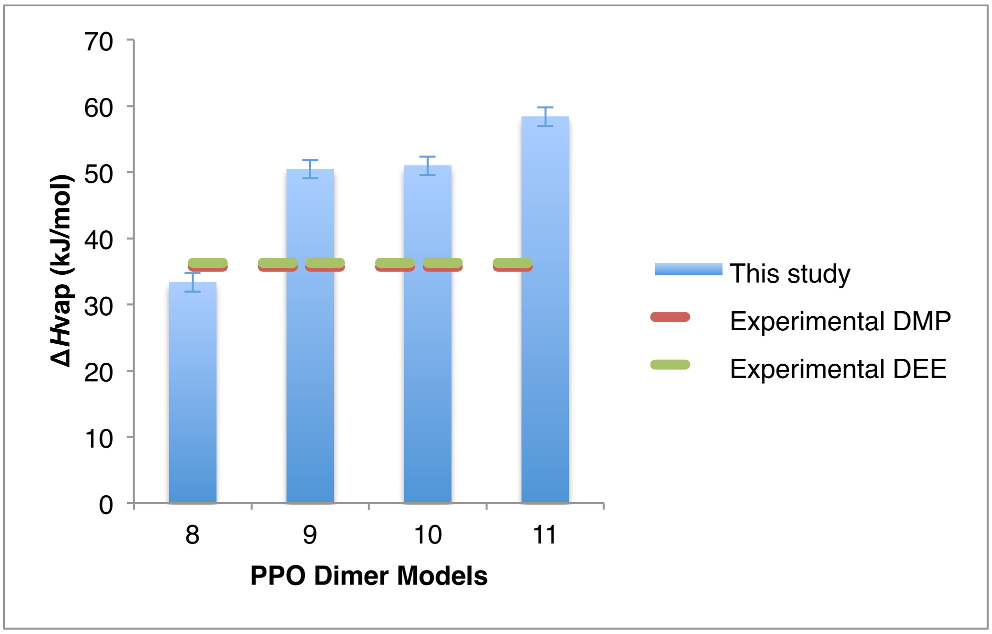

b)

Figures 5.6a-b: Comparison between the enthalpy of vaporisation of this study's models[15, 17-23] and experimental data for **a)** DME[27, 66] and **b)** DMP[26] and DEE.[65]

In **Figures 5.7a-b** the self-solvation free energies of the PEO2 models and the PPO2 models are shown. A complete table of all of these results can again be seen in **Tables 5.20a-c** in **Appendix B**. The solvation energies again fit with expected theory, decreasing with increasing σ and ε parameters.[34, 35, 36, 59] This is because the strength of the solvent-solute interactions increased, making ΔG_{solv} more favourable. As these simulations were CG dimers with rigid bonds, the intramolecular forces seem to have a negligible effect on the overall solvation free energy.[59]

The 1 and 8 models' ΔG_{solv} here appear to be closest to a previous AA study's results of -17.0 ± 0.9 kJ/mol for DME and -15.0 ± 0.9 kJ/mol for DMP, though far outside the margins of error.[25] These models were also the closest to the estimated experimental data, within the margins of error for the ΔG_{solv} of -19.32 kJ/mol for DME[57, 66], -20.43 kJ/mol for DMP[26, 57], and -21.78 kJ/mol for DEE.[64, 65].

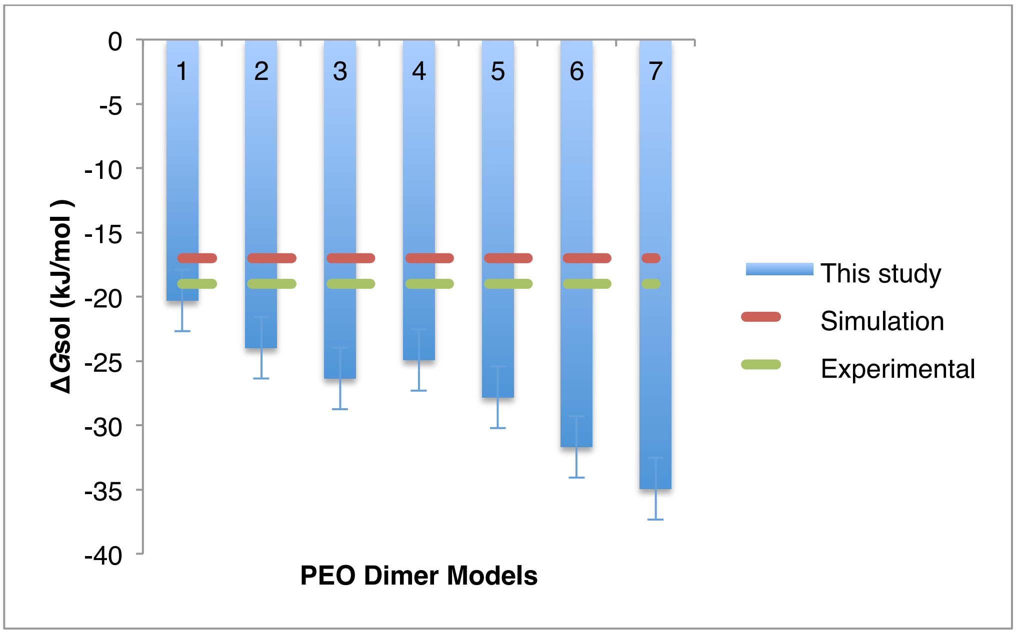

a)

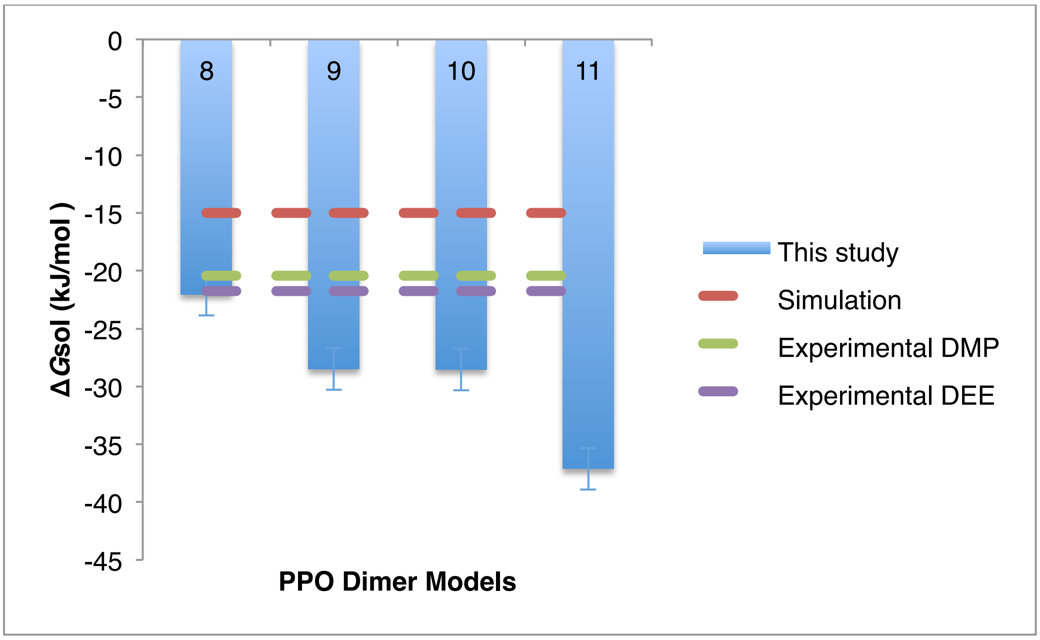

b)

Figures 5.7a-b: Comparison between the self-solvation of this study's models[15,17-23] and a previous AA simulation study's data[25] as well as calculated experimental data for **a)** DME[57, 66] and **b)** DMP[26, 57] and DEE.[64, 65]

Figures 5.8a-b express the self-diffusion coefficients for the PEO2 and PPO2 models. A complete table of these results compared to experimental values can be seen in **Tables 5.21a-b** in **Appendix B**. The D results are inline with expected theory, in terms of density and ε.[33, 53, 60, 61] Self-diffusion coefficients exhibit a strong dependence on the number of particles in the simulated system, and thus a strong dependency on the density of the system.[60, 61] The simulations were thus kept at the same number of particles and configuration for every simulation type (i.e. dimer-dimer simulations were kept at one size, dimers in water another, etc), for consistency between models and as these configurations had lead to density near experimental values.[28, 29] As can be seen in the figures, the PEO2 model 1 self-diffusion results were the only model's results within the margin of error to the experimental value for DME of 3.2 x $10^{-9}m^2/s$[28], while the PPO2 model 8 results were the closest to the AA simulation study's results for DMP of 3.6 x $10^{-9}m^2/s$.[25]

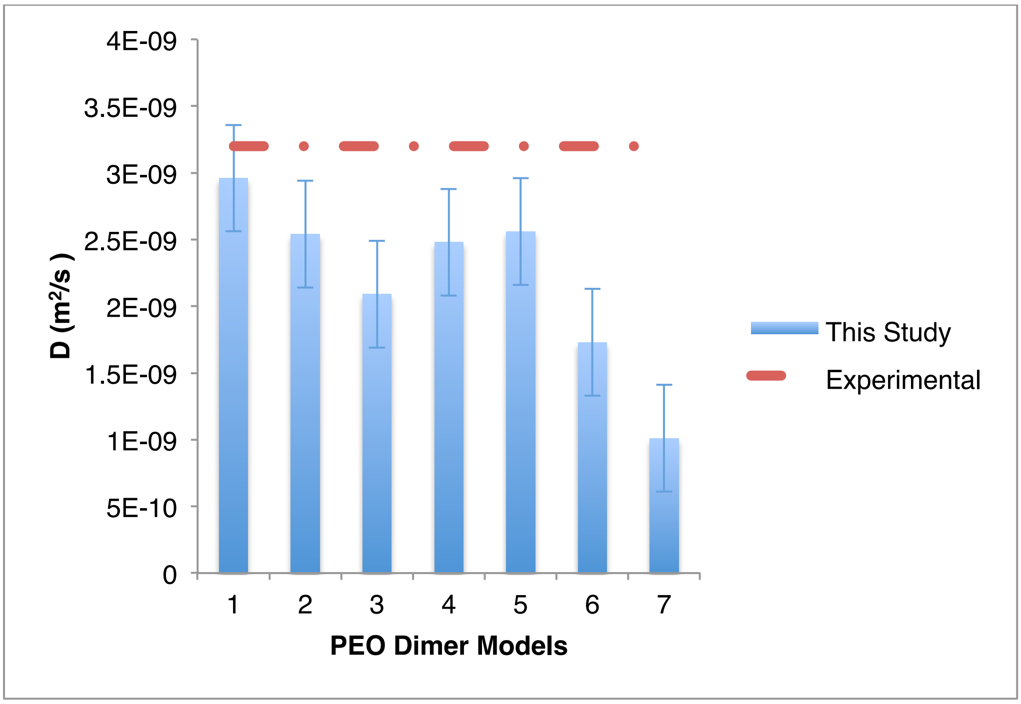
4E-09
3.5E-09
3E-09
2.5E-09
2E-09
1.5E-09
1E-09
5E-10
0
D (m²/s)
1
2
3
4
5
6
7
PEO Dimer Models
This Study
Experimental

a)

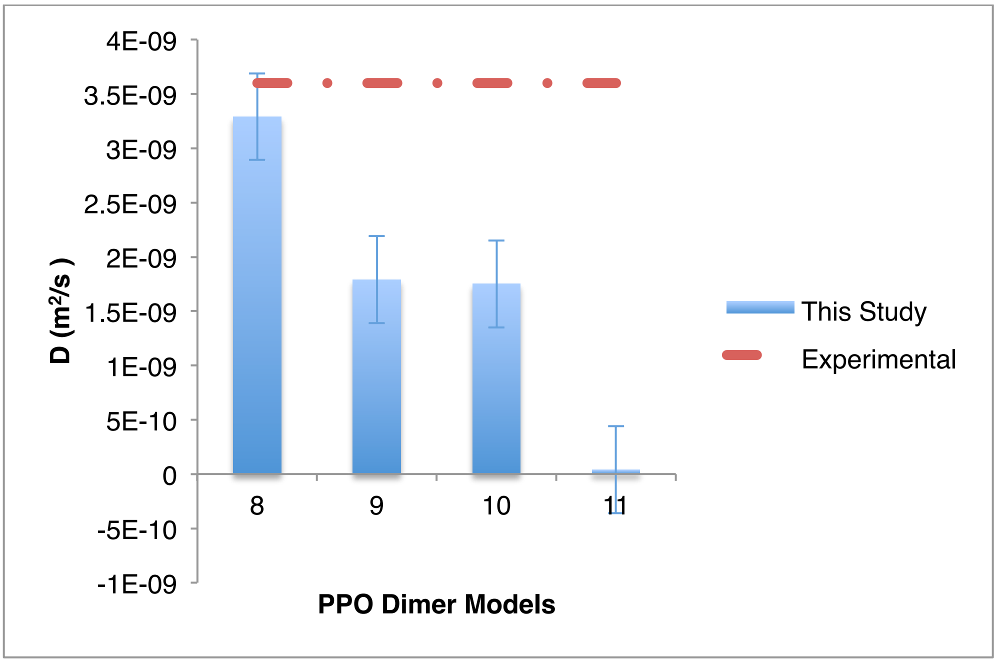

b)

Figures 5.8a-b: Self-diffusion coefficient results for this study's **a)** PEO2 models compared to the experimental data for DME[28], and **b)** PPO2 models compared against simulation results from a previous study for DMP.[25]

In **Figures 5.9a-b**, we can see the shear viscosity results for the PEO2 and PPO2 models. A complete table of these results compared to experimental values can again be found in **Tables 5.22a-b** in **Appendix B**. When there is a change in the total potential energy between two molecules, it affects the total viscosity of a substance, meaning a liquid with smaller molecules with lower LJ forces has a lower viscosity, or ability for molecules to slide past each other, than a liquid with larger molecules with higher LJ forces.[60, 61] The viscosity of our models therefore adhere to η theory as it increases with *ε*.[60, 61] The results again seem to validate models 1 and 8, with model 1's shear viscosity results being the closest to the experimental shear viscosity of 0.41m^2/s for DME[29], while model 8's results compared most closely with the AA simulation results of 0.34m^2/s for DMP.[25] It should be noted however, that models 2 through 5 also fall within the margin of error for DME, though are higher than the results for model 1.[29] Coupled with the D results, the η results provided addition confirmation of the suitability of models 1 and 8 for use with these copolymer components.

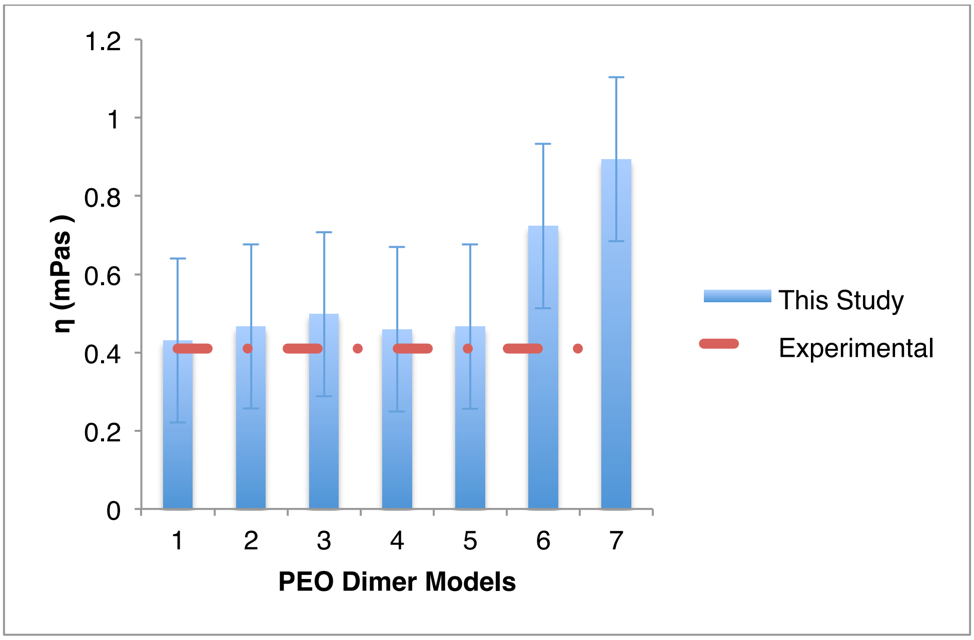

a)

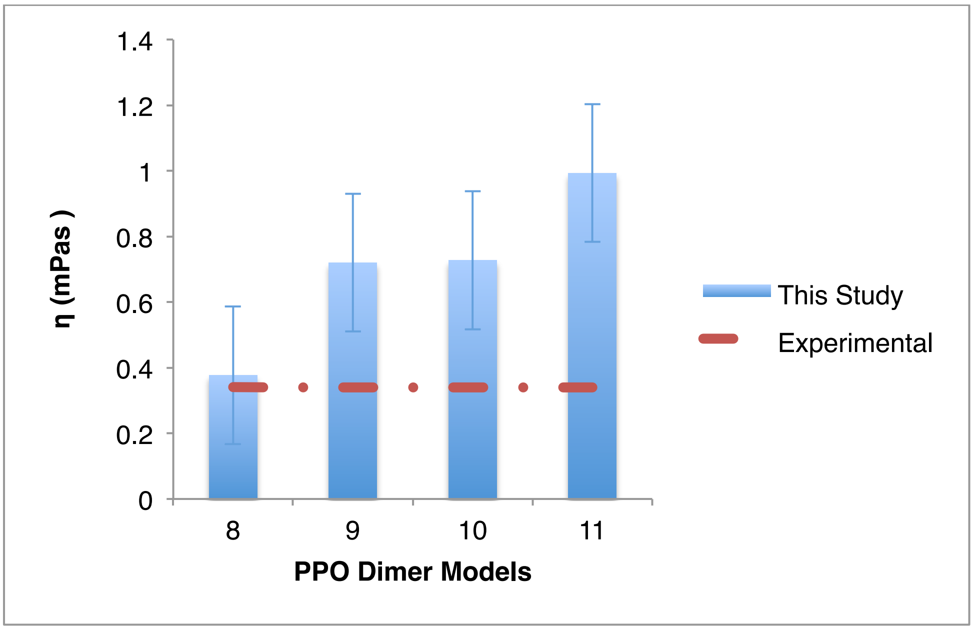

b)

Figures 5.9a-b: Shear viscosity results for this study's **a)** PEO2 models compared against simulation results from a previous study for DME, and **b)** PPO2 models compared against a separate simulation results from a previous study for DMP.[25, 29]

5.2.3 PEO2 and PPO2 in water

Figures 5.10a-b show the solvation free energies of the PEO2 and PPO2 models in water. A complete table of these results is again available in **Tables 5.23a-b** in **Appendix B**. The solvation free energies in MARTINI water also appear to adhere to expected theory regarding non-bonded σ and ε parameters, though only model 8 falls inside the margin of error for the respective comparable experimental and previous AA study ΔG_{solv} values.[25, 27, 28, 47, 58, 59]

The 1 and 8 models provided the closest results to the experimental data of -20.9 kJ/mol for DME[27, 28], and previous study's result of -16.0 kJ/mol for DMP.[25] These results are more favourable than the self-solvation energies, implying that model 1 and 8's dimers are more likely to easily dissolve in water.[4, 7, 47]

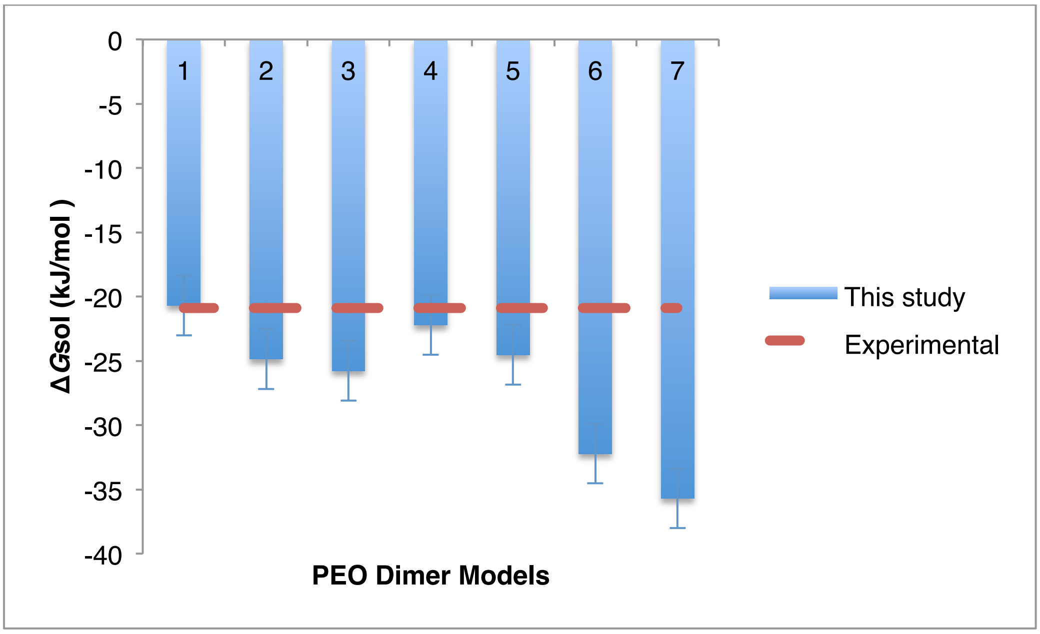

a)

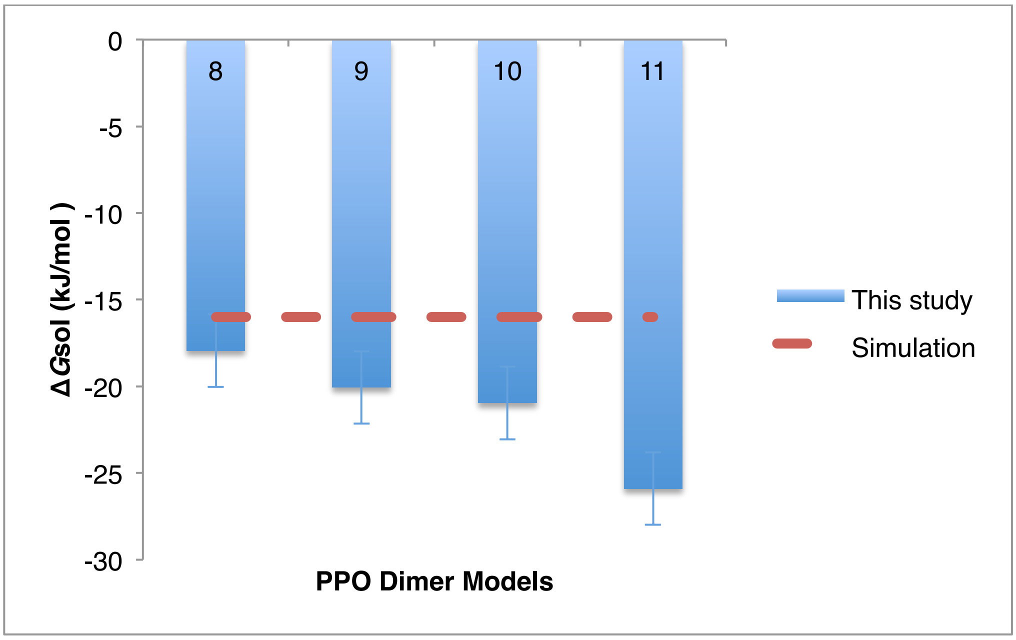

b)

Figures 5.10a-b: Comparison between the solvation in water of this study's models[15-23] and **a)** experimental data for DME[27, 28] and **b)** previous simulation data for DMP.[25]

Based on the above results, it seemed clear that model 1 and model 8 were the best matched for PEO2 and PPO2, therefore those were the models chosen for calibration of interaction parameters with our alkane models (section 5.2.4). They were also further validated for properties of longer PEO and PPO chains in both water and alkane solvents (section 5.2.5).

5.2.4 PEO2 and PPO2 in alkanes

After models 1 and 8 were chosen for PEO and PPO, their non-bonded interactions with our alkane models were calibrated so that free energies of solvation could be calculated.

The only experimental values for free energies of solvation that could be compared to PEO, PPO, and PEO2 in alkanes were found for the solvation of DE, MOE, and DME in hexadecane.[24] In order to parameterise the non-bonded interactions for model 1 and model 8 (i.e. PEO and PPO) in our hexadecane model, we ran solvation simulations of single PEO and PPO beads in our 4:1 mapped 4-bead hexadecane model (see **Table 5.3**), and also in a 2:1 mapped 8-bead hexadecane model (using our 2:1 mapped bead parameters, available in Chapter 4 in **Tables 4.9a-c**). Both of these hexadecane models were used so that non-bonded parameters for our 3:1 and 3.5:1 mapped models could be interpolated, and those results could be used to estimate non-bonded parameters for the PEO and PPO models in our heptane and hexane models. The σ for the non-bonded interaction of PEO and PPO in the 4:1 and 2:1 mapped models were found by fixing the σ to 0.47nm (the MARTINI standard), and the ε values were fitted using a similar process to that used in Chapter 4, running simulations at the same σ over varying ε values. When non-bonded interactions were matched to experimental values for both the PEO and PPO models in our 4:1 and

2:1 mapped hexadecane models, those for our 3:1 and 3.5:1 mapped models were interpolated, and these results can be seen in **Table 5.5**.

Mapping Scheme	**Non-bonded Interactions**			
	PEO-Alkanes		**PPO-Alkanes**	
	σ **(nm)**	***ε*** **(kJ/mol)**	***σ*** **(nm)**	***ε*** **(kJ/mol)**
2:1	0.47	3.0	0.47	3.14
3:1	0.47	*2.87*	0.47	*3.02*
3.5:1	0.47	*2.75*	0.47	*2.89*
4:1	0.47	2.64	0.47	2.76

Table 5.5: Non-bonded interactions for this study's models of PEO[15] and PPO[20] in our 2:1, 3:1, 3.5:1, and 4:1 alkane models. Fitted data is underlined, while interpolated data is italicised.

These results again adhere to ΔG_{solv} theory in regards to σ and ε.[47, 58, 59] The ΔG_{solv} experimental values in comparison with the results from the chosen PEO and PPO models in all our hexadecane models can be seen in **Tables 5.6a-b**.

Hexadecane Models	ΔGsol (this study, kJ/mol)	ΔGsol (experimental [24], kJ/mol)
2:1	-6.20 ± 0.43	-6.21
3:1	-6.17 ± 0.46	-6.21
3.5:1	-6.18 ± 0.42	-6.21
4:1	-6.19 ± 0.54	-6.21

a)

Hexadecane Models	ΔGsol (this study, kJ/mol)	ΔGsol (experimental [24], kJ/mol)
2:1	-8.48 ± 0.45	-8.49
3:1	-8.46 ± 0.49	-8.49
3.5:1	-8.47 ± 0.46	-8.49
4:1	-8.47 ± 0.47	-8.49

b)

Tables 5.6a-b: Free energy of solvation results in our hexadecane models for this study's chosen **a)** PEO monomer model[15] compared against experimental data for DE[24], and **b)** PPO monomer model[20] compared against experimental data for MOE.[24]

As there was experimental data for DME in hexadecane, the chosen PEO2 was also solvated in the hexadecane models, and the free energies of solvation compared against the experimental value can be seen in **Table 5.7**.

Hexadecane Models	ΔGsol (this study, kJ/mol)	ΔGsol (experimental [24], kJ/mol)
2:1	-15.21 ± 0.49	-15.17
3:1	-15.17 ± 0.42	-15.17
3.5:1	-15.12 ± 0.40	-15.17
4:1	-15.09 ± 0.44	-15.17

Table 5.7: Free energy of solvation results in our hexadecane models for this study's PEO2 model[15] compared against experimental data for DME[24].

All of the calibrations of the non-bonded interactions between the selected PEO, PPO, and PEO2 models in our hexadecane models fell within the margins of error for the experimental values of DE, MOE, and DME, and were deemed good parameter pairs to estimate interaction levels for the PEO2 and PPO2 models in our heptane model, and the PEO2 model in our hexane model.

In **Table 5.8**, the solvation free energy results for both the PEO2 and the PPO2 models in our heptane beads can be seen. The heptane beads used in both the PEO2 and PPO2 simulations were based on an interaction level estimated from our PEO and PPO model non-bonded interaction levels in hexadecane (i.e. $\sigma = 0.47$ and $\varepsilon = 2.66$ for PEO2 in heptane, and $\sigma = 0.47$ and $\varepsilon = 2.72$ for PPO2 in heptane). These interaction levels ensured that models 1 and 8 were within the AA study's results of -11.1 ± 0.5 kJ/mol for DME and -12.7 ± 0.5 kJ/mol for DMP.[25] As there is no known solvation experimental data for DME, DMP, or DEE in heptane, however, this only serves to show an encouraging trend between ΔG_{solv} and the interaction levels used, as well as added validation of the capabilities of our alkane models from Chapter 4.

PEO/PPO Models	**ΔGsol (this study, kJ/mol)**	**ΔGsol (simulation [25], kJ/mol)**
PEO2	-11.76 ± 0.43	-11.1 ± 0.5
PPO2	-13.08 ± 0.49	-12.7 ± 0.5

Table 5.8: Free energy of solvation results in our heptane models for this study's PEO2[15] and PPO2[20] models compared against simulated data for DME[25] and DMP[25].

Table 5.9 shows the solvation free energy of the PEO2 models in our hexane model compared with three simulation studies.[15, 30, 32] The CG study by Lee et al. 2011[30], and the AA study by Jorgensen et al.[32] were chosen for comparison as they had been used for evaluation in the Taddese et al. study.[15] As mentioned before, the Lennard-Jones interaction parameters between the models and our hexane were estimated from our interaction levels in hexadecane, and ended up matching those from the CG simulation study done by

Taddese et al.[15] (i.e. $\sigma = 0.47$ and $\varepsilon = 2.9$), while retaining the original bonded parameters of the PEO model.[15] The solvation free energy of model 1 again seems to fit with expected theory, and model 1 was within the margins of error for the CG study by Taddese et al.'s results[15], but were lower than the AA study by Jorgensen et al.'s results[32], and the CG model proposed by Lee et al.'s results.[15, 30] Model 1 was well within the margin of error for the results from Taddese et al.[15] and the interpolated results from Jorgensen et al.[32], which was decided to be a good level of agreement. As there is again no available data for the solvation of DME in hexane, these simulations helped to further show theoretical trend of ΔG_{solv}, and advance the validation of our own CG MARTINI alkanes for use with PEO.

PEO Models	**ΔGsol (this study, kJ/mol)**	**ΔGsol (simulation [15], kJ/mol)**	**ΔGsol (simulation [32], kJ/mol)**	**ΔGsol (simulation [15, 30], kJ/mol)**
PEO2	-13.84 ± 0.63	-14.08 ± 0.01	-14.66 ± 0.3	-17.73 ± 0.01

Table 5.9: Comparison between this study's chosen model of PEO2[15] in our CG MARTINI hexane and simulation data.[15, 30, 32]

5.2.5 PEO and PPO chains

To help further the validation of models 1 and 8 for PEO and PPO, longer chains were created for testing using their respective studies' angle and dihedral bonded interaction information as well as the bonded information from 3 other studies. The bonded interactions ultimately chosen can be seen in **Table 5.10**[15, 20], and the angle and dihedral parameters for all of the PEO and PPO models can be found in **Tables 5.23a-b** in **Appendix B**.

PEO and PPO Model	**Bonded Interactions**			
	θ (deg.)	**kθ (kJ/mol)**	**Φ (deg.)**	**kΦ (kJ/mol)**
1[20]	124	50	180	1.96. .18, .33, .12
8 [15]	120	50	180	1.96. 5.0, .33, .12

Table 5.10: Bonded angle and dihedral interaction parameters for out chosen CG MARTINI PEO and PPO model's beads.[15, 20]

In **Figures 5.11a-b** and **Figures 5.12a-b** the end-to-end distances of PEO and PPO homopolymers based on our chosen models of lengths 2 and 36, in MARTINI water and our heptane model, respectively, in comparison to a previous study's AA simulation work, can be seen.[51]

Tables of these results compared to experimental data are shown in **Tables 5.25a-b** in **Appendix B**. While the radius of gyration is a significant measure of the overall size of a long polymer chain, the end-to-end distance is an effective way to calculate the coil size.[67, 68] The results of these chains adhere to expected theory of end-to-end distances, increasing significantly with the length of the chain, the more hydrophobic PPO chains with decreased ε Lennard-Jones interaction parameters with the solvents producing shorter chains in the solvent, and all results generally decreasing in the alkane solvent with lower polarity from those in water.[67, 68] While this study's results are slightly increased relating to the AA study, all of the end-to-end distance results fall within the margin of error of those from the previous simulation work.[51] Since the comparison is to simulated results, it is again important to note that this study's results are to primarily show trend.

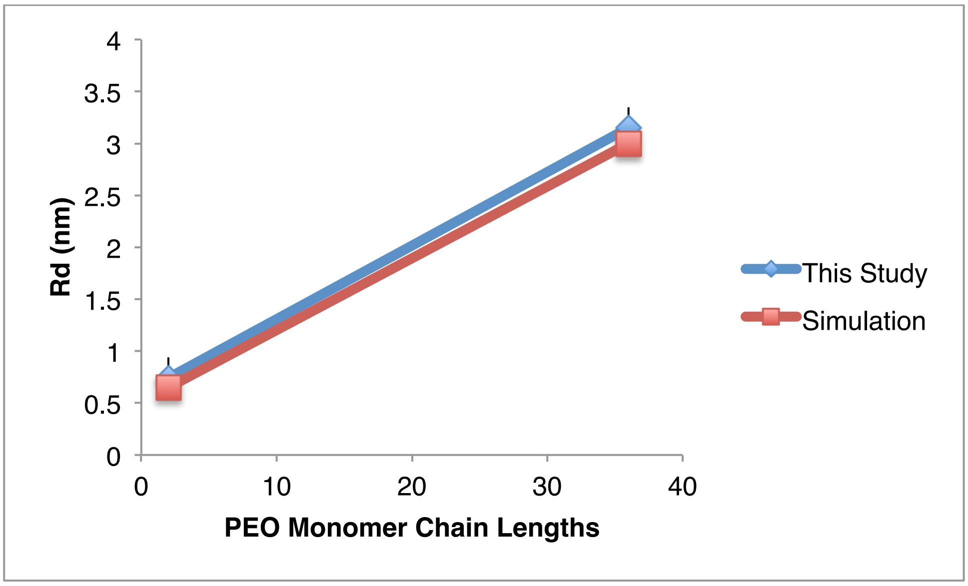

a)

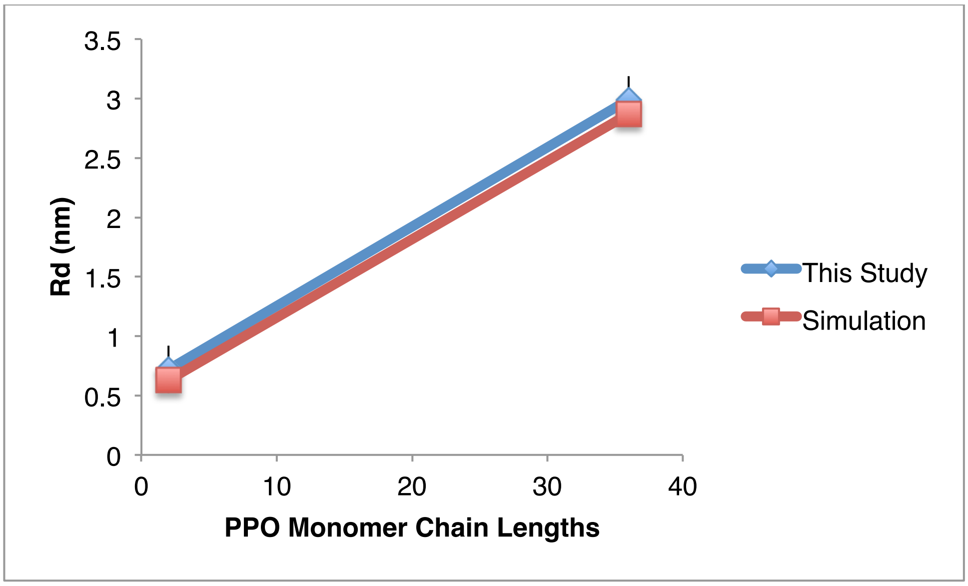

b)

Figures 5.11a-b: End-to-end distances for this study's **a)** PEO and **b)** PPO homopolymers of lengths 2 and 36 in CG MARTINI water compared to a previous simulation study.[51]

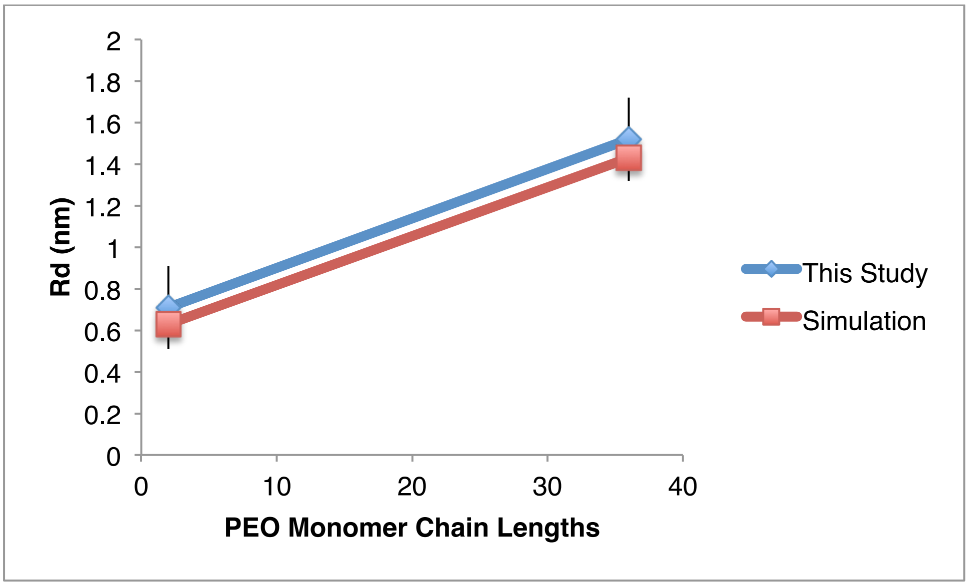

a)

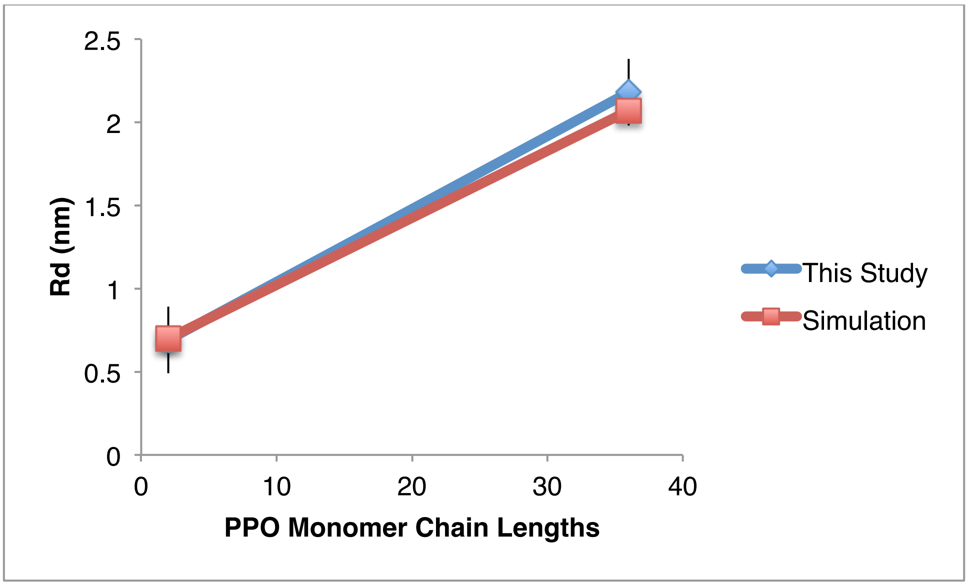

b)

Figures 5.12a-b: End-to-end distances for this study's **a)** PEO and **b)** PPO homopolymers of lengths 2 and 36 in our heptane models compared to a previous simulation study.[51]

Tables 5.11a-b show the persistence lengths of PEO and PPO monomers compared to a previous study's CG simulation work.[20] The persistence length is the distance along a molecule where the orientation of a single segment loses its correlation with the orientation of a different segment.[67, 69] The persistence lengths of both the PEO and PPO models are fairly similar, which is expected as end-to-end distances of both PEO2 and PPO2 in water and heptane were also very close to each other.[69] Comparison of the PEO persistence length to a further AA study was done for an extra level of detail, though again these results are to primarily show trend as no experimental data was available.

PEO/PPO Monomers	**Persistence Length (this study, nm)**	**Persistence Length (simulation, [20], nm)**
PEO	0.41 ± 0.10	0.37
PPO	0.45 ± 0.08	0.40

a)

PEO/PPO Monomers	**Persistence Length (this study, nm)**	**Persistence Length (simulation, [31], nm)**
PEO	0.41 ± 0.10	0.37

b)

Tables 5.11a-b: Persistence lengths for **a)** this study's chosen PEO and PPO models compared against a previous CG simulation[20], and **b)** just our PEO model compared to a separate AA simulation study, for further validation.[31]

Tables 5.12a-b, and **Table 5.13**, show the relaxation times of PEO and PPO monomer chains for lengths of 36 in MARTINI water and our hexane compared to a previous study's CG simulation work[20], and PEO and PPO monomer chains for lengths of 30 in our heptane compared to a previous study's AA simulation work.[51] The relaxation times show that in all three solvents the PEO homopolymers are characterised by faster relaxation times than those of the PPO homopolymers models. This meets with predicted theory, due to the longer bond length of the PPO model as well as the decreased ε Lennard-Jones interaction parameters between PPO and the solvents.[15, 20, 70] This study's results are within the margin of errors for the results of the previous CG simulation, and as the PPO is taken directly from that study it makes sense that its homopolymers relaxation time in MARTINI water in **Table 5.12a** is nearly exactly the same as the one done by the original researchers.[20] The much faster relaxation times of both of this study's models in hexane than those in MARTINI hexane as seen in **Table 5.12b** can be accounted for by the vastly different non-bonded and bonded interaction parameters of our hexane model.[20] As shown in **Table 5.13**, the CG models relaxed faster, significantly so in the case of PPO, in our heptane model than the models in the AA simulation study.[51, 70]

PEO/PPO Homopolymers	Relaxation Time in Water (this study, ps)	Relaxation Time in Water (simulation, [20], ps)
PEO30	155 ± 0.09	160
PPO30	250 ± 0.11	251

a)

PEO/PPO Homopolymers	Relaxation Time in Hexane (this study, ps)	Relaxation Time in Hexane (simulation, [20], ps)
PEO30	34 ± 0.10	41
PPO30	37 ± 0.11	49

b)

Tables 5.12a-b: Relaxation times for this study's CG MARTINI PEO and PPO homopolymers of lengths 30 in **a)** MARTINI water and **b)** our hexane model compared to a previous simulation study.[20]

PEO/PPO Homopolymers	Relaxation Time in Heptane (this study, ps)	Relaxation Time in Heptane (simulation, [51], ps)
PEO36	85 ± 0.13	157.7
PPO36	109 ± 0.12	604.8

Table 5.13: Relaxation times for this study's CG MARTINI PEO and PPO homopolymers of lengths 36 in our heptane model compared to a previous simulation study.[51]

Figures 5.13a-b shows the radii of gyration for PEO and PPO chains based on our chosen models, of lengths 30, 60, and 90, in comparison to a previous study's work.[12] A complete table of these results compared to experimental values can again be found in **Table 5.26** in **Appendix B**. As the radius of gyration is the average squared distance of any point in a molecule chain from it's centre of mass, the results are expected with theory.[7, 62, 63] This means the longer the bond length and larger the bond angle or dihedrals, as well as an increase in molecular weight, the larger the radius of gyration.[7, 54, 56, 62, 63] The simulated results also from this study for the various chains appeared to be within the margin of error.[12] The simulated molecules in the solution can therefore also be interpreted to be within accepted parameters and also of the correct size for their compositions.[7, 12, 63]

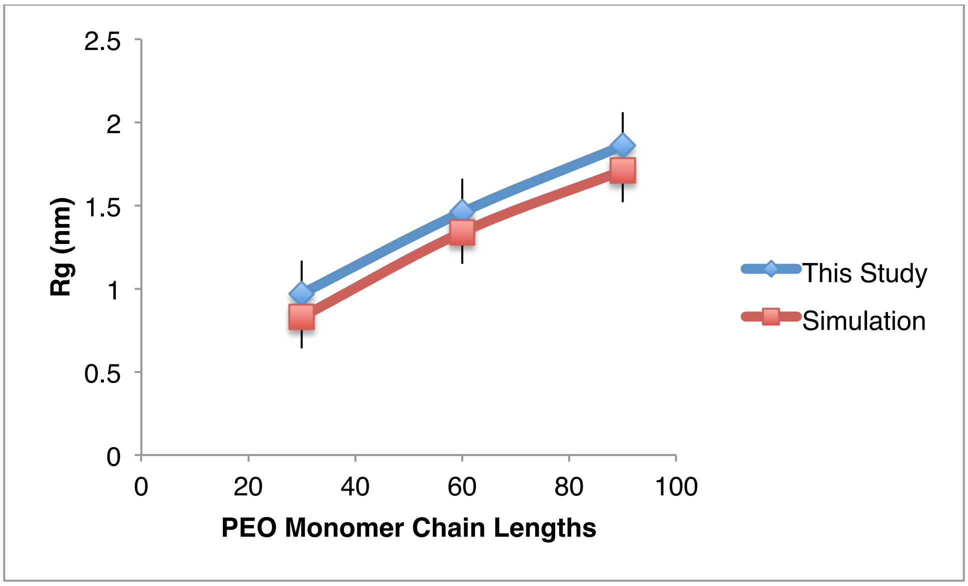

a)

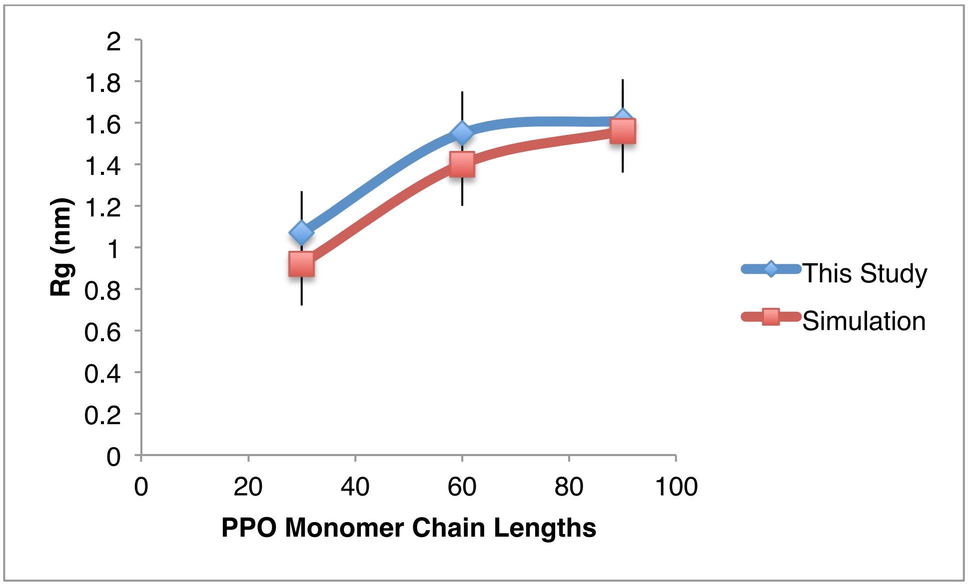

b)

Figures 5.13a-b: Radius of gyration results for this study's CG MARTINI **a)** PEO and **b)** PPO monomers of lengths 30, 60, and 90 in CG MARTINI water compared to the results from a previous study.[12]

Table 5.14 shows the radii of gyration for PEO and PPO chains based on our chosen models, of lengths 36, in our CG MARTINI heptane model in comparison to a previous study's work.[51] These results help to further confirm our alkane parameters, as the radii are again within the margin of error with the other simulation results, again increasing with the weight of the molecules, and can be interpreted to be proficient models for chain behaviour in PEO and PPO monomers.[4] Example snapshots, taken from VMD, of the 36 monomer PEO and PPO simulations can be seen in **Figures 5.14a-d**, where the hydrophilic and hydrophilic propensities of PEO and PPO in water (and the reverse in heptane) are evident. [50]

PEO/PPO Monomers	Radius of Gyration in Heptane (this study, nm)	Radius of Gyration in Heptane (simulation, [51], nm)
36 PEO	0.87 ± 0.29	0.75 ± 0.01
36 PPO	1.13 ± 0.22	0.99 ± 0.03

Table 5.14: Radius of gyration results for this study's CG MARTINI PEO and PPO monomers of length 36 compared to the results from a previous study.[51]

Evident in the example snapshots in **Figures 5.14a-b**, when the PEO chains were simulated in the water they assumed a stretched conformation, while when simulated in the hexane they were significantly more coiled. This is in line with expected theory and experiments on the nature of real chains of this polymer, as well as self-assembly behaviour of surfactants using these polymers as their block component.[1, 2, 4, 5] This is because polar aqueous solutions cause hydrophilicity in PEO, while nonpolar aqueous solutions cause lipophobicity in PEO.[1, 2, 4, 5]

Shown in **Figures 5.14c-d,** the simulated PPO chains curl in on themselves when solvated in water and stretch out more when solvated in heptane, showing hydrophobicity expected from real PPO chains in polar aqueous solutions, and their lipophilicity in nonpolar aqueous solutions.[1, 2, 4, 50] These results were quite promising, as they imply that models 1 and 8 are showing the correct qualitative behaviour in different solvents[1, 2, 4, 50], and thus could potentially lead to self-assembly of Pluronic block copolymers, as seen in experimental studies.[78-82]

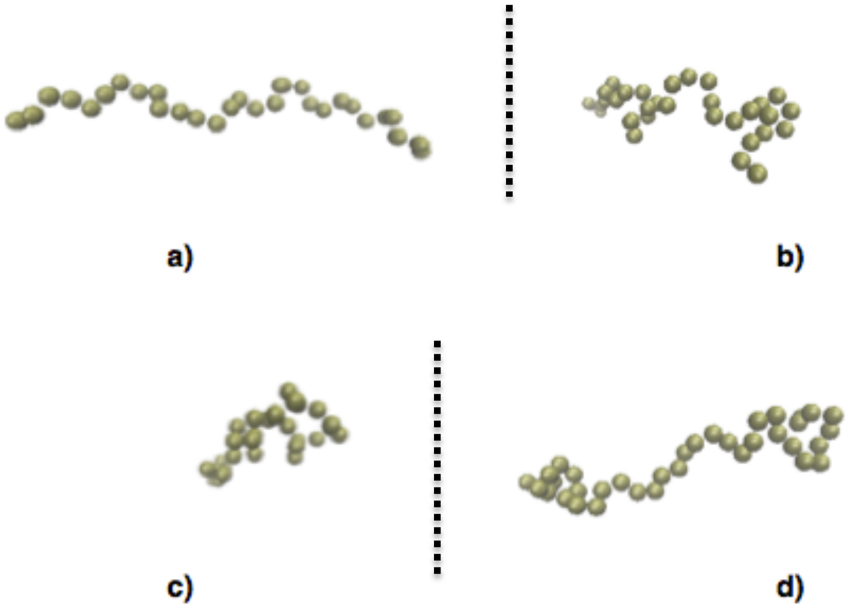

Figures 5.14a-d: Snapshots of the 36 monomer chains solvated in MARTINI water and our heptane model; **a)** PEO in water, **b)** PEO in heptane, **c)** PPO in water, and **d)** PPO in heptane. The solvent molecules have been removed for clarity.

5.3 Conclusions

In this chapter, by testing and comparing established PEO and PPO CG parameters from eight previous explored studies [15, 17-23], we were ultimately able to evaluate and select the most apt models with the best adherence to experimental and simulated data for both PEO and PPO, and also provide a validation for our CG MARTINI alkane solvent models, important for future work with Pluronic surfactants.

Our initial PEO and PPO monomer 1-bead simulations adhered well to expected theory for LJ parameters for ρ, $\Delta\mathrm{H}_{\mathrm{vap}}$, and $\Delta\mathrm{G}_{\mathrm{solv}}$, and were able to match model 1 to DE's experimental density. These results were overall inconclusive for selecting models of PEO and PPO for longer beaded models.

Due to the nature of MARTINI 1-bead simulations, and for the best potential experimental and simulation validation, this study focused primarily on PEO2 and PPO2. For comparison of the PEO2 models, the widely accepted PEO dimer 1,2-dimethoxyethane, DME, with a wide breadth of experimental and simulation data, was chosen.[2, 10, 28, 57] While there was no available experimental, or even simulation, data for the true PPO dimer, 1-3ethoxy-2-methoxypropane, experimental and simulation data for a well-established short oligomer of PPO, only a single methyl group away from the actual dimer, 1,2-dimethoxypropane, DMP, as well as a closer representation of the PPO dimer, 1,2-diethoxyethane, DEE, were chosen for comparison.[2, 10, 28, 57, 64, 65]

The parameters of these block copolymer surfactant components were used in CG MARTINI simulations of PEO2 and PPO2 with themselves, in CG MARTINI water, and within our parameterised MARTINI alkane models from Chapter 5, in order to further validate them. The non-bonded interaction parameters between our chosen PEO and PPO models were calibrated in our hexadecane model at 2:1 and 4:1 bead mappings, and the results for 3:1 and 3.5:1 bead mapping were interpolated, and the results were compared to experimental data for DE (to represent the PEO monomer) and MOE (to represent the PPO monomer). The PEO2 models were then simulated in our MARTINI hexadecane, heptane, and hexane models, while due to a lack of comparative data, the PPO2 models were only simulated in our MARTINI heptane model. These alkane models were specifically selected for the available solvation data of DME, DMP, and DEE in these alkanes, and for the variety in our MARTINI alkane bead models used within them.[15, 24, 25, 30, 32] Calibration of our MARTINI alkane models for use with PEO2 and PPO2 had to be completed for their use in this study, which helped both to evaluate the PEO and PPO models and to better establish our own alkane models for future use.

Self-solvation, $\Delta\mathrm{G}_{\mathrm{solv}}$ in water and our alkane models, $\Delta\mathrm{H}_{\mathrm{vap}}$, and ρ calculated from these simulations were then compared to known data for DME, DMP, and DEE to evaluate agreement to real PEO and PPO.[24, 26, 27, 28, 52, 57, 64, 65, 66] In the case that data was not available, these properties were compared to those from other AA and CG simulation studies for possibly agreement and to show trend which could be compared to theory.[15, 25, 30, 32] The ΔG_{solv} results were especially important as ΔG_{solv} implies whether or not a longer polymer chain might self-assemble.[1] The ΔG_{solv} results in all of the solutions, as well as the ΔH_{vap} and ρ observed an expected theoretical trend in regards to Lennard-Jones parameters and inter- and intramolecular forces[11, 33, 34, 35, 36, 37, 38], with model 1 for PEO2 and model 8 for PPO2 adhering the most consistently to expected experimental and simulated results for ΔG_{solv} [15, 24, 55, 26, 27, 28, 30, 32, 34, 57, 64, 65], ΔH_{vap}[26, 27, 65, 66], and ρ.[26, 52, 64, 65, 66]

Further testing was done to find the D and η results of the models, and the ensuing values also appeared to follow established theory for their behaviours[26, 33, 40, 41], with model 1 and model 8 again showing the closest adherence to experimental and simulated results for both D[25, 29] and η.[25, 29]

These 2 most realistic models for PEO2 and PPO2, models 1 and 8 respectively, were then selected and their bond angle and dihedral parameters were used for longer chain simulations of PEO and PPO monomers in MARTINI water beads as well as in our heptane models.

The R_g of these monomer chains were then compared to previous simulation work[12, 51] for comparison and to establish trend with increasing chain lengths, and it was confirmed that their behaviour in the solvents adhered to theory for aggregation (i.e. if the models might ultimately self-assembly when used in Pluronic surfactant simulations).[45, 46] The R_g of these longer monomer chains gave chains with structure and chain responses as expected due to the hydrophilic and hydrophobic propensities of PEO and PPO in solvents.[12, 45, 46, 51] The end-to-end distances, persistence lengths, and relaxation times of these two models also compared well to simulated and experimental results, further implying their suitability.[20, 31, 51]

By using recognised models and a large number of thermodynamic and physical properties, we were able to choose the most appropriate PEO and PPO models, with the best overall better adherence to known data. The ultimate hydrophobicity and hydrophilicity results for longer chains of these models in MARTINI water and our heptane model, coupled with the adherence of these models with numerous other properties, suggests that these models will be the best for use in future Pluronic surfactant simulation work. It is also our hope that the additional development of our own MARTINI alkane models in this study for use with these Pluronic surfactant block components will also lead to self-assembly of simulated Pluronic surfactants solvated in them in later work.

5.4 References

. [1] C. Tanford. *The hydrophobic effect: formation of micelles and biological membranes*. Wiley Interscience publication. Wiley,1973.

. [2] M. Rosen & J Kunjappu. Surfactants and Interfacial Phenomena. John Wiley Sons.123-212, 2012.

. [3] E. Batrakova & A. Kabanov. Pluronic block copolymers: Evolution of drug delivery concept from inert nanocarriers to biological response modifiers. J Control Release., 130(2):98–106, 2008.

. [4] A. Denkova, E. Mendes, & C. Coppens. Non-equilibrium dynamics of block copolymer micelles in solution: recent insights and open questions. Soft Matter, 6:235-2357, 2010.

. [5] P. Alexandridis & T. Hatton. Poly(ethylene oxide)-poly(propylene oxide)-poly(ethylene oxide) block copolymer surfactants in aqueous solutions and at interfaces: thermodynamics, structure, dynamics, and modeling. Colloids Surf. A Physicochem. Eng. Asp., 96:1–46, 1995.

. [6] J. Klepeis, K. Lindor-Larsen, R.O. Dror, & D.E. Shaw. Long-timescale molecular dynamics simulations of protein structure and function. Current opinion in structural biology, 19:120–127, 2009.

. [7] B. J. Alder, & T. E. Wainwright. Studies in Molecular Dynamics. I. General Method. *J. Chem. Phys*. 31 (2): 459, 1959.

. [8] V.S. Bystrov. Molecular modeling and molecular dynamics simulation of the polarization switching phenomena in the ferroelectric polymers pvdf at the nanoscale. Physics B: Condensed Matter, 432:21–25, 2014.

. [9] J. Barnound, & L. Monticelli. Coarse-grained force fields for molecular simulations. Methods Mol Biol., (1215):125– 149, 2015.

. [10] T. Aoyagi. Computer Simulation of Polymeric Materials. Springer Singapore,139-141, 2016.

. [11] K. Kremer, P. Kremer, & C. Kremer. Multiscale simulation of soft matter systems: from the atomistic to the coarse-grained level and back. Soft Matter, 124(15), 2009.

. [12] M. van Gunsteren & M. van Gunsteren, C. van Gunsteren. Multigraining: an algorithm for simultaneous fine-grained and coarse-grained simulation of molecular systems. The Journal of chemical physics, 124(15), 2006.

. [13] S. Marrink & P. Tieleman. Perspective on the martini model. Chem. Soc. Rev., 42:6801–6822, 2013.

. [14] M. Henkel. Conformal invariance and critical phenomena. Springer Science & Business Media, 2013.

. [15] T. Taddese, & P. Carbone. Effect of Chain Length on the Partition Properties of Poly (ethylene oxide): Comparison between MARTINI Coarse-Grained and Atomistic Models. *The Journal of Physical Chemistry B*, *121*(7):1601-1609, 2017.

. [16] S. Nawaz, & P. Carbone. Correction to "Coarse-Graining Poly(ethylene-oxide)–Poly(propylene-oxide)–Poly(ethylene-oxide) (PEO–PPO–PEO) Block Copolymers Using the MARTINI Force Field. *The Journal of Physical Chemistry B*, *118*(6):1648-1659, 2014.

. [17] H. Lee, A. H. de Vries, S. J. Marrink, and R. W. Pastor. A coarse- grained model for polyethylene oxide and polyethylene glycol: Conformation and hydrodynamics. J. Phys. Chem., 113(40):13186-13194, 2009.

. [18] G. Rossi, P. Fuchs, J. Barnoud, & L. Monticelli. A coarse-grained MARTINI model of polyethylene glycol and of polyoxyethylene alkyl ether surfactants. *The Journal of Physical Chemistry B*, *116*(49):14353-14362, 2012.

. [19] F. Grunewald, G. Rossi, A. de Vries, S. Marrink, & L. Monticelli. Transferable MARTINI Model of Poly (ethylene Oxide). *The Journal of Physical Chemistry B*, *122*(29):7436-7449, 2018.

. [20] S. Nawaz, & P. Carbone. Coarse-graining poly (ethylene oxide)–poly (propylene oxide)–poly (ethylene oxide)(PEO–PPO–PEO) block copolymers using the MARTINI force field. *The Journal of Physical Chemistry B*, *118*(6):1648-1659, 2014.

. [21] M. Hatakeyama, & R. Faller. Coarse-grained simulations of ABA amphiphilic triblock copolymer solutions in thin films. *Physical Chemistry Chemical Physics*, *9*(33):4662-4672, 2007.

. [22] S. Hezaveh, S. Samanta, A. De Nicola, G. Milano, & D. Roccatano. Understanding the interaction of block copolymers with DMPC lipid bilayer using coarse-grained molecular dynamics simulations. *The Journal of Physical Chemistry B*, *116*(49), 14333-14345, 2012.

. [23] I. Wood, M. Martini, J. Albano, M. Cuestas, V. Mathet, & M. Pickholz. Coarse grained study of pluronic F127: Comparison with shorter co-polymers in its interaction with lipid bilayers and self-aggregation in water. *Journal of Molecular Structure*, *1109*:106-113, 2016.

. [24] A. R. Katritzky, A. A. Oliferenko, P. V. Oliferenko, R. Petrukhin, D. B. Tatham, U. Maran, A. Lomaka, & W. E. Acree. A General Treatment of Solubility. 1. The QSPR Correlation of Solvation Free Energies of Single Solutes in Series of Solvents. *J. Chem. Inf. Comput. Sci.* 43:1794, 2003.

. [25] S. Hezaveh, S. Samanta, G. Milano, & D. Roccatano. Structure and dynamics of 1, 2-dimethoxyethane and 1, 2-dimethoxypropane in aqueous and non-aqueous solutions: A molecular dynamics study. *The Journal of chemical physics*, *135*(16):164501, 2011.

. [26] Céondo GmbH. 1,2-Dimethoxypropane, https://www.chemeo.com/cid/27-929-1/2%2C2-Dimethoxypropane.pdf, [Accessed 7 19 2018].

. [27] V. Majer, V. Svoboda, H. V. Kehiaian, & International Union of Pure and Applied Chemistry. Enthalpies of Vaporization of Organic Compounds: A Critical Review and Data Compilation, Blackwell Scientific, Oxford, 1985.

. [28] D. Bedrov, O. Borodin, G. D. Smith, F. Trouw, & C. Mayne, Simulation and QENS studies of molecular dynamics in aqueous solutions of 1, 2-dimethoxyethane. *The Journal of Physical Chemistry B*, *104*(21), 5151-5154, 2000.

. [29] J. Barthel, R. Neueder, & H. Roch. Density, relative permittivity, and viscosity of propylene carbonate+ dimethoxyethane mixtures from 25° C to 125° C. *Journal of*

Chemical & Engineering Data, *45*(6), 1007-1011, 2000.

. [30] H. Lee, & R. W. Pastor. Coarse-Grained Model for Pegylated Lipids: Effect of Pegylation on the Size and Shape of Self-Assembled Structures. *J. Phys. Chem. B* , *115*, 7830-7837, 2011.

. [31] H. Lee, R. M. Venable, A. D. Mackerell, & R. W. Pastor. Molecular dynamics studies of polyethylene oxide and polyethylene glycol: hydrodynamic radius and shape anisotropy. *Biophysical journal*, *95*(4), 1590-9, 2008.

. [32] W. L. Jorgensen, D. S. Maxwell, & J .Tirado-Rives. Development and Testing of the Opls All-Atom Force Field on Conformational Energetics and Properties of Organic Liquids. *J. Am. Chem. Soc.,118*, 11225-11236, 1996.

. [33] B. Smit. Phase diagrams of Lennard-Jones fluids. *Journal of Chemical Physics*, 96 (11): 8639, 1992.

. [34] E. Bett., J. S. Rowlinson, & G. Saville,. Thermodynamics for Chemical Engineers , Athlone Press, London, 1975.

. [35] M. Griebel, S. Knapek, and G. Zumbusch. *Numerical simulation in molecular dynamics*. Berlin: Springer,193-197, 2007.

. [36] D. Oxtoby, H. Gills, and A. Campion. *Principles of modern chemistry* (7th ed.). Belmont, Calif.: Brooks/Cole Cengage Learning, 2012.

. [37] W. Greiner, L. Neise, and H. Stöcker. *Thermodynamics and statistical mechanics*. Springer-Verlag. 101, 1995.

. [38] D. W. Ball, J. W. Hill, and R. J. Scott. *The Basics of General Organic and Biological Chemistry*, Flat World Education, 128-133, 2011.

. [39] J. G. Kirkwood. Statistical mechanics of fluid mixtures, J. Chem. Phys., 3:300-313,1935.

. [40] D. Evans, *Response theory as a free energy extremum*, Phys. Rev. A 32, 2923, 1985.

. [41] M. S. Green. Markoff Random Processes and the Statistical Mechanics of Time-

Dependent Phenomena. II. Irreversible Processes in Fluids, J. Chem. Phys. 22: 398–413, 1954.

. [42] J. P. Holman. *Heat Transfer*. McGraw-Hill, 372-375, 2002.

. [43] F. Incropera and D. P. DeWitt. *Fundamentals of Heat and Mass Transfer*. Wiley, 298-299 2007.

. [44] H. B. Philllips. “A Formula for the Viscosity of Liquids”. *Proceedings of the National Academy of Sciences of the United States of America*, 7(6):172-177, 1921.

. [45] S. O. Nielsen, C. Lopez, G. Srinivas, and M. Klein. “A coarse grain model for n-alkanes parameterized from surface tension data”. J. Chem. Phys., 114(14), 2003.

. [46] G. Toth and A. Baranyai. Molecular dynamics analog of the reverse Monte Carlo method. J. Chem. Phys. 114, 2027, 2001.

. [47] R. D. Levine. Molecular reaction dynamics. Cambridge University Press, 662-667, 2005.

. [48] H. Su, A. Strachan, & W. A. Goddard. Density functional theory and molecular dynamics studies of the energetics and kinetics of electroactive polymers: Pvdf and p(vdf-trfe). Phys. Rev. B, 70(6), 2004.

. [49] S. Pronk, S. P, R. Schulz, P. Larsson, P. Bjelkmar, P. Apostolov, & M. Shirts. Gromacs 4.5: a high-throughput and highly parallel open source molecular simulation toolkit. Bioinformatics, 55, 2013.

. [50] NIH Biomedical Research Center for Macromolecular Modeling and Bioinformatic. Vmd users manual version 1.9.2. 1.9.2, 2014.

. [51] S. Hezaveh, S. Samanta, A. De Nicola, G. Milano, & D. Roccatano. Molecular dynamics simulation study of solvent effects on conformation and dynamics of polyethylene oxide and polypropylene oxide chains in water and in common organic solvents. *The Journal of Physical Chemistry B*, *136*(12):, 124901, 2012.

. [52] M. Roy, B. Sarkar, & R. Chanda. Viscosity, density, and speed of sound for the binary mixtures of formamide with 2-methoxyethanol, acetophenone, acetonitrile, 1, 2-

dimethoxyethane, and dimethylsulfoxide at different temperatures. *Journal of Chemical & Engineering Data*, *52*(5), 1630-1637, 2007.

. [53] J.E. Lennard-Jones. On the Determination of Molecular Fields. *Proc. R. Soc. Lond. A*, 106 (738): 463–477, 1924.

. [54] J. Tersoff. New Empirical approach for the structure and energy of covalent systems. Phys. Rev. B, 37:6991, 1988.

. [55] K. Daoulas & M. Müller. Comparison of Simulations of Lipid Membranes with Membranes of Block Copolymers. In Polymer Membranes/Biomembranes. W. P. Meier, W. Knoll, Eds.; Springer: Berlin, Heidelberg, 224, 43–85, 2009.

. [56] R. Stepto, T. Chang, P. Kratochvíl, M. Hess, K. Horie, T. Sato, & J. Vohlídal. Definitions of terms relating to individual macromolecules, macromolecular assemblies, polymer solutions, and amorphous bulk polymers. *Pure Appl Chem*. 87 (1): 71, 2015.

. [57] A. Aucejo, S, Loras, R. Muñoz, R. Reich, & H. Segura. Isobaric Vapor– Liquid Equilibrium in the Systems 2-Methylpentane+ Methyl 1, 1-Dimethylethyl Ether,+ Ethyl 1, 1-Dimethylethyl Ether, and+ Methyl 1, 1-Dimethylpropyl Ether. *Journal of Chemical & Engineering Data*, *43*(6), 973-977, 1998.

. [58] D. Evans, *Response theory as a free energy extremum*, Phys. Rev. A 32, 2923, 1985.

. [59] I. Müller. *A History of Thermodynamics – the Doctrine of Energy and Entropy*. Springer. ISBN 978-3-540-46226-2, 2007.

. [60] J. C. Li, & P. Chang. Self-Diffusion Coefficient and Viscosity in Liquids. *The Journal of Chemical Physics*, *23*(3), 518-520, 1955.

. [61] R. Zwanzig. On the relation between self-diffusion and viscosity of liquids. *The Journal of chemical physics*, *79*(9), 4507-4508, 1983.

. [62] H. Yamakawa. *Modern theory of polymer solutions.* Harper & Row, 10-35, 1971.

. [63] J. G. Curro, & K. S. Schweizer. Equilibrium theory of polymer liquids: Linear chains.

The Journal of chemical physics, *87*(3), 1842-1846, 1987.

. [64] N.C.B.I., National Center for Biotechnology Information. PubChem Compound Database; CID=12375, https://pubchem.ncbi.nlm.nih.gov/compound/12375, [Accessed 10 6 2018].

. [65] CSID:13835376, http://www.chemspider.com/Chemical-Structure.13835376.html, [Accessed 10 6 2018].

. [66] N.C.B.I., National Center for Biotechnology Information. PubChem Compound Database; CID=8071, https://pubchem.ncbi.nlm.nih.gov/compound/8071, [Accessed 09 15 2018].

. [67] S. Asakura, & F. Oosawa. On interaction between two bodies immersed in a solution of macromolecules. *The Journal of Chemical Physics*, *22*(7), 1255-1256, 1954.

. [68] Y. H. Zang, & P. J. Carreau. A correlation between critical end-to-end distance for entanglements and molecular chain diameter of polymers. *Journal of applied polymer science*, *42*(7), 1965-1968, 1991.

. [69] H. Li, & T. A. Witten. Fluctuations and persistence length of charged flexible polymers. *Macromolecules*, *28*(17), 5921-5927, 1995.

. [70] M. L. Williams, R. F. Landel, & J. D. Ferry. The temperature dependence of relaxation mechanisms in amorphous polymers and other glass-forming liquids. *Journal of the American Chemical society*, *77*(14), 3701-3707, 1955.

. [71] F. Oellien and M. C. Nicklaus. Online SMILES translator and structure file generator. 2004.

. [72] NIH Biomedical Research Center for Macromolecular Modeling and Bioinformatic. Vmd users manual version 1.9.2. 1.9.2, 2014.

. [73] R. Gautam, & W. D. Seider. Computation of phase and chemical equilibrium: Part I. Local and constrained minima in Gibbs free energy. *AIChE Journal*, *25*(6), 991-999, 1979.

. [74] F. Oellien and M. C. Nicklaus. Online SMILES translator and structure file generator.

2004.

. [75] NIH Biomedical Research Center for Macromolecular Modeling and Bioinformatic. Vmd users manual version 1.9.2. 1.9.2, 2014.

. [76] National Center for Biotechnology Information. PubChem Compound Database; CID=8254, https://pubchem.ncbi.nlm.nih.gov/compound/8254, [Accessed 07 12 2018].

. [77] National Center for Biotechnology Information. PubChem Compound Database; CID=10903, https://pubchem.ncbi.nlm.nih.gov/compound/10903, [Accessed 07 12 2018].

. [78] D. Zhao, J. Feng, Q. Huo, N. Melosh, G. Fredrickson, B. Chmelka, & G. Stucky. Triblock copolymer syntheses of mesoporous silica with periodic 50 to 300 angstrom pores. Science, 279(5350):548–52, 1998.

. [79] J. Sun, H. Zhang, D. Ma, Y. Chen, X. Bao, A. Klein-Hoffman, N. Pfander, & D. S. Su. Alkanes-assosted low temperature formation of highly ordered SBA-15 with large cylindrical mesopores. Chem. Comm., 5343, 2005.

. [80] M. Kruk, M. Jaroniec, C. Ko, & R. Ryoo. Characterization of the porous structure of sba-15. Chem. Mater., 12(7):1961–1968, 2000.

. [81] Y. Ding, H. Dana, X. Lua, Y. Wub, S. Yuana, & X. Maoa. Facile route to synthesize mesoporous silica sba-15 platelets. Materials Chemistry and Physics, 148(1-2):17-20, 2014.

. [82] I. Melez-Ortiza, B. Puente-Urbinab, G. Castruita-de Leona, J. Mata-Padillab, & L. GarcUriosteguic. Synthesis of spherical sba-15 mesoporous silica, influence of reaction conditions on the structural order and stability. Ceramics International, 42(6):7564-7570, 2016.

. [83] CSID:7956, http://www.chemspider.com/Chemical-Structure.7956.html, [Accessed 10 12 2018].

. [84] CSID:10441, http://www.chemspider.com/Chemical-Structure.10441.html, [Accessed 10 12 2018].

COARSE-GRAINED MODEL FOR PLURONIC TRIBLOCK COPOLYMERS

6

In this chapter, we furthered the PEO and PPO modeling work done in Chapter 5 in order to model full Pluronic surfactants, and it is the culmination of our previous CG work in Chapters 4 and 5. After validating the PEO-PPO interaction parameters taken from the study of our chosen PPO model[1], keeping in mind those from the other three PPO model studies in Chapter 5[2, 3, 4] for a potential trial and error approach, varying Pluronic triblock copolymer systems were simulated in different solvents. These Pluronic systems were tested for dynamic properties as well as self-assembly and micellisation behaviour to validate our models.

6.1 Methodology

6.1.1 Simulation protocol

As with our previous work in Chapters 4 and 5, the CG simulations run in this chapter used GROMACS software, and were performed using an isothermal-isobaric NPT ensemble.[5] The original AA models used as a basis for our coarse-graining were again converted from their chemical structures using the online SMILES generator, and then mapped to the CG models using Residue-Based Coarse Graining (RBCG) Builder in VMD.[6, 7] Again to yield the most accurate thermodynamic results, a V-rescale thermostat and a Parrinello-Rahman barostat were applied to maintain conditions of 273 K to 300K, and 1 bar respectively, and the simulations used a time-step of 20 fs, with a leap-frog stochastic dynamics integrator for the equations of motion.[5, 8, 9] The normal dispersion was again controlled by a switched group cutoff scheme with cutoff between 1.0 - 1.3 nm, and long-range dispersion corrections were applied to energy and pressure of the system.[5, 8] In order to account for finite-size effects, the cubic box lengths were kept between 15 nm and 60 nm, depending on the size or number of the CG Pluronic model chains.[10]

6.1.2 Coarse-grained models

As with our previous work, this study made use of the MARTINI force field, which was explained in full in Chapter 2, or in a smaller capacity in Chapter 4.[5]

To substantiate the PEO and PPO parameters chosen in Chapter 5 for use with block copolymers, several Pluronics simulation systems were created. The PEO and PPO work had not needed an interaction level between them for their individual testing, so one needed to be chosen and validated. The study behind our chosen model of PPO had definitive non-bonded parameters between PEO and PPO beads, here as model 1[1], so its parameters were first tested for a single generic Pluronic chain (i.e. PEO$_{10}$ PPO$_{10}$ PEO$_{10}$) in MARTINI water and then put into VMD software[7] to observe their behaviour in the presence of a solvent. The interaction parameters for PEO-PPO taken from the three other PPO model studies were noted (i.e. models 2, 3, and 4[2,3,4]) in case of potential adjustment if model 1's parameters did not yield adequate results. All the PEO-PPO interaction parameter models can be seen in **Table 6.1**.[1-4]

PEO-PPO Models	**PEO-PPO**							
	Non-bonded Interactions		**Bonded Interactions**					
	σ (nm)	**ε (kJ/mol)**	**r$_0$ (nm)**	**k$_b$ (kJ/mol*nm^2)**	**θ (deg.)**	**k$_\theta$ (kJ/mol)**	**Φ (deg.)**	**kΦ (kJ/mol)**
1[1]	0.43	3.75	0.355	17000	120	50	180	1.96, 5, .33, .12
2[2]	0.47	3.4	0.47	1250	180	25	n/a	n/a
3[3]	0.47	2.9	0.28	5000	180	25	n/a	n/a
4[4]	0.47	2.6	0.33	17000	130	50	180	1.96. .18, .33, .12

Table 6.1: Lennard-Jones non-bonded and bonded interaction parameters for PEO-PPO models.[1-4]

The PEO and PPO monomer block structures that comprise the triblock copolymers modeled and simulated in this study can be seen in **Table 6.2.**[11, 12]

Pluronic Block Copolymers	**Number of PEO blocks (n)**	**Number of PPO blocks (m)**	**Molecular Weight (g/mol)**
L31	2	16	1100
L35	11	16	1900
L44	10	23	2200
L62	5	30	2500
L64	13	30	2900
P85	26	40	4600
P123	20	70	5750
F38	43	15	4700

Table 6.2: PEO and PPO block compositions for the 8 Pluronic triblock copolymers in this study.[11, 12]

These specific Pluronic triblock copolymers were selected because of their varied PEO and PPO block lengths, and their commonness in simulation work.[1-4, 11, 12] This allowed for a more thorough examination of our Pluronic model parameters, and their responses to the CG solvents. It should be noted, however, that Pluronic L35 was specifically chosen for our on-going collaborative work with researchers at the University of Averio.[63]

Bulk liquid simulations of all the models, save for Pluronic L35, were run at room temperature, and their density was calculated and compared to known Pluronic data.[14] Bulk simulations for Pluronics L44, L62, L64, P85, and P123 were then run at varying temperatures (i.e. 298.15K and 333.15K) and their shear viscosities were calculated and compared against known Pluronic data.[13, 14] An additional bulk simulation was run for a model of Pluronic F38, and the heat capacities of the models for Pluronics P85, P123, and F38 were calculated and compared to experimental data.[15, 16, 17]

Six of the single chain models (i.e. models for Pluronics L31, L44, L62, L64, P85, and F38) were then simulated in MARTINI water at 300K, and then three of those single chains (i.e. models for Pluronics L64, P85, and F38) were simulated in MARTINI water at 273K, and their radius of gyration results were observed and compared to previous simulated data.[1, 3]

Two-hundred chains of Pluronics L44 and P123 and three-hundred chains of Pluronic L35, were then simulated in MARTINI water, and eighty chains of Pluronic P123 in our hexane model (using the non-bonded interaction parameters between our alkane models and PEO and PPO previously calibrated in Chapter 5). The resulting files from these simulations in water were put into VMD software to observe their self-assembly behaviour[7], and the aggregation numbers were then calculated for the simulations in water and examined to see if the values appeared to be within acceptable ranges. In the absence of time, aggregation numbers were calculated using GROMACS, though it is important to note that our collaborative work with German Pérez-Sánchez has produced a new cluster counting code capable of deeper analysis of micellar properties which will be used in any future work.[63]

The radial distribution functions, RDFs, for the Pluronic L44 and P123 models in water were calculated and compared to previous work for justification.[18] New simulations for the micelles in the systems with water were run (i.e. based on the methods explained in Chapter 3), and the free energy of micellisation for the micelles was then calculated and compared to experimental data.[19]

A complete overview of the simulated systems of Pluronics in this study can be seen in **Table 6.3**.

Pluronic Model Solutes	Solvated Systems		
	MARTINI Water	Themselves	Our Hexane
Generic Pluronic	✓		
Pluronic L31	✓	✓	
300 Pluronic L35	✓		
Pluronic L44	✓	✓	
200 Pluronic L44	✓		
Pluronic L62	✓	✓	
Pluronic L64	✓	✓	
Pluronic P85	✓	✓	
Pluronic P123	✓	✓	
80 Pluronic P123			✓
200 Pluronic P123	✓		
Pluronic F38	✓	✓	

Table 6.3: Simulation details for our Pluronic model work.

All of these results were used to evaluate the structure and dynamics of Pluronics models and analyse their ability to self-assemble.

6.1.3 Data analysis

The densities for the Pluronic models in this study were compared against experimental data from a catalogue from the Pluronic manufacturer BASF.[14]

The shear viscosity results of the Pluronic models were compared to experimental data from a study by Alexandridis et al.[13] and the manufacturer catalogue for Pluronics produced by BASF.[14]

The heat capacity results for our Pluronic P85, P123, and F38 models were compared against interpolated experimental data from Meilleur et al.[15], as well as standard experimental data for Pluronic L44 from Naskar et al.[16], and standard experimental data for Pluronic P123 taken from a study by Shvartzman-Cohen.[17]

As has been covered in previous chapters, radii of gyration are next to impossible to analyse through current experimental methodology, so our radius of gyration results were compared to previous simulation work; the Pluronic models in water at 300K were compared to results from the CG study that provided us with our PPO model by Nawaz et al.[1], and the Pluronic models in water at 273K were compared to results from a CG study by Hezaveh et al.[3]

As with radius of gyration, radial distribution functions are also inherently difficult to examine, so the RDF results for the 200 Pluronic

L44 and P123 simulations performed in this study were compared to an AA study by Song et al.[18]

The micellisation free energy results for the individual micelles created from the 200 Pluronic P123 chain simulations in water were compared against known experimental values from a study by He et al.[19], while the micellisation free energy results from the 200 Pluronic L44 simulations in water were compared to interpolated data from the study by Naskar et al.[16] An example of the interpolation process for finding the micellisation free energy from Naskar et al.[16], which is indicative of both interpolations done for comparable data in this study, can be seen in **Figure 6.1**.

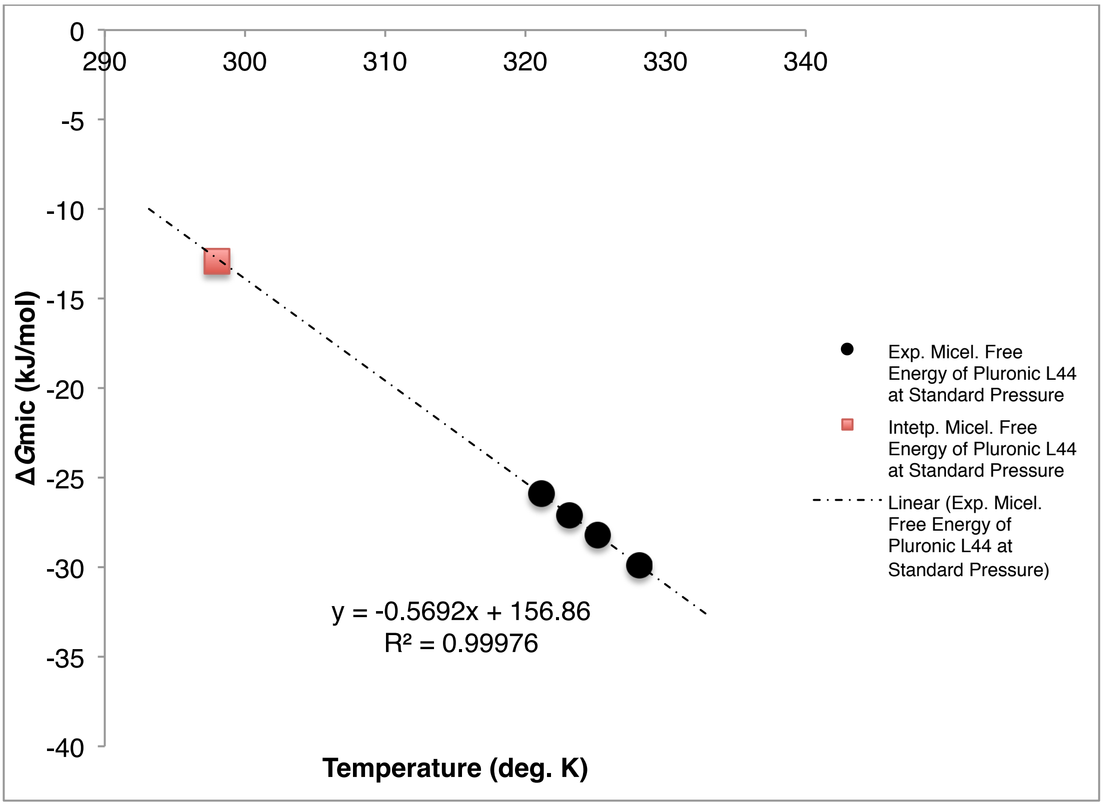

Figure 6.1: Experimental and interpolated micellisation free energies of Pluronic L44 at different temperatures. The black circles represent known values, the dashed black line represents the linear interpolation of these values based on data trend, and the red square represents the interpolated value for Pluronic L44 at room temperature.[16]

All of the results in this study were calculated again using the equations described in Chapter 3.

6.2 Results

6.2.1 PEO-PPO interaction results

Figure 6.2 shows the VMD snapshot for results of a PEO_{10} PPO_{10} PEO_{10} Pluronic chain in water, using the PEO-PPO interaction parameters from Nawaz et al.[1] These parameters were ultimately chosen because they are from the same study as our PPO model[1], as there was only a slight change between all four models when observing them in VMD, which was deemed to be inconclusive. The Pluronic model was examined to see if the PEO modelled portions showed signs of their experimental counterparts' hydrophilicity, and if the PPO modelled portions showed signs of the hydrophobicity seen by experimental PPO in an aqueous solution.[21-24, 27] When joined in a Pluronic triblock copolymer, the PPO portion should curl inwards, while the PEO end chains should move to surround them, pulled inwards by the curling of the PPO, but still moving towards the water.[24, 27, 32] This particular arrangement can be seen in the Pluronic model in **Figure 6.2**, initially validating our chosen PEO-PPO parameters[1] for further use in this study. An example VMD snapshot of the modelled Pluronic using some of the rejected parameters can be found in **Figure 6.11** in **Appendix C**.

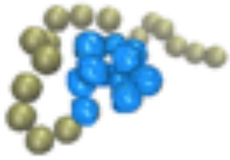

Figure 6.2: A VMD snapshot of our Pluronic (i.e. PEO_{10} PPO_{10} PEO_{10}) model with PEO-PPO parameters from Nawaz et al.[1]The yellow beads represent PEO and the blue beads represent PPO.

6.2.2 Pluronic block copolymer results

The density results for the bulk liquid simulations of our Pluronic models as a function of molecular weight are shown in **Figure 6.3**. The ρ results of these models mainly adhere to theory, as while theoretically the density should increase with the increased number of monomers, were they homologous, the increasing number of PEO blocks has a not insignificant effect on the density results here.[32, 33, 42] This is due to the increased molecular weight of PPO when compared to PEO, and the disparate combinations of PEO and PPO blocks in the Pluronic models, as if all PEO blocks were kept equal, the ρ would increase with increasing chains of PPO blocks (and vice versa with the PPO blocks being kept equal).[32, 33, 42, 43, 44] All of the Pluronic model ρ results fit within the margin of error for the densities of experimental Pluronic triblock copolymers, except for our Pluronic F38 model.[14] This can potentially be attributed to the much longer PEO blocks of Pluronic F38 coupled with the slight overestimation of ρ seen in the PEO model in Chapter 5, as well as the remarkably lower experimental bulk density of Pluronic F38 at room temperature.[14] A complete table of all of these ρ results can be found in **Table 6.5** in **Appendix C**.

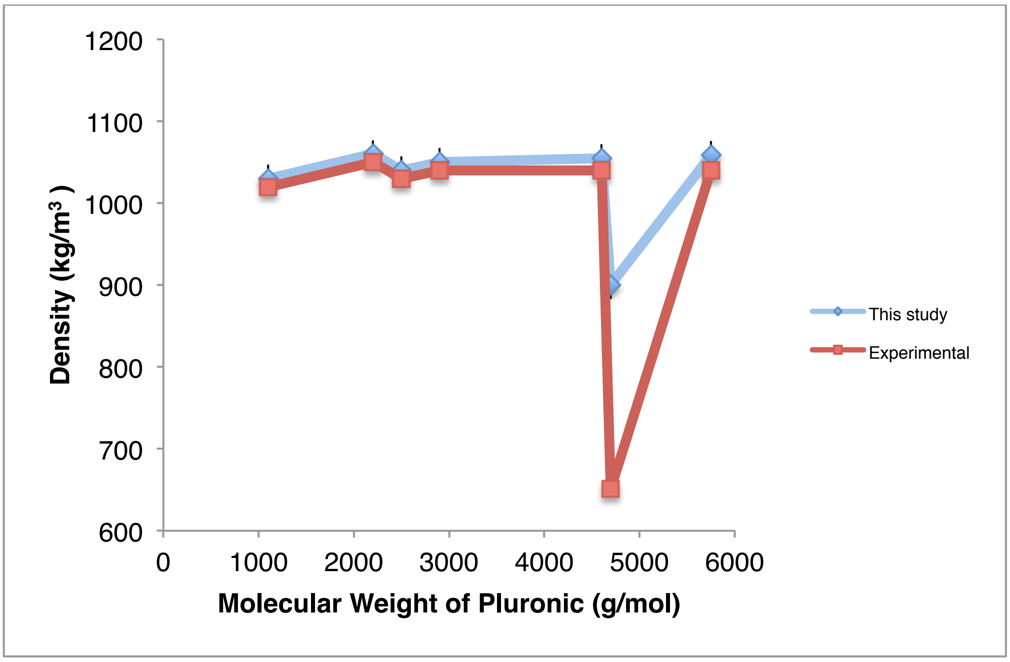

Figure 6.3: Comparison between the mass density of this study's Pluronic models by molecular weight, Pluronics L31, L44, L62, and L64, P85, P123, and F38, and experimental data for these triblock copolymers at room temperature.[14]

In **Figures 6.4a-b**, we can see the shear viscosity results for all of the Pluronics models compared to the known data for each experimental Pluronic surfactant, with liquid Pluronics L44, L62, and L64 (i.e. denoted by L, as explained in Chapter 1) at 298.15K, and the paste Pluronics P85 and P123 (i.e. denoted by P, as also explained in Chapter 1) at 333.15K.[13, 14] Complete tables of these results compared to experimental values are again shown in **Tables 6.6a-b** in **Appendix C**. These results also are in good agreement with theory, as when there is a change in the total potential energy between two molecules, it affects the total viscosity of a substance, and the increase of total molecular energy between all of the Pluronic models (e.g. through the increase number of PPO CG beads, etc.) means that the η results increase between models.[30, 31, 47, 48] The significantly lower results for the paste Pluronics can be attributed to the much higher temperature of the simulation, which also adheres to theory through the phenomenon of viscosity to decrease as temperature increases.[30, 31, 47, 48] It should be noted though, that this is a simplistic interpretation of theory, as viscosity of polymers is a bit more complicated than this (i.e. it includes molecular entanglement, whether or not a polymer chain is coiled or stretched, etc.).[30, 31, 47, 48] The η results here unfortunately do not lie within the margins of error for experimental viscosities of these Pluronics, but they do show a favourable trend that observes theoretical expectations.[13, 14, 30, 31, 44, 47, 48]

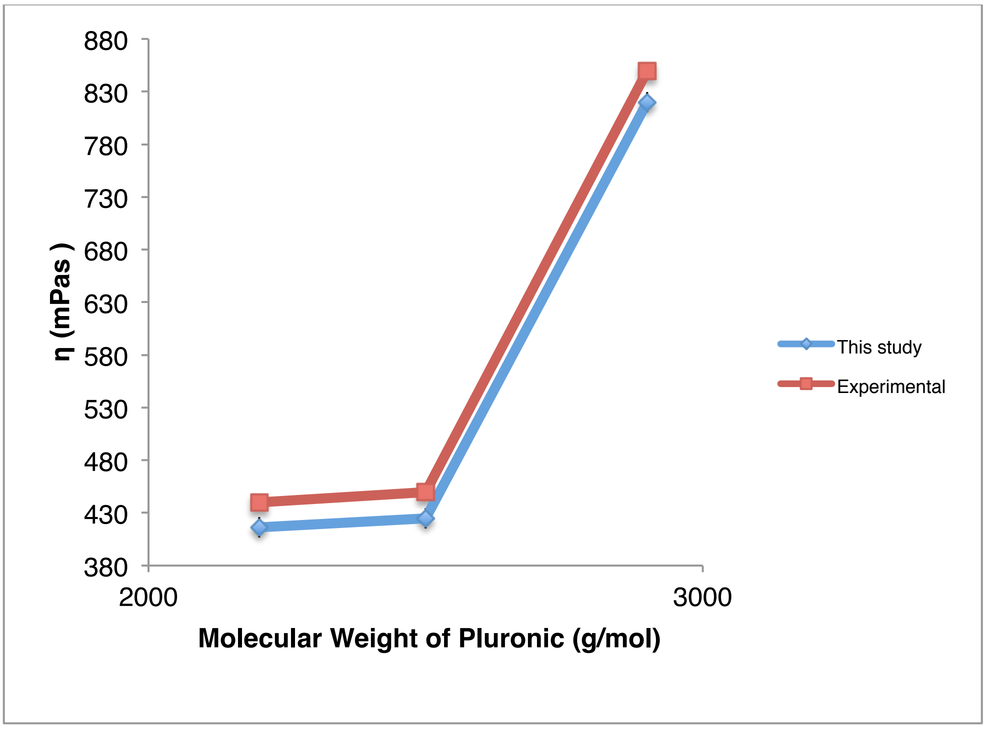
880
830
780
730
680
630
580
530
480
430
380
η (mPas)
2000
3000
Molecular Weight of Pluronic (g/mol)
This study
Experimental

a)

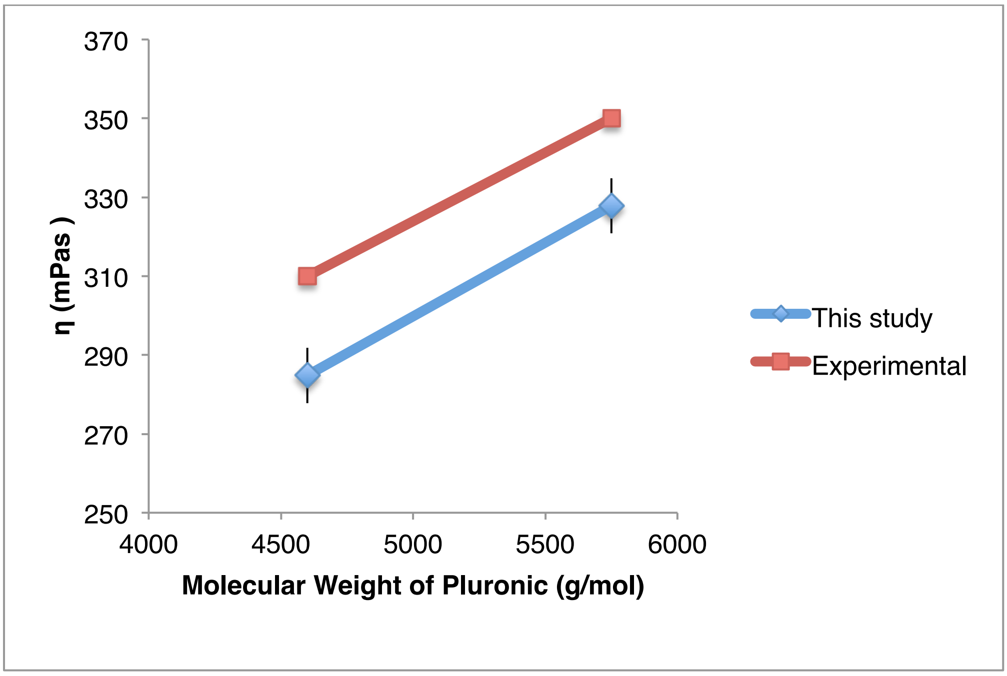

b)

Figures 6.4a-b: Comparison between the shear viscosities of this study's Pluronic models **a)** Pluronics L31, L44, and L64 at 278.15K and **b)** Pluronics P85 and P123 at 333.15K, and experimental data for these triblock copolymers at those temperatures.[13, 14]

Figure 6.5 shows the heat capacity results for our Pluronic P85, P123, and F38 models as a function of the number of CG beads. The heat capacities of our models fall within the margin of error for the known values for these polymers, and are expected with theory.[15, 16, 17, 28, 29, 33, 34] While the increased bond force constant in the PPO modelled blocks does contribute to a greater molecular energy and thus a greater enthalpy (e.g. an important component for the calculation of Cp), the increased bond length of the PPO model compared to the PEO model contributes to a decrease in enthalpy and Cp.[34, 45, 46] It should also be noted that as the results are also within 2kg/mol*K of one another, the heat capacity results for these models are not out of what could be expected from CG models, discounting the specifics of the PPO block parameters. A complete table of these results can again be found in **Table 6.7** in **Appendix C**.

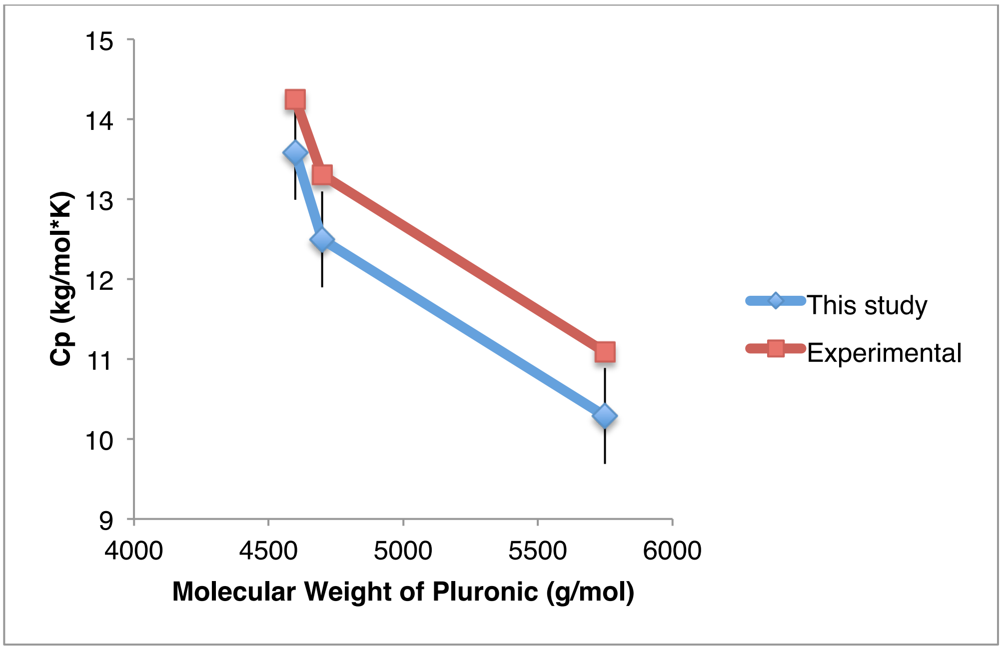

Figure 6.5: Comparison between the heat capacities of this study's Pluronic P85, P123, and F38 models, and interpolated and standard experimental data for these triblock copolymers at room temperature and standard pressure.[15, 16, 17]

Figures 6.6a-b show the radii of gyration of single Pluronic triblock copolymer chains of L31, L44, L62, L64, P85, and F38 in CG MARTINI water at 300K, and single Pluronic chains of L64, P85, and F38 in CG MARTINI water at 273K compared against the results of two separate simulation studies, respectively.[1, 3] Complete tables of these results are again shown in **Tables 6.8a-b** in **Appendix C**. The radii all fit within the margins of error from the previous works (i.e. establishing trend) as well as theory in regards to chain length, potentially indicating a realistic stretching tendency.[1, 3, 25, 26, 28, 32, 36, 49] These results at both temperatures also appear to increase with the PEO and PPO blocks and molecular weight of the Pluronics, L31< L44 < L62 < L64< P85 < F38, which is in accordance with theory, as the radius of gyration is the average squared distance of any point in a molecule chain from it's centre of mass.[14, 25, 26, 28, 32, 36, 49]

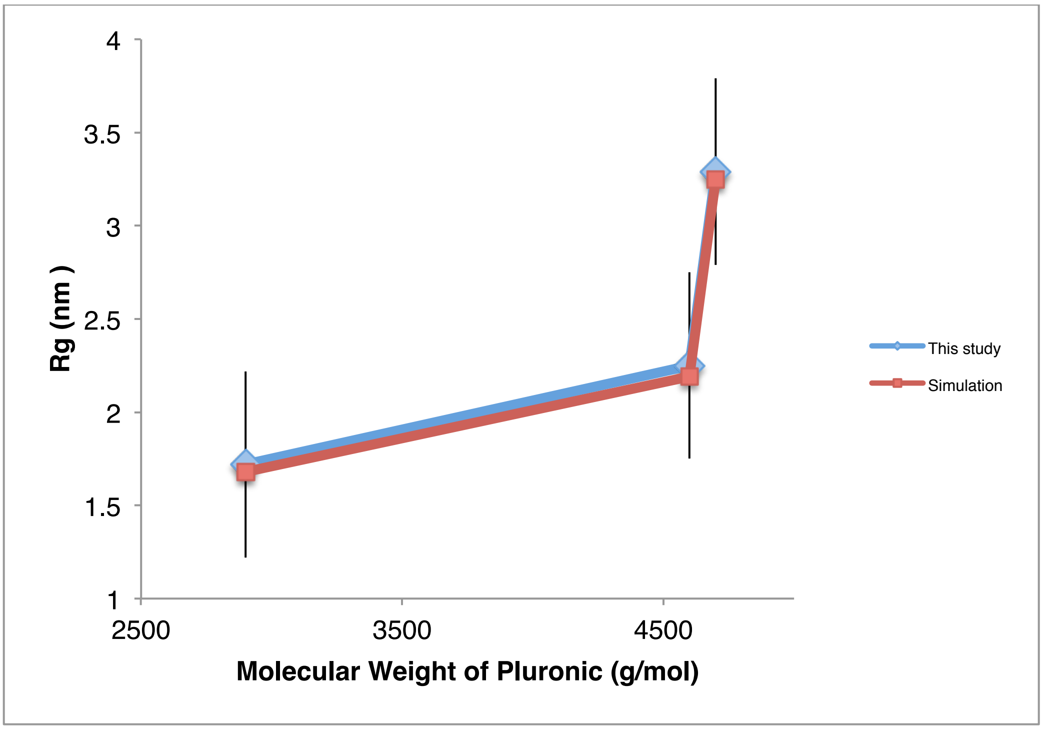
4
3.5
3
2.5
2
1.5
1
Rg (nm)
2500
3500
4500
Molecular Weight of Pluronic (g/mol)
This study
Simulation

a)

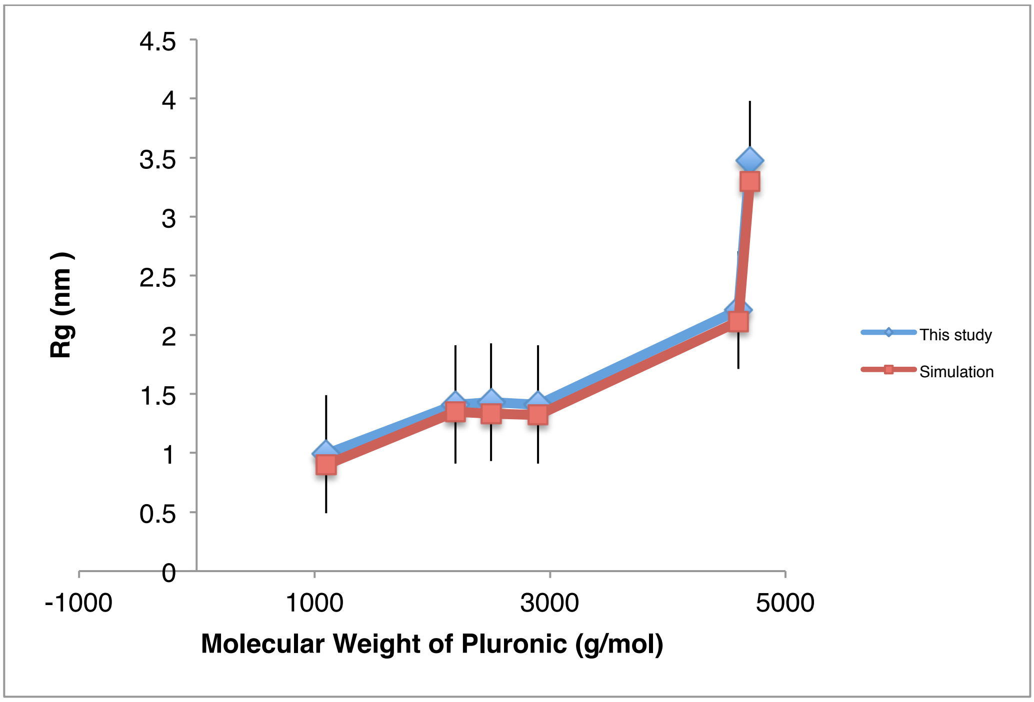

b)

Figures 6.6a-b: Comparison between the radius of gyration results of this study's Pluronic models **a)** Pluronics L31, L44, L64, P85, and F38 at 300K and **b)** Pluronics L64, P85, and P123 at 273K, and simulated data for these triblock copolymers at those temperatures; 300K[1] and 273K.[3]

The VMD snapshots of 200 chain simulations of Pluronics L44 and P123, and 300 chain simulations of Pluronic L35, in MARTINI water can be seen in **Figures 6.7a-f**. Self-assembly of the chains was readily apparent for the L44, P123, and L35 in water, with aggregation increasing over time as would be expected of both surfactant theory and of experimental Pluronic copolymers.[20-23, 26, 27, 32, 35, 36, 37, 41] This is possibly the greatest validation for our PEO and PPO models, as the ultimate goal of this study was to create Pluronic triblock copolymer surfactant models that could self-assemble and aggregate.[20-23, 26, 27, 32, 35, 36, 37, 41] This implies that the chosen LJ, bonded, and non-bonded parameters for our models allow for the correct hydroplicity and hydrophobicity of Pluronic models to provide comparisons with experimental behaviour of Pluronics in water.[1, 20-23, 26, 27, 32, 35, 36, 37, 41]

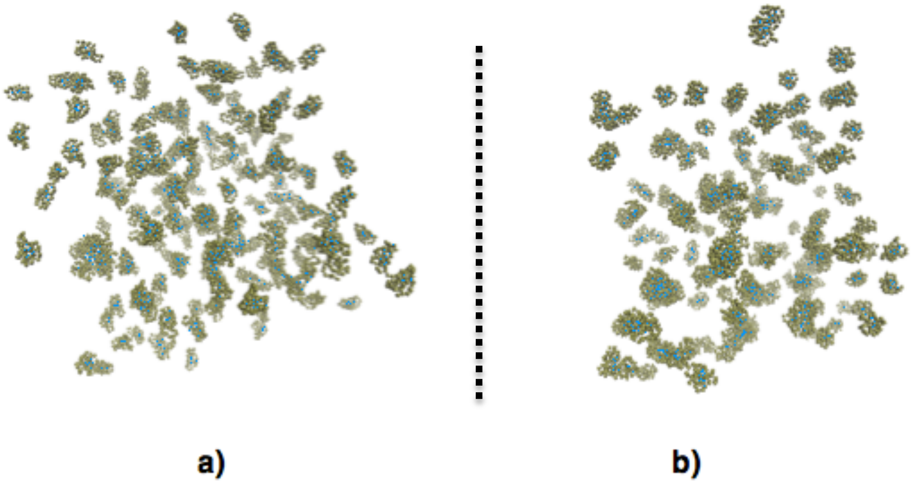

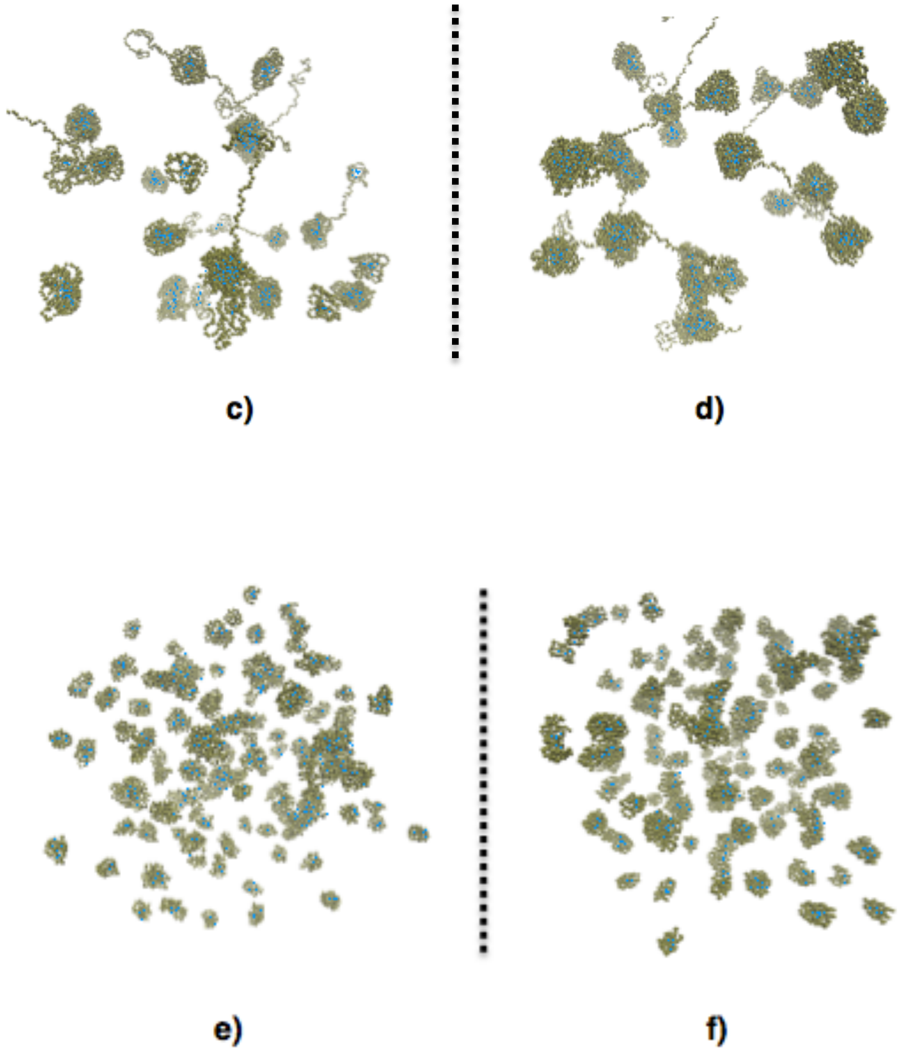
c) d) e) f)

Figures 6.7a-f: Snapshots of the 200 Pluronic chain simulations before and after the simulation runs in water, **a)** L44 before, **b)** L44 after, **c)** P123 before, **d)** P123 after, **e)** L35 before, and **f)** L35 after; solvent molecules have been removed for clarity. The yellow beads represent PEO and the blue beads represent PPO.

As with 200 Pluronic P123 surfactant chain in water simulation, self-assembly and aggregation behaviour was also apparent in the 80 Pluronic P123 chains in our hexane model simulation, as shown in **Figures 6.8a-b**. It is evident in the VMD snapshots here and in **Figures 6.7c-d** that the Pluronic P123 model shows the correct qualitative behaviour in different solvents, as it can be observed that the simulated PPO chains seem to stretch out in our hexane model, while curling in on themselves when solvated in water. This implies the block PEO and PPO components maintain the expected behaviour when joined together in our Pluronic model.[55, 56]

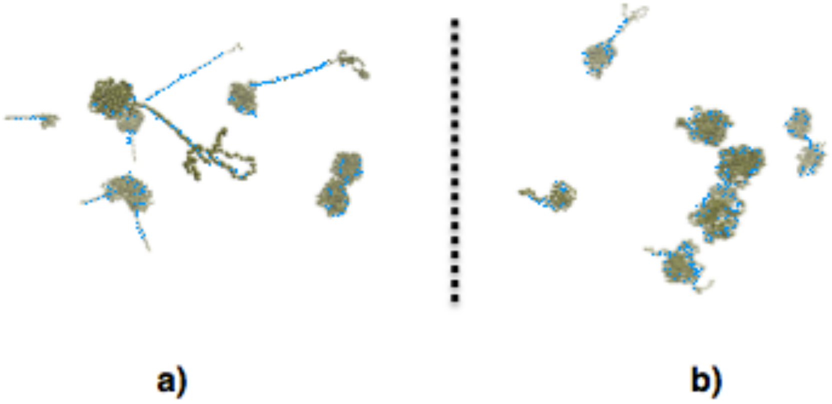

Figures 6.8a-b: Snapshots of the 80 Pluronic P123 chain simulations before and after the simulation runs in our hexane model, **a)** P123 before, and **b)** P123 after; solvent molecules have been removed for clarity. The yellow beads represent PEO and the blue beads represent PPO.

Experimental aggregation numbers, or the number of surfactants present in a micelle after the CMC has been reached[55, 56], tend to vary widely for Pluronics, with multiple aggregation numbers being reported for the same Pluronic surfactant at the same temperature.[20, 57, 61, 62] It has been noted, however, that aggregation numbers can be dependant on temperature[58, 60] as well as the molecular weight of the Pluronic surfactant being used (i.e. the larger the molecular weight of the Pluronic, the larger the theoretical aggregation number, though this is not an exact trend).[54, 59] Because temperature of the simulations was kept constant, the aggregation numbers were evaluated for adherence to trend based on the molecular weight of the Pluronic chain, and were found to increase based on the molecular weight of the total surfactants being simulated (i.e. 200 chains of Pluronic L44 < 300 chains of Pluronic L35 < 200 chains of Pluronic P123).[14] The aggregation numbers here, while having no experimental comparison, were also not out of the realm of possibility for other known experimental values, which was encouraging.[20, 57, 61, 62] These results can be seen in **Table 6.4**.

Pluronic Surfactant Model	Aggregation Number
L35	22
L44	19
P123	30

Table 6.4: Aggregation numbers of the micelles from the Pluronic L44, P123, and L35 chains simulated in water.

Figures 6.9a-b show the radial distribution functions, calculated for all pairs of beads with a distance less than the cutoff value, from the 200 chain simulations of Pluronics L44 and P123 in comparison with simulation results from an AA study.[18] The RDF results are aligned with theory, with the RDF results increasing with increasing chain length and molecular weights.[25, 26, 50, 51] While neither of this study's simulation results match those from the other works, with L44's radial distribution function exhibiting a smaller peak and P123 a higher peak, their distributions appear relatively similar to those from the AA study.[18] This discrepancy may be attributed to the lower degree of resolution inherent in CG modelling when compared to AA modelling.[52, 53] The sharp peak of this study's results for Pluronic P123 at 1 nm theoretically indicates a stronger ability to self-assemble, as it implies higher aggregation behaviour, which is expected with theory.[25, 26, 38, 41, 50, 51]

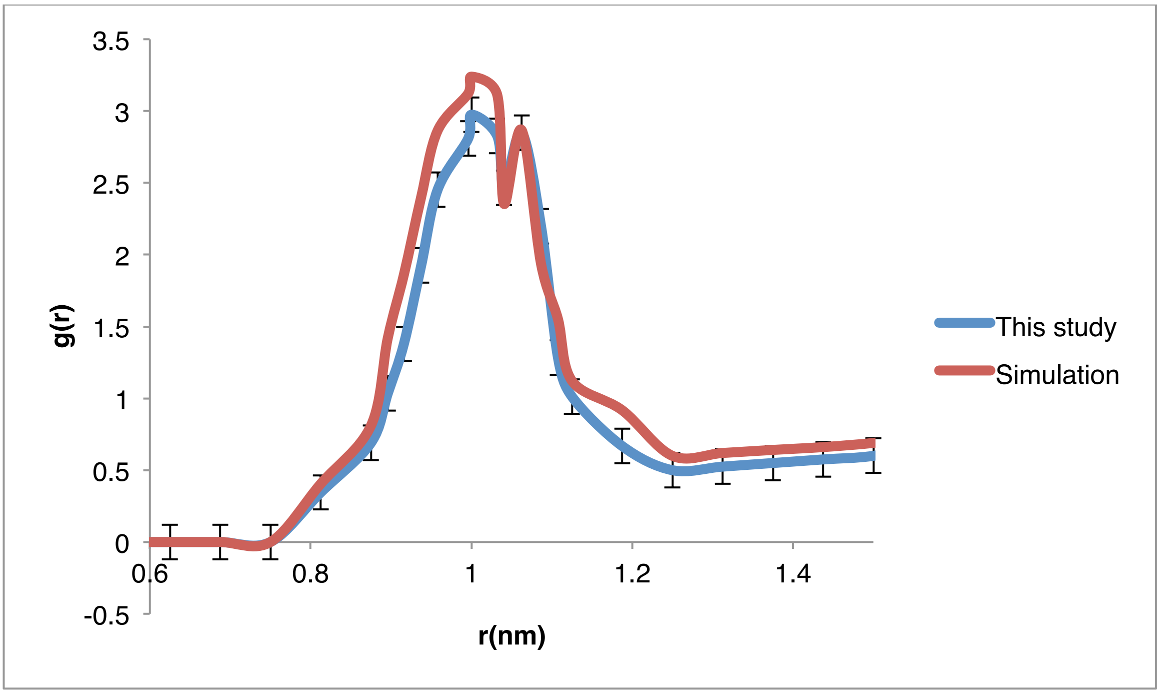

a)

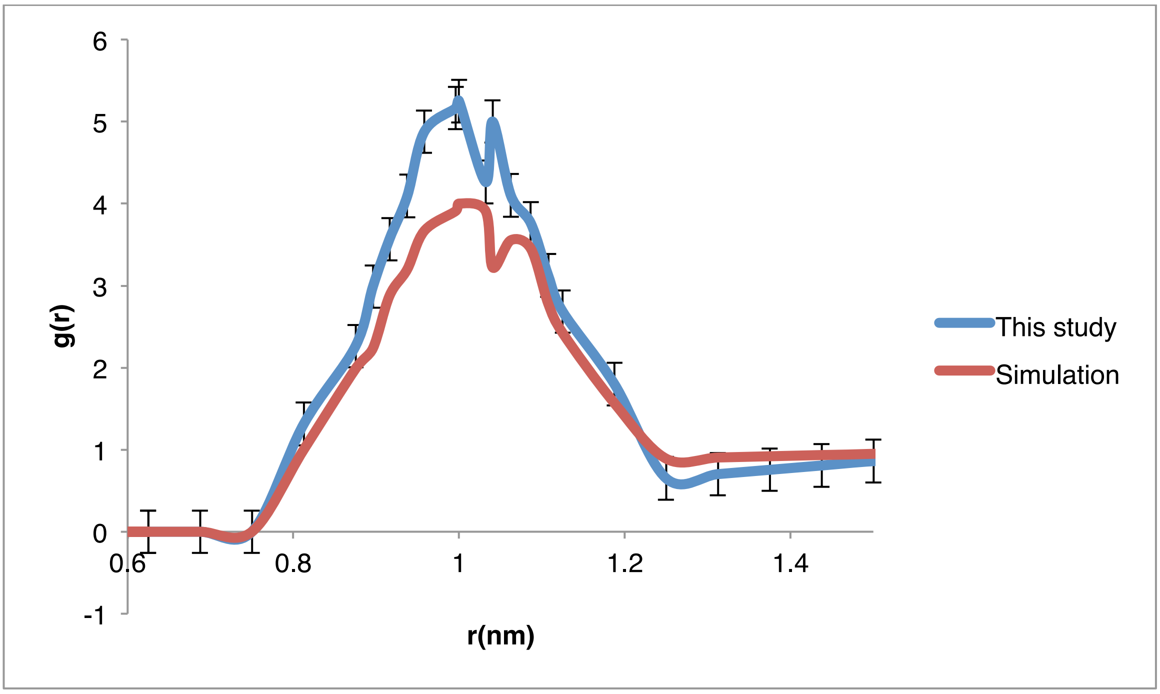

b)

Figures 6.9a-b: Radial distribution functions of our 200 monomer simulations charted against simulation results of previous work[18] for **a)** Pluronic L44 and **b)** Pluronic P123.

Figure 6.10 shows the micellisation free energy for the micelles created from our 200 monomer simulations of Pluronics L44 and P123 in comparison with interpolated and standard experimental values.[16, 19] A comprehensive table of these results is again available in **Table 6.9** in **Appendix C**. The results here do not fall within the margins of errors for ΔGmic results from experimental micelles[16, 19], though they are in good agreement with theory (i.e. the ΔGmic decreases with increasing size of both the single Pluronic surfactant chains, and the increasing size of the micelles between the Pluronic L44 and Pluronic P123 models[37-41]), and they do seem to have a similar trend to experimental values. The difference between our results and the experimental values may be attributed to the fact that no consistent or dependable experimental values of aggregation numbers for these Pluronics could be obtained, and thus our own aggregation numbers and the number of potential surfactant-surfactant interactions used in our free energy calculations may be extremely off from real values.[37-41]

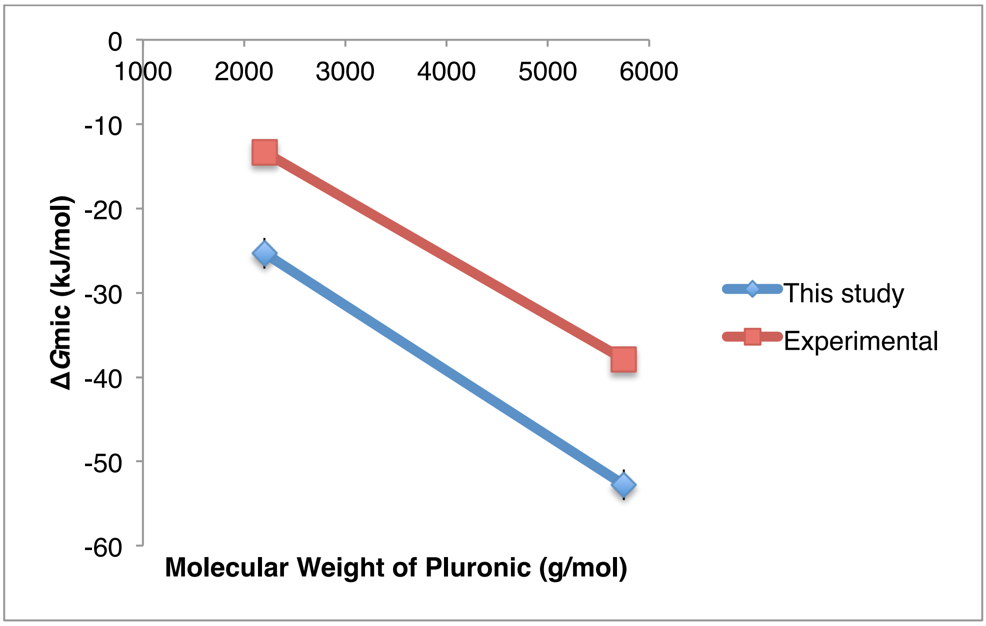

Figure 6.10: Micellisation free energy results for the micelles produced in our 200 monomer chain simulations of Pluronics L44 and P123 compared to experimental values for; Pluronic L44[16] and Pluroinc P123.[19]

6.3 Conclusions

In this chapter, by using the PEO and PPO models select in Chapter 5 and the hexane model created in Chapter 4, we were able to choose PEO-PPO non bonded interaction parameters and create seven Pluronic triblock copolymer models that adhered more closely to known data and expected behaviour in water and alkane solvents, and ultimately self-assembled into aggregated micelles.

The PEO-PPO non bonded interaction parameters from the study we took our PPO model from Nawaz et al.[1] were chosen as they were from the same study as our chosen PPO model, and they supplied apparently normal Pluronic behaviour for a generic Pluronic chain with the structure PEO_{10} PPO_{10} PEO_{10}.

Bulk density results of these Pluronic models when simulated in bulk were mainly within the margin of error for experimental results[14], with the exception of the Pluronic F38 model, possibly because of the much longer PEO blocks of Pluronic F38 and the slight overestimation of density seen in the PEO model in Chapter 5, and the much lower experimental density of Pluronic F38 compared to the other Pluronics. The ρ were all in good agreement with established theory, however, considering the chemical structures of the Pluronics being simulated and their varying PEO and PPO blocks.[32, 33, 42]

The shear viscosity results for the Pluronic L44, L62, and L64 models at 298.15K, and the paste Pluronic P85 and P123 models at 333.15K, were also within good agreement with expected η theory, for both chain length and temperature[30, 31, 44, 47, 48], though they were all lower or significantly lower than established experimental values.[13, 14]

Unlike the discrepancies in the density and shear viscosity results, the heat capacity results for our Pluronic P85, P123, and F38 models all fell within the margins of error for their respective experimental values.[15, 16, 17] The results adherence to theory and experimental results helped to validate the models, and also imply a potential connection to future Cp results that also fall close to experimental values, if known values are ever determined.

The Rg of single Pluronic triblock copolymer chains of L31, L44, L62, L64, P85, and F38 in CG MARTINI water at 300K, and single Pluronic chains of L64, P85, and F38 in CG MARTINI water at 273K were then compared to previous simulation work[1, 3] to establish trend with varying Pluronic structures.[25, 26, 28, 32, 36, 49] The Rg of these longer polymer chains had structure and chain responses that were expected due to the hydrophilic and hydrophilic properties in solvents of the PEO and PPO blocks which comprised the Pluronics.[14, 25, 26, 28, 32, 36, 49]

Simulations of 200 monomer chain simulations of Pluronics L44 and P123, and 300 monomer chain simulations of Pluronic L35 in MARTINI water, and 80 monomer chain simulations of Pluronic P123 in our 2-bead hexane model were next performed, and self-assembly and micelle aggregation was observed. This was the most paramount validation for our alkane models from Chapter 4, and our selected PEO and PPO models from Chapter 5, for use in CG Pluronic modelling as they were proven to create a Pluronic model capable of self-assembling in both polar and nonpolar solutions.[20-23, 26, 27, 32, 35, 36, 37, 41] This corroborated our models' chosen parameters through the correct hydroplicity and hydrophobicity they displayed in our Pluronic models.[1, 20-23, 26, 27, 32, 35, 36, 37, 41]

The aggregation numbers of the micelles created from our Pluronic L44, P123, and L35 simulations in water, while having no experimental counterparts, were not unreasonable in regards to previously observed values for other surfactants/concentrations/temperatures[20, 57, 61, 62], and did show a trend with molecular weight of the surfactants[54, 59], helping to further validate our Pluronics models.

The RDFs calculated for these self-assembling simulations both fell mostly within the margins of error of a previous AA study[18], though as they were in good agreement with expected theory, these results were mainly to establish trend.[25, 26, 38, 41, 50, 51]

The Δ*G*mic for the micelles created from our 200 monomer simulations of Pluronics L44 and P123, while not quantitatively meeting the experimental data[16, 19], did again show good observance of anticipated theory and a recognisable and comparable trend.[37-41] These results helped to further validate our Pluronic models.

These new insights into CG Pluronic and CG alkane modelling Pluronic simulations afforded by this study should aid in the design of more accurate synthesis simulations using Pluronic triblock copolymers in the future.

6.4 References

. [1] S. Nawaz, & P. Carbone. Coarse-graining poly (ethylene oxide)–poly (propylene oxide)–poly (ethylene oxide)(PEO–PPO–PEO) block copolymers using the MARTINI force field. *The Journal of Physical Chemistry B*, *118*(6):1648-1659, 2014.

. [2] M. Hatakeyama, & R. Faller. Coarse-grained simulations of ABA amphiphilic triblock copolymer solutions in thin films. *Physical Chemistry Chemical Physics*, *9*(33):4662-4672, 2007.

. [3] S. Hezaveh, S. Samanta, A. De Nicola, G. Milano, & D. Roccatano. Understanding the interaction of block copolymers with DMPC lipid bilayer using coarse-grained molecular dynamics simulations. *The Journal of Physical Chemistry B*, *116*(49), 14333-14345, 2012.

. [4] I. Wood, M. Martini, J. Albano, M. Cuestas, V. Mathet, & M. Pickholz. Coarse grained study of pluronic F127: Comparison with shorter co-polymers in its interaction with lipid bilayers and self-aggregation in water. *Journal of Molecular Structure*, *1109*:106-113, 2016.

. [5] S. Marrink and P. Tieleman. Perspective on the martini model. Chem. Soc. Rev., 42:6801–6822, 2013.

. [6] F. Oellien and M. C. Nicklaus. Online SMILES translator and structure file generator. 2004.

. [7] NIH Biomedical Research Center for Macromolecular Modeling and Bioinformatic. Vmd users manual version 1.9.2. 1.9.2, 2014.

. [8] K. Kremer, P. Kremer, and C. Kremer. Multiscale simulation of soft matter systems: from the atomistic to the coarse-grained level and back. Soft Matter, 124(15), 2009.

. [9] M. van Gunsteren and M. van Gunsteren, C. van Gunsteren. Multigraining: an algorithm for simultaneous fine-grained and coarse-grained simulation of molecular systems. The Journal of chemical physics, 124(15), 2006.

. [10] M. Henkel. Conformal invariance and critical phenomena. Springer Science & Business Media, 2013.

. [11] E. Batrakova and A. Kabanov. Pluronic block copolymers: Evolution of drug delivery concept from inert nanocarriers to biological response modifiers. J Control Release., 130(2):98–106, 2008.

. [12] J. C. Shelley, & M. Y. Shelley. Computer simulation of surfactant solutions. *Current opinion in colloid & interface science*, *5*(1-2), 101-110, 2000.

. [13] P. Alexandridis, & T. A. Hatton. Poly (ethylene oxide)- poly (propylene oxide)-poly (ethylene oxide) block copolymer surfactants in aqueous solutions and at interfaces: thermodynamics, structure, dynamics, and modeling. *Colloids and Surfaces A: Physicochemical and Engineering Aspects*, *96*(1-2), 1-46, 1995.

. [14] "BASF - Product information the chemicals catalog - Pluronics". *BASF Corporation Website*. Available at: https://worldaccount.basf.com/wa/NAFTA/Catalog/ChemicalsNAFTA/pi/BASF/Brand/ pluronic, 2016. [Accessed 28 10 2018].

. [15] L. Meilleur, A. Hardy, & F Quirion. Probing the Structure of Pluronic PEO-PPO-PEO Block Copolymer Solutions with Their Apparent Volume and Heat Capacity. *Langmuir, 12,* 4697-4703, 1996.

. [16] B. Naskar, S. Ghosh, & S. P. Moulik. Solution behavior of normal and reverse triblock copolymers (Pluronic L44 and 10R5) individually and in binary mixture. *Langmuir*, *28*(18), 7134-7146, 2012.

. [17] R. Shvartzman-Cohen, C. L. Ren, I. Szleifer, & R. Yerushalmi-Rozen. An isotopic effect in self-assembly of amphiphilic block copolymers: the role of hydrogen bonds. *Soft Matter*, *5*(24), 5003-5011, 2009.

. [18] X. Song, S. Zhao, S.Fang, Y. Ma, & M. Duan. Mesoscopic simulations of adsorption and association of PEO-PPO-PEO triblock copolymers on a hydrophobic surface: From mushroom hemisphere to rectangle brush. *Langmuir*, *32*(44):1375-11385, 2016.

. [19] Z. He, & P. Alexandridis. Micellization thermodynamics of Pluronic P123 (EO20PO70EO20) amphiphilic block copolymer in aqueous ethylammonium nitrate (EAN) solutions. *Polymers*, *10*(1), 32, 2017.

. [20] R. Nagarajan. Solubilization of hydrocarbons and resulting aggregate shape transitions in aqueous solutions of Pluronic®(PEO–PPO–PEO) block copolymers. *Colloids and Surfaces B: Biointerfaces*, *16*(1-4), 55-72, 1999.

. [21] C. Tanford. *The hydrophobic effect: formation of micelles and biological membranes*. Wiley Interscience publication. Wiley,1973.

. [22] M. Rosen and J Kunjappu. Surfactants and Interfacial Phenomena. John Wiley Sons.123-212, 2012.

. [23] A. Denkova, E. Mendes, and C. Coppens. Non-equilibrium dynamics of block copolymer micelles in solution: recent insights and open questions. Soft Matter, 6:235-2357, 2010.

. [24] P. Bahadur. Block copolymers–Their microdomain formation (in solid state) and surfactant behaviour (in solution). *Current Science*, 1002-1007, 2001.

. [25] M. Fixman. Radius of gyration of polymer chains. *The Journal of Chemical Physics*, *36*(2), 306-310, 1962.

. [26] M. Fixman. Radius of gyration of polymer chains. II. Segment density and excluded volume effects. *The Journal of Chemical Physics*, *36*(12), 3123-3129, 1962.

. [27] K. Nakashima, & P. Bahadur. Aggregation of water-soluble block copolymers in aqueous solutions: recent trends. *Advances in colloid and interface science*, *123*, 75-96, 2006.

. [28] K. M. Hong, & J. Noolandi. Theory of inhomogeneous multicomponent polymer systems. *Macromolecules*, *14*(3), 727-736, 1981.

. [29] E. Helfand. Block copolymer theory. III. Statistical mechanics of the microdomain structure. *Macromolecules*, *8*(4), 552-556, 1975.

. [30] P. E. Rouse Jr. A theory of the linear viscoelastic properties of dilute solutions of coiling polymers. *The Journal of Chemical Physics*, *21*(7), 1272-1280, 1953.

. [31] K. F. Freed, & S. F. Edwards Polymer viscosity in concentrated solutions. *The Journal of Chemical Physics*, *61*(9), 3626-3633,1974.

. [32] M. Doi, & S. F. Edwards. *The theory of polymer dynamics*. oxford university press.,(73), 1988.

. [33] J. E. Mark. *Physical properties of polymers handbook*. New York, Springer, (1076), 825, 2007.

. [34] W. H. Stockmayer, & C. E. Hecht. Heat capacity of chain polymeric crystals. *The Journal of Chemical Physics*, *21*(11), 1954-1958, 1953.

. [35] L. Leibler, H. Orland, & J. C. Wheeler. Theory of critical micelle concentration for solutions of block copolymers. *The Journal of chemical physics*, *79*(7), 3550-3557, 1983.

. [36] J. Noolandi, & K. M. Hong. Theory of block copolymer micelles in solution. *Macromolecules*, *16*(9), 1443-1448, 1983.

. [37] C. Tanford. *The hydrophobic effect: formation of micelles and biological membranes*. Wiley Interscience publication. Wiley,1973.

. [38] J. N. Israelachvili, D. J. Mitchell, & B. W. Ninham. 'Theory of self-assembly of hydrocarbon amphiphiles into micelles and bilayers'. *Journal of Chemical Socirty, Faraday Transaction 2 (*72),1525–1568, 1976.

. [39] R. Nagarajan, & E. Ruckenstein. 'Aggregation of amphiphiles as micelles or vesicles in aqueous media'. *Journal of Colloid and Interface Science* 71(3), 580–604, 1979.

. [40] J. B. Hayter, & J. Penfold. Determination of micelle structure and charge by neutron small-angle scattering. *Colloid and Polymer Science*, *261*(12), 1022-1030, 1983.

. [41] R. Nagarajan, & K. Ganesh. Block copolymer self-assembly in selective solvents: theory of solubilization in spherical micelles. *Macromolecules*, *22*(11), 4312-4325, 1989.

. [42] L. J. Fetters, D. J. Lohse, D. Richter, T. A. Witten, & A. Zirkel. Connection between polymer molecular weight, density, chain dimensions, and melt viscoelastic properties. *Macromolecules*, *27*(17), 4639-4647, 1994.

. [43] J. Barthel, R. Neueder, & H. Roch. Density, relative permittivity, and viscosity of propylene carbonate+ dimethoxyethane mixtures from 25° C to 125° C. *Journal of Chemical & Engineering Data*, *45*(6), 1007-1011, 2000.

. [44] N.C.B.I., National Center for Biotechnology Information. PubChem Compound Database; CID=12375, https://pubchem.ncbi.nlm.nih.gov/compound/12375, [Accessed 10 6 2018].

. [45] J. P. Holman. *Heat Transfer*. McGraw-Hill, 372-375, 2002.

. [46] F. Incropera and D. P. DeWitt. *Fundamentals of Heat and Mass Transfer*. Wiley, 298-299 2007

. [47] J. G. Kirkwood. Statistical mechanics of fluid mixtures, J. Chem. Phys., 3:300-313,1935.

. [48] J. C. Li, & P. Chang. Self-Diffusion Coefficient and Viscosity in Liquids. *The Journal of Chemical Physics*, *23*(3), 518-520, 1955.

. [49] M. A. Abramowicz, J. C. Miller, & Z. Stuchlík. Concept of radius of gyration in general relativity. *Physical Review D*, *47*(4), 1440, 1993.

. [50] H. Yamakawa. *Modern theory of polymer solutions*. Harper & Row, 10-35, 1971.

. [51] J. G. Curro, & K. S. Schweizer. Equilibrium theory of polymer liquids: Linear chains. *The Journal of chemical physics*, *87*(3), 1842-1846, 1987.

. [52] J. Barnound & L. Monticelli. Coarse-grained force fields for molecular simulations. Methods Mol Biol., (1215):125– 149, 2015.

. [53] K. Kremer, P. Kremer, & C. Kremer. Multiscale simulation of soft matter systems: from the atomistic to the coarse-grained level and back. Soft Matter, 124(15), 2009.

. [54] L. Fan, M. Degen, N. Grupido, S. Bendle, & P. Pennartz. Effects of molecular weight, temperature and salt on the self assembly of triblock copolymer solutions. *Materials Science and Engineering: A*, *528*(1), 127-136, 2010.

. [55] Y. Moroi. Micelles: theoretical and applied aspects. Springer Science & Business Media, 1992.

. [56] N. E. Olesen. Journal of Colloid and Interface Science. 453, 79-89, 2015.

. [57] S. H. Chen, M. Broccio, Y. Liu, E. Fratini, & P. Baglioni. The two-Yukawa model and its applications: the cases of charged proteins and copolymer micellar solutions. *Applied Crystallography*, *40*(s1), s321-s326, 2007.

. [58] P. Linse, & M. Malmsten. Temperature-dependent micellization in aqueous block copolymer solutions. *Macromolecules*, *25*(20), 5434-5439, 1992.

. [59] R. Serra-Gómez, C. A. Dreiss, J. González-Benito, & G. González-Gaitano. Structure and rheology of poloxamine T1107 and its nanocomposite hydrogels with cyclodextrin-modified barium titanate nanoparticles. *Langmuir*, *32*(25), 6398-6408, 2016.

. [60] R. De Lisi, S. Milioto, & N. Muratore. Thermodynamics of surfactants, block copolymers and their mixtures in water: the role of the isothermal calorimetry. *International journal of molecular sciences*, *10*(7), 2873-2895, 2009.

. [61] I. Goldmints, F. K. von Gottberg, K. A. Smith, & T. A. Hatton. Small-Angle Neutron Scattering Study of PEO– PPO– PEO Micelle Structure in the Unimer-to-Micelle Transition Region. *Langmuir*, *13*(14), 3659-3664, 1997.

. [62] J. S. Lettow, T. M. Lancaster, C. J. Glinka, & J. Y. Ying. Small-angle neutron scattering and theoretical investigation of poly (ethylene oxide)– poly (propylene oxide)– poly (ethylene oxide) stabilized oil-in-water microemulsions. *Langmuir*, *21*(13), 5738-5746, 2005.

. [63] G. Pérez-Sánchez, F. A. Vicente, N. Schaeffer, I. S. Cardoso, S. P. M. Ventura, O. N. Sobek, M. Jorge, & J. A. P. Coutinho. Rationalizing the phase behavior of triblock-copolymers through experiments and multi-scale modeling, In preparation.

CONCLUSIONS AND FUTURE WORK

7

The research described in this thesis focused on developing and validating CG simulation models to investigate the structural and dynamical behaviour of self- assembling triblock copolymers. In Chapter 4, an evaluation of standard MARTINI beads, testing of MARTINI alkane models, and a thorough parameterisation and validation and of our own alkane and polyethylene models was presented. This process has lead to improved mapping schemes and adjusted parameters for alkane solvent models, PEO and PPO models with the most accurate properties in themselves and in those alkane solvents, and ultimately, Pluronic models with self-assembly behaviour.

The MARTINI model inadequately replicated realistic alkane behaviour, save for enthalpy of vaporisation, justifying a complete parameterisation for alkanes. Through extensive parameterisation against experimental values such as Gibbs free energies of solvation, enthalpies of vaporisation, densities, self-diffusion coefficients, and radii of gyration, we were able to create 2:1, 3:2, 4:1, and 5:1 mapped alkane models (consisting of 1 to 4 beads) with good agreement to known experimental and simulated data. Our 5:1 mapped models, however, start to break down in terms of enthalpy of vaporisation at more than 2 CG beads, which does question their validity for long alkane chains. The underestimation of enthalpies of vaporisation is an inherent problem in our alkane modelling, potentially due to the inability to match such large values to coarse-grained beads while maintaining other properties, and further work would need to be done to isolate the cause and possibly rectify it. Arguably, however, for their use within future self-assembling Pluronic simulations, the free energy results were of greater importance, due to the previously explained nature of estimating self-assembling surfactant properties. These models were further parameterised for free energy of solvation in themselves and in MARTINI water, and longer chains of our 2:1 and 4:1 mapped models were also validated for use as polyethylene in polyethylene melts.

Overall, our alkane models provide better adherence to known data than the standard MARTINI models, and it is the hope that this parameterisation will help facilitate not only further research involving coarse-grained alkanes, but more importantly, future surfactant self-assembly in future PEO, PPO, and Pluronic optimisation work.

In order to move forward to actually modelling self-assembling Pluronic surfactants, adequate PEO and PPO models needed to be selected. Chapter 5 consisted of validation work for seven established PEO models and four established PPO models, comparing structural and dynamic properties of 1-bead and 2-bead models, such as Gibbs free energies of solvation, enthalpies of vaporisation, densities, and self-diffusion coefficients, to known experimental and simulated data. From the 2-bead simulations, two models, one for PEO and one for PPO, were ultimately selected, and these results were mostly all in good agreement with the known data (save for a slight density overestimation with the PEO model), but the enthalpy of vaporisation of our chosen PEO model was significantly lower than experimental values. This may create problems in future simulations relying on that property, and like the enthalpy of vaporisation results from Chapter 4, may possibly need to be re-examined and properly parameterised.

Free energies of solvation were validated for the models in themselves, MARTINI water, and were calibrated for free energy of solvation in our hexadecane and hexane models from Chapter 4, and a parameterised heptane model interpolated from that work. This helped to establish the transferability of the models between solvents, as well as further our alkane models from Chapter 4.

The PEO 1-bead and 2-bead models had a fair amount of experimental and simulation data available for the PEO monomer and dimer (i.e. DE and DME, respectively), it should be noted that there was no available experimental, or even simulation, data for the true PPO monomer or dimer. This means that the while their comparison was to polymers with similar chemical structures, including a short PPO oligomer (i.e. MOE, DMP, and DEE), they lacked the methyl groups on their carbon backbones characteristic of true PPO. This could possibly mean that the validation of the PPO models does not truly represent the true values of PPO, and if successful experimental work is done in the future, the models may need to be reevaluated and potentially parameterised.

Longer monomer chains of these models were validated against simulated end-to-end distances, relaxation times and radii of gyration data. The 36-bead models were then observed in polar and nonpolar solvents (i.e. water and heptane) and it was established that their behaviour adhered to theory for self-assembly (i.e. the models displayed the correct hydrophobicity and hydrophilicity typical of PEO and PPO within these solvents). These results, along with the numerous other properties validated against known data, implied that our selected PEO and PPO models were suitable for self-assembling Pluronic surfactant simulation work, in multiple solvents.

The ultimate hydrophobicity and hydrophilicity results of our chosen PEO and PPO models in MARTINI water and our heptane model, coupled with the adherence of these models with numerous other properties, suggests that these models will be the best for use in future Pluronic surfactant simulation work. It is also our hope that the additional development of our own MARTINI alkane models in this study for use with these Pluronic surfactant block components will also lead to self-assembly of simulated Pluronic surfactants solvated in them in later work.

In our final chapter, Chapter 6, we were able to create eight Pluronic models, three with apparent self-assembly properties. We began by validating PEO-PPO parameters, so that the models could be combined into the specific blocks needed for the Pluronic structures, and a PEO-PPO model was selected from four established models. The models were tested in a generic Pluronic chain with the structure PEO_{10} PPO_{10} PEO_{10} in MARTINI water, and as the models were all observed to have normal behaviour in reagrds to self-assembly theory (i.e. in water the PPO portion curl inwards, while the PEO end chains move to surround them, pulled inwards by the curling of the PPO), we chose the model was from the study we had taken our PPO model from. These nonbonded parameters were then used to produce models for Pluronic L31, L35, L44, L62, L64, P85, P123, and F38, and simulations of the melts of Pluronics L31, L44, L62, L64, P85, P123, and F38 were found to be in good agreement with experimental and simulated properties including densities, shear viscosities, heat capacities, and radii of gyration. While the shear viscosity results of these models showed an expected trend and adherence to theory, it is important to note they were all lower or significantly lower than established experimental values. As shear viscosity is dependant on the volume of the simulation system, however, this property could potentially be re-parameterised for future simulation through adjusting the simulation size.

Ultimately, the 200 chain simulations of our Pluronic L44 and P123 models in MARTINI water, 300 chain simulations of Pluronic L35 in

MARTINI water, and 80 monomer chain simulations of Pluronic P123 in our 2-bead hexane model, successfully aggregated, validating their self-assembly properties. The aggregation numbers of the micelles these simulations created were also reasonable in regards to theory further validating our Pluronics models, and the RDFs of the 200 chain simulations of our Pluronic L44 and P123 were found to be in good agreement with previous simulation work. The micellisation free energy of the aggregates in these simulations were calculated and had a similar trend to experimental values, though with much lower results. The discrepancy between our models micellisation free energy and known values may be attributed to the nature of the CG models, or the difference in aggregation numbers (and thus the number of interactions of a surfactant in the micelle core used to calculate our values) and those in real Pluronic L44 and P123 self-assembly aggregation. No known reliable experimental aggregation number data, however, could be attained for these Pluronics to test this theory.

The new insights into CG Pluronic and CG alkane modelling Pluronic simulations afforded by these new models should hopefully aid in the design of more accurate synthesis simulations using Pluronic triblock copolymers in the future.

It is unfortunate that our work was too time-consuming to progress into actual synthesis modelling, though we have provided new, more accurate, coarse-grained alkane models suitable for use in a multitude of applications, including the simulation of mesoporous silica synthesis. We have also laid the groundwork for a new model of coarse-grained Pluronics, which while incomplete, is a novel starting point for future work.

Our results are very promising for future work. There are numerous potential avenues for future work with our models, so it should be noted that those suggested here are in no way comprehensive.

If results were too far outside of expected experimental parameters at any point in these theoretical future simulations, we could consider going back to the above mentioned problems in our own models (i.e. the alkanes, PEO, PPO, or Pluronic surfactants) to reparemterise them and retest this future work.

If we had had more time in my PhD., we would first attempt to combine established CG silica precursor models with our Pluronic models to observe their behaviour. To our knowledge there is no experimental value that could help validate these silica precursor models with our Pluronic models, so the methods used in the parameterisation of MCM-41 CG synthesis simulations would be attempted.[1-6]

Once we had found or parameterised a suitable silica precursor model that lead to the synthesis, we could then do testing of different synthesis variables on the resulting mesostructures. This might include varying pH values, temperature values, or any other variable used in experimental synthesis of SBA-15. The resulting mesostructures could then be matched to known experimental pore diameters, and could be further validated or parameterised to them. Assuming this was successful, we could ultimately attempt a synthesis simulation with novel synthesis variables, and then find a lab to replicate them for comparison. This would imply our models could be used to predict experimental behaviour, which would be an invaluable tool for future research or commercial use.

7.1 References

. [1] F. R. Siperstein, & K. E. Gubbins. Synthesis and characterization of templated mesoporous materials using molecular simulation. *Molecular Simulation*, *27*(5-6), 339-352, 2001.

. [2] F. R. Siperstein, & K. E. Gubbins. Phase separation and liquid crystal self-assembly in surfactant– inorganic– solvent systems. *Langmuir*, *19*(6), 2049-2057, 2003.

. [3] L. Jin, S. M. Auerbach, & P. A. Monson. Simulating the formation of surfactant-templated mesoporous silica materials: a model with both surfactant self-assembly and silica polymerization. *Langmuir*, *29*(2), 766-780, 2012.

. [4] M. Jorge, J. R. B. Gomes, M. N. D. S. Cordeiro, & N. A. Seaton. Molecular simulation of silica/surfactant self-assembly in the synthesis of periodic mesoporous silicas. *Journal of the American Chemical Society*, *129*(50), 15414-15415, 2007.

. [5] G. Pérez-Sánchez, J. R. B. Gomes, & M. Jorge. Modeling self-assembly of silica/surfactant mesostructures in the templated synthesis of nanoporous solids. *Langmuir*, *29*(7), 2387-2396, 2013.

. [6] G. Pérez-Sánchez, S.-C. Chien, J. R. B. Gomes, M. N. D. S. Cordeiro, S. M. Auerbach, P. A. Monson, & M. Jorge. Multiscale model for the templated synthesis of mesoporous silica: the essential role of silica oligomers. *Chemistry of Materials*, *28*(8), 2715-2727, 2016.

APPENDIX A

MARTINI Alkane Models	**Number of Beads**	**ΔGsol (this study, kJ/mol)**	**ΔGsol (experimental [46, 47, 51], kJ/mol)**
Propane (C_3H_8)	1	-5.90 ± 0.62	*-5.98*
Butane (C_4H_{10})	1	-5.90 ± 0.62	*-9.16*
Octane (C_8H_{18})	2	-16.98 ± 0.59	-20.96
Dodecane ($C_{12}H_{26}$)	3	-28.47 ± 0.66	-32.88
Hexadecane ($C_{16}H_{34}$)	4	-40.38± 0.57	-43.96

Table 4.11: Free energy of solvation in hexadecane results for MARTINI alkane, compared to the interpolated experimental and experimental data for linear alkanes.[46, 47, 51] Italicised results represent interpolated data.

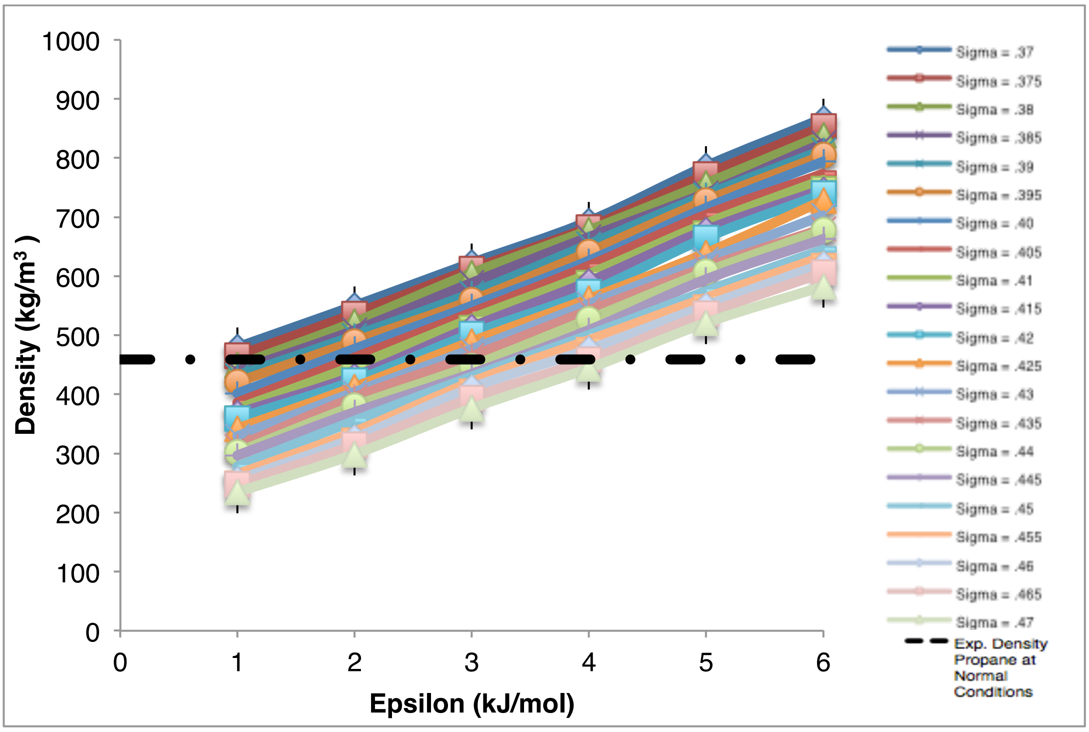

Density (kg/m³)
1000
900
800
700
600
500
400
300
200
100
0
0
1
2
3
4
5
6
Epsilon (kJ/mol)
Sigma = .37
Sigma = .375
Sigma = .38
Sigma = .385
Sigma = .39
Sigma = .395
Sigma = .40
Sigma = .405
Sigma = .41
Sigma = .415
Sigma = .42
Sigma = .425
Sigma = .43
Sigma = .435
Sigma = .44
Sigma = .445
Sigma = .45
Sigma = .455
Sigma = .46
Sigma = .465
Sigma = .47
Exp. Density Propane at Normal Conditions

a)

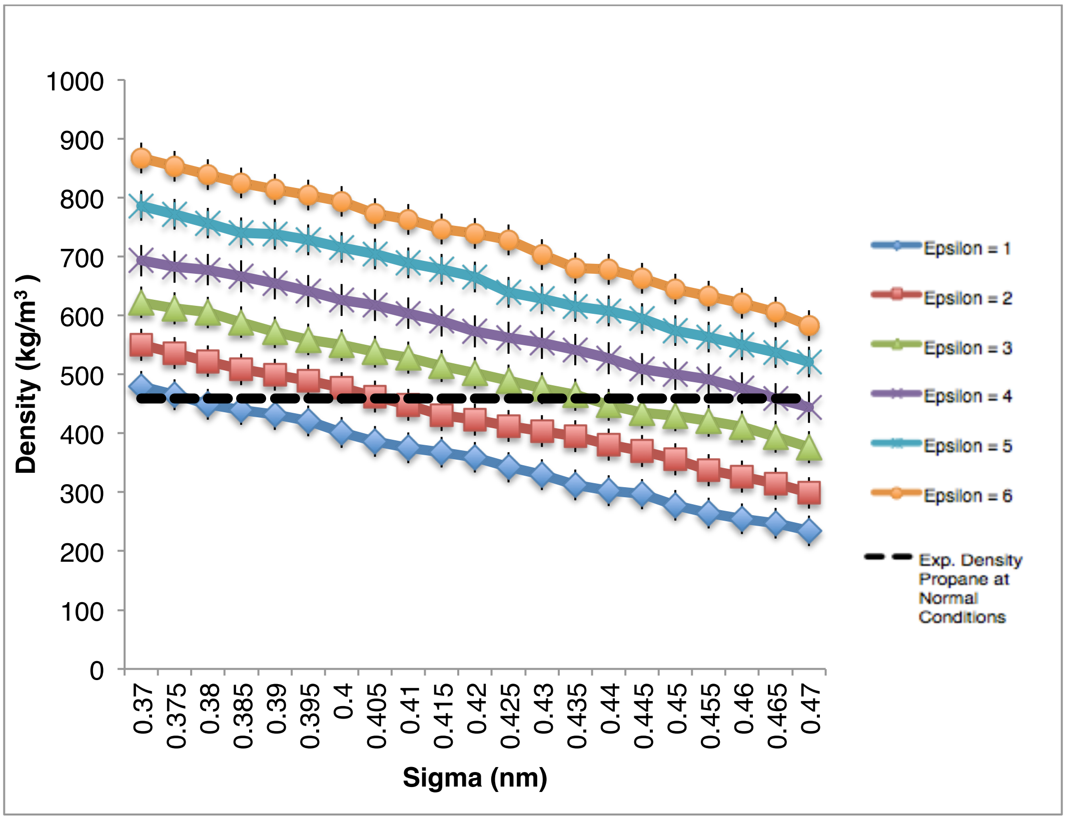

b)

Figures 4.33a-b: Densities determined for propane's molecular weight, of the 1-bead solvent systems for different values of the Lennard-Jones parameters: **a)** epsilon; **b)** sigma. The black dashed line represents the experimental reference values for propane at room temperature.[52, 53]

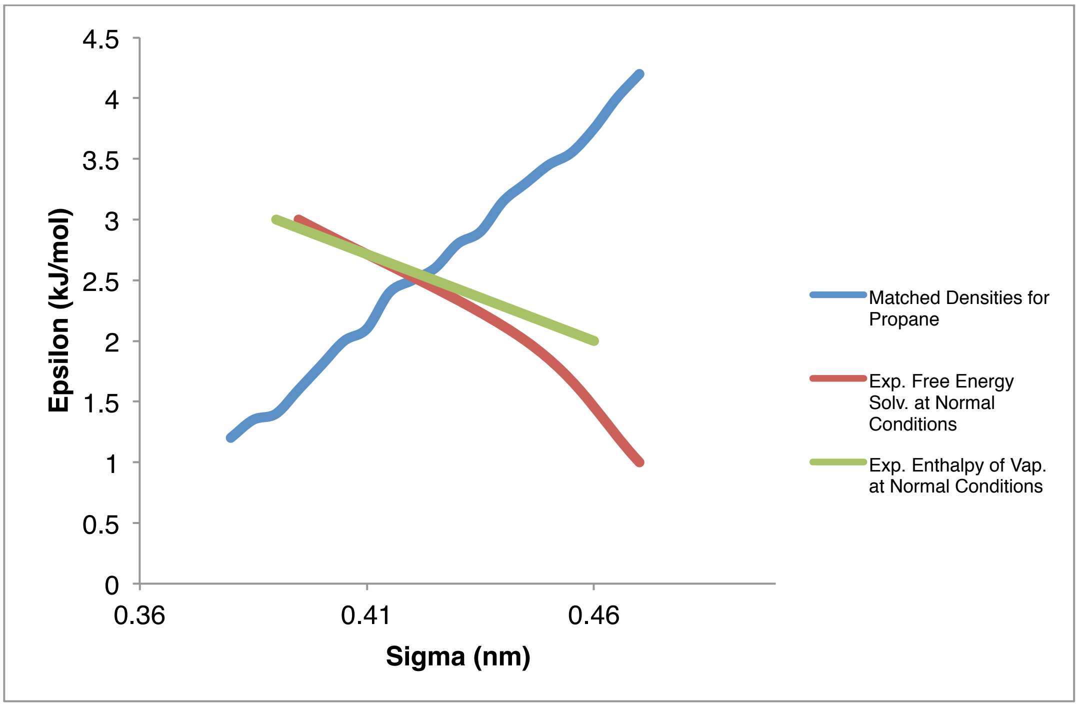

Figure 4.34: Determination of optimal set of parameters for the 3:1 mapped 1-bead. The full lines show each property at standard temperature and pressure: density (blue), free energy of self-solvation (red), and enthalpy of vaporisation (green).[46, 47, 48, 49, 50, 51, 52, 53]

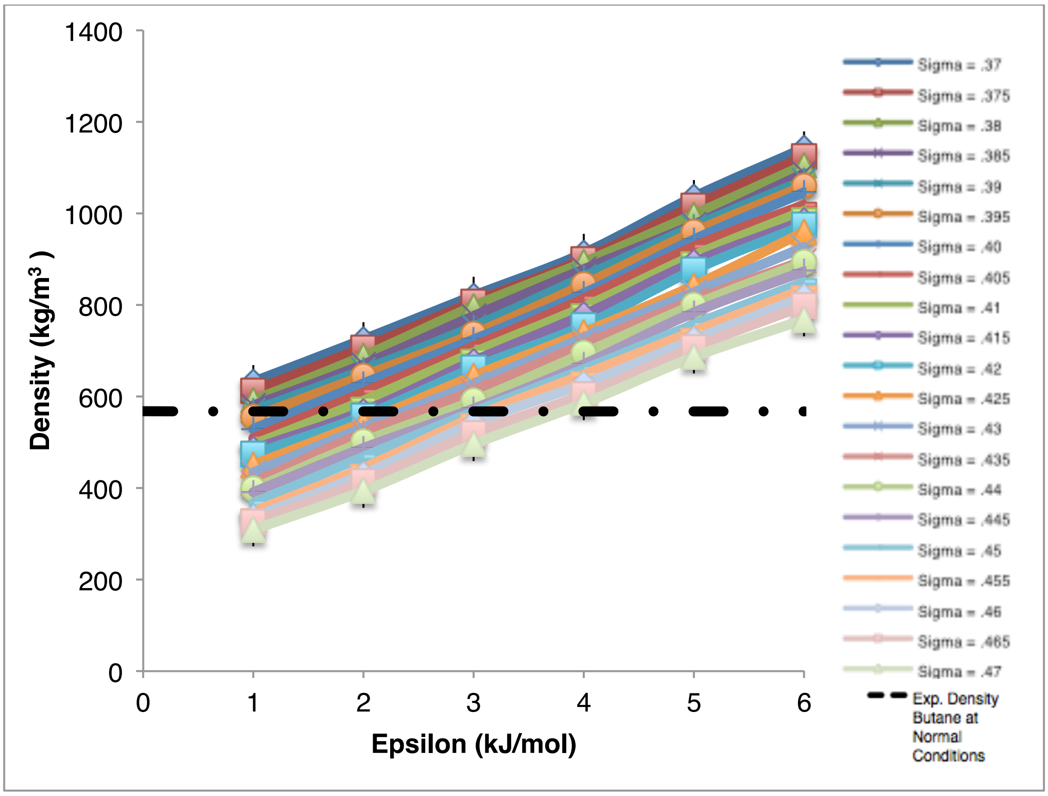
Density (kg/m^3)
1400
1200
1000
800
600
400
200
0
Epsilon (kJ/mol)
0
1
2
3
4
5
6
Sigma = .37
Sigma = .375
Sigma = .38
Sigma = .385
Sigma = .39
Sigma = .395
Sigma = .40
Sigma = .405
Sigma = .41
Sigma = .415
Sigma = .42
Sigma = .425
Sigma = .43
Sigma = .435
Sigma = .44
Sigma = .445
Sigma = .45
Sigma = .455
Sigma = .46
Sigma = .465
Sigma = .47
Exp. Density Butane at Normal Conditions

a)

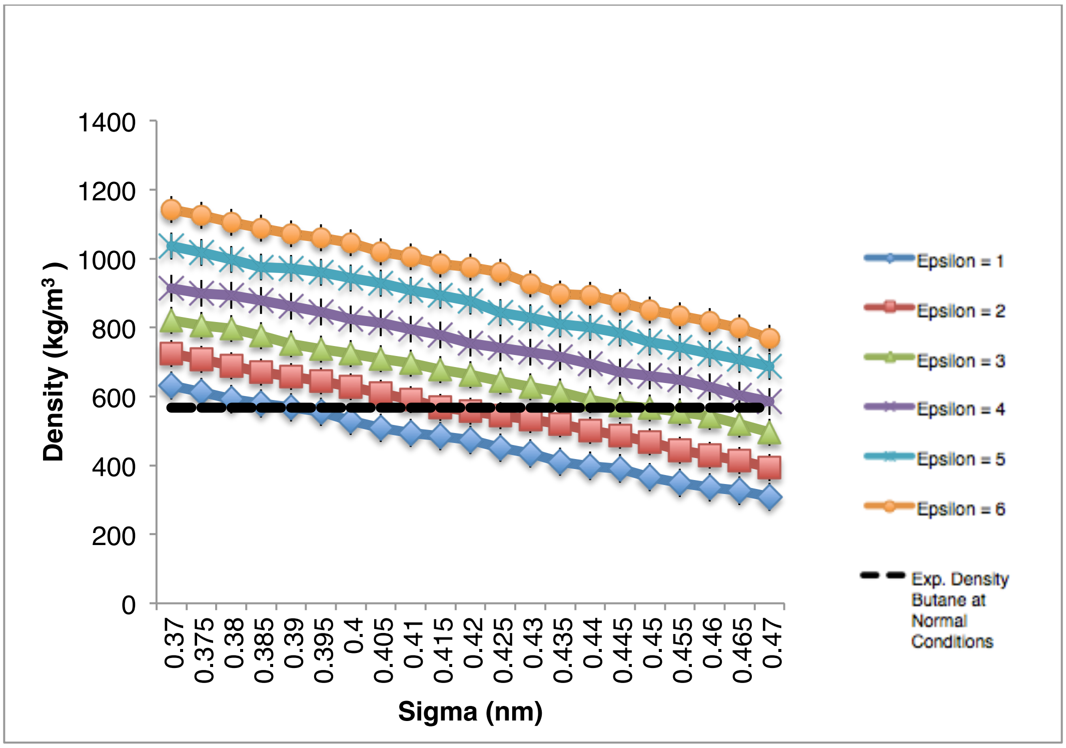

b)

Figures 4.35a-b: Densities determined for butane's molecular weight, of the 1-bead solvent systems for different values of the Lennard-Jones parameters: **a)** epsilon; **b)** sigma. The black dashed line represents the experimental reference values for butane at room temperature.[52, 53]

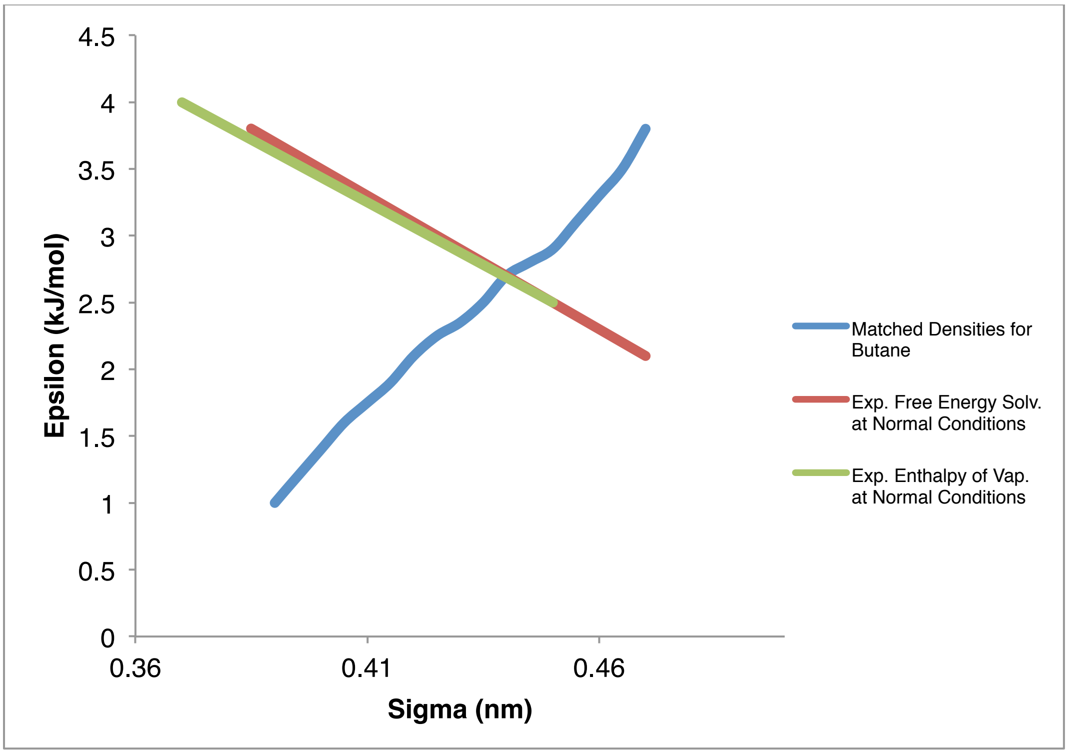

Figure 4.36: Determination of optimal set of parameters for the 4:1 mapped 1-bead. The full lines show each property at standard temperature and pressure: density (blue), free energy of self-solvation (red), and enthalpy of vaporisation (green).[46, 47, 48, 49, 50, 51, 52, 53]

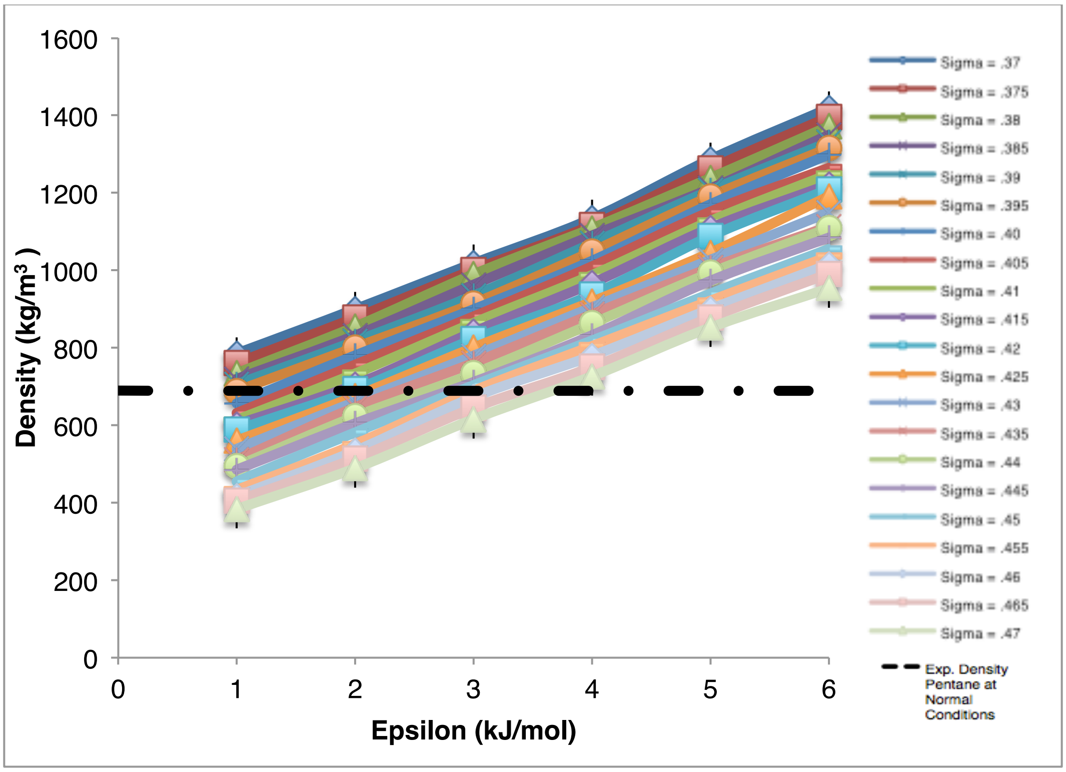
1600
1400
1200
1000
800
600
400
200
0
Density (kg/m^3)
0
1
2
3
4
5
6
Epsilon (kJ/mol)
Sigma = .37
Sigma = .375
Sigma = .38
Sigma = .385
Sigma = .39
Sigma = .395
Sigma = .40
Sigma = .405
Sigma = .41
Sigma = .415
Sigma = .42
Sigma = .425
Sigma = .43
Sigma = .435
Sigma = .44
Sigma = .445
Sigma = .45
Sigma = .455
Sigma = .46
Sigma = .465
Sigma = .47
Exp. Density Pentane at Normal Conditions

a)

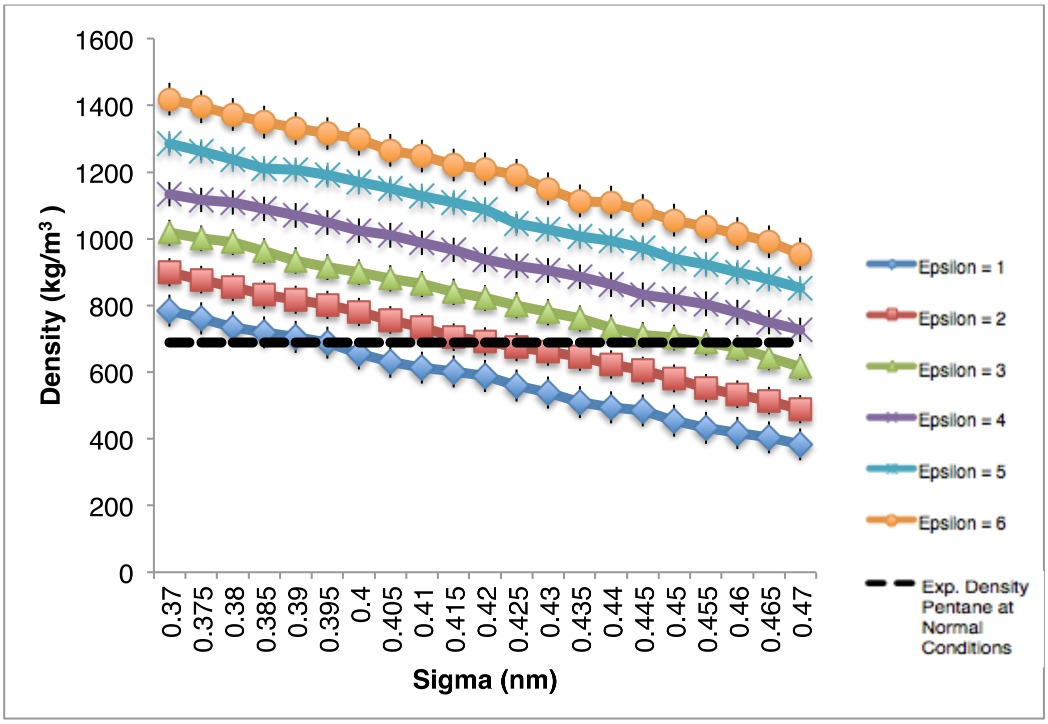

b)

Figures 4.37a-b: Densities determined for pentane's molecular weight, of the 1-bead solvent systems for different values of the Lennard-Jones parameters: **a)** epsilon; **b)** sigma. The black dashed line represents the experimental reference values for pentane at room temperature.[52, 53]

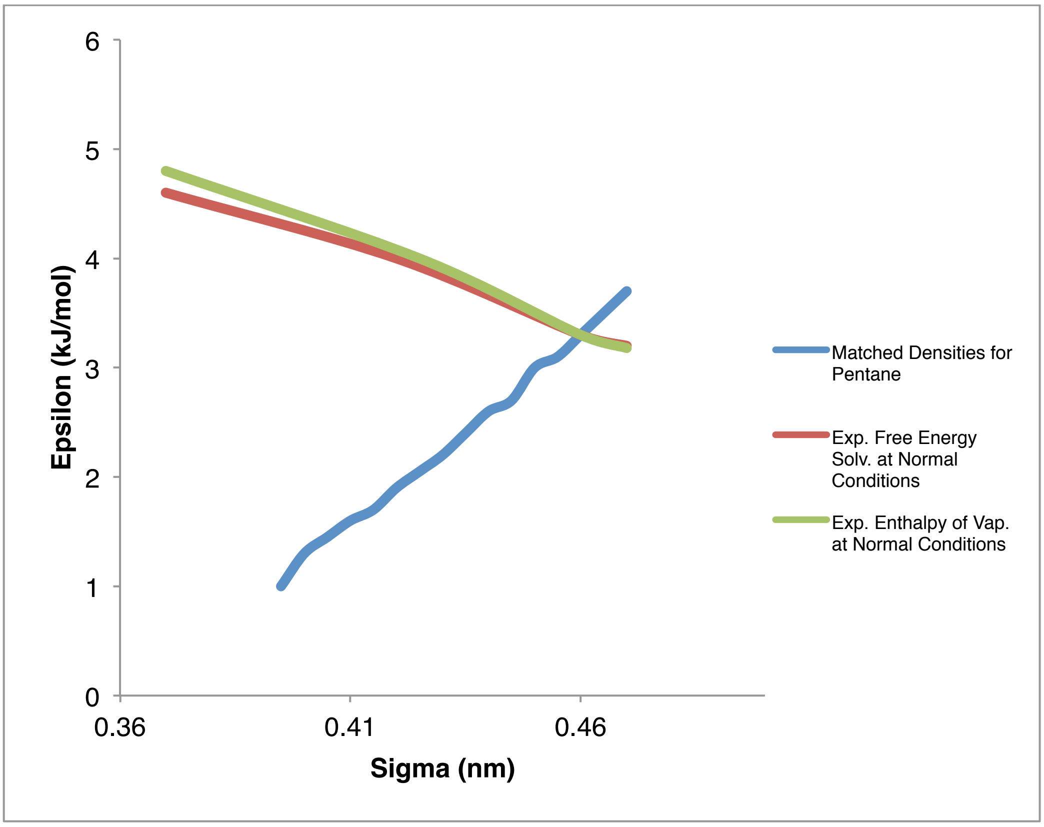

Figure 4.38: Determination of optimal set of parameters for the 5:1 mapped 1-bead. The full lines show each property at standard temperature and pressure: density (blue), free energy of self-solvation (red), and enthalpy of vaporisation (green).[46, 47, 48, 49, 50, 51, 52, 53]

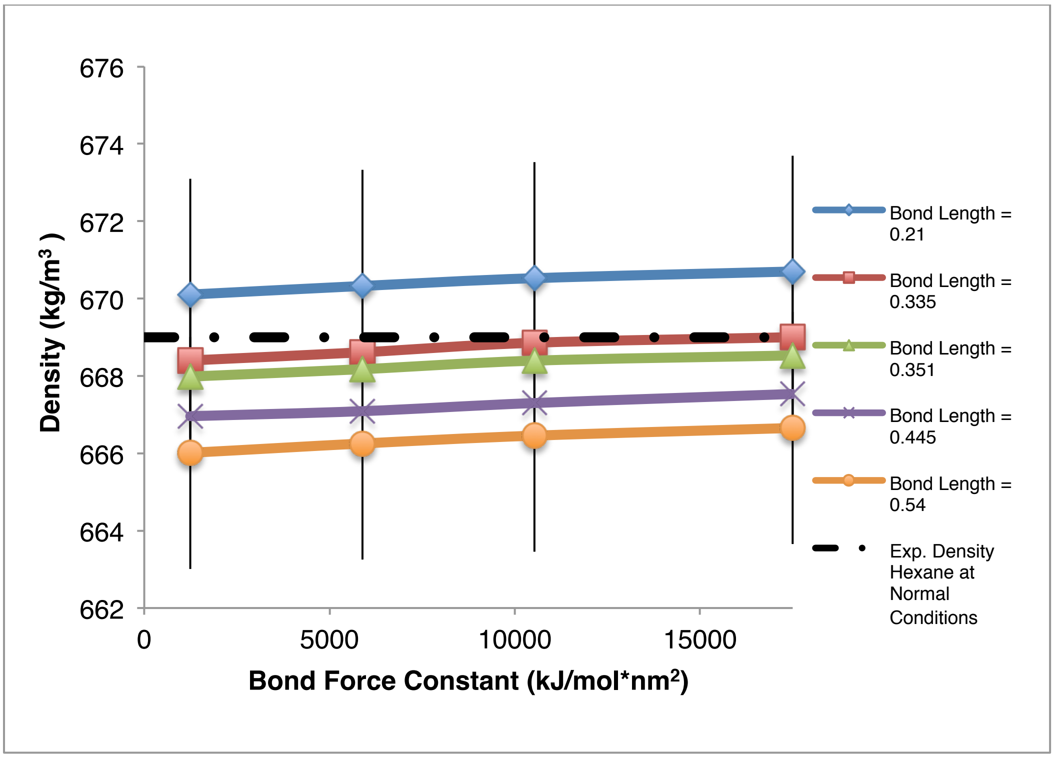
676
674
672
670
668
666
664
662
0
5000
10000
15000
Density (kg/m³)
Bond Force Constant (kJ/mol*nm²)
Bond Length = 0.21
Bond Length = 0.335
Bond Length = 0.351
Bond Length = 0.445
Bond Length = 0.54
Exp. Density Hexane at Normal Conditions

a)

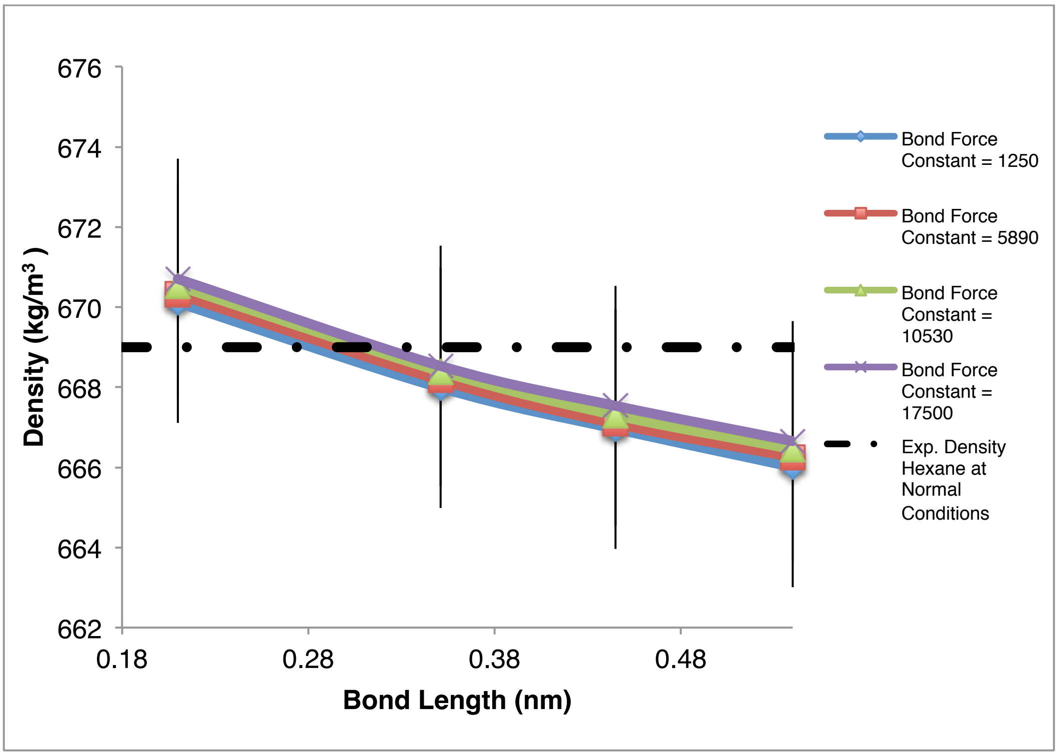

b)

Figures 4.39a-b: Selected densities determined for hexane’s molecular weight, of the 2-bead solvent systems for different values of the bond length and bond force constant parameters: **a)** selected bond lengths at different bond force constants, and **b)** bond force constants at different bond length values. The black dashed line represents the experimental reference values for hexane at room temperature.[52, 53]

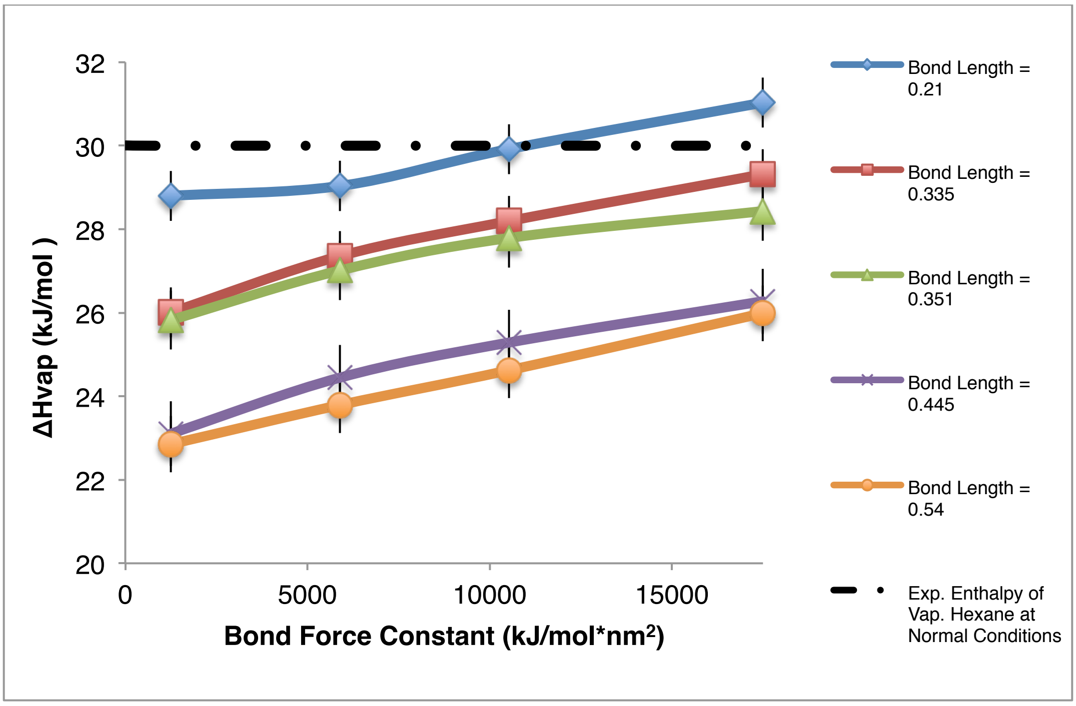
32
30
28
26
24
22
20
ΔHvap (kJ/mol)
0
5000
10000
15000
Bond Force Constant (kJ/mol*nm²)
Bond Length = 0.21
Bond Length = 0.335
Bond Length = 0.351
Bond Length = 0.445
Bond Length = 0.54
Exp. Enthalpy of Vap. Hexane at Normal Conditions

a)

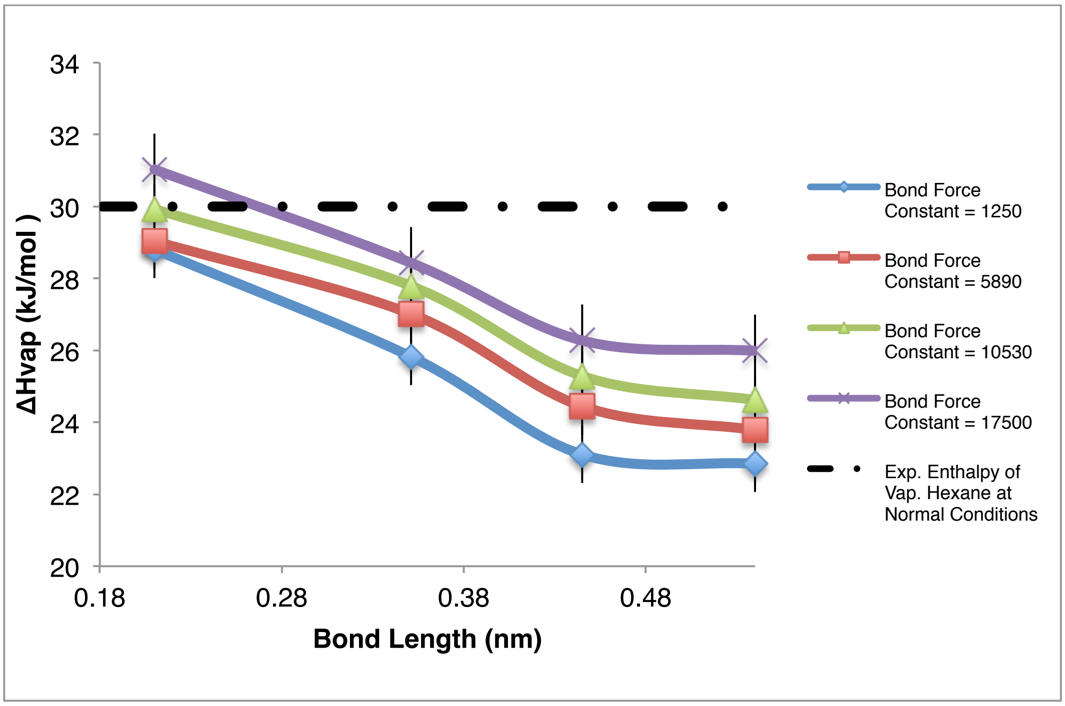

b)

Figures 4.40a-b: Selected enthalpies of vaporization of the 2-bead solvent systems for different values of the bond length and bond force constant parameters: **a)** selected bond lengths at different bond force constants, and **b)** bond force constants at different bond length values. The black dashed line represents the experimental reference values for hexane at room temperature.[48, 49, 50]

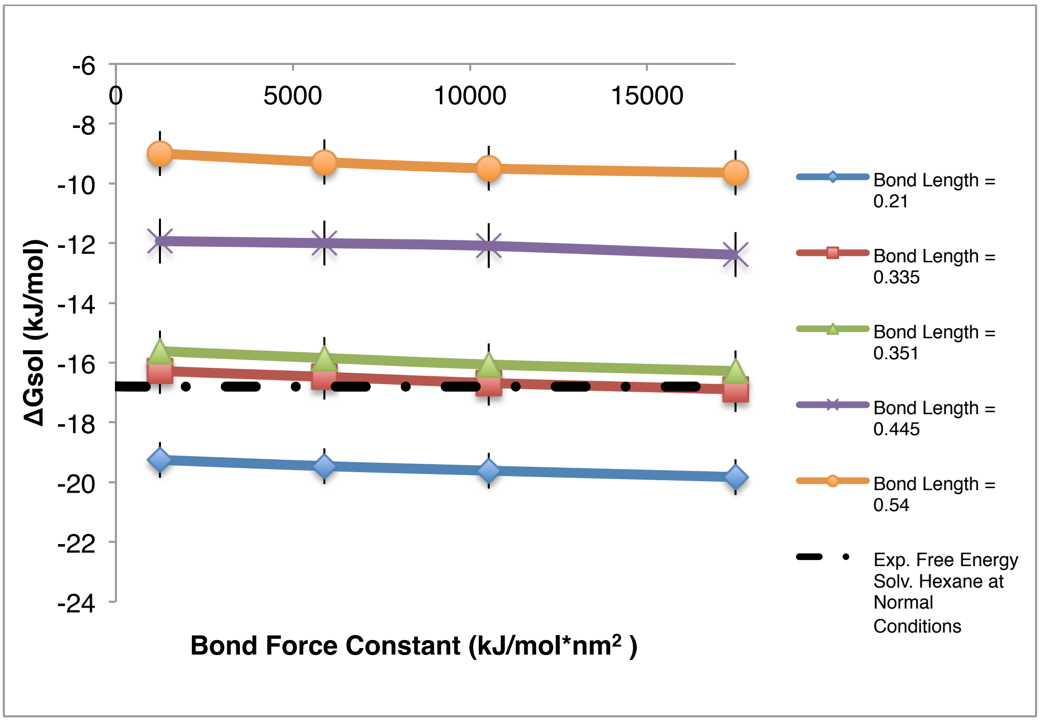
-6
-8
-10
-12
-14
-16
-18
-20
-22
-24
0
5000
10000
15000
ΔGsol (kJ/mol)
Bond Force Constant (kJ/mol*nm^2)
Bond Length = 0.21
Bond Length = 0.335
Bond Length = 0.351
Bond Length = 0.445
Bond Length = 0.54
Exp. Free Energy Solv. Hexane at Normal Conditions

a)

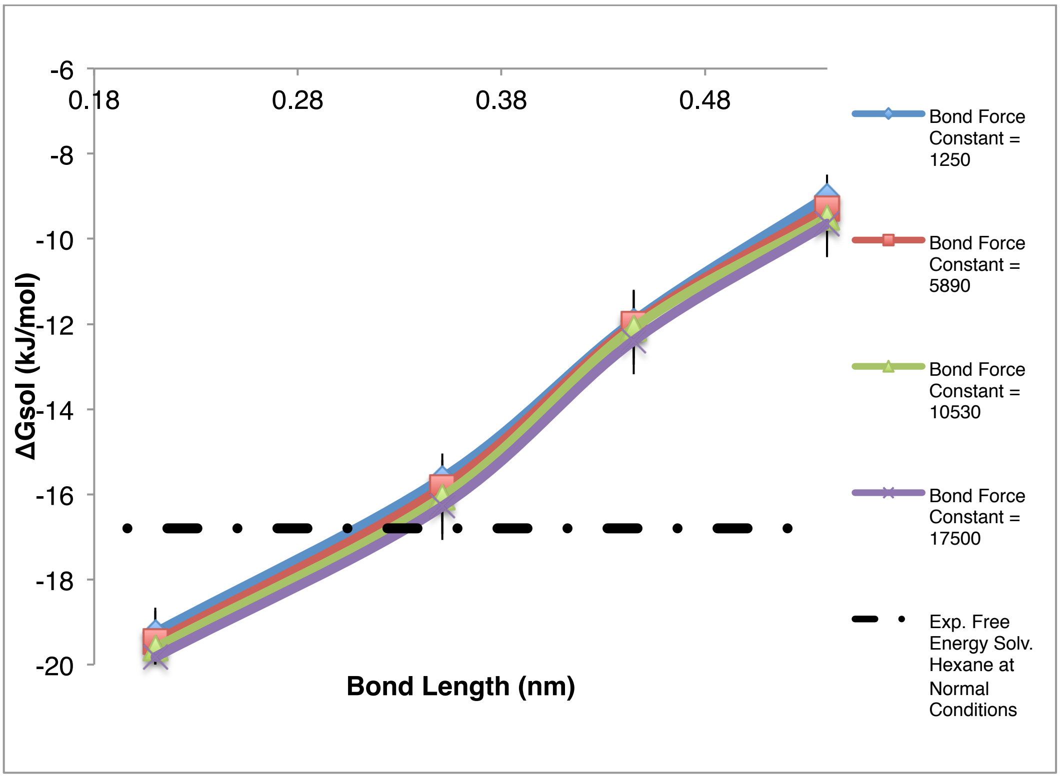

b)

Figures 4.41a-b: Selected self-solvation free energies of the 2-bead solvent systems for different values of the bond length and bond force constant parameters: **a)** selected bond lengths at different bond force constants, and **b)** bond force constants at different bond length values. The black dashed line represents the experimental reference values for hexane at room temperature.[46, 47, 51]

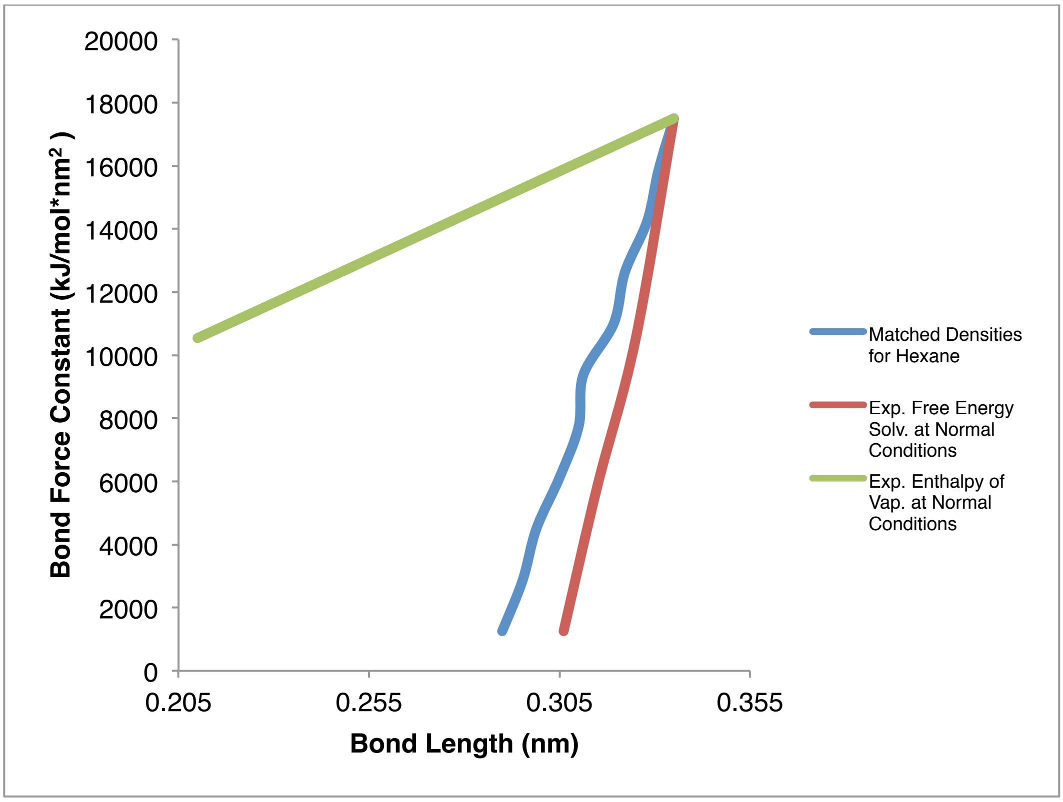

Figure 4.42: Determination of optimal set of parameters for the 3:1 mapped 2-bead models. The full lines show each property at standard temperature and pressure: density (blue), free energy of self-solvation (red), and enthalpy of vaporisation (green). [46, 47, 48, 49, 50, 51, 52, 53]

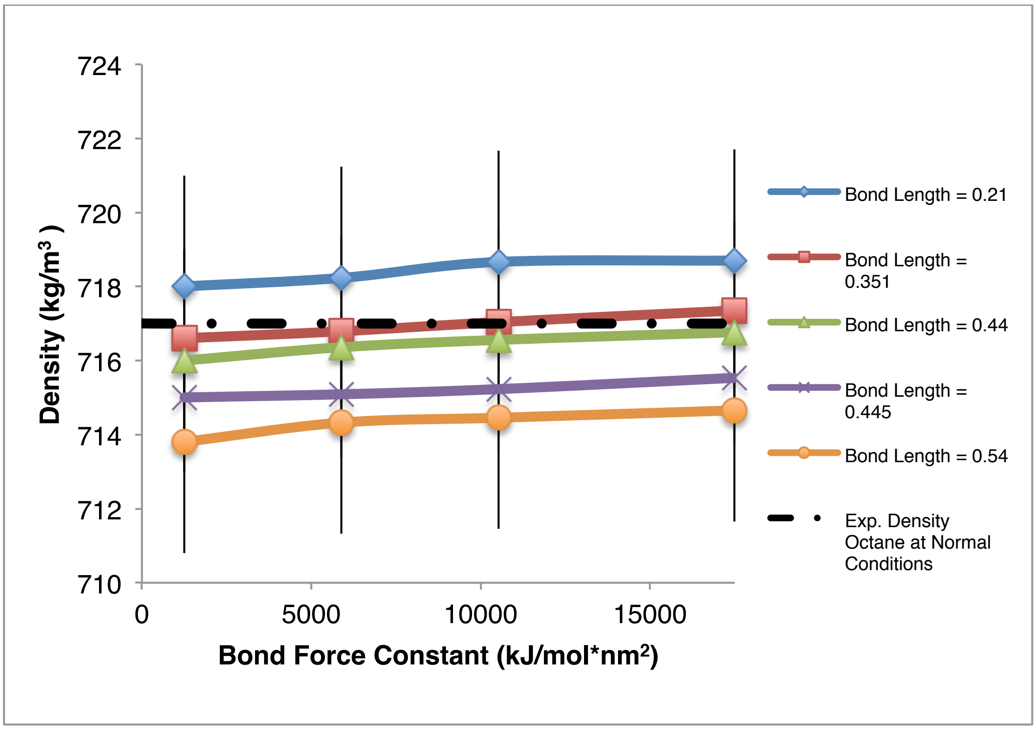
Density (kg/m³)
724
722
720
718
716
714
712
710
0
5000
10000
15000
Bond Force Constant (kJ/mol*nm²)
Bond Length = 0.21
Bond Length = 0.351
Bond Length = 0.44
Bond Length = 0.445
Bond Length = 0.54
Exp. Density Octane at Normal Conditions

a)

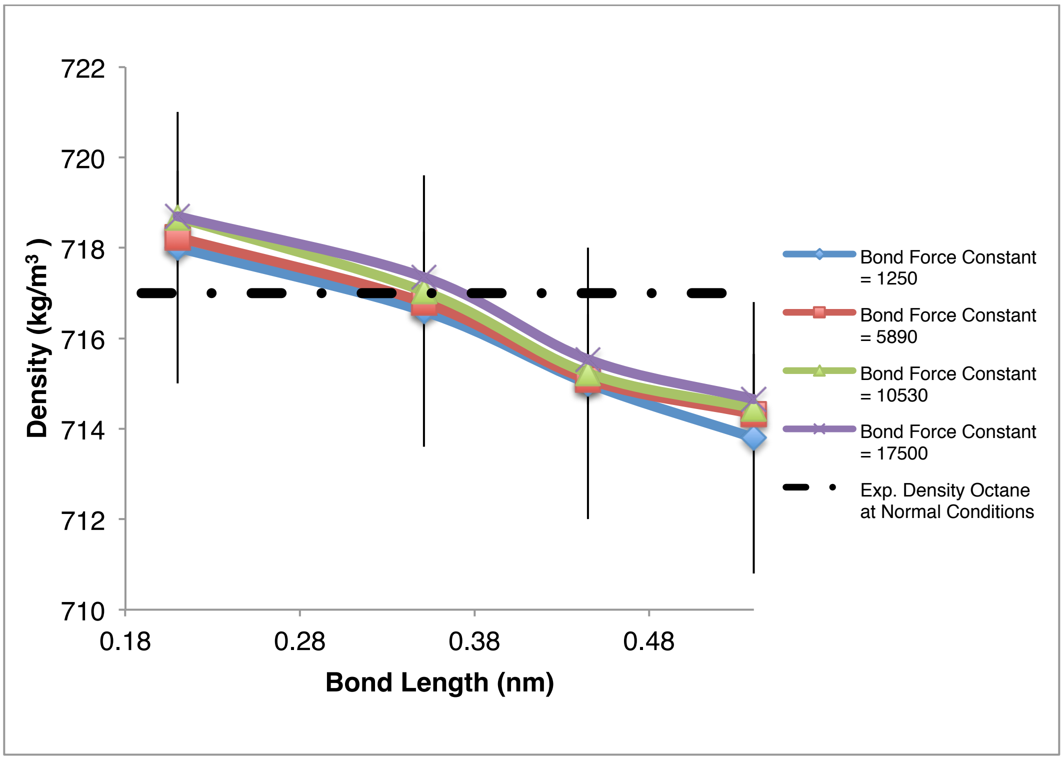

b)

Figures 4.43a-b: Selected densities determined for octane's molecular weight, of the 2-bead solvent systems for different values of the bond length and bond force constant parameters: **a)** selected bond lengths at different bond force constants, and **b)** bond force constants at different bond length values. The black dashed line represents the experimental reference values for octane at room temperature.[52, 53]

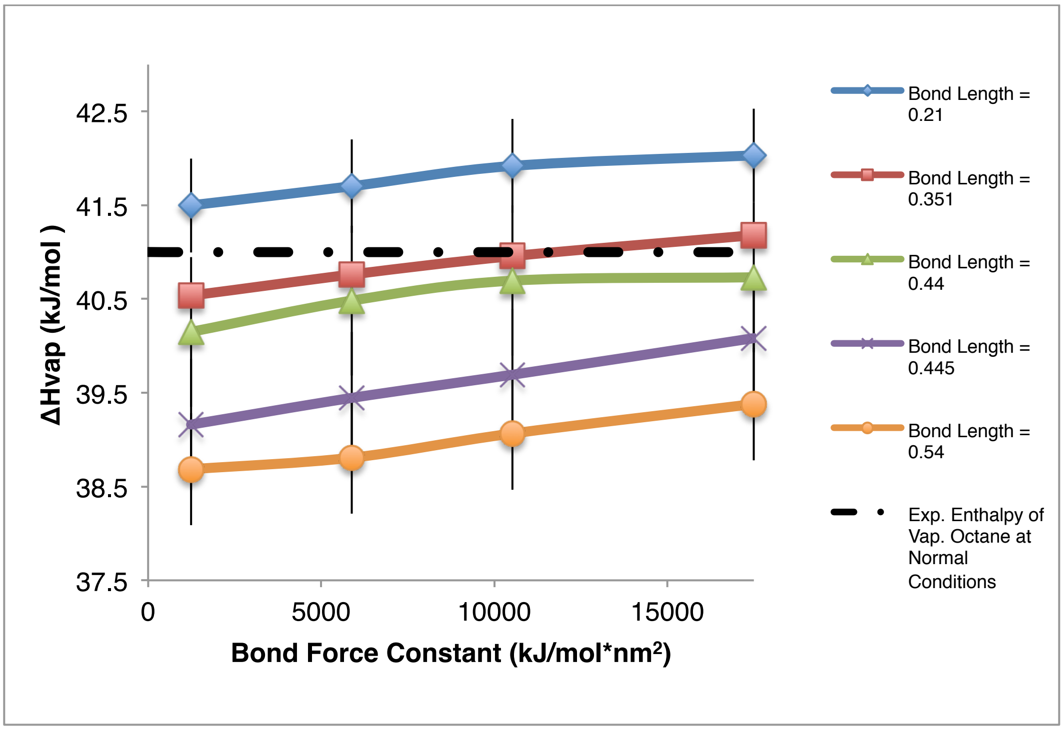
42.5
41.5
40.5
39.5
38.5
37.5
0
5000
10000
15000
ΔHvap (kJ/mol)
Bond Force Constant (kJ/mol*nm²)
Bond Length = 0.21
Bond Length = 0.351
Bond Length = 0.44
Bond Length = 0.445
Bond Length = 0.54
Exp. Enthalpy of Vap. Octane at Normal Conditions

a)

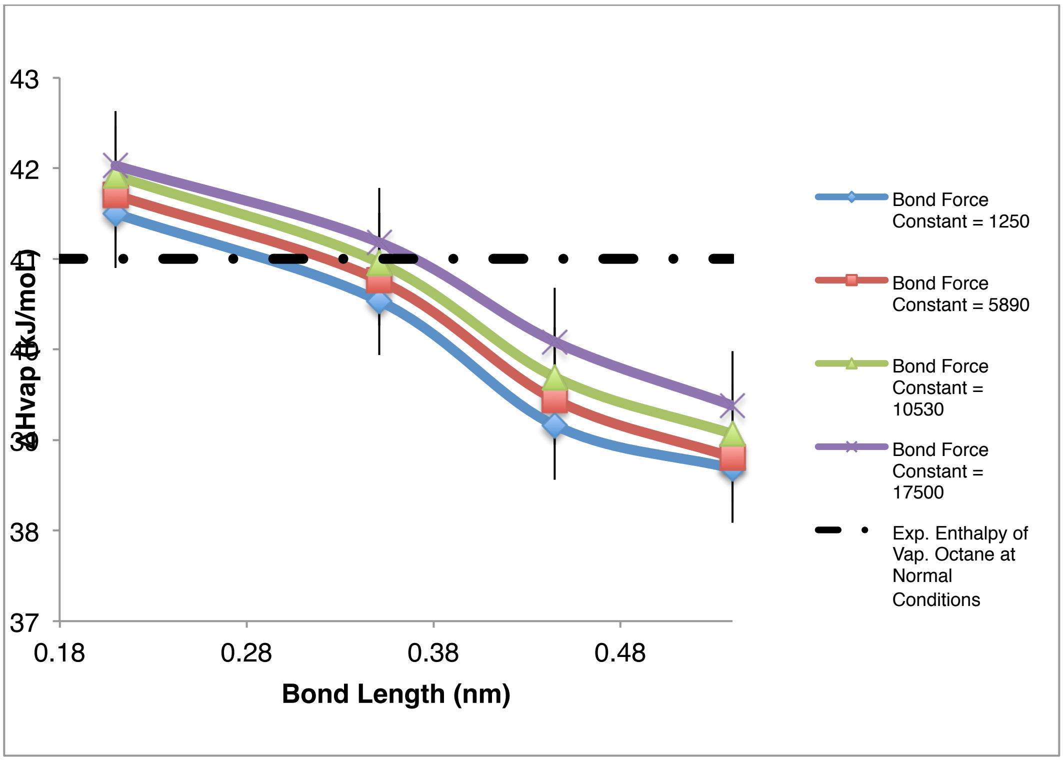

b)

Figures 4.44a-b: Selected enthalpies of vaporization of the 2-bead solvent systems for different values of the bond length and bond force constant parameters: **a)** selected bond lengths at different bond force constants, and **b)** bond force constants at different bond length values. The black dashed line represents the experimental reference values for octane at room temperature.[48, 49, 50]

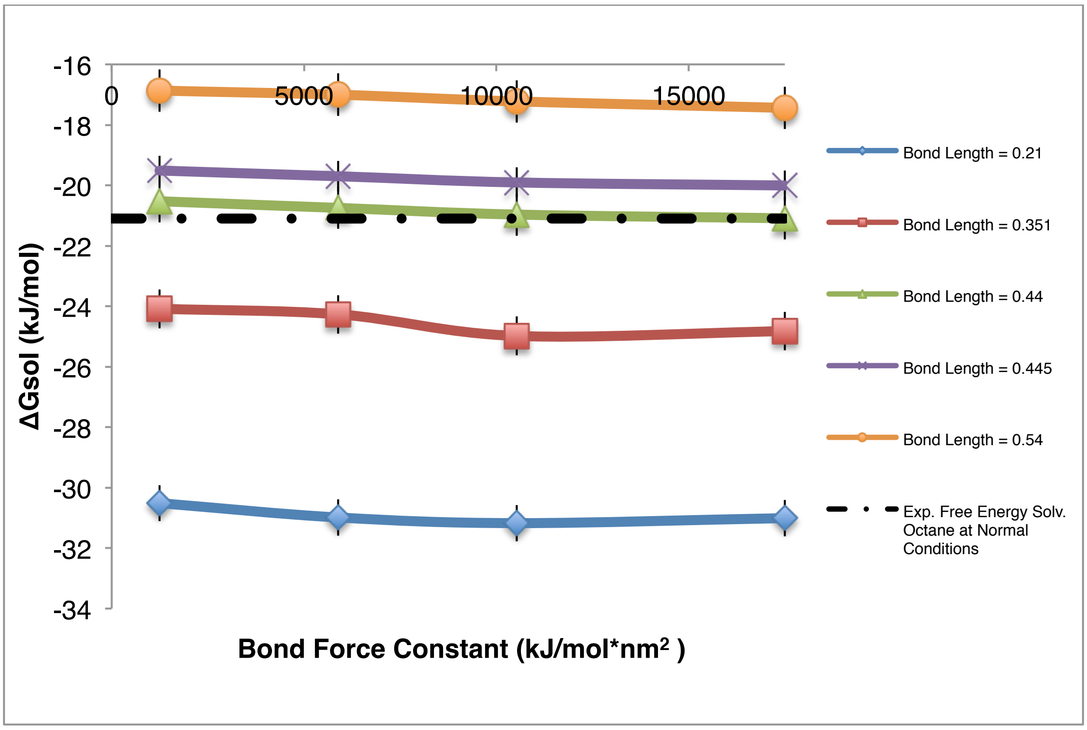
-16
-18
-20
-22
-24
-26
-28
-30
-32
-34
0
5000
10000
15000
ΔGsol (kJ/mol)
Bond Force Constant (kJ/mol*nm^2)
Bond Length = 0.21
Bond Length = 0.351
Bond Length = 0.44
Bond Length = 0.445
Bond Length = 0.54
Exp. Free Energy Solv. Octane at Normal Conditions

a)

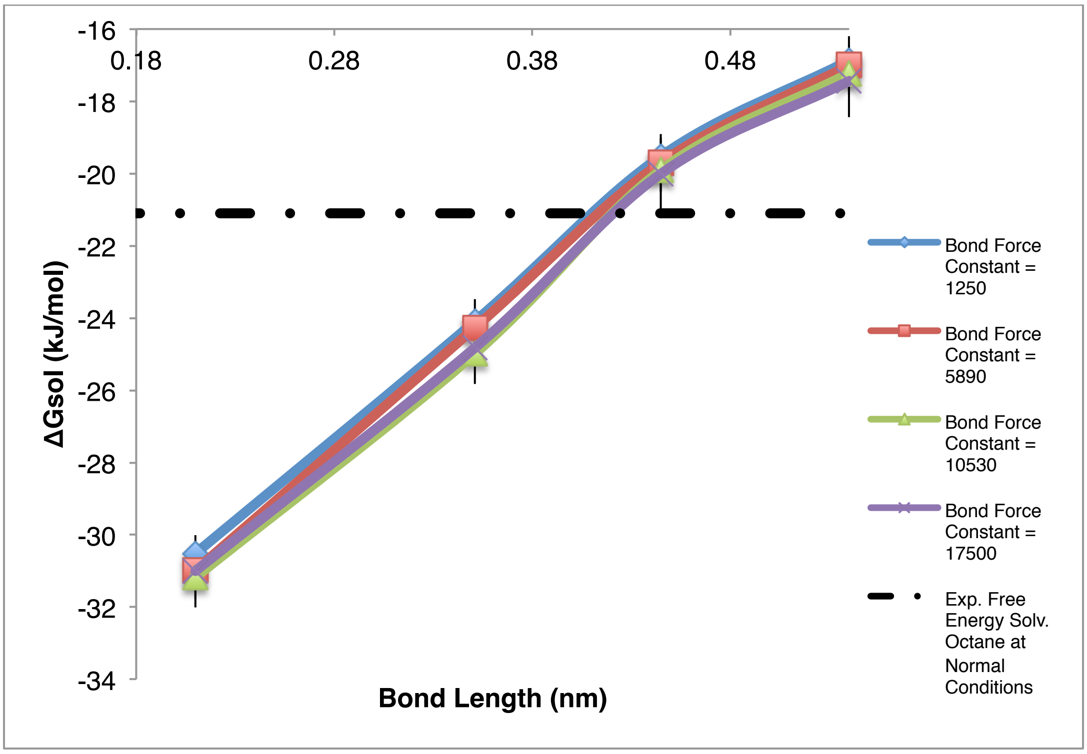

b)

Figures 4.45a-b: Selected self-solvation free energies of the 2-bead solvent systems for different values of the bond length and bond force constant parameters: **a)** selected bond lengths at different bond force constants, and **b)** bond force constants at different bond length values. The black dashed line represents the experimental reference values for octane at room temperature.[46, 47, 51]

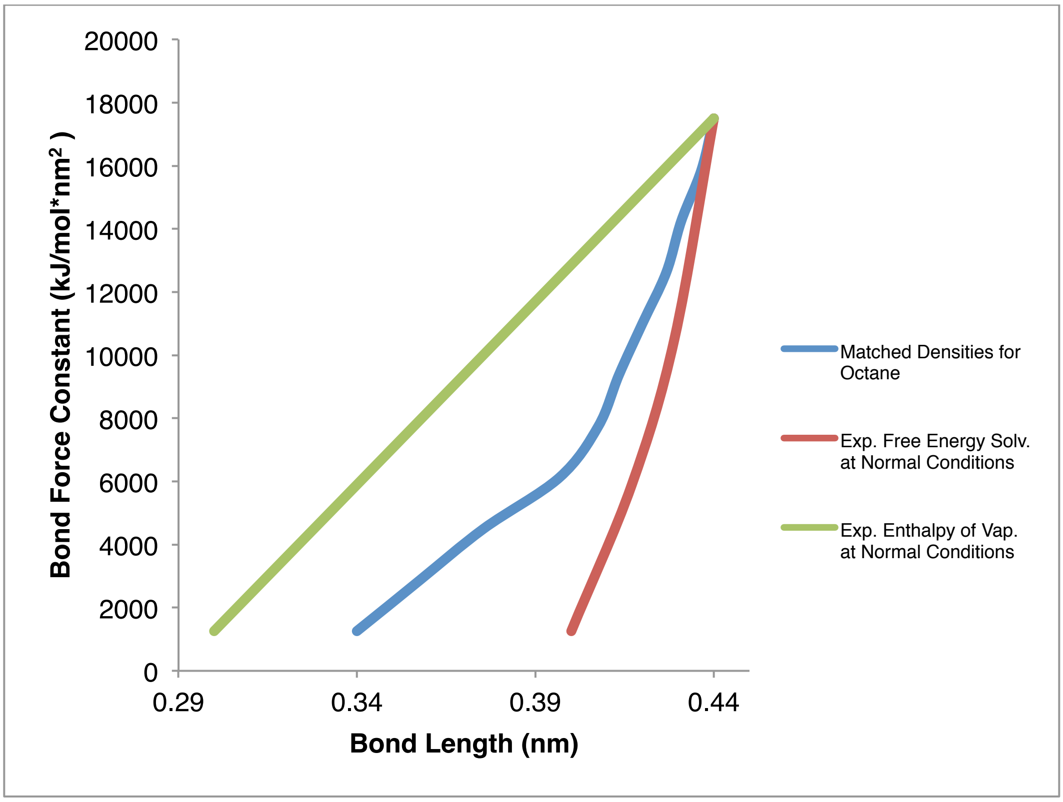

Figure 4.46: Determination of optimal set of parameters for the 4:1 mapped 2-bead models. The full lines show each property at standard temperature and pressure: density (blue), free energy of self-solvation (red), and enthalpy of vaporisation (green).[46, 47, 48, 49, 50, 51, 52, 53]

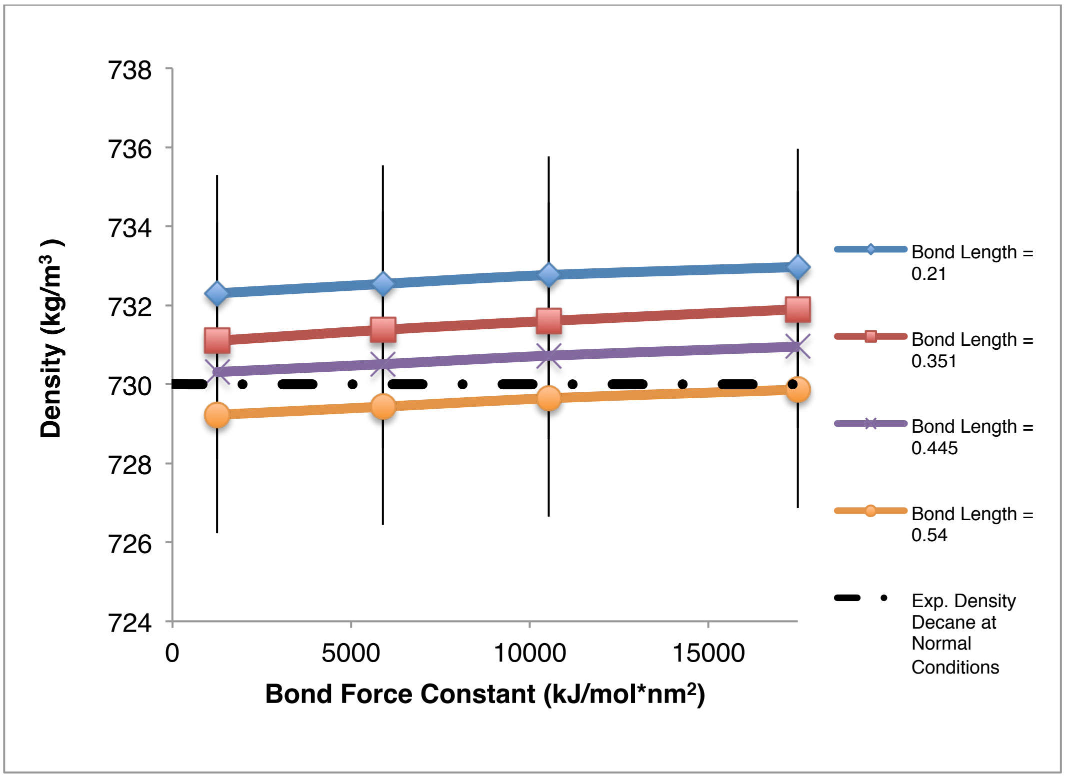
738
736
734
732
730
728
726
724
Density (kg/m³)
0
5000
10000
15000
Bond Force Constant (kJ/mol*nm²)
Bond Length = 0.21
Bond Length = 0.351
Bond Length = 0.445
Bond Length = 0.54
Exp. Density Decane at Normal Conditions

a)

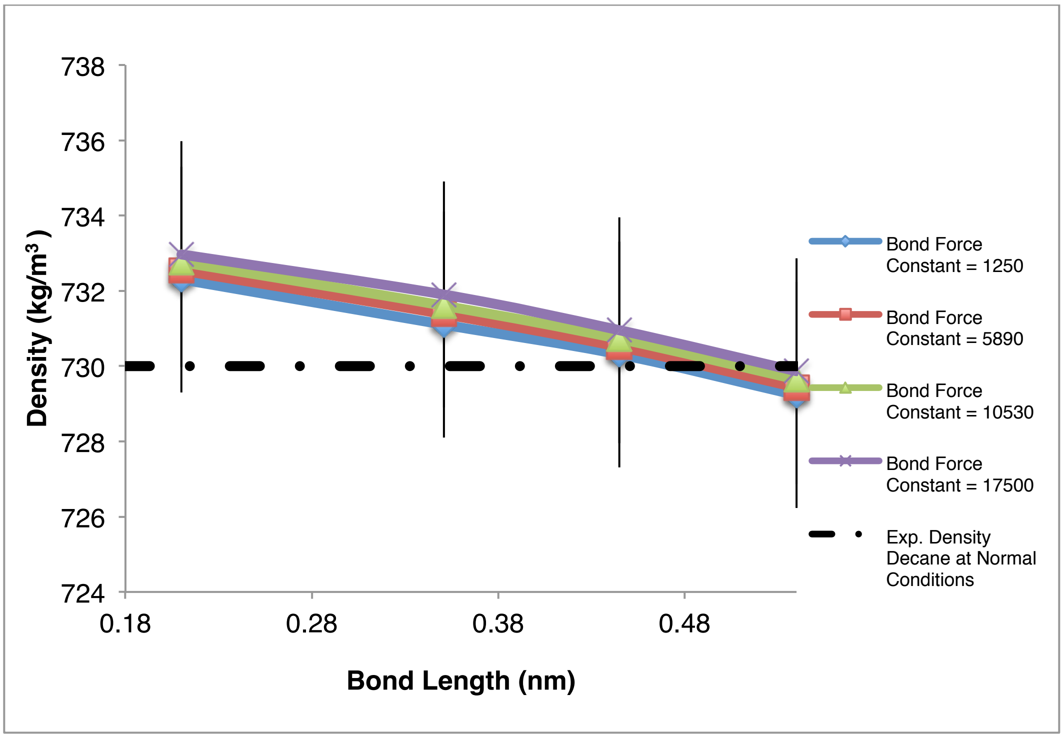

b)

Figures 4.47a-b: Selected densities determined for decane's molecular weight, of the 2-bead solvent systems for different values of the bond angle and bond angle force constant parameters: **a)** selected bond angles at different bond force constants, and **b)** bond angle force constants at different bond length values. The black dashed line represents the experimental reference values for decane at room temperature.[52, 53]

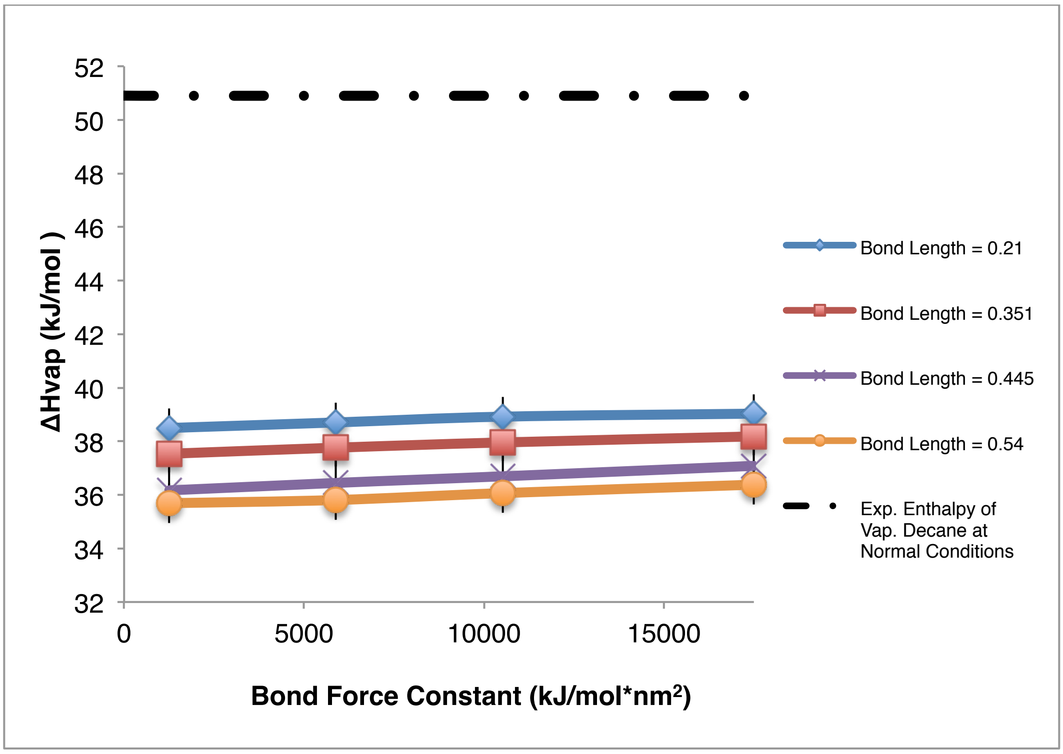
52
50
48
46
44
42
40
38
36
34
32
ΔHvap (kJ/mol)
0
5000
10000
15000
Bond Force Constant (kJ/mol*nm^2)
Bond Length = 0.21
Bond Length = 0.351
Bond Length = 0.445
Bond Length = 0.54
Exp. Enthalpy of Vap. Decane at Normal Conditions

a)

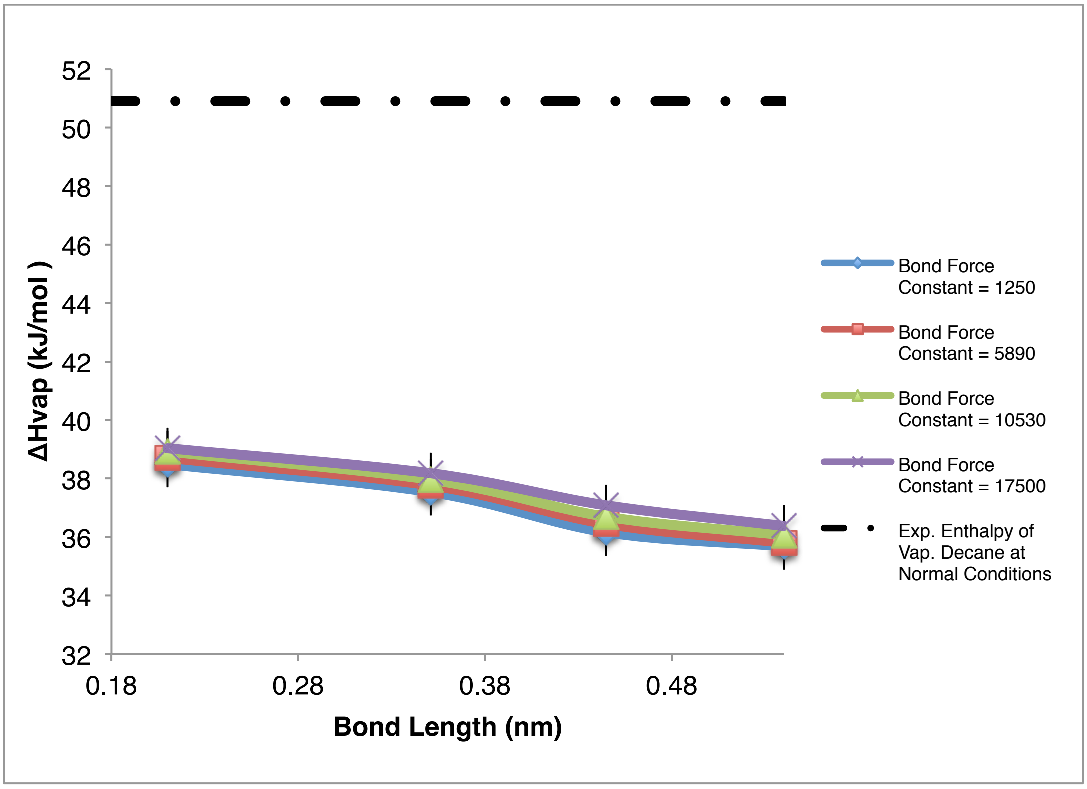

b)

Figures 4.48a-b: Selected enthalpies of vaporization of the 2-bead solvent systems for different values of the bond angle and bond angle force constant parameters: **a)** selected bond angles at different bond angle force constants, and **b)** bond angle force constants at different bond angle values. The black dashed line represents the experimental reference values for decane at room temperature.[48, 49, 50]

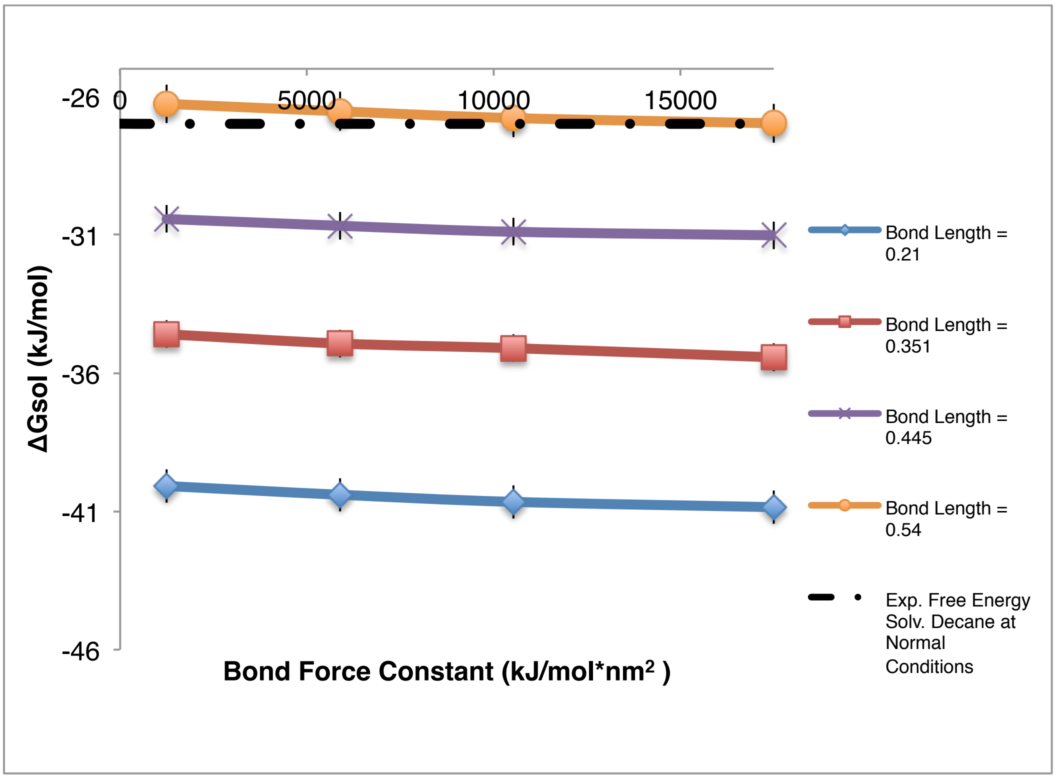
ΔGsol (kJ/mol)
-26
-31
-36
-41
-46
0
5000
10000
15000
Bond Force Constant (kJ/mol*nm²)
Bond Length = 0.21
Bond Length = 0.351
Bond Length = 0.445
Bond Length = 0.54
Exp. Free Energy Solv. Decane at Normal Conditions

a)

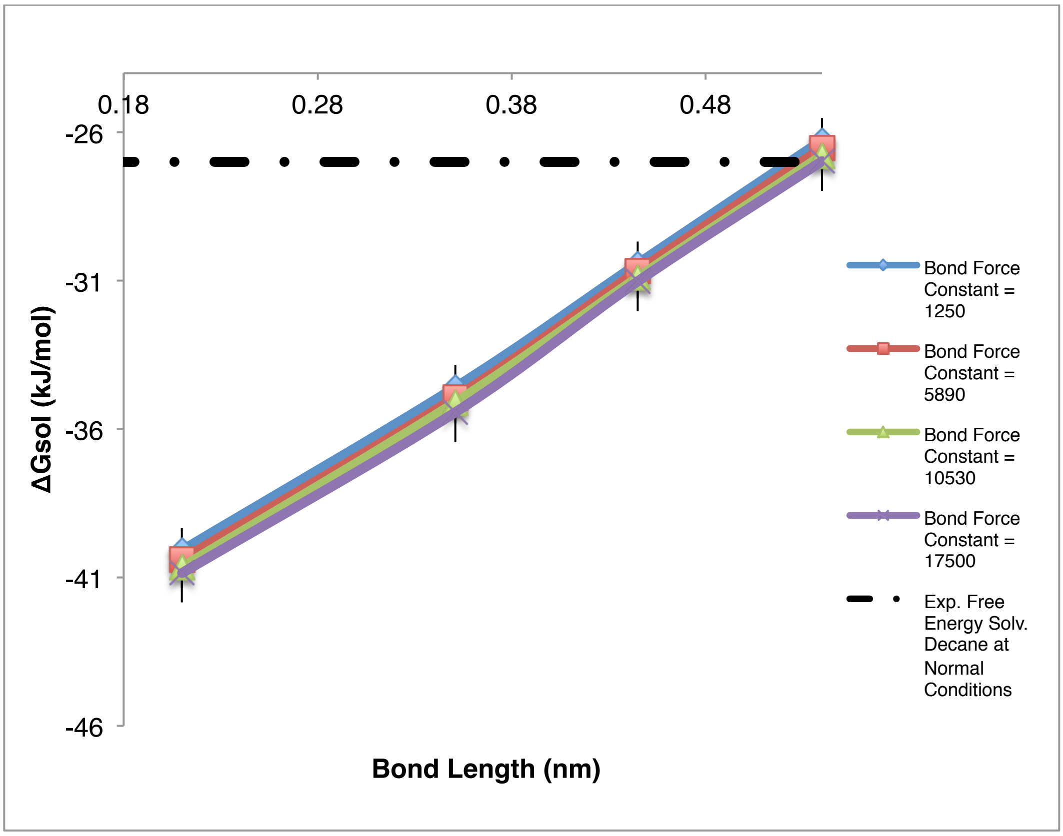

b)

Figures 4.49a-b: Selected self-solvation free energies of the 2-bead solvent systems for different values of the bond length and bond force constant parameters: **a)** selected bond lengths at different bond force constants, and **b)** bond force constants at different bond length values. The black dashed line represents the experimental reference values for decane at room temperature.[46, 47, 50]

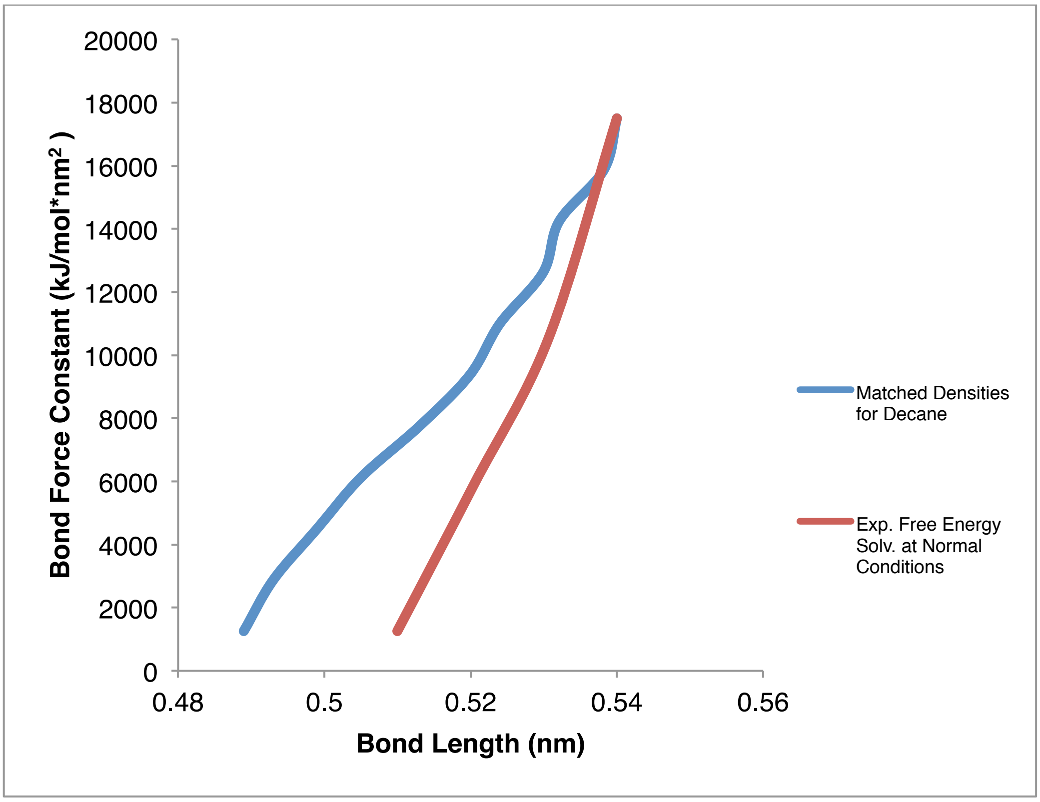

Figure 4.50: Determination of optimal set of parameters for the 5:1 mapped 2-bead models. The full lines show each property at standard temperature and pressure: density (blue), and free energy of self-solvation (red).[46, 47, 51, 52, 53]

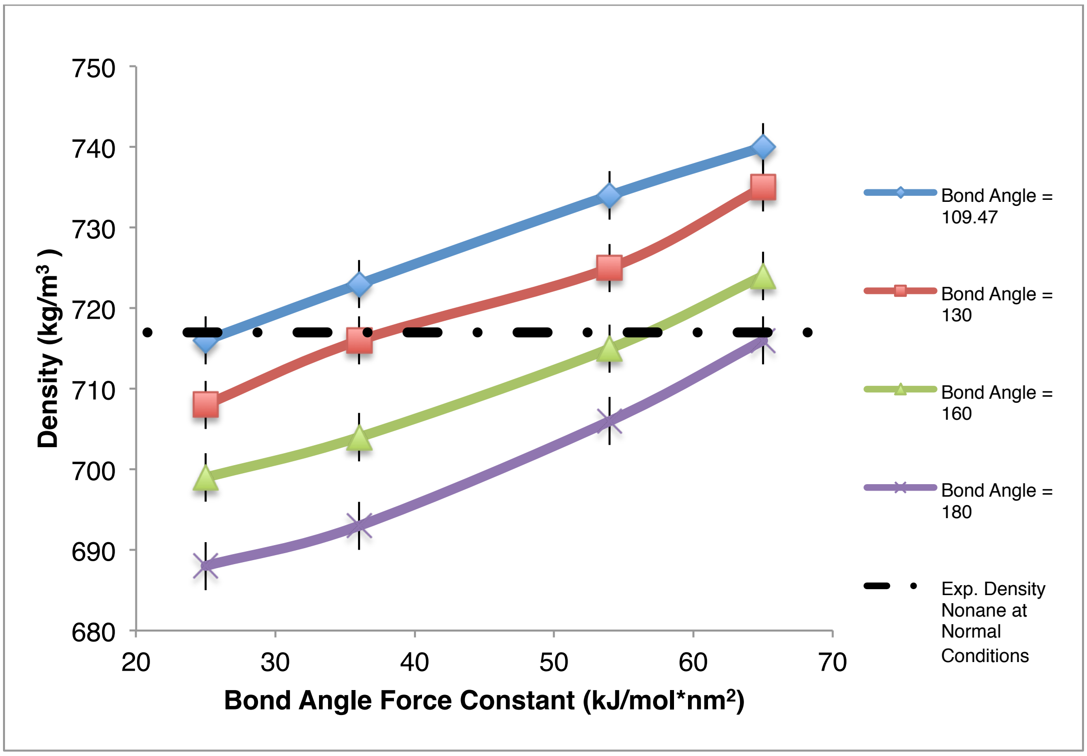
750
740
730
720
710
700
690
680
20
30
40
50
60
70
Density (kg/m³)
Bond Angle Force Constant (kJ/mol*nm²)
Bond Angle = 109.47
Bond Angle = 130
Bond Angle = 160
Bond Angle = 180
Exp. Density Nonane at Normal Conditions

a)

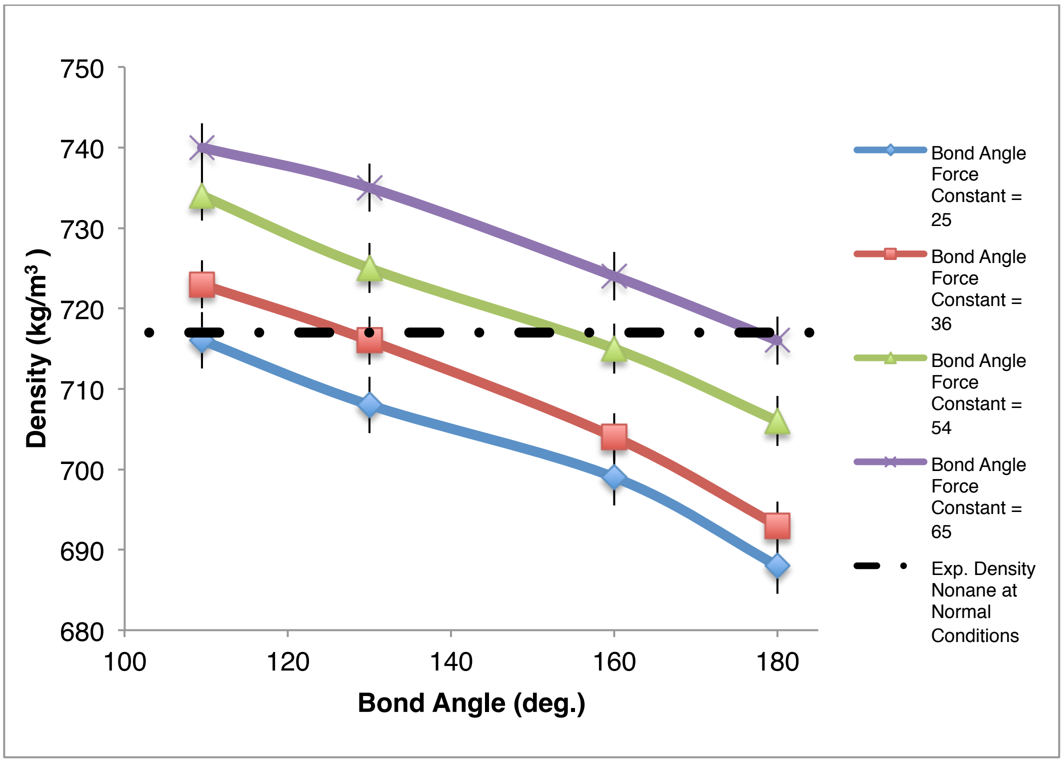

b)

Figures 4.51a-b: Selected densities determined for nonane's molecular weight, of the 3-bead solvent systems for different values of the bond angle and bond angle force constant parameters: **a)** selected bond angles at different bond angle force constants, and **b)** bond angle force constants at different bond angle values. The black dashed line represents the experimental reference values for nonane at room temperature.[52, 53]

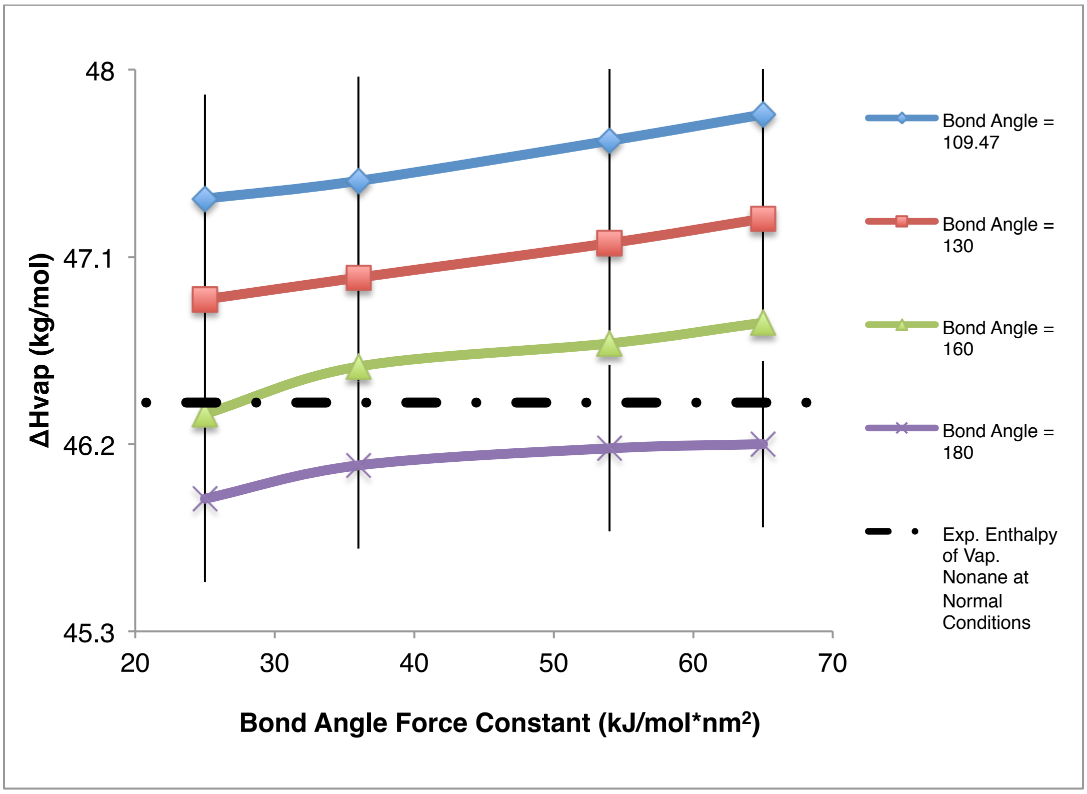
48
47.1
46.2
45.3
20
30
40
50
60
70
ΔHvap (kg/mol)
Bond Angle Force Constant (kJ/mol*nm²)
Bond Angle = 109.47
Bond Angle = 130
Bond Angle = 160
Bond Angle = 180
Exp. Enthalpy of Vap. Nonane at Normal Conditions

a)

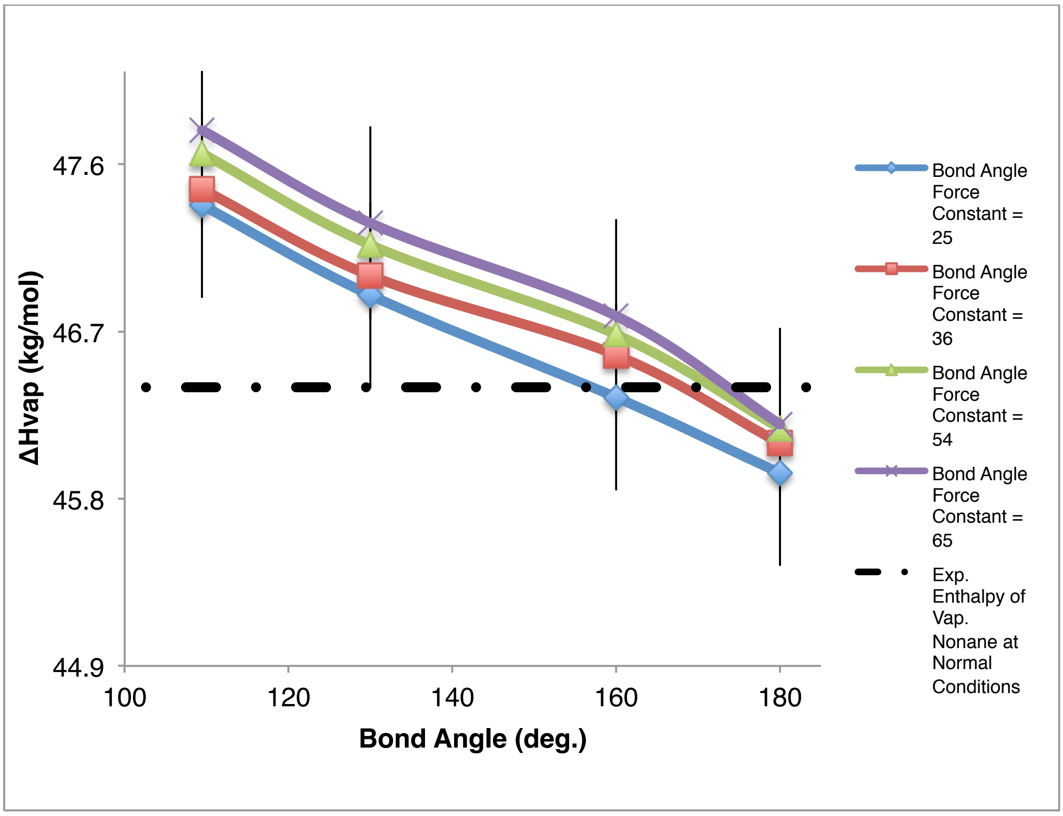

b)

Figures 4.52a-b: Selected enthalpies of vaporization of the 3-bead solvent systems for different values of the bond angle and bond angle force constant parameters: **a)** selected bond angles at different bond angle force constants, and **b)** bond angle force constants at different bond angle values. The black dashed line represents the experimental reference values for nonane at room temperature.[48, 49, 50]

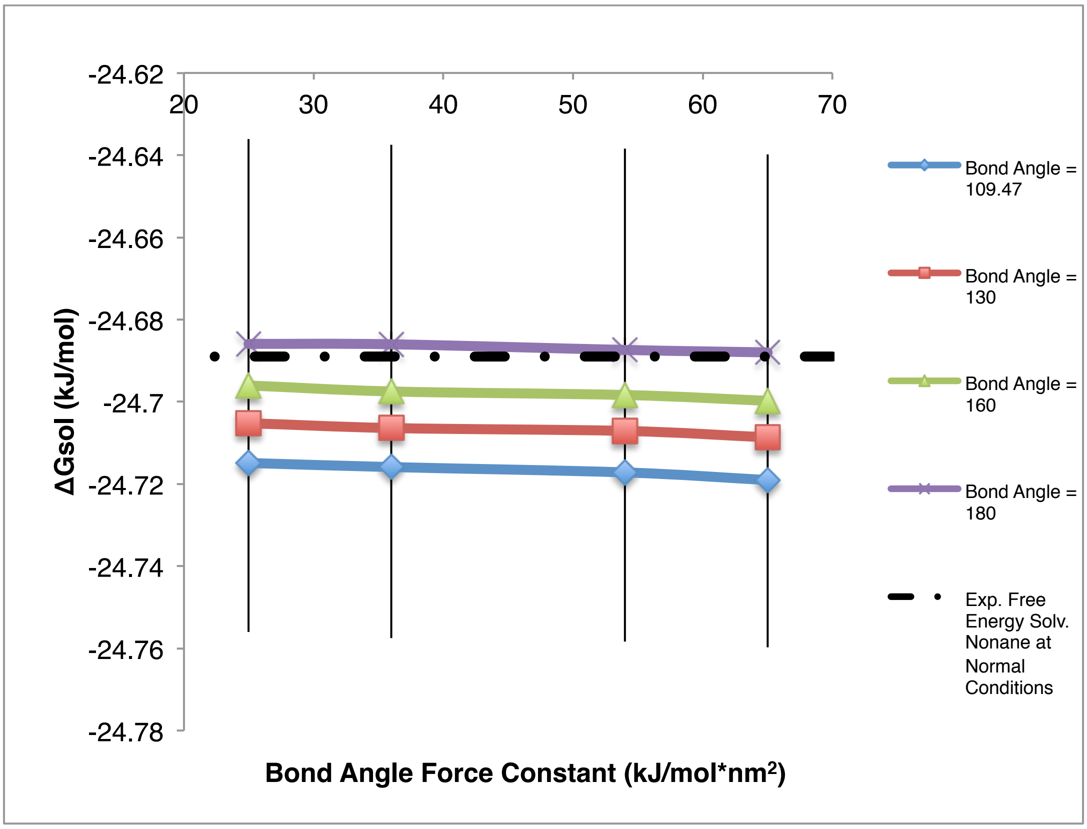
-24.62
-24.64
-24.66
-24.68
-24.7
-24.72
-24.74
-24.76
-24.78
20
30
40
50
60
70
ΔGsol (kJ/mol)
Bond Angle Force Constant (kJ/mol*nm²)
Bond Angle = 109.47
Bond Angle = 130
Bond Angle = 160
Bond Angle = 180
Exp. Free Energy Solv. Nonane at Normal Conditions

a)

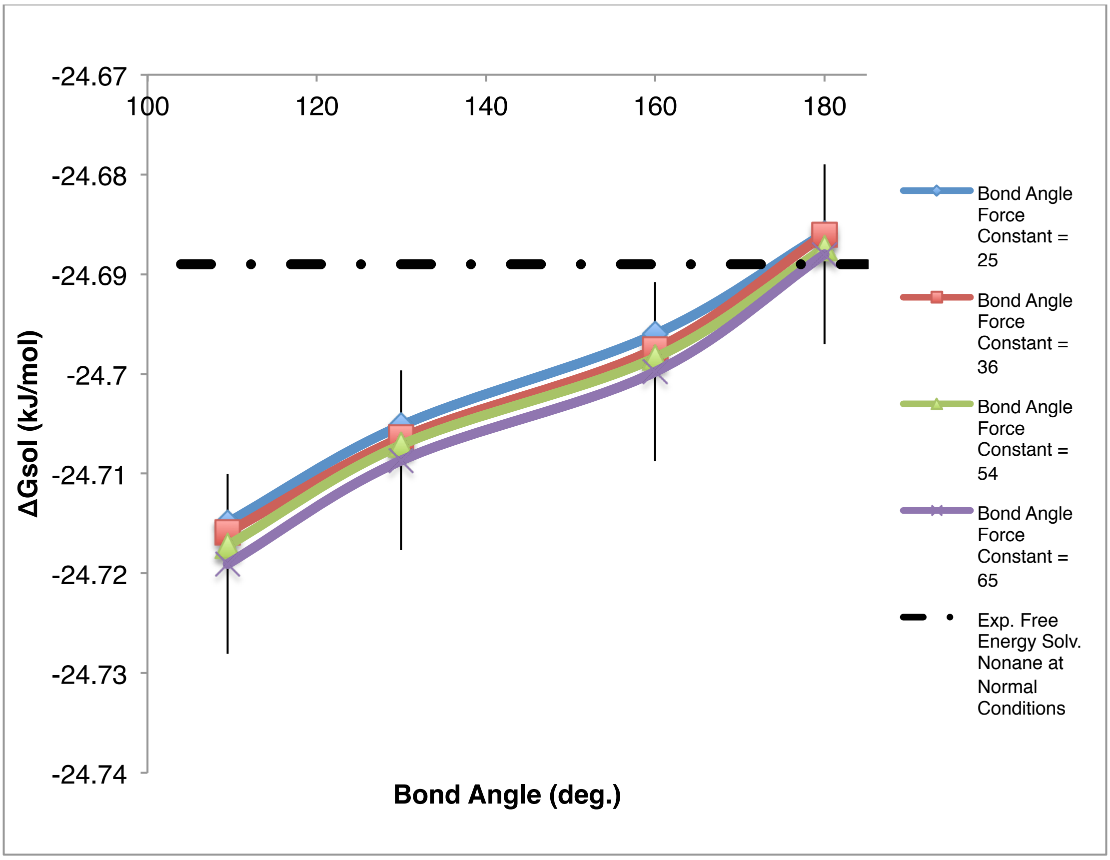

b)

Figures 4.53a-b: Selected self-solvation free energies of the 3-bead solvent systems for different values of the bond angle and bond angle force constant parameters: **a)** selected bond lengths at different bond angle force constants, and **b)** bond angle force constants at different bond angle values. The black dashed line represents the experimental reference values for nonane at room temperature.[46, 47, 51]

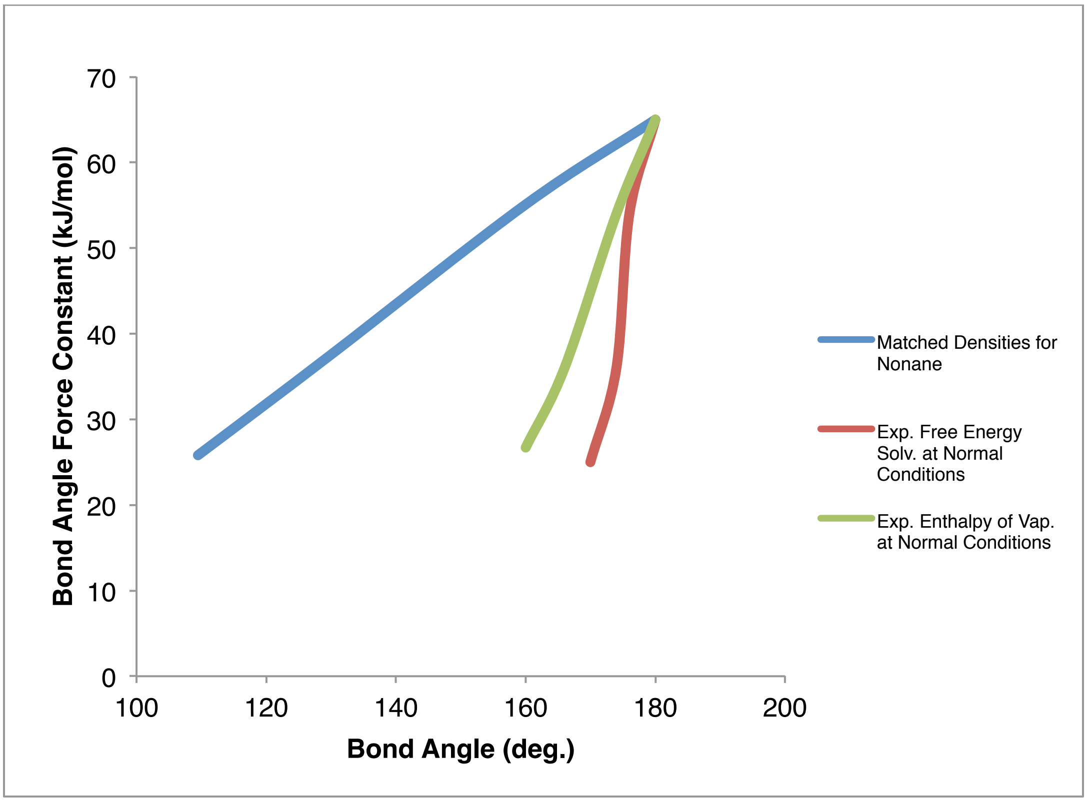

Figure 4.54: Determination of optimal set of parameters for the 3:1 mapped 3-bead models. The full lines show each property at standard temperature and pressure: density (blue), free energy of self-solvation (red), and enthalpy of vaporisation (green).[46, 47, 48, 49, 50, 51, 52, 53]

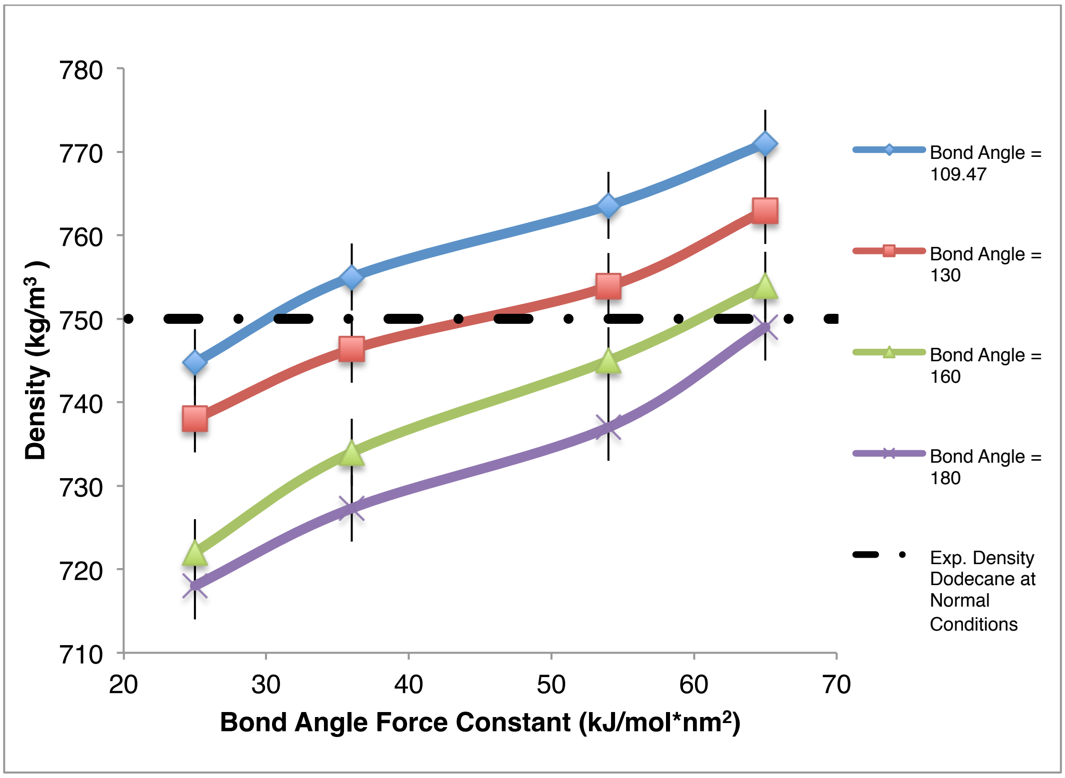
780
770
760
750
740
730
720
710
Density (kg/m^3)
20
30
40
50
60
70
Bond Angle Force Constant (kJ/mol*nm^2)
Bond Angle = 109.47
Bond Angle = 130
Bond Angle = 160
Bond Angle = 180
Exp. Density Dodecane at Normal Conditions

a)

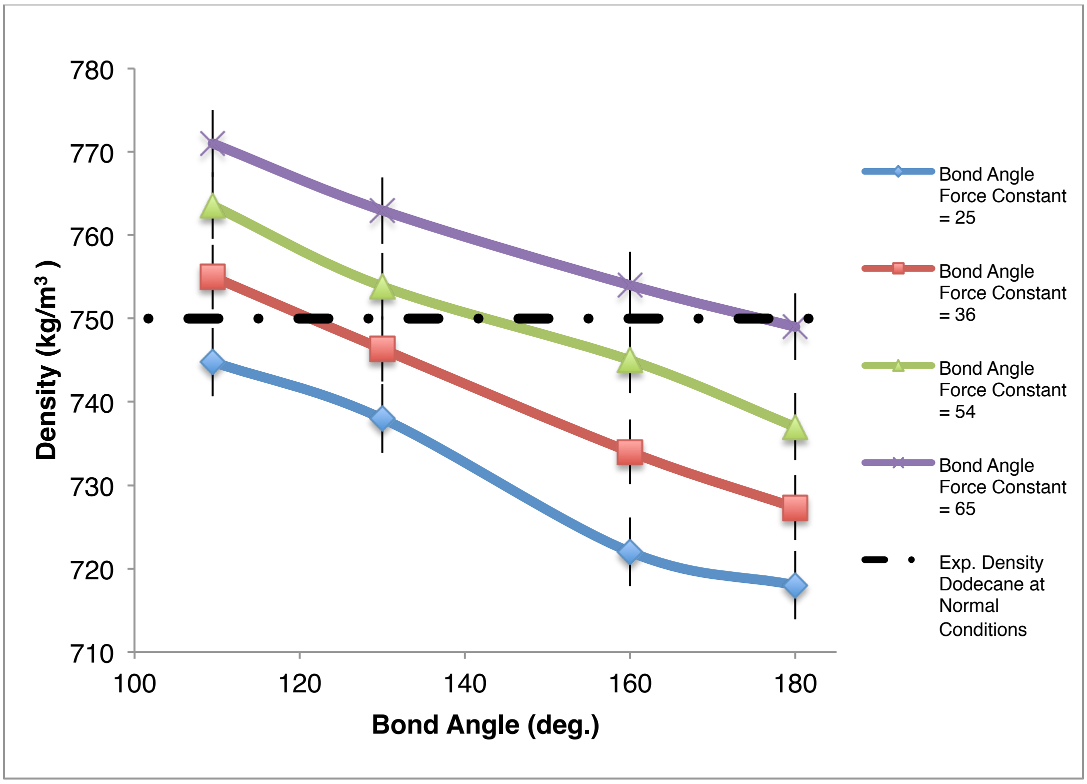

b)

Figures 4.55a-b: Selected densities determined for dodecane's molecular weight, of the 3-bead solvent systems for different values of the bond angle and bond angle force constant parameters: **a)** selected bond angles at different bond angle force constants, and **b)** bond angle force constants at different bond length values. The black dashed line represents the experimental reference values for dodecane at room temperature.[52, 53]

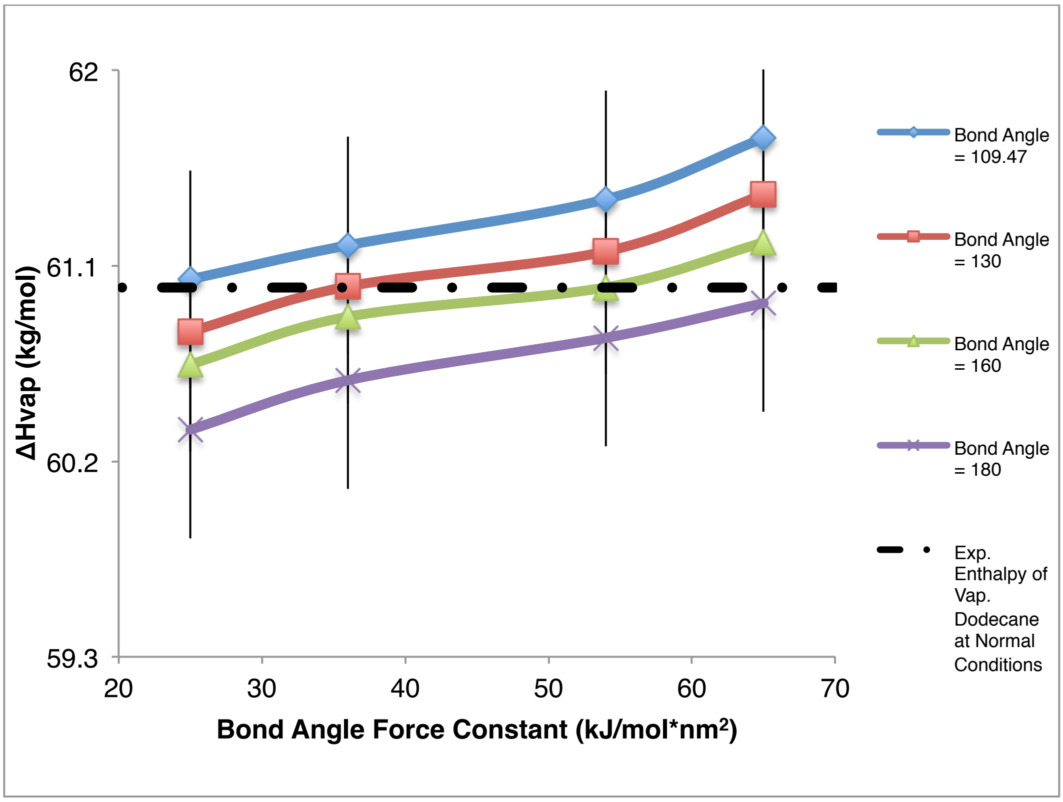
62
61.1
60.2
59.3
ΔHvap (kg/mol)
20
30
40
50
60
70
Bond Angle Force Constant (kJ/mol*nm²)
Bond Angle = 109.47
Bond Angle = 130
Bond Angle = 160
Bond Angle = 180
Exp. Enthalpy of Vap. Dodecane at Normal Conditions

a)

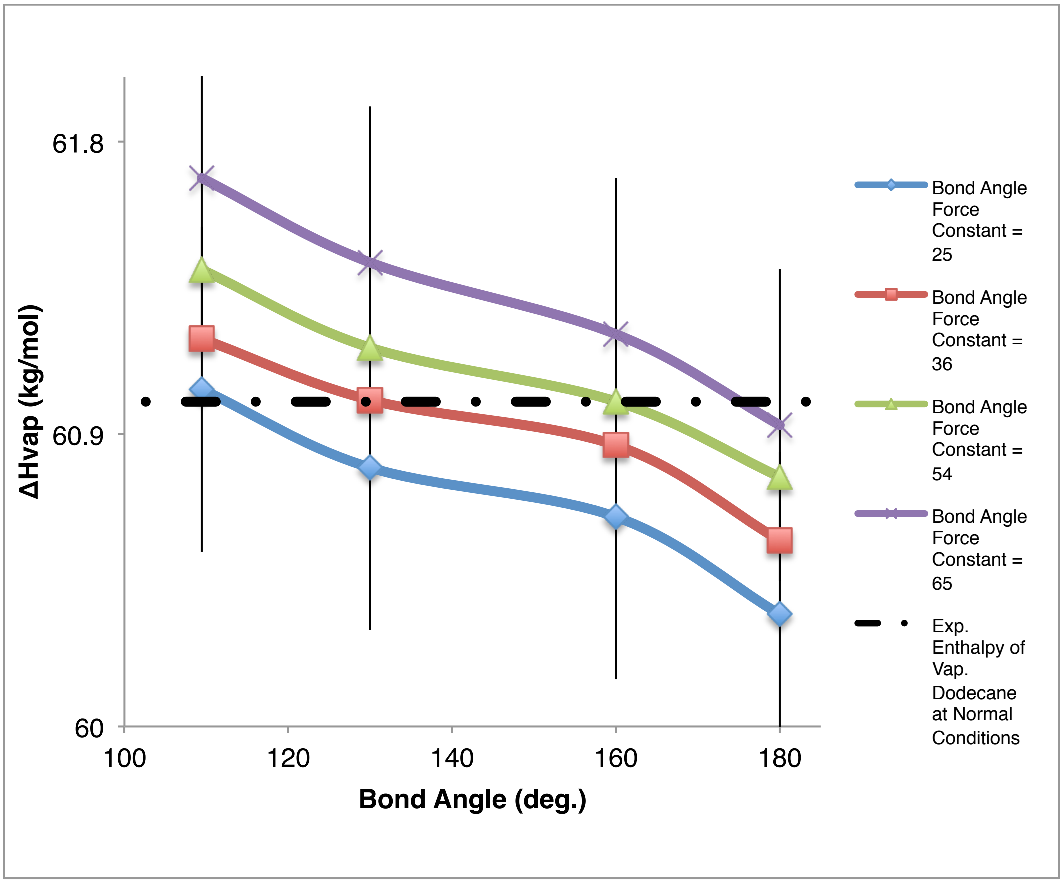

b)

Figures 4.56a-b: Selected enthalpies of vaporization of the 3-bead solvent systems for different values of the bond angle and bond angle force constant parameters: **a)** selected bond angles at different bond angle force constants, and **b)** bond angle force constants at different bond angle values. The black dashed line represents the experimental reference values for dodecane at room temperature.[48, 49, 50]

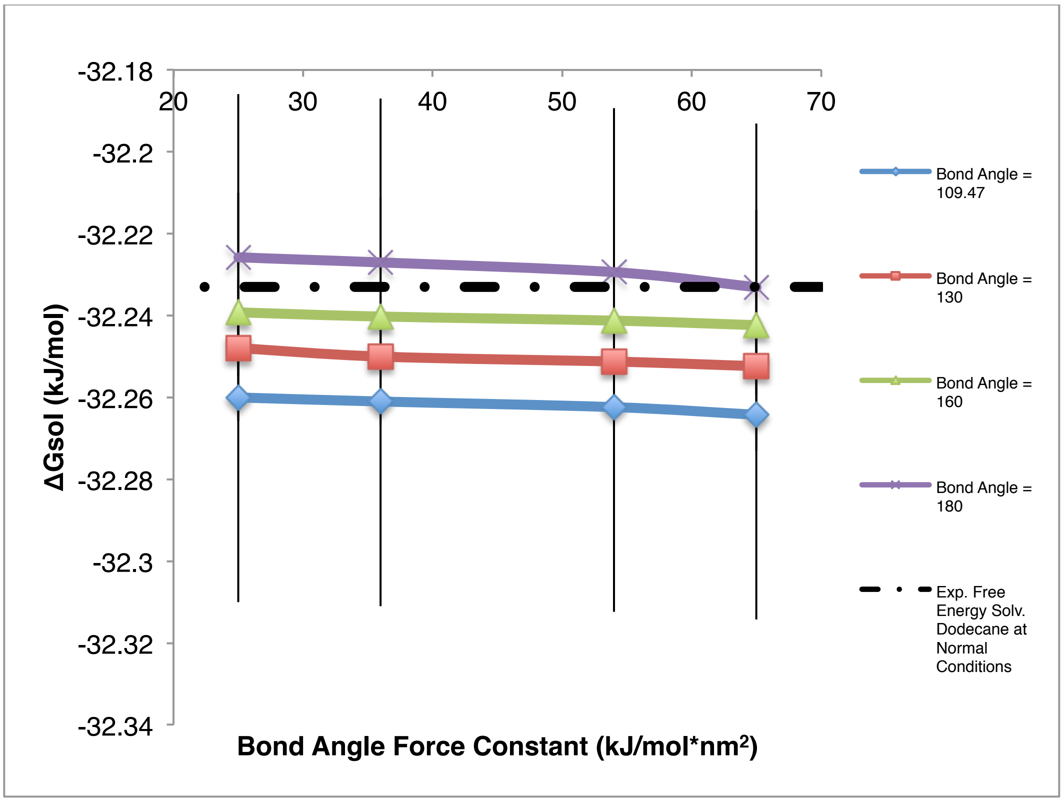
-32.18
-32.2
-32.22
-32.24
-32.26
-32.28
-32.3
-32.32
-32.34
20
30
40
50
60
70
ΔGsol (kJ/mol)
Bond Angle Force Constant (kJ/mol*nm²)
Bond Angle = 109.47
Bond Angle = 130
Bond Angle = 160
Bond Angle = 180
Exp. Free Energy Solv. Dodecane at Normal Conditions

a)

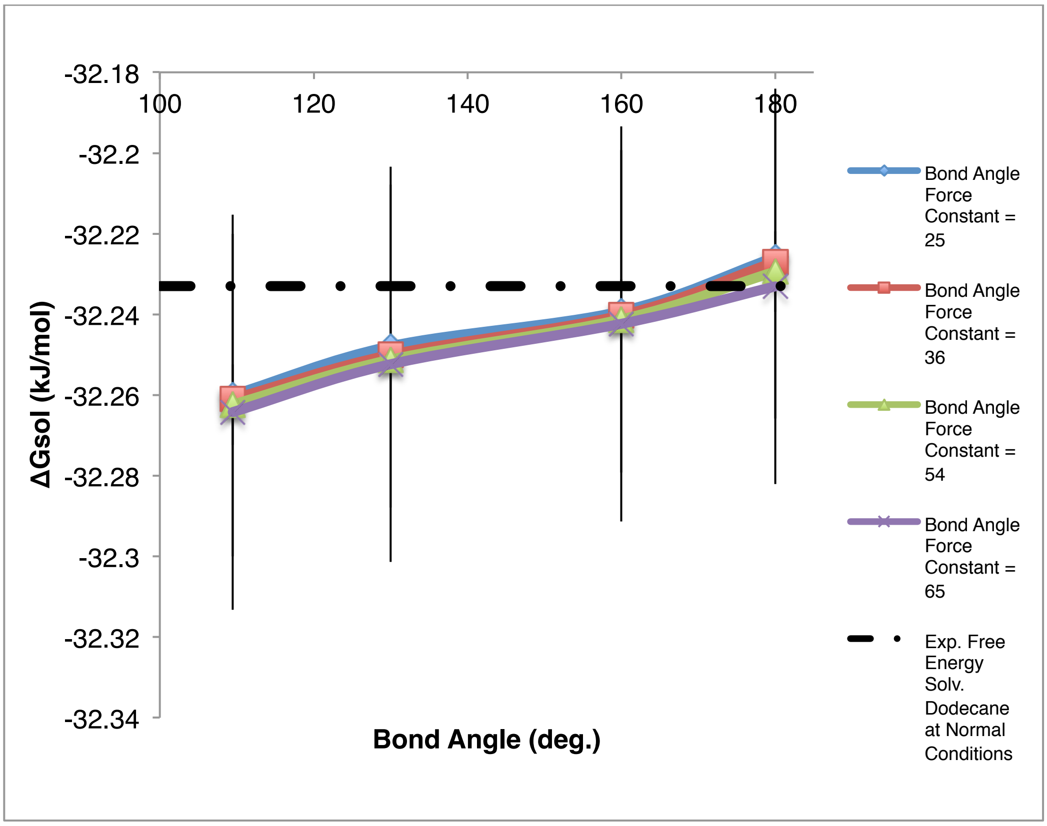

b)

Figures 4.57a-b: Selected self-solvation free energies of the 3-bead solvent systems for different values of the bond angles and bond angle force constant parameters: **a)** selected bond angles at different bond angle force constants, and **b)** bond angle force constants at different bond angle values. The black dashed line represents the experimental reference values for dodecane at room temperature.[46, 47, 51]

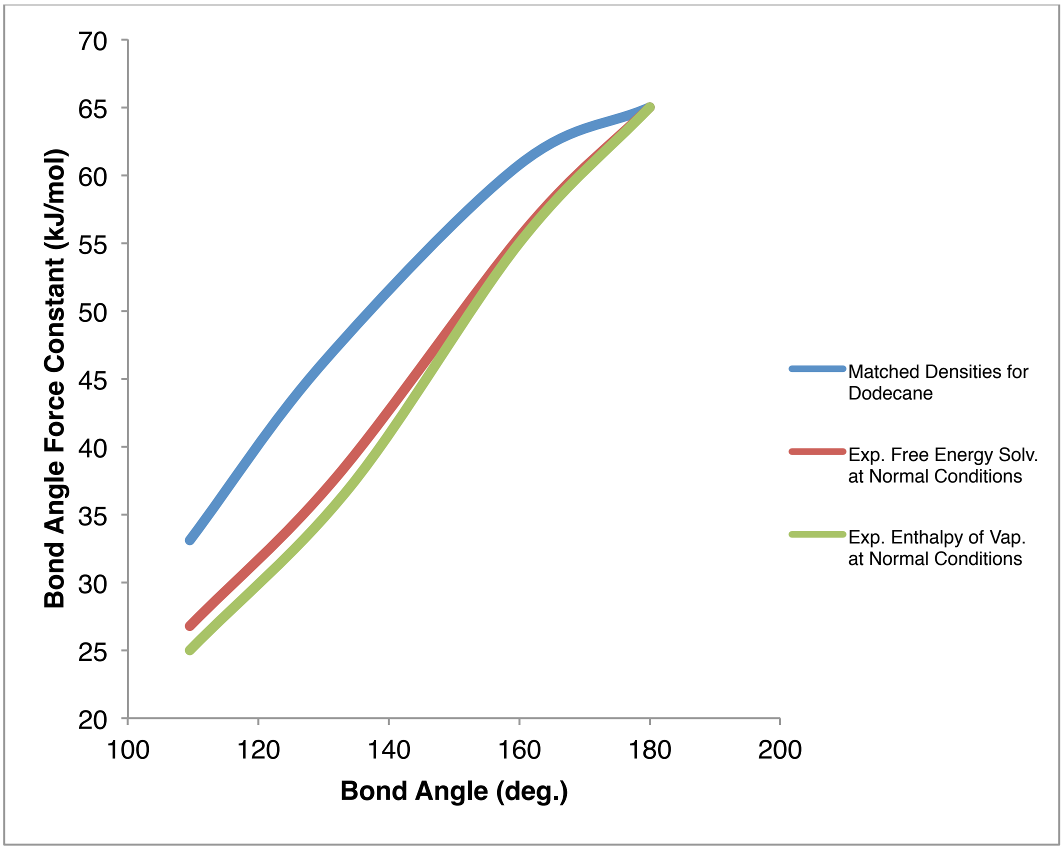

Figure 4.58: Determination of optimal set of parameters for the 4:1 mapped 3-bead models. The full lines show each property at standard temperature and pressure: density (blue), free energy of self-solvation (red), and enthalpy of vaporisation (green).[46, 47, 48, 49, 50, 51, 52, 53]

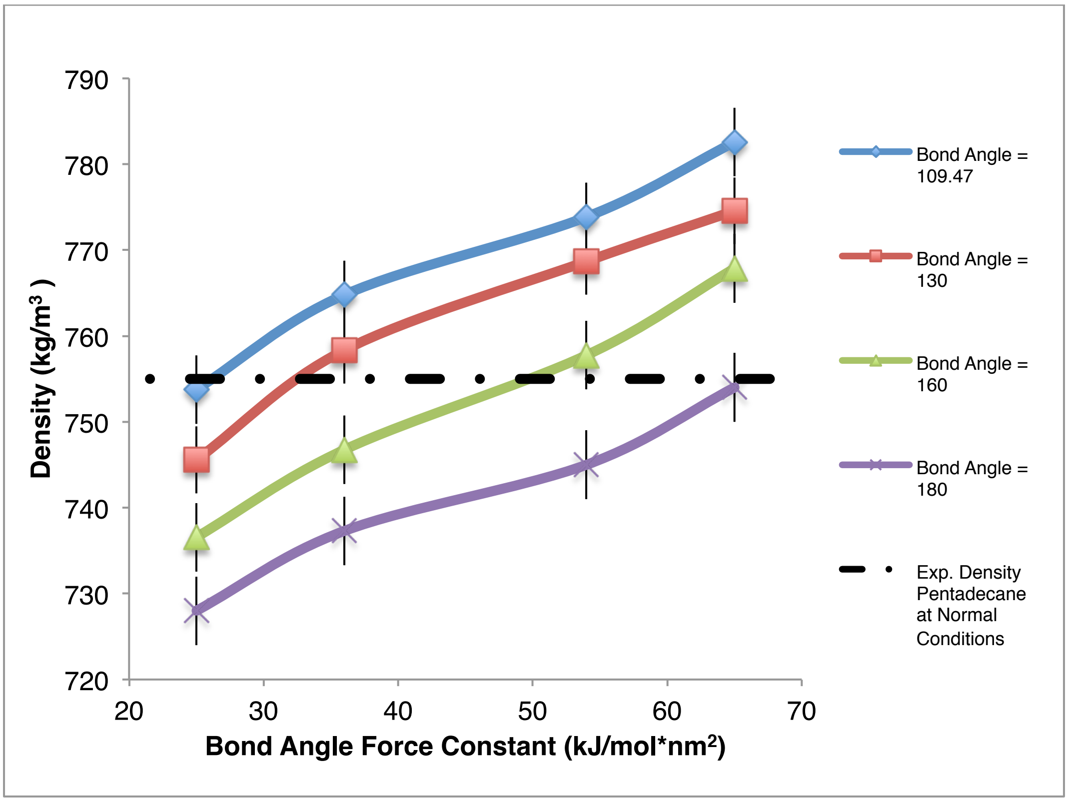
790
780
770
760
750
740
730
720
Density (kg/m³)
20
30
40
50
60
70
Bond Angle Force Constant (kJ/mol*nm²)
Bond Angle = 109.47
Bond Angle = 130
Bond Angle = 160
Bond Angle = 180
Exp. Density Pentadecane at Normal Conditions

a)

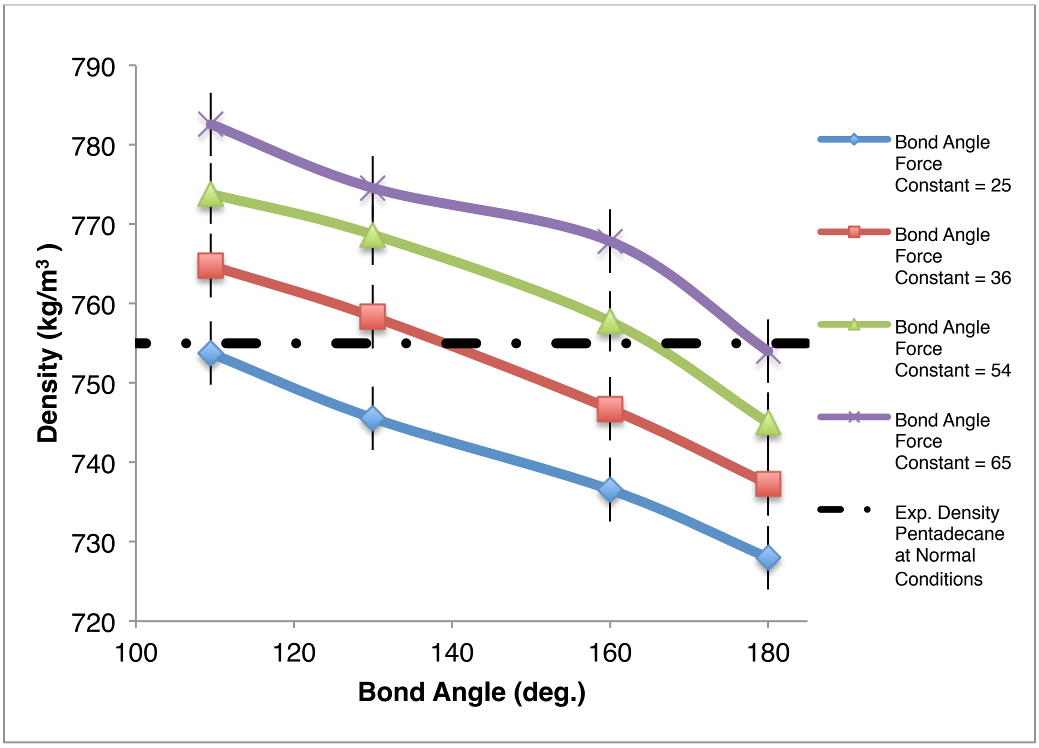

b)

Figures 4.59a-b: Selected densities determined for pentadecane's molecular weight, of the 3-bead solvent systems for different values of the bond angle and bond angle force constant parameters: **a)** selected bond angles at different bond angle force constants, and **b)** bond angle force constants at different bond length values. The black dashed line represents the experimental reference values for pentadecane at room temperature.[52, 53]

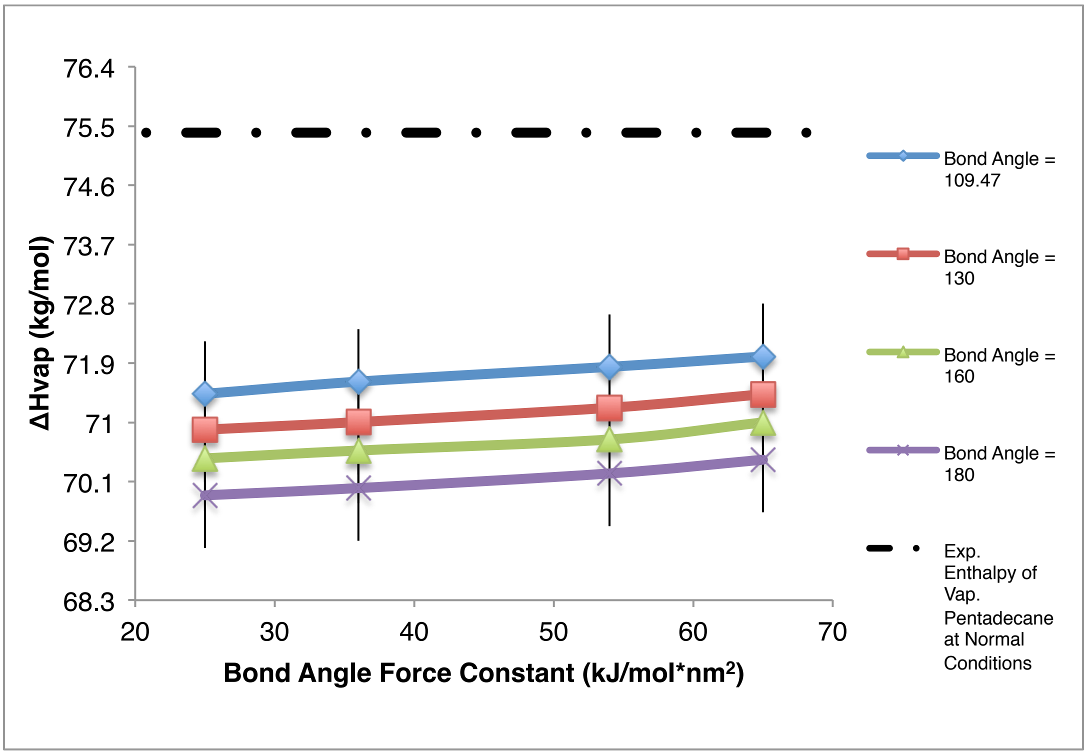
76.4
75.5
74.6
73.7
72.8
71.9
71
70.1
69.2
68.3
ΔHvap (kg/mol)
20
30
40
50
60
70
Bond Angle Force Constant (kJ/mol*nm²)
Bond Angle = 109.47
Bond Angle = 130
Bond Angle = 160
Bond Angle = 180
Exp. Enthalpy of Vap. Pentadecane at Normal Conditions

a)

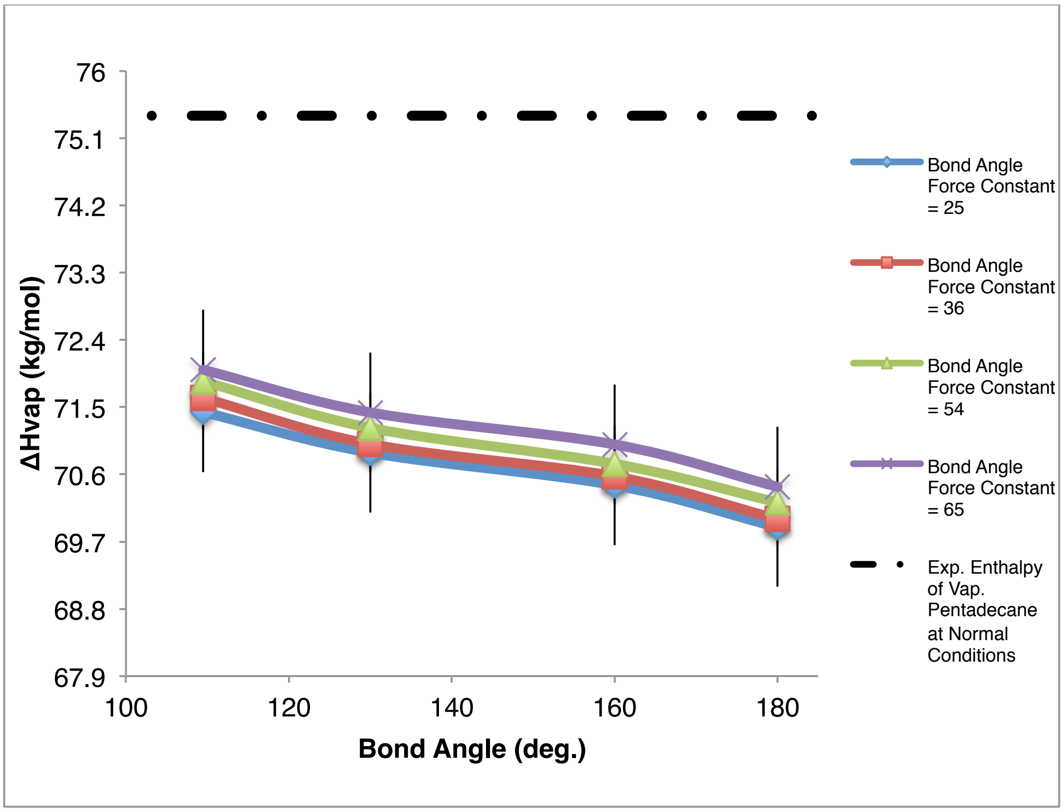

b)

Figures 4.60a-b: Selected enthalpies of vaporization of the 3-bead solvent systems for different values of the bond angle and bond angle force constant parameters: **a)** selected bond angles at different bond angle force constants, and **b)** bond angle force constants at different bond angle values. The black dashed line represents the experimental reference values for pentadecane at room temperature.[48, 49, 50]

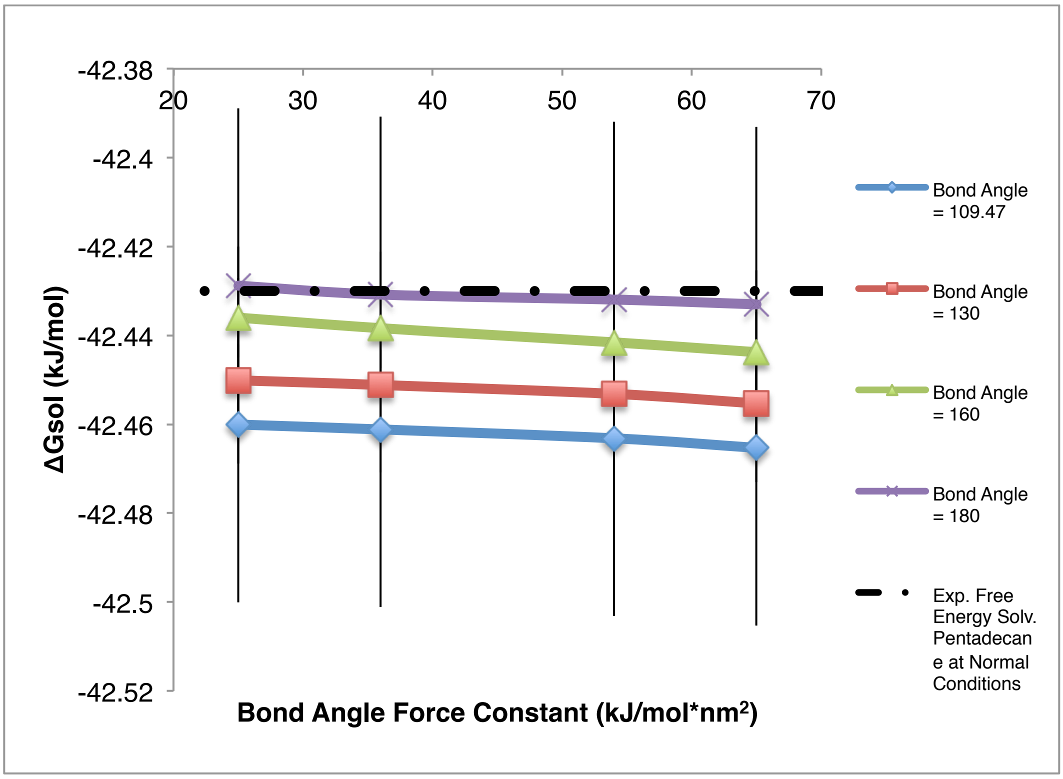
-42.38
-42.4
-42.42
-42.44
-42.46
-42.48
-42.5
-42.52
20
30
40
50
60
70
ΔGsol (kJ/mol)
Bond Angle Force Constant (kJ/mol*nm²)
Bond Angle = 109.47
Bond Angle = 130
Bond Angle = 160
Bond Angle = 180
Exp. Free Energy Solv. Pentadecane at Normal Conditions

a)

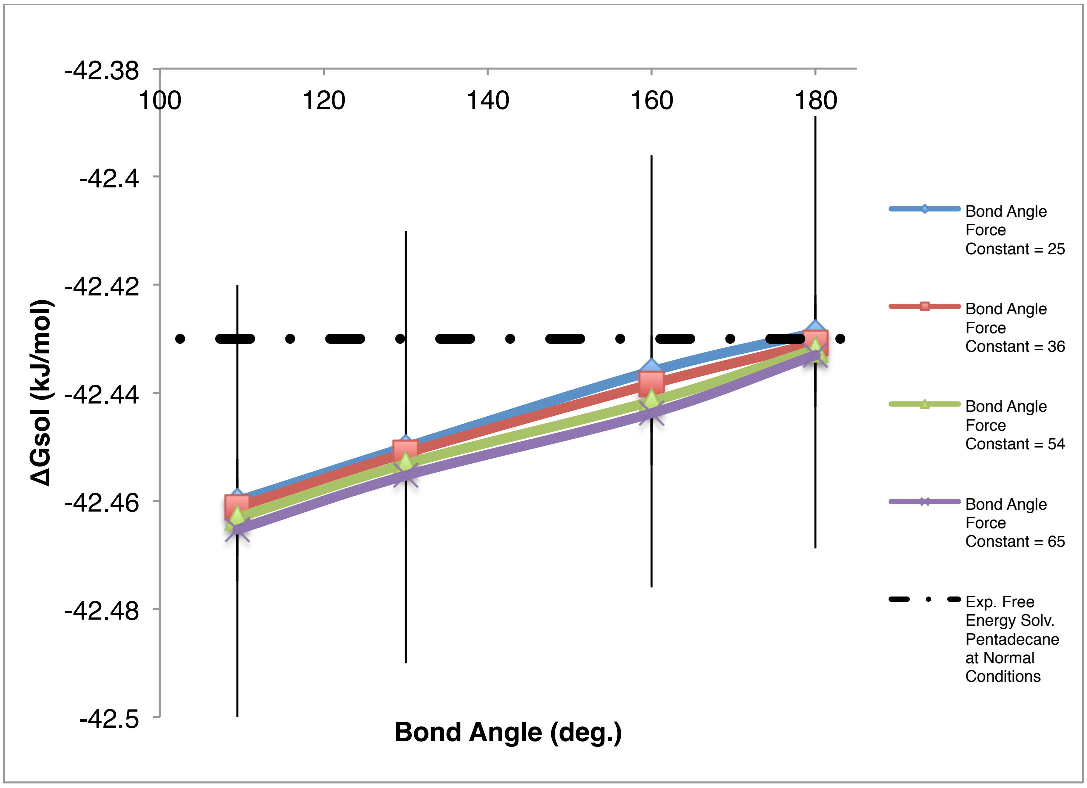

b)

Figures 4.61a-b: Selected self-solvation free energies of the 3-bead solvent systems for different values of the bond angles and bond angle force constant parameters: **a)** selected bond angles at different bond angle force constants, and **b)** bond angle force constants at different bond angle values. The black dashed line represents the experimental reference values for pentadecane at room temperature.[46, 47, 51]

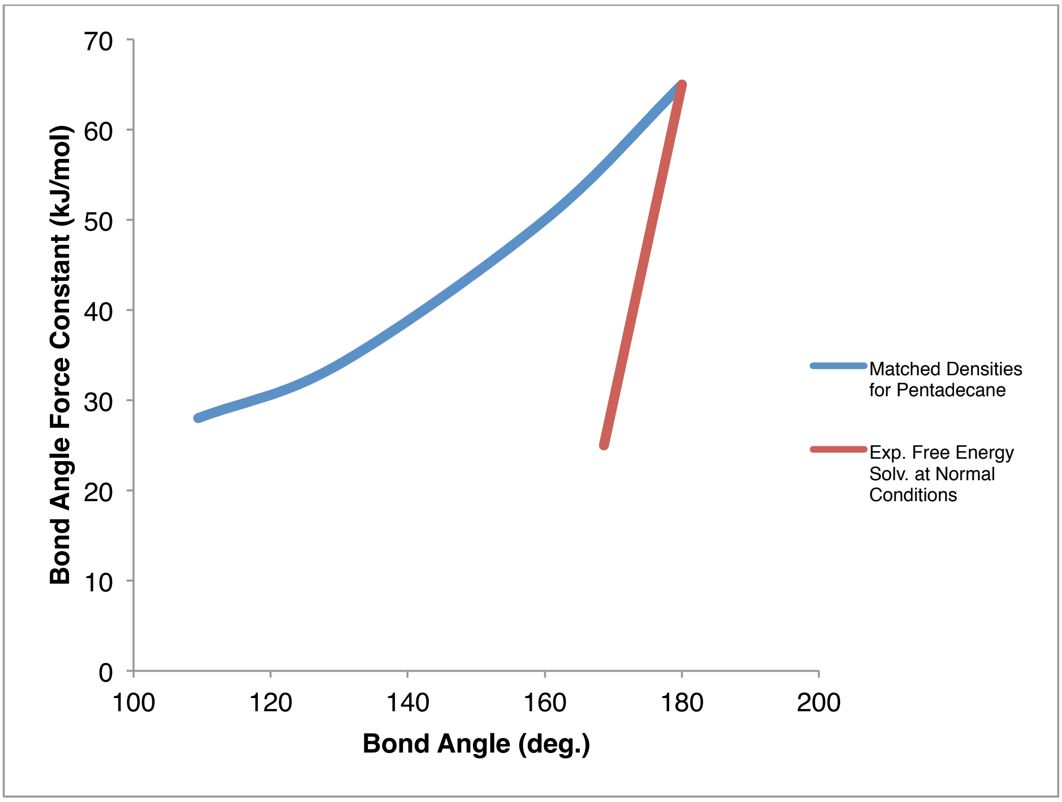

Figure 4.62: Determination of optimal set of parameters for the 5:1 mapped 3-bead models. The full lines show each property at standard temperature and pressure: density (blue), and free energy of self-solvation (red).[46, 47, 51, 52, 53]

Mapping Scheme	CG Alkane Models	Number of Beads	Density (this study, kg/m^3)	Density (experimental [52, 53], kg/m^3)
2:1	Ethane (C_2H_6)	1	320.92 ± 4.96	325
3:1	Propane (C_3H_8)	1	454.57 ± 4.64	459
4:1	Butane (C_4H_{10})	1	575.76 ± 4.29	576
5:1	Pentane (C_5H_{12})	1	638.95 ± 4.51	643
2:1	Butane (C_4H_{10})	2	573.76 ± 4.63	576
3:1	Hexane (C_6H_{14})	2	665.48 ± 4.49	669
4:1	Octane (C_8H_{18})	2	690.25 ± 4.42	692
5:1	Decane ($C_{10}H_{22}$)	2	725.66 ± 4.73	730
2:1	Hexane (C_6H_{14})	3	664.89 ± 4.56	669
3:1	Nonane (C_9H_{20})	3	714.57 ± 4.39	717
4:1	Dodecane ($C_{12}H_{26}$)	3	746.38 ± 4.48	750
5:1	Pentadecane ($C_{15}H_{32}$)	3	750.83 ± 4.60	755
2:1	Octane (C_8H_{18})	4	689.58 ± 3.81	692
3:1	Dodecane ($C_{12}H_{26}$)	4	747.53 ± 4.79	750
4:1	Hexadecane ($C_{16}H_{34}$)	4	766.64 ± 4.87	770
5:1	Eicosane ($C_{20}H_{42}$)	4	784.52 ± 4.64	789

Table 4.12: Density results for this study's models for 2:1, 3:1, 4:1, and 5:1 mapping and 1-bead systems, 2-bead systems, 3-bead systems, and 4-bead systems, compared to experimental data for linear alkanes.[52, 53]

Mapping Scheme	CG Alkane Models	Number of Beads	ΔHvap (this study, kJ/mol)	ΔHvap (experimental [48, 49, 50], kJ/mol)
2:1	Ethane (C2H6)	1	13.96 ± 0.84	13.7
3:1	Propane (C3H8)	1	17.20 ± 0.43	16.5
4:1	Butane (C4H10)	1	22.38 ± 0.59	22.4
5:1	Pentane (C5H12)	1	26.77 ± 0.66	27.4
2:1	Butane (C4H10)	2	19.63 ± 0.72	22.4
3:1	Hexane (C6H14)	2	29.59 ± 0.65	30
4:1	Octane (C8H18)	2	39.71 ± 0.82	41
5:1	Decane (C10H22)	2	44.46 ± 0.73	50.9
2:1	Hexane (C6H14)	3	29.36 ± 0.78	30
3:1	Nonane (C9H20)	3	48.01 ± 0.53	46.4
4:1	Dodecane (C12H26)	3	60.89 ± 0.48	61
5:1	Pentadecane (C15H32)	3	70.42 ± 0.76	75.4
2:1	Octane (C8H18)	4	39.82 ± 0.65	41
3:1	Dodecane (C12H26)	4	60.58 ± 0.69	61
4:1	Hexadecane (C16H34)	4	78.85 ± 0.72	80.6
5:1	Eicosane (C20H42)	4	87.89 ± 0.79	100.1

Table 4.13: Enthalpy of vaporisation results for this study's models for 2:1, 3:1, 4:1, and 5:1 mapping and 1-bead systems, 2-bead systems, 3-bead systems, and 4-bead systems, compared to the interpolated experimental and experimental data results compared to experimental data for linear alkanes.[48, 49, 50]

Mapping Scheme	**CG Alkane Models**	**Number of Beads**	**ΔGsol (this study, kJ/mol)**	**ΔGsol (experimental [46, 47, 51], kJ/mol)**
2:1	Ethane (C_2H_6)	1	-4.78 ± 0.66	*-4.79*
3:1	Propane (C_3H_8)	1	-6.10 ± 0.56	*-5.99*
4:1	Butane (C_4H_{10})	1	-10.82 ± 0.79	*-11.48*
5:1	Pentane (C_5H_{12})	1	-15.23 ± 0.48	-14.8
2:1	Butane (C_4H_{10})	2	-10.94 ± 0.65	*-11.48*
3:1	Hexane (C_6H_{14})	2	-16.04 ± 0.74	-16.88
4:1	Octane (C_8H_{18})	2	-22.08 ± 0.65	-22.1
5:1	Decane ($C_{10}H_{22}$)	2	-26.95 ± 0.57	*-26.99*
2:1	Hexane (C_6H_{14})	3	-15.69 ± 0.06	-16.88
3:1	Nonane (C_9H_{20})	3	-24.61 ± 0.07	-24.69
4:1	Dodecane ($C_{12}H_{26}$)	3	-32.65 ± 0.04	*-31.23*
5:1	Pentadecane ($C_{15}H_{32}$)	3	-41.76 ± 0.04	*-42.43*
2:1	Octane (C_8H_{18})	4	-22.34 ± 0.78	*-22.1*
3:1	Dodecane ($C_{12}H_{26}$)	4	-32.12 ± 0.69	*-31.23*
4:1	Hexadecane ($C_{16}H_{34}$)	4	-43.91± 0.82	-43.96
5:1	Eicosane ($C_{20}H_{42}$)	4	-59.88 ± 0.77	*-60.21*

Table 4.14: Free energy of self-solvation results for this study's models for 2:1, 3:1, 4:1, and 5:1 mapping and 1-bead systems, 2-bead systems, 3-bead systems, and 4-bead systems, compared to the interpolated experimental and experimental data for linear alkanes.[46, 47, 51] Italicised results represent interpolated data.

Mapping Scheme	**CG Alkane Models**	**Number of Beads**	**Self-Diffusion Coefficient (this study, m^2/s)**	**Self-Diffusion Coefficient (experimental [54], m^2/s)**
2:1	Ethane (C2H6)	1	1.13 x 10^{-7} ± 0.33	*1.26 x 10^{-7}*
3:1	Propane (C3H8)	1	9.27 x 10^{-8} ± 0.36	*9.43 x 10^{-8}*
4:1	Butane (C4H10)	1	8.41 x 10^{-8} ± 0.29	*8.53 x 10^{-8}*
5:1	Pentane (C5H12)	1	7.05 x 10^{-8} ± 0.42	*7.21 x 10^{-8}*
2:1	Butane (C4H10)	2	8.39 x 10^{-8} ± 0.87	*8.53 x 10^{-8}*
3:1	Hexane (C6H14)	2	6.67 x 10^{-8} ± 0.66	*6.85 x 10^{-8}*
4:1	Octane (C8H18)	2	5.54 x 10^{-8} ± 0.71	*5.41 x 10^{-8}*
5:1	Decane (C10H22)	2	4.15 x 10^{-8} ± 0.69	*4.49 x 10^{-8}*
2:1	Hexane (C6H14)	3	6.58 x 10^{-8} ± 0.34	*6.85 x 10^{-8}*
3:1	Nonane (C9H20)	3	3.48 x 10^{-8} ± 0.51	*4.07 x 10^{-8}*
4:1	Dodecane (C12H26)	3	11.38 x 10^{-10} ± 0.37	*11.92 x 10^{-10}*
5:1	Pentadecane (C15H32)	3	7.42 x 10^{-10} ± 0.40	*6.01 x 10^{-10}*
2:1	Octane (C8H18)	4	8.61 x 10^{-8} ± 0.56	*5.41 x 10^{-8}*
3:1	Dodecane (C12H26)	4	11.28 x 10^{-10} ± 0.42	*11.92 x 10^{-10}*
4:1	Hexadecane (C16H34)	4	7.54 x 10^{-10} ± 0.45	*7.87 x 10^{-10}*
5:1	Eicosane (C20H42)	4	4.11 x 10^{-10} ± 0.53	*4.34 x 10^{-10}*

Table 4.15: Self-diffusion coefficient results for this study's models for 2:1, 3:1, 4:1, and 5:1 mapping and 1-bead systems, 2-bead systems, 3-bead systems, and 4-bead systems, compared to the interpolated experimental and experimental data results compared to the interpolated experimental and experimental data for linear alkanes.[54] Italicised results represent interpolated data.

Mapping Scheme	CG Alkane Models	Number of Beads	Shear Viscosity (this study, mPas)	Shear Viscosity (experimental [58, 59], mPas)
2:1	Ethane (C2H6)	1	0.119 ± 0.28	n/a
3:1	Propane (C3H8)	1	0.303 ± 0.14	n/a
4:1	Butane (C4H10)	1	0.401 ± 0.21	*0.33*
5:1	Pentane (C5H12)	1	0.491 ± 0.23	0.38
2:1	Butane (C4H10)	2	0.321 ± 0.29	*0.33*
3:1	Hexane (C6H14)	2	0.474 ± 0.14	0.41
4:1	Octane (C8H18)	2	0.631 ± 0.18	0.56
5:1	Decane (C10H22)	2	0.786 ± 0.11	0.73
2:1	Hexane (C6H14)	3	0.53 ± 0.29	0.41
3:1	Nonane (C9H20)	3	0.832 ± 0.35	0.66
4:1	Dodecane (C12H26)	3	1.13 ± 0.27	1.24
5:1	Pentadecane (C15H32)	3	1.41 ± 0.31	n/a
2:1	Octane (C8H18)	4	0.726 ± 0.22	0.56
3:1	Dodecane (C12H26)	4	1.172 ± 0.16	1.24
4:1	Hexadecane (C16H34)	4	1.50 ± 0.19	*1.62*
5:1	Eicosane (C20H42)	4	1.87 ± 0.25	n/a

Table 4.16: Shear viscosity results for this study's models for 2:1, 3:1, 4:1, and 5:1 mapping and 1-bead systems, 2-bead systems, 3-bead systems, and 4-bead systems, compared to the interpolated experimental and experimental data results compared to the interpolated experimental and experimental for linear alkanes.[58, 59] Italicised results represent interpolated data.

Mapping Scheme	CG Alkane Models	Number of Beads	Radius of Gyration (this study, nm)	Radius of Gyration (simulations; AA [60], CG [31], nm)
2:1	Butane (C_4H_{10})	2	0.093 ± 0.36	0.282
3:1	Hexane (C_6H_{14})	2	0.292 ± 0.29	0.476
4:1	Octane (C_8H_{18})	2	0.445 ± 0.31	0.692
5:1	Decane ($C_{10}H_{22}$)	2	0.641 ± 0.30	0.903
2:1	Hexane (C_6H_{14})	3	0.343 ± 0.23	0.476
3:1	Nonane (C_9H_{20})	3	0.762 ± 0.37	0.933
4:1	Dodecane ($C_{12}H_{26}$)	3	1.24 ± 0.24	1.455
5:1	Pentadecane ($C_{15}H_{32}$)	3	1.881 ± 0.36	n/a
2:1	Octane (C_8H_{18})	4	0.312 ± 0.36	0.692
3:1	Dodecane ($C_{12}H_{26}$)	4	1.056 ± 0.45	1.455
4:1	Hexadecane ($C_{16}H_{34}$)	4	1.995 ± 0.38	2.324
5:1	Eicosane ($C_{20}H_{42}$)	4	2.879 ± 0.55	n/a

Table 4.17: Radius of gyration results for this study's models for 2:1, 3:1, 4:1, and 5:1 mapping and 1-bead systems, 2-bead systems, 3-bead systems, and 4-bead systems, compared to the **a)** AA simulation data[60], and **b)** CG simulated data for linear alkanes.[31]

Mapping Scheme	**CG Alkane Models**	**Number of Beads**	**ΔGsol (this study, kJ/mol)**	**ΔGsol (experimental [65, 66, 67, 68], kJ/mol)**
2:1	Ethane (C_2H_6)	1	14.99 ± 0.65	15.57
3:1	Propane (C_3H_8)	1	15.82 ± 0.52	16.09
4:1	Butane (C_4H_{10})	1	16.40 ± 0.67	16.58
5:1	Pentane (C_5H_{12})	1	17.08 ± 0.46	17.48
2:1	Butane (C_4H_{10})	2	16.39 ± 0.62	16.58
3:1	Hexane (C_6H_{14})	2	17.72 ± 0.67	18.06
4:1	Octane (C_8H_{18})	2	19.35 ± 0.56	19.42
5:1	Decane ($C_{10}H_{22}$)	2	20.38 ± 0.66	20.7
2:1	Hexane (C_6H_{14})	3	18.05 ± 0.58	18.06
3:1	Nonane (C_9H_{20})	3	21.01 ± 0.51	21
4:1	Dodecane ($C_{12}H_{26}$)	3	24.63 ± 0.55	24.8
5:1	Pentadecane ($C_{15}H_{32}$)	3	25.31 ± 0.59	*25.63*
2:1	Octane (C_8H_{18})	4	19.38 ± 0.84	19.42
3:1	Dodecane ($C_{12}H_{26}$)	4	24.71 ± 0.68	24.8
4:1	Hexadecane ($C_{16}H_{34}$)	4	27.09 ± 0.54	27.26
5:1	Eicosane ($C_{20}H_{42}$)	4	28.29 ± 0.63	28.47

Table 4.18: Free energy of solvation in water results for this study's models for 2:1, 3:1, 4:1, and 5:1 mapping and 1-bead systems, 2-bead systems, 3-bead systems, and 4-bead systems, compared to the interpolated experimental and experimental data results for linear alkanes.[65, 66, 67, 68] Italicised results represent interpolated data.

APPENDIX B

PEO Models	Density (this study, kg/m^3)	Density (experimental [76], kg/m^3)
1[15]	773.01 ± 5.51	735
2[17,23]	811.47 ± 4.78	735
3[18]	831.66 ± 5.22	735
4[19]	812.80 ± 4.90	735
5[20]	810.43 ± 5.03	735
6[21]	989.23 ± 5.65	735
7[22]	995.34 ± 5.08	735

a)

PPO Models	Density (this study, kg/m^3)	Density (experimental [77], kg/m^3)
8[20]	729.12 ± 5.60	725
9[23]	850.74 ± 4.39	725
10[21]	852.36 ± 6.28	725
11[22]	908.84 ± 5.16	725

b)

Tables 5.15a-b: Density results for this study's **a)** PEO monomer models compared to the experimental data for DE[76], and **b)** PPO monomer models compared against simulation results from a previous study for MOE.[77]

PEO Models	ΔHvap (this study, kJ/mol)	ΔHvap (experimental [83], kJ/mol)
1[15]	20.20 ± 0.61	19.8
2[17,23]	27.45 ± 0.64	19.8
3[18]	31.42 ± 0.69	19.8
4[19]	26.99 ± 0.70	19.8
5[20]	30.11 ± 0.68	19.8
6[21]	36.20 ± 0.63	19.8
7[22]	37.03 ± 0.62	19.8

a)

PPO Models	ΔHvap (this study, kJ/mol)	ΔHvap (experimental [84], kJ/mol)
8[20]	20.57 ± 0.55	24.5
9[23]	25.02 ± 0.59	24.5
10[21]	25.04 ± 0.63	24.5
11[22]	29.98 ± 0.56	24.5

b)

Tables 5.16a-b: Enthalpy of vaporisation results for this study's **a)** PEO monomer models compared to the experimental data for DE[83], and **b)** PPO monomer models compared against simulation results from a previous study for MOE.[84]

PEO Models	ΔGsol (this study, kJ/mol)	ΔGsol (experimental [76], kJ/mol)
1[15]	-10.62 ± 0.59	-11.08
2[17,23]	-12.59 ± 0.78	-11.08
3[18]	-13.66 ± 0.65	-11.08
4[19]	-12.72 ± 0.73	-11.08
5[20]	-12.61 ± 0.57	-11.08
6[21]	-14.67 ± 0.66	-11.08
7[22]	-14.92 ± 0.70	-11.08

a)

PPO Models	ΔGsol (this study, kJ/mol)	ΔGsol (experimental [77], kJ/mol)
8[20]	-9.32 ± 0.46	-13.09
9[23]	-14.29 ± 0.58	-13.09
10[21]	-14.31 ± 0.60	-13.09
11[22]	-15.67 ± 0.49	-13.09

b)

Tables 5.17a-b: Free energy of self-solvation results for this study's **a)** PEO monomer models compared to the experimental data for DE[76], and **b)** PPO monomer models compared against simulation results from a previous study for MOE.[77]

PEO2 Models	Density (this study, kg/m^3)	Density (experimental [52, 66], kg/m^3)
1[15]	1004.90 ± 6.40	945
2[17,23]	1054.03 ± 5.83	945
3[18]	1061.92 ± 6.02	945
4[19]	1055.11 ± 5.77	945
5[20]	1081.26 ± 6.12	945
6[21]	1365.62 ± 5.95	945
7[22]	1464.58 ± 5.46	945

a)

PPO2 Models	Density (this study, kg/m^3)	Density (experimental [26, 52], kg/m^3)
8[20]	957.48 ± 5.30	855
9[23]	1095.23 ± 5.62	855
10[21]	1099.62 ± 6.01	855
11[22]	1181.06 ± 6.13	855

b)

PPO2 Models	Density (this study, kg/m^3)	Density (experimental [64, 65], kg/m^3)
8[20]	1086.81 ± 5.60	801
9[23]	1130.99 ± 5.20	801
10[21]	1142.41 ± 5.88	801
11[22]	1340.75 ± 6.17	801

c)

Tables 5.18a-c: Comparison between the mass density of this study's models[15,17-23] and experimental data for **a)** DME[52, 66] **b)** DMP[26, 52], and **c)** DEE.[64, 65]

PEO2 Models	ΔHvap (this study, kJ/mol)	ΔHvap (experimental [27, 66], kJ/mol)
1[15]	30.87 ± 0.67	36.40
2[17,23]	37.33 ± 0.24	36.40
3[18]	40.34 ± 0.52	36.40
4[19]	36.28 ± 0.44	36.40
5[20]	39.48 ± 0.49	36.40
6[21]	45.56 ± 0.70	36.40
7[22]	46.69 ± 0.51	36.40

a)

PPO2 Models	ΔHvap (this study, kJ/mol)	ΔHvap (experimental [26], kJ/mol)
8[20]	33.34 ± 0.63	37.02
9[23]	50.46 ± 0.49	37.02
10[21]	50.55 ± 0.55	37.02
11[22]	58.36 ± 0.60	37.02

b)

PPO2 Models	ΔHvap (this study, kJ/mol)	ΔHvap (experimental [65], kJ/mol)
8[20]	33.34 ± 0.63	36.30
9[23]	50.46 ± 0.49	36.30
10[21]	50.55 ± 0.55	36.30
11[22]	58.36 ± 0.60	36.30

c)

Tables 5.19a-c: Comparison between the enthalpy of vaporisation of this study's models[15, 17-23] and experimental data for **a)** DME[27, 66] and **b)** DMP[26] and **c)** DEE.[65]

PEO2 Models	ΔGsol (this study, kJ/mol)	ΔGsol (experimental [57, 66], kJ/mol)
1[15]	-20.29 ± 0.78	-19.32
2[17,23]	-23.96 ± 0.81	-19.32
3[18]	-26.34 ± 0.67	-19.32
4[19]	-24.92 ± 0.72	-19.32
5[20]	-27.81 ± 0.70	-19.32
6[21]	-31.67 ± 0.63	-19.32
7[22]	-34.88 ± 0.62	-19.32

a)

PPO2 Models	ΔGsol (this study, kJ/mol)	ΔGsol (experimental [26, 57], kJ/mol)
8[20]	-21.01 ± 0.65	-20.43
9[23]	-28.33 ± 0.61	-20.43
10[21]	-29.98 ± 0.54	-20.43
11[22]	-37.11 ± 0.59	-20.43

b)

PPO2 Models	ΔGsol (this study, kJ/mol)	ΔGsol (experimental [64, 65], kJ/mol)
8[20]	-21.01 ± 0.65	-21.78
9[23]	-28.33 ± 0.61	-21.78
10[21]	-29.98 ± 0.54	-21.78
11[22]	-37.11 ± 0.59	-21.78

c)

Tables 5.20a-c: Comparison between the free energies of self-solvation of this study's models[15,17-23] and estimated experimental data for **a)** DME[57, 66] and **b)** DMP[26, 57] and **c)** DEE.[64, 65]

PEO2 Models	Self-Diffusion Coefficient (this study, m^2/s)	Self-Diffusion Coefficient (experimental [28], m^2/s)
1[15]	$2.96 \times 10^{-9} \pm 0.34 \times 10^{-9}$	3.2×10^{-9}
2[17,23]	$2.54 \times 10^{-9} \pm 0.26 \times 10^{-9}$	3.2×10^{-9}
3[18]	$2.09 \times 10^{-9} \pm 0.38 \times 10^{-9}$	3.2×10^{-9}
4[19]	$2.48 \times 10^{-9} \pm 0.27 \times 10^{-9}$	3.2×10^{-9}
5[20]	$2.56 \times 10^{-9} \pm 0.32 \times 10^{-9}$	3.2×10^{-9}
6[21]	$1.73 \times 10^{-9} \pm 0.25 \times 10^{-9}$	3.2×10^{-9}
7[22]	$1.01 \times 10^{-9} \pm 0.30 \times 10^{-9}$	3.2×10^{-9}

a)

PPO2 Models	Self-Diffusion Coefficient (this study, m^2/s)	Self-Diffusion Coefficient (simulation [25], m^2/s)
8[20]	$3.29 \times 10^{-9} \pm 0.21 \times 10^{-9}$	3.6×10^{-9}
9[23]	$1.79 \times 10^{-9} \pm 0.28 \times 10^{-9}$	3.6×10^{-9}
10[21]	$1.75 \times 10^{-9} \pm 0.26 \times 10^{-9}$	3.6×10^{-9}
11[22]	$0.04 \times 10^{-9} \pm 0.32 \times 10^{-9}$	3.6×10^{-9}

b)

Tables 5.21a-b: Self-diffusion coefficient results for this study's **a)** PEO2 models compared to the experimental data for DME, and **b)** PPO2 models compared against simulation results from a previous study for DMP.[25, 28]

PEO2 Models	Shear Viscosity (this study, mPas)	Shear Viscosity (experimental [29], mPas)
1[15]	0.431 ± 0.24	0.41
2[17,23]	0.467 ± 0.21	0.41
3[18]	0.498 ± 0.27	0.41
4[19]	0.459 ± 0.26	0.41
5[20]	0.466 ± 0.33	0.41
6[21]	0.723 ± 0.28	0.41
7[22]	0.894 ± 0.31	0.41

a)

PPO2 Models	Shear Viscosity (this study, mPas)	Shear Viscosity (simulation [25], mPas)
8[20]	0.377 ± 0.18	0.34
9[23]	0.720 ± 0.25	0.34
10[21]	0.727 ± 0.21	0.34
11[22]	0.993 ± 0.24	0.34

b)

Tables 5.22a-b: Shear viscosity results for this study's **a)** PEO2 models compared against simulation results from a previous study for DME, and **b)** PPO2 models compared against a separate simulation results from a previous study for DMP.[25, 29]

PEO2 Models	ΔGsol (this study, kJ/mol)	ΔGsol (experimental [27, 28], kJ/mol)
1[15]	-20.68 ± 0.53	-20.90
2[17,23]	-24.86 ± 0.72	-20.90
3[18]	-25.77 ± 0.80	-20.90
4[19]	-22.21 ± 0.64	-20.90
5[20]	-24.50 ± 0.71	-20.90
6[21]	-33.22 ± 0.59	-20.90
7[22]	-35.67 ± 0.58	-20.90

a)

PPO2 Models	ΔGsol (this study, kJ/mol)	ΔGsol (simulation [25], kJ/mol)
8[20]	-17.93 ± 0.69	-16.0
9[23]	-20.06 ± 0.58	-16.0
10[21]	-20.64 ± 0.66	-16.0
11[22]	-25.89 ± 0.60	-16.0

b)

Tables 5.23a-b: Comparison between the solvation in water of this study's models[15-23] and **a)** experimental data for DME[27, 28] and **b)** previous simulation data for DMP.[25]

PEO Models	**Bonded Interactions**			
	θ (deg.)	**kθ (kJ/mol)**	**Φ (deg.)**	**kΦ (kJ/mol)**
1[15]	124	50	180	1.96. .18, .33, .12
2[17]	130	80	180	1.96. .18, .33, .12
3[18]	122	400	180	1.96. .18, .33, .12
4[19]	140	25	n/a	n/a
5[20]	115	50	180	1.96. .18, .33, .12
6[21]	180	25	n/a	n/a
7[22]	155	40	n/a	n/a

a)

PPO Models	**Bonded Interactions**			
	θ (deg.)	**kθ (kJ/mol)**	**Φ (deg.)**	**kΦ (kJ/mol)**
8[20]	120	50	180	1.96, 5, .33, .12
9[23]	130	50	180	1.96. .18, .33, .12
10[21]	180	25	n/a	n/a
11[22]	140	40	n/a	n/a

b)

Tables 5.24a-b: Bonded interaction parameters for bond angle and bond angle force constants, and dihedral angle and dihedral angle force constants for the **a)** PEO models with themselves and **b)** PPO models with themselves.[15, 17 ,18, 19 , 20, 21, 22, 23]

PEO/PPO Homopolymers	**End-to-end Distance in Water (this study, nm)**	**End-to-end Distance in Water (simulation, [51], nm)**
PEO2	0.74 ± 0.23	0.65 ± 0.001
PEO36	3.15 ± 0.19	3.00 ± 0.08
PPO2	0.72 ± 0.20	0.63 ± 0.002
PPO36	2.99 ± 0.22	2.87 ± 0.17

a)

PEO/PPO Homopolymers	End-to-end Distance in Heptane (this study, nm)	End-to-end Distance in Heptane (simulation, [51], nm)
PEO2	0.71 ± 0.20	0.63 ± 0.002
PEO36	1.52 ± 0.21	1.43 ± 0.05
PPO2	0.69 ± 0.28	0.70 ± 0.002
PPO36	2.18 ± 0.25	2.07 ± 0.18

b)

Tables 5.25a-b: End-to-end distances for this study's PEO and PPO homopolymers of lengths 2 and 36 in **a)** CG MARTINI water and **b)** our heptane model compared to a previous simulation study.[51]

PEO/PPO Monomers	Radius of Gyration (this study at 298 K, nm)	Radius of Gyration (simulation at 300 K [12], nm)
30 PEO	0.97 ± 0.16	0.83 ± 0.11
60 PEO	1.46 ± 0.24	1.34 ± 0.21
90 PEO	1.86 ± 0.18	1.71 ± 0.29
30 PPO	1.07 ± 0.22	0.92 ± 0.14
60 PPO	1.55 ± 0.19	1.40 ± 0.17
90 PPO	1.61 ± 0.13	1.56 ± 0.20

Table 5.26: Radius of gyration results for this study's CG MARTINI PEO and PPO monomers of lengths 30, 60, and 90 compared to the results from a previous study.[12]

APPENDIX C

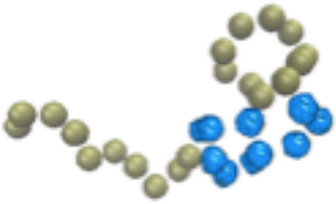

Figure 6.11: A VMD snapshot of a Pluronic (i.e. PEO_{10} PPO_{10} PEO_{10}) model with PEO-PPO parameters from an ultimately rejected study.[3] The yellow beads represent PEO and the blue beads represent PPO.

Pluronic Models	**Density (this study, kg/m^3)**	**Density (experimental [14], kg/m^3)**
L31	1026.33 ± 6.5	1010
L44	1045.71 ± 5.1	1050
L62	1034.62 ± 6.9	1030
L64	1046.05 ± 5.3	1040
P85	1054.47 ± 6.2	1040
P123	1043.89 ± 4.8	1040
F38	902.34 ± 5.0	651

Table 6.5: Comparison between the mass density of this study's Pluronic models Pluronics L31, L44, L62, and L64, P85, P123, and F38, and experimental data for these triblock copolymers at room temperature.[14]

Pluronic Models	Shear Viscosity at 278.15K (this study, mPas)	Shear Viscosity at 278.15K (simulation [13, 14], mPas)
L31	416.46 ± 0.48	440
L44	424.87 ± 0.62	450
L64	519.69 ± 0.74	850

a)

Pluronic Models	Shear Viscosity at 333.15K (this study, mPas)	Shear Viscosity at 333.15K (simulation [13, 14], mPas)
P85	284.13 ± 0.68	310
P123	327.55 ± 0.59	350

b)

Tables 6.6a-b: Comparison between the shear viscosities of this study's Pluronic models **a)** Pluronics L31, L44, and L64 at 278.15K and **b)** Pluronics P85 and P123 at 333.15K, and experimental data for these triblock copolymers at those temperatures.[13, 14]

Pluronic Models	**Heat Capacity (this study, kg/mol*K)**	**Heat Capacity (experimental [15, 16, 17], kg/mol*K)**
P85	10.41± 0.85	*11.09*
P123	13.72 ± 0.79	14.24
F38	12.79 ± 0.81	*13.30*

Table 6.7: Comparison between the heat capacities of this study's Pluronic P85, P123, and F38 models, and interpolated and standard experimental data for these triblock copolymers at room temperature and standard pressure.[15, 16, 17] Italicised results represent interpolated data.

Single Pluronic Chain Models	**Radius of Gyration in Water (this study at 300 K, nm)**	**Radius of Gyration in Water (previous study at 300 K [1], nm)**
L31	0.99 ± 0.28	0.90 ± 0.25
L44	1.41 ± 0.31	1.35 ± 0.18
L61	1.39 ± 0.33	1.30 ± 0.25
L62	1.43 ± 0.34	1.33 ± 0.26
L64	1.41 ± 0.29	1.32 ± 0.20
P85	2.21 ± 0.30	2.11 ± 0.20
F38	3.48 ± 0.34	3.30 ± 0.24

a)

Single Pluronic Chain Models	Radius of Gyration in Water (this study at 293 K, nm)	Radius of Gyration in Water (previous study at 293 K [3], nm)
L64	1.72 ± 0.22	1.68 ± 0.08
P85	2.25 ± 0.37	2.19 ± 0.20
F38	3.29 ± 0.31	3.25 ± 0.22

b)

Tables 6.8a-b: Comparison between the radius of gyration results of this study's Pluronic models **a)** Pluronics L31, L44, L64, P85, and F38 at 300K and **b)** Pluronics L64, P85, and P123 at 273K, and simulated data for these triblock copolymers at those temperatures; 300K[1] and 273K.[3]

Pluronic Models	Micellisation Free Energy (this study, kg/mol*K)	Micellisation Free Energy (experimental [16, 19], kg/mol*K)
L44	-25.32 ± 1.84	*-13.36*
P123	-52.76 ± 2.05	-37.88

Table 6.9: Micellisation free energy results for the micelles produced in our 200 monomer chain simulations of Pluronics L44 and P123 compared to experimental values for; Pluronic L44[16] and Pluroinc P123.[19] Italicised results represent interpolated data.